



**HAL**  
open science

# Out-of-equilibrium electron dynamics of Dirac semimetals and strongly correlated materials

Niloufar Nilforoushan

► **To cite this version:**

Niloufar Nilforoushan. Out-of-equilibrium electron dynamics of Dirac semimetals and strongly correlated materials. Strongly Correlated Electrons [cond-mat.str-el]. Université Paris Saclay (COMUE), 2018. English. NNT: 2018SACLS573 . tel-02058653

**HAL Id: tel-02058653**

**<https://theses.hal.science/tel-02058653>**

Submitted on 6 Mar 2019

**HAL** is a multi-disciplinary open access archive for the deposit and dissemination of scientific research documents, whether they are published or not. The documents may come from teaching and research institutions in France or abroad, or from public or private research centers.

L'archive ouverte pluridisciplinaire **HAL**, est destinée au dépôt et à la diffusion de documents scientifiques de niveau recherche, publiés ou non, émanant des établissements d'enseignement et de recherche français ou étrangers, des laboratoires publics ou privés.

# Out-of-equilibrium electron dynamics of Dirac semimetals and strongly correlated materials

Thèse de doctorat de l'Université Paris-Saclay  
préparée à l'Université Paris-Sud

Ecole doctorale n°564: Physique en Île-de-France (PIF)  
Spécialité de doctorat: Physique

Thèse présentée et soutenue à Orsay, le 17 décembre 2018, par

**MME. NILOUFAR NILFOROUSHAN**

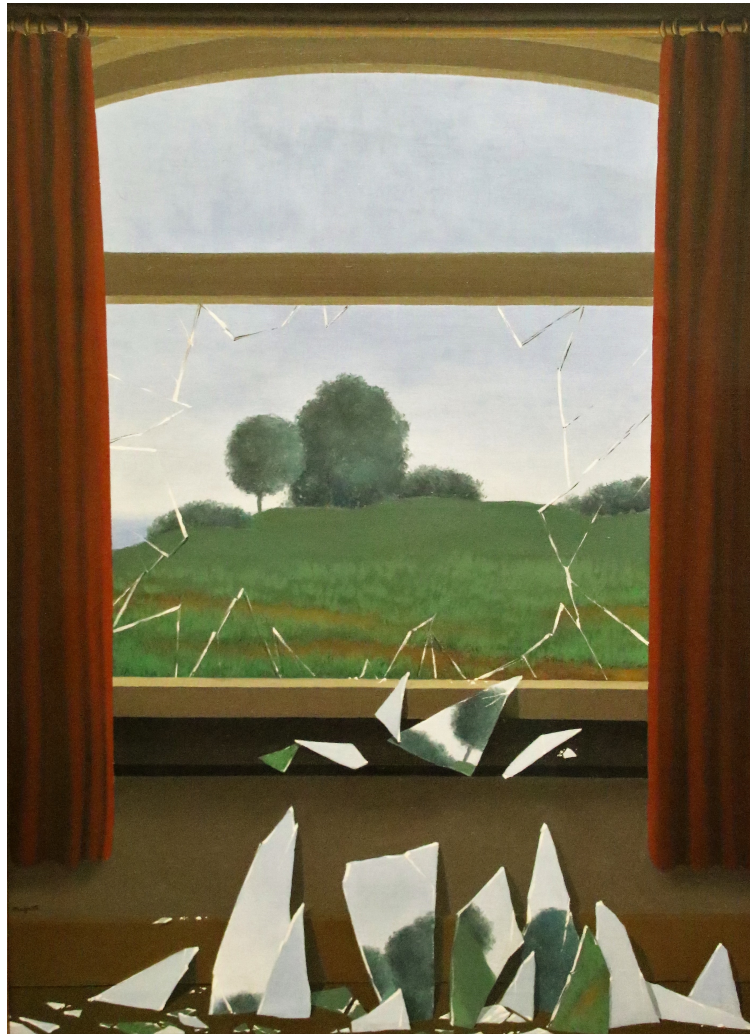
Composition du Jury :

M. Marc Gabay Professeur, Université Paris-Saclay (LPS)	Président du Jury
M. Karol Hricovini Professeur, Université Cergy-Pontoise (LPMS)	Rapporteur
M. Abhay Shukla Professeur, Sorbonne Université (IMPMC)	Rapporteur
Mme. Véronique Brouet Directrice de recherche, Université Paris-Saclay (LPS)	Examinatrice
M. Mustapha Zaghrioui Professeur, IUT de Blois, Département de Mesures Physiques (MP)	Examineur
M. Marino Marsi Professeur, Université Paris-Saclay (LPS)	Directeur de thèse
M. Evangelos Papalazarou Maître de Conférence, Université Paris-Saclay (LPS)	Co-encadrant de thèse (Membre invité)



*To Payam.*





*René Magritte. La clef des champs, 1936.*



# Acknowledgment

I truly owe to my advisor Marino Marsi for his continuous support, endless guidance and patience, and for his profound comprehension of everything. He taught me many things scientifically, professionally and most importantly, personally. He gave me the opportunity to work and interact with many people and to discover different places and laboratories. I am also deeply grateful to his trust on me by giving me the endless pleasure to teach and giving lectures. I thank my co-advisor, Evangelos Papalazarou. With him, I discovered what a real experiment on solids was all about. He explained me many times all steps of the experiment and was always there to help me. I miss all those fascinating discussions that we had all distance long from SOLEIL to the train station when we were missing the last bus.

I would like to thank my thesis committee Karol Hricovini, Abhay Shukla, Marc Gabay, Véronique Brouet, and Mustapha Zaghrioui, for the time they spent to read my dissertation and specially for their encouragement, insightful comments and discussion during my defense.

I am truly grateful to our collaborators at Sorbonne University. In particular, to Michele Casula, first for his enormous theoretical work and non-stop collaboration to interpret and understand the underlying physics of our work and second, for his excellent humor. It was always a great pleasure to work and discuss with him. I thank Andrea Gauzzi, Yannick Klein, and David Santos-Cottin for their collaboration and also for providing me the samples. I also thank our theorist collaborators at SISSA, Michele Fabrizio and Adriano Amaricci for their beautiful and fundamental interpretation of the data.

I am deeply thankful to Davide Boschetto from the LOA. I had a great chance to know him, learn from him, and to ask him my countless questions. Whenever he explained me a physical phenomenon or notion in any scale, I could not seize my great enthusiasm to hear and ask even more and to appreciate the way he explained every single thing. I am also grateful to him for his patience to read and correct my manuscript. I also thank Mariusz Lejman for his great help to perform the experiments.

I am happy to have the opportunity to work with people at the LPS and to have their help during my PhD especially Pascal Simons, Vincent Jacques, David Le Bolloc'h, and Nicolas Moisan. I also thank André Thiaville and Philippe Mendels for their care and attention to my work. I am thankful to Luca Perfetti and Zhesheng Chen for the stimulating discussions and in particular for their ideas and help for performing and improving the experiments on the FemtoARPES setup. I acknowledge the help and collaboration from people at the synchrotron Elettra with a special mention to Alexei Victorovich Barinov, Ivana Vobornik, Jun Fujii, and Pranab Das Kumar. From the T-Rex and Tera-Fermi laboratories, I would like to thank Federico Cilento, Andrea Perucchi, and Paola Di Pietro. In synchrotron SOLEIL, I am truly grateful to Claire Laulhé for her endless help and support during and after the beamtimes. I thank my great friend Marco Caputo for the long-lasting discussions, sleepless nights we were working together during the beamtimes, showing me wonderful places in Trieste, and of course for his great patience in explaining me the very fundamental notions in experimental physics. I would also like to thank my forever

wonderful and encouraging friend Isabel González Vallejo. Doing this PhD, offered me her precious friendship.

I am thankful to Philippe Mendels. I set the first step in the vast world of condensed matter physics while being completely absorbed by his lectures during my masters. I am also grateful to Marc Gabay. Without his support, it would not have been possible for me to reach to the point where I am now. I would also like to thank Natacha Kirova for her pure spirit of life and for her never-ending inspiration. She is a role model for me.

I owe to my mother, my first and forever support and life-coach. I am also deeply grateful to my father. He taught me strength and perseverance. I thank my sister not only for her constant moral and emotional support in my life, but simply for her being. I really owe it all to Payam who gave a meaning to everything, always stood by me and told me that I could. Without him, nothing is possible.

In the end, I would like to thank all people who helped me to accomplish my PhD and from whom I learned but I might have forgotten to mention. Life is a complex phenomenon. Every single interaction at its very microscopic scale, changes slightly our path and leads us towards improvements and better being in a bigger scale.

# Contents

<b>List of Figures</b>	<b>9</b>
<b>1 The physics of quantum materials</b>	<b>19</b>
1.1 Introduction . . . . .	19
1.2 Fermi liquid theory . . . . .	19
1.3 Strongly correlated materials: Metal to insulator transition . . . . .	21
1.3.1 Theoretical models . . . . .	23
1.3.1.1 Density functional theory . . . . .	24
1.3.1.2 Dynamical mean-field theory . . . . .	24
1.3.2 $V_2O_3$ , a prototype Mott-Hubbard material . . . . .	27
1.3.2.1 Crystal structure and electronic configuration . . . . .	27
1.4 Dirac semimetals . . . . .	29
1.4.1 Topological insulators . . . . .	32
1.4.2 Graphene, a prototype of Dirac materials . . . . .	34
1.4.2.1 Electronic chirality . . . . .	35
1.4.2.2 Superconductivity in graphene . . . . .	35
1.4.3 Dirac and Weyl semimetals . . . . .	37
1.4.3.1 Weyl semimetals . . . . .	37
1.4.3.2 Material consideration . . . . .	38
1.4.3.3 Dirac semimetals in 2D: ZrSiS . . . . .	39
1.4.3.4 Massive Dirac fermions in 2D: $Fe_3Sn_2$ . . . . .	40
1.5 $BaCo_{1-x}Ni_xS_2$ , a moderately correlated system . . . . .	40
1.5.1 Very large Rashba band splitting in $BaNiS_2$ . . . . .	43
1.5.2 Quantum oscillations studies . . . . .	46
1.5.3 Similarities of $BaCo_{1-x}Ni_xS_2$ with iron pnictides . . . . .	48
<b>2 Time-resolved studies of quantum materials</b>	<b>51</b>
2.1 Introduction . . . . .	51
2.2 Time-resolved studies: general considerations . . . . .	52
2.2.1 Electron excitation and relaxation processes . . . . .	52
2.2.2 Two-temperature model . . . . .	53
2.2.3 Three-temperature model . . . . .	54
2.2.4 Choice of the pump pulse wavelength . . . . .	56
2.3 Out-of-equilibrium studies of (strongly) correlated materials . . . . .	56
2.3.1 Instantaneous gap collapse in vanadium oxides . . . . .	56
2.3.2 Coherent optical phonons in iron pnictide superconductors . . . . .	60
2.4 Out-of equilibrium studies of Dirac fermions . . . . .	60

2.4.1	Dirac carrier relaxation in graphene . . . . .	60
2.4.2	Dynamics of the Weyl semimetal MoTe <sub>2</sub> . . . . .	61
2.4.3	Broken time-reversal symmetry and Floquet states . . . . .	62
<b>3</b>	<b>Experimental methods</b>	<b>67</b>
3.1	Introduction . . . . .	67
3.2	Angle-resolved photoelectron spectroscopy . . . . .	67
3.2.1	General description . . . . .	68
3.2.2	Photoemission intensity . . . . .	69
3.2.3	One-particle spectral function . . . . .	72
3.2.4	Matrix elements and light polarization . . . . .	72
3.2.5	Surface sensitivity and angular resolution . . . . .	73
3.3	Synchrotron light sources . . . . .	74
3.3.1	Spectromicroscopy beamline . . . . .	75
3.3.2	Advanced Photoelectric Effect experiment beamline . . . . .	76
3.4	Pump-probe techniques . . . . .	77
3.4.1	Time-resolved ARPES . . . . .	78
3.4.1.1	Laser-based photoemission spectroscopy . . . . .	78
3.4.1.2	Time-resolved ARPES . . . . .	78
3.4.1.3	FemtoARPES setup . . . . .	79
3.4.2	Time-resolved X-ray diffraction . . . . .	80
3.4.2.1	X-ray diffraction . . . . .	80
3.4.2.2	Time-resolved X-ray diffraction . . . . .	82
3.4.2.3	X-ray free electron laser . . . . .	82
3.4.2.4	XPP beamline at Linac Coherent Light Source . . . . .	84
3.4.2.5	Cristal beamline at synchrotron SOLEIL . . . . .	86
3.4.3	Time-resolved optical spectroscopy . . . . .	86
3.4.3.1	Motivation . . . . .	86
3.4.3.2	Coherent oscillations of optical phonons . . . . .	88
3.4.3.3	Extracting the electron-phonon coupling constant . . . . .	90
3.4.3.4	Pump and probe experiments with tunable wavelength . . . . .	91
3.4.3.5	Time-resolved optical spectroscopy with broadband probe . . . . .	92
<b>4</b>	<b>Electronic band structure of BaNiS<sub>2</sub> and BaCoS<sub>2</sub></b>	<b>95</b>
4.1	Introduction . . . . .	95
4.2	Correlated Dirac fermions in BaNiS <sub>2</sub> . . . . .	95
4.2.1	Introduction . . . . .	95
4.2.2	Results . . . . .	97
4.2.2.1	ARPES measurements . . . . .	97
4.2.2.2	<i>ab initio</i> electronic band structure calculations and polarization-resolved band structure . . . . .	101
4.2.3	Symmetry analysis of the Dirac bands . . . . .	103
4.2.4	Effective Dirac Hamiltonian . . . . .	104
4.2.5	Discussion . . . . .	108
4.3	k <sub>z</sub> dispersion . . . . .	109
4.4	Temperature dependence of the density of states . . . . .	109
4.5	Electronic band structure of BaCoS <sub>2</sub> . . . . .	111
4.5.1	ARPES measurements . . . . .	112

<b>5</b>	<b>Out-of-equilibrium electron dynamics of Dirac carriers</b>	<b>117</b>
5.1	Introduction . . . . .	117
5.2	Time-resolved ARPES . . . . .	117
5.3	Time-resolved optical spectroscopy . . . . .	122
5.3.1	Observation of coherent optical phonons in BaNiS <sub>2</sub> . . . . .	122
5.3.2	Electron-phonon coupling constant . . . . .	123
5.4	Photoinduced vs. thermal effects . . . . .	126
5.5	Discussion . . . . .	129
<b>6</b>	<b>Ultrafast electron and lattice dynamics of (V<sub>1-x</sub>Cr<sub>x</sub>)<sub>2</sub>O<sub>3</sub></b>	<b>133</b>
6.1	Time-resolved X-ray diffraction . . . . .	133
6.2	Ultrafast photoinduced phase transition . . . . .	135
6.3	Time-resolved mid-infrared optical spectroscopy . . . . .	136
<b>7</b>	<b>Conclusion and Perspectives</b>	<b>141</b>
	<b>Bibliography</b>	<b>145</b>



# List of Figures

1.1	The pentagon shows various degrees of freedom of quantum materials. These entangled constituents determine the collective behavior of the system, such as magnetic and electric properties. Adopted from [175]. . . . .	19
1.2	(a) Density of states of a Mott insulator. (b) Phase diagram of a generic stoichiometric high- $T_c$ cuprate superconductor. . . . .	23
1.3	DMFT describes the interaction between one site and a bath. The quantum state of the site varies in time as electrons are emitted or absorbed by that site with the amplitude of $V_\nu$ . From [91]. . . . .	25
1.4	(a-d) Density of states from DMFT in strongly correlated materials with respect to the ratio of $U$ (Coulomb repulsion) and $W$ (bandwidth), from [91]. (e) Approximate phase diagram for the Hubbard model with nearest-neighbor and next-to-nearest-neighbor hopping $t_2/t_1 = 1/\sqrt{3}$ . The first-order paramagnetic metal to insulator transition ends at the critical point (square). The system then goes to the crossover region. The phase diagram is calculated for a single-band model and is adopted from [50]. . . . .	26
1.5	(a) Phase diagram of $V_2O_3$ as a function of chemical substitution and temperature. (b) Resistivity perpendicular to the $c$ axis of the crystal vs. temperature for several doped samples. From [115]. . . . .	28
1.6	(a) Crystal structure of $V_2O_3$ from [155] in the high-temperature paramagnetic phase. The green circles indicate the V atoms. The violet circles are oxygens. (b) Arrangement of atoms in the PI and PM phase. $a$ and $c$ are the units cell parameters and $d$ is the distance between the neighboring vanadium atoms. . . .	28
1.7	Variation of $c/a$ during the Mott transition. . . . .	29
1.8	(a) Energy level splitting in $V_2O_3$ . (b) Orbital geometry. The bonding $a_{1g}$ orbital is along the $c$ -axis and while the $e_g^\pi$ orbital is in the $a$ - $b$ plane. (c) LDA+DMFT spectra for paramagnetic $(V_{0.962}Cr_{0.038})_2O_3$ (iso.) and $V_2O_3$ (met.) at $U = 4.5, 5,$ and $5.5$ eV, and $T = 1000$ K [64]. . . . .	30
1.9	(a - c) High-resolution hard X-ray photoemission spectra of $(V_{1-x}Cr_x)_2O_3$ ( $x=0$ and $0.015$ ) near the Fermi level in all phases. (d) Difference between the AFI and PI spectra. The lower Hubbard band is located at the same energy for all of the studied point within the phase diagram suggesting that the parameter $U$ remains constant. From [45]. . . . .	31
1.10	(a) Schematic figure of a 2D TI. (b) The electronic band structure presents gapless chiral edge states. (c) Current distribution on the surface of a 3D TI. (d) The electronic band structure of $Bi_2Se_3$ . (e) Schematic of the spin-polarized Dirac-like surface-state dispersion, from [150]. . . . .	33

- 1.11 (a) Graphene lattice with sublattices A and B. (b) Hexagonal Brillouin zone. The inequivalent valleys are  $K_{\pm}$  and the wavevector of  $\mathbf{q}$  is measured from the center of the valley. (c) ARPES spectra of monolayer graphene, showing several slices through the Dirac cone, from [165]. . . . . 34
- 1.12 An applied voltage shifts the position of the Fermi level with respect to the Dirac point and changes the conductivity. . . . . 34
- 1.13 (a) The calculated band structure of twisted bilayer graphene at  $\theta= 1.05^{\circ}$  in the new Brillouin zone. (b) The density of states zoomed in to -10 to 10 meV. The purple lines show the DOS of two sheets of graphene without neither layer interaction nor twist angle. The red dashed line shows the Fermi energy at half-filling of the lower branch. The superconductivity is observed near this half-filled state. (c) Measured resistivity for two twisted angles. (d) The phase diagram of the bilayer graphene with angle  $1.05^{\circ}$ . The color scale represents the resistivity for various temperature and carrier number. From [22]. . . . . 36
- 1.14 Schematics of a Dirac/Weyl semimetal phase in  $\beta$ -cristobalite  $\text{BiO}_2$ . (a) The symmetry protected Dirac point occurs at three symmetry related X-points. (b) Four Weyl points migrate to the boundaries of the Brillouin zone due to the broken inversion symmetry. (c) A magnetic field breaks the TRS and results in two Weyl point. (d) Gapped phase is obtained by breaking the fourfold rotation symmetry. From [198]. . . . . 36
- 1.15 (a) Fermi arc in a 3D Weyl semimetal. (b) Pair of surface state (SS) Fermi arcs in a 3D DSM. (c) Surface states in a 3D TI. . . . . 38
- 1.16 (a) ARPES spectrum of  $\text{Cd}_3\text{As}_2$ . The compound shows a very high mobility of  $\sim 10^6$  m/s. The Dirac points are located at 250 meV below the Fermi level and their corresponding position in the Brillouin zone is show in the right side. (b) Band dispersion of the topological insulator  $\text{Bi}_2\text{Se}_3$ . The surface states connect two gapped states. (c) The critical composition to achieve a DSM starting from the topological insulating phase is  $\delta = 0.5$ . Adopted from [129]. . . . . 38
- 1.17 (a) Crystal structure of  $\text{ZrSiS}$  together with the Brillouin zone. The orange contour on the Brillouin zone shows the Dirac line nodes. (b) The band structure along the  $\Gamma\text{X}$  shows two Dirac cones. The one at X is protected by the crystal symmetry. (c) The iso-energy surface spectrum at the Fermi level reveals the Dirac line nodes. The Dirac node is slightly above the Fermi level. From reference [162]. . . . . 39
- 1.18 Massive Dirac fermions in  $\text{Fe}_3\text{Sn}_2$ . (a) The hexagonal BZ. (b) Doubled Dirac cone along the dashed green line in the BZ. . . . . 40
- 1.19 (a) Tetragonal  $P4/nmm$  structure of  $\text{BaNiS}_2$  and its corresponding Brillouin zone. (b) Interatomic distances inside the unit cell. (c) Evolution of the lattice vector sizes as a function of chemical substitution in Ni. . . . . 41
- 1.20 (a) Phase diagram of  $\text{BaCo}_{1-x}\text{Ni}_x\text{S}_2$  in the T-p-x space from [195]. (b) Phase diagram in the T-x plane. . . . . 42
- 1.21 Results of the antiferromagnetic LDA + U calculation of the total and partial densities of states for  $\text{BaCoS}_2$ : (a) total density of states; (b) partial density of Co d-states; and (c, d) partial density of p states of apical and in-plane sulfur atoms, respectively. From [200]. . . . . 43

- 1.22 (a) 26 eV ARPES bands compared with the GGA+U bands with (light blue line) and without (yellow line) spin-orbit coupling. (b) Calculated electronic band structure of BaNiS<sub>2</sub> by GGA+U method. Left panels are total (red line) and projected (black area) density of states for each 3d orbital component. False colors indicate the d-orbital component for each band. The symmetry character of the relevant bands near the Fermi level are labeled. From reference [156]. . . . . 44
- 1.23 (a) Crystal structure of NaCaBi. The two separate sectors (CaBi layers) forming the inversion partners used for spin-polarization analysis are labeled by  $\alpha$  and  $\beta$ . (b) Local spin polarization is represented by green (on the  $\alpha$ -sector) and orange (on the  $\beta$ -sector) arrows for the split valence bands. From [205]. (c) Two inversion partner inside the unit cell of BaNiS<sub>2</sub> are called sector 1 and sector 2. (d) The band dispersion along RA shows a band split of 150 meV. The left panel shows the second derivative of the ARPES spectrum [156]. (e) Schematics of the conduction band splitting at R point. The contribution of the electronic wave function from each sector is shown for each sub-band.  $k_R$  shows the k-shift due to the band splitting. . . . . 45
- 1.24 (a) Left panel: oscillating part of the longitudinal magnetoresistance  $\Delta R$ . Right panel: Fourier transform of the oscillations. (b) Parameters relevant to the three detected orbits projected in the  $k_x - k_y$  plane. The cross section areas are given in percentage of the first Brillouin zone area. The ratio between the big and small axis of the elliptical pocket is labeled by  $\xi$  and  $m^*$  shows the effective mass. (c) Calculated Fermi surface. The high symmetry direction are shown in the right panel. The  $\gamma$  and  $\beta$  pockets are of electron and hole nature, respectively. From [86]. 47
- 1.25 (a) Crystallographic structure and (b) phase diagram of BaFe<sub>2</sub>As<sub>2</sub>. (c,d) ARPES intensity plots of BaFe<sub>1.85</sub>Co<sub>0.15</sub>As<sub>2</sub> ( $T_c = 25.5$  K) as a function of wavevector and binding energy measured at 8 K along the  $\Gamma X$  and the  $\Gamma M$  together with the band dispersion from the first-principle calculations for  $k_z=0$  and  $k_z=\frac{\pi}{c}$ . (e) The Fermi surface shows a small electron and hole pocket. From reference [173]. . . . . 49
- 2.1 Pathway for photoinduced phase transition along the dynamical free-energy landscape from [204]. . . . . 51
- 2.2 Timeline of electron dynamics on the Dirac cone in graphene: (a) At time zero electrons (black spheres) and holes (yellow spheres) are generated by 1.5 eV pump pulses (straight arrows). (b)-(c) Within 30 fs the excited electrons and holes undergo scattering processes (b) within and (c) between the bands by Auger recombination (black curled arrows) and electron-electron scattering (magenta arrows). This leads to a thermalized hot electron distribution. (d)-(f) The decay dynamics occurs within 200 fs by (d) emission of optical phonons (blue wiggled arrows), which is followed by (e) slower supercollisions involving acoustic phonons (green wiggled arrows) and impurities. The image is taken from [178]. 53
- 2.3 Sketch of the 3TM. Electron are coupled to hot and cold phonons with  $\lambda_1$  and  $\lambda_2$ , respectively. Dashed black arrows show the decay time constants. . . . . 55

- 2.4 Ultrafast transient phase in VO<sub>2</sub> (from [185]). (a) Time-resolved density of states. The dynamics of the excited electrons and holes are shown below the spectrum. (b) By photoexcitation the monoclinic insulator phase passes through a non-thermal monoclinic metallic phase and then eventually evolves to the rutile phase. The evolution of the DOS as a function of temperature are shown. (c) Comparison between the photoinduced and thermally induced phases. (d) Theoretical DOS for the equilibrium phase (blue curve) and the non-equilibrium phase (red curve). The latter is obtained by introducing a dynamical screened Coulomb interaction to the self-energy. The shaded curve corresponds to the DOS of the rutile phase. . . . . 57
- 2.5 Ultrafast transient phase in V<sub>2</sub>O<sub>3</sub> (from [96]). (a) Dynamics of the in-gap states. (b) The transient metallic state is non-thermal with a lifetime of 1.7 ps. (c) Comparison of the A<sub>1g</sub> frequency at equilibrium and out-of-equilibrium. (d) Schematics of the photoinduced gap filling process. . . . . 58
- 2.6 Time-resolved reflectivity studies on Ba(Fe<sub>1-x</sub>Co<sub>x</sub>)<sub>2</sub>As<sub>2</sub>. (a) Spectrum at 10 K showing A<sub>1g</sub> mode. (b) Coherent optical lattice oscillation of the superconducting and metallic phases at 10 and 25 K. Damping time (c) and amplitude (d) as a function of the pump fluence. From [107]. . . . . 59
- 2.7 (a) ARPES difference spectra. The red signal shows the excited electrons above the Fermi level. (b) The evolution of the temperatures obtained by the 3TM. (c) The carrier multiplication and number of photoinduced Dirac carriers are shown as a function of time. From [78]. . . . . 61
- 2.8 (a) The theoretical band dispersion of MoTe<sub>2</sub>. The Weyl node is shown in green. (b) Experimental band dispersion. (c) Left panel: Band dispersion along ΓX for low (brown) and high (grey) temperatures before optical excitation. Right panel: Effect of optical excitation at Weyl semimetal phase at 50 K. The dynamics of the excited states corresponding to boxes 1 and 4 are shown in (d) and (e) respectively. The fit to the data shows a slower dynamics for the gapped phase at 300 K. From [31]. . . . . 62
- 2.9 Schematics of the bands subjecting to the AC electric field of the MIR pulses at 10 μm (from [181]). (a) With linear polarization of light the surface states at a negative delay are shown in (b). (c) The spectrum at the negative delay is subtracted from the spectra at time zero for two different directions in order to highlight the photoinduced effects. Dashed orange lines are guides to the eye. (d) Sketch of the Floquet states of different order as induced by the MIR excitation. The numbers show the band index of the states. Band gaps occur at several momenta due to the hybridization between the states. (e) The projection of the CPL electric field on the surface plane (light blue) is elliptical. (f) ARPES spectrum at time zero. (g) Photoinduced effects at the arrival of the pump pulse. (h) Band gaps occur at several momenta however, the band gap that is induced by the TRS breaking is at the Dirac point, 2κ ~ 50 meV. . . . . 63

2.10	Engineering the non-trivial states in $\text{Na}_3\text{Bi}$ . (a) CPL in the $y$ - $z$ plane. (b) The Dirac cone splits along the $k_x$ direction at the Fermi level, resulting in a Floquet-Weyl semimetal. (c) The separation of the transient states can be tuned by the amplitude of the incident light. (d) The lattice distortion along the $a$ -axis of the unit cell induced by strain makes the Dirac fermions massive and opens the gap. By applying femtosecond CPL, one is able to close the band gap. (e) If intensity of light is above the threshold, Floquet-Weyl states with different chirality appear. From [72]. . . . .	65
3.1	(a) The electron energy distribution (from [33]) produced by the incoming photons, and measured as a function of the kinetic energy $E_{kin}$ of the photoelectrons. The left diagram shows the density of states of the solid in terms of the binding energy. The Fermi level corresponds to the zero binding energy. (b) Representation of the hemispherical photoelectron analyzer and the geometry of the experiment. . . . .	70
3.2	Spectral function and Fermi distribution of an electronic system with (a), and without interaction (b). The figure is inspired from [34]. . . . .	71
3.3	Symmetry of orbitals in the photoemission process [33]. . . . .	72
3.4	Mean free path of electrons from [164]. . . . .	73
3.5	Synchrotron facility. . . . .	74
3.6	Instruments at the Spectromicroscopy beamline. (a) Shwarzschild objective. (b) The geometry of the experiment from [37]. For the ARPES mode the analyzer angles change while for the surface cartography the position of the sample is scanned. (c) The beamline has two SO's. One for the 27 eV and the other for the 74 eV beam. . . . .	75
3.7	(a) Instruments at APE beamline. (b) Undulators for the HE and LE beamlines. (c) Monochromator section. It is based on twin plane grating-spherical mirror assemblies. . . . .	76
3.8	Schematic of a time-resolved experiment. The pump pulse arrives at time zero and initiates a dynamics in the system. The probe pulse comes after a controllable delay and maps out the photoinduced changes of the signal, $\Delta S(t)$ . . . . .	77
3.9	The fourth harmonic generation by frequency mixing. L: lens with $f=20\text{cm}$ , DM: dichroic mirror, DL: delay line. The off axis parabolas have $f=5\text{-}10\text{ cm}$ focal length depending on their location. The frequency mixing setup uses 50% of the laser energy that is $3\ \mu\text{J}$ . . . . .	79
3.10	Experimental chamber of the FemtoARPES setup. . . . .	80
3.11	Ewald's sphere. The center of the reciprocal space is shown with O. . . . .	81
3.12	(a) Low-gain FEL. (b) SASE FEL. The interaction of light and electrons orders the electrons with a periodicity equal to the X-ray radiation wavelength. . . . .	83
3.13	LCLS XFEL and XPP beamline. . . . .	85
3.14	Diagram of the synchrotron. (a) Storage ring and the Cristal beamline. The X-rays arrive at 2 kHz (in the low-alpha mode) and the system is pumped at 1 kHz. (b) Time structure of different synchrotron filling modes. The low-alpha mode has the minimum time resolution. . . . .	87
3.15	Top panel: schematic DOS for the half-filled Hubbard model for a metallic and an insulating state. Bottom panel: The optical conductivity spectra for the corresponding states. . . . .	88
3.16	The time-resolved reflectivity setup at LOA with 800 nm as probe and MIR as pump. . . . .	92

- 3.17 (a) Dispersion of the reflected white-light pulse through the prism onto the linear array sensor. The calibration procedure for the system consists in the assignment of a wavelength to every pixel of the array. (b) Time- and spectrum- resolved reflectivity. . . . . 92
- 4.1 (a) Crystal structure of BaNiS<sub>2</sub>. Blue, yellow and green spheres represent the Ni, S and Ba atoms, respectively. The tetragonal unit cell is indicated by black solid lines. The lattice parameters are  $a = 4.44 \text{ \AA}$  and  $c = 8.93 \text{ \AA}$ [56]. On the top the projection of the unit cell in the  $xy$  plane, containing two Ni atoms is shown. (b) Gliding plane symmetry relating the Ni atoms inside the unit cell. (c) First Brillouin zone, and high-symmetry directions. . . . . 97
- 4.2 Experimental electronic band structure of BaNiS<sub>2</sub>. (a) A three-dimensional ARPES map acquired with 70 eV photon energy. The top surface shows the Fermi surface and the sides of the cube present the band dispersion along the high symmetry directions depicted with the white arrows. The linearly dispersing bands along the  $\Gamma$ M cross each other at the Fermi level, creating four Dirac nodes on the Fermi surface. (b) Stacking plots of constant-energy contours show the band structure evolution with respect to the binding energy. Particularly, we observe the ellipse-shaped section of the linearly dispersing bands on the  $k_x - k_y$  plane that loses symmetry as the binding energy increases. (c) Elliptical section of the Dirac cone for the binding energy of 100 meV. The band dispersion along the small and big axis of the ellipse are also shown. (d) The ARPES yield along the  $\Gamma$ M direction with different photon energies for the region where bands are linearly dispersed. The dashed blue lines are the guide to the eyes along the linearly dispersing bands. 98
- 4.3 (a) The Dirac cone as obtained by 60 eV of photon energy. (b) MDC at the binding energy of 0.29 eV. The photoemission peaks of the  $d_{z^2}$  and  $d_{x^2-y^2}$  bands are fitted by a Gaussian function and a linear background and are shown in blue and orange curves, respectively. (c) The continuity of the bands above the Fermi level are obtained by fitting. The reconstructed band dispersion for each band with a polynomial function. The crossing point of the fits gives the position of the Dirac point. . . . . 99
- 4.4 Band structure calculations and  $d$ -orbital character of the Dirac bands revealed by laser-based ARPES. (a) Comparison between the electronic band structure calculations with the HSE method and the experimental data acquired with 70 eV of photon energy. (b) Mirror plane emission of the  $d_{z^2}$  band. (c)  $P$ -polarized photon with the electric field indicated as  $A_p$  allows the detection of the out-of-plane  $d_{z^2}$  band. The right hand side figure shows the orbital-resolved band structure. (d) Mirror plane emission of the  $d_{x^2-y^2}$  band. (e)  $s$ -polarized photon with the electric field indicated as  $A_s$  reveals only the band dispersion of the in-plane  $d_{x^2-y^2}$  band. The color scale of the calculations indicates the relative weight of the given  $d$ -orbital component for the studied bands. . . . . 102

- 4.5 Band structure calculations and band symmetries along the  $M\Gamma$  direction. (a) Band symmetries along the  $M\Gamma$  direction. At the right (left) -hand side of the panel, the symmetries at  $\Gamma$  ( $M$ ) is shown, while the symmetries in between follow the irreps of the  $C_{2v}$  point group, represented by the color code in the key. The outer  $+/-$  signs indicate the parity of the respective Bloch wave functions at the beginning and at the end of the  $k$ -path. (b) Evolution of the energy splitting between even and odd combinations of  $d$  orbitals along  $M\Gamma$ . The red (dark-green) vertical arrows indicate the splitting between the  $d_{x^2-y^2}$  ( $d_{z^2}$ ) bands at  $\Gamma$  due to the hybridization with the ligand  $p_z$  orbitals. The blue arrow is the splitting of  $d_{xz}/d_{yz}$  bands at  $\Gamma$  due to their hybridization with the  $p_x/p_y$  orbitals. . . . . 104
- 4.6 (a)-(b) Constant energy contour near the Fermi level as obtained experimentally (left) and from the effective Dirac model (Eq. 4.4). The comparison highlights the agreement between theory and experiment. The effective model explains the presence of elliptically shaped Dirac cones, as observed in ARPES measurements, along  $\Gamma M$  direction. (c) Electronic dispersion near the Fermi level from the  $5 \times 5$  Hamiltonian (Eq. 4.1) and the linearized effective Dirac model in Eq. 4.4. This is in qualitative agreement with the widening of the energy pockets observed in ARPES data (see figure 4.2 (b)). (d) Elliptical shape of the Dirac cones. . . . . 107
- 4.7  $k_z$  dispersion of the electronic band dispersion. (a) ARPES yield along the  $\Gamma M$  high symmetry direction for different photon energy. Dirac bands do not show a significant  $k_z$  dispersion while other bands below the Fermi level have rather a 3D character. (b) Comparison with HSE (7%) method. The blue spectra shows the band dispersion for  $k_z = 0$  and the orange shows the bands for  $k_z = \pi/c$ . The left and right panels are acquired with 25 eV and 70 eV of photon energy, respectively. (c) Iso-energy contours at the Fermi level for different photon energies. The  $\alpha$  and  $\beta$  pockets are shown. In addition, the Rashba split pocket at X point is also observed and is shown by an oval contour. The data suggest that the electronic band structure at the Fermi level have a quasi 2D nature. . . . . 110
- 4.8 Temperature dependent density of states. (a) The blue contour shows the integration window of the spectral function. (b) The density of states for different temperatures. (c) Comparison between the spectral weight transfer upon heating for a normal metal and a correlated metal. The density of states at high and low temperatures are shown in red and blue, respectively. . . . . 112
- 4.9 (a) Iso-energy surface of  $\text{BaCoS}_2$  at  $E-E_f = -1.23$  eV. The border of the Brillouin zone is shown with a yellow contour and the high symmetry directions are shown with white arrows. (b) Top panel: A series of ARPES spectra along the high symmetry directions for the PI phase. Bottom panel: The DMFT calculations of the band structure. (c) The density of states of  $\text{BaCoS}_2$  in the AFI phase ( $T=110$  K) and PI phase ( $T=300$  K) compared with the DMFT calculation. The inset is a zoom to the DOS for the AFI and PI phases. . . . . 114
- 4.10 Comparison between  $\text{BaCoS}_2$  (top panel) and  $\text{BaNiS}_2$  (bottom panel). The dashed lines are guide to the eyes. (a) and (b) Along the  $\Gamma X$  direction the band number 2 and 3 get closer to each other at  $\sim 0.8 \text{ \AA}^{-1}$ . (c) and (d) A remnant of the Dirac cone in  $\text{BaNiS}_2$  (band number 2) can be detected on the band dispersion of  $\text{BaCoS}_2$ . 115

- 5.1 (a) ARPES reference image for the out-of-plane  $d_{z^2}$  band. (b) Difference tr-ARPES images before and after photoexcitation. The red and blue signal show gain and loss of signal, respectively. A non-rigid shift of the band below the Fermi level is observed upon photoexcitation. (c, d) Evolution of the in-plane  $d_{x^2-y^2}$  band for different time delays. . . . . 118
- 5.2 Time-resolved dynamics of the shape of the bands. (a)  $d_{z^2}$  band. (b) The MDC at  $E-E_f = -0.14$  eV that is shown by a blue line in the ARPES image. The red curve shows the fit with a Gaussian function and a linear base line. The center of the Gaussian shows the wavevector for each binding energy. In this way, the band dispersion can be reconstructed for each time delay. (c) Stacking of the reconstructed band dispersion for all delays. The intensity at each point shows the position of the wavevector for that point in the  $E-t$  plane. The bottom panel shows the same procedure for the  $d_{x^2-y^2}$  band. . . . . 118
- 5.3 Dynamics of the Dirac cone. (a1)  $d_{z^2}$  band: the reconstructed band dispersion,  $E(k)$ , before and after arrival of the pump pulse. This is obtained by a vertical line profile from figure 5.2 (c). The band crossings at the Fermi level does not show any shift and remains still for all time delays. (b1) The photoinduced renormalization of the band for different time delays. (c1)  $dE/dk$  curves. Figures a2 - c2 show the same study on the  $d_{x^2-y^2}$  band. (d) Evolution of the Fermi velocity for both bands. The Fermi velocity decreases up to 250 fs. . . . . 119
- 5.4 (a) By combining previous studies, I show how the Dirac cone evolves upon photoexcitation. (b) The dynamics of the excited states above the Fermi level. (c) The averaged shift of the band shows a dynamics of 1 ps starting from 250 fs. . . 121
- 5.5 Dirac cone of  $\text{BaNiS}_2$  studied by 6.28 eV as the probe pulse. The polarization of the light is not well defined so that both branches are observed. (a) Negative delay image. (b) 250 fs after the arrival of the pump pulse. The color scale is maximally saturated in the logarithmic scale in order to better visualize the excited states above the Fermi level. . . . . 122
- 5.6 (a) Spectrum- and time-resolved reflectivity of  $\text{BaNiS}_2$  with the fluence of  $4 \text{ mJ/cm}^2$ . (b) Photoinduced reflectivity changes for several wavelengths obtained by horizontal line profiles in the continuum spectrum. . . . . 123
- 5.7 (a) Time-resolved changes in the reflectivity of 996 nm. The raw data was fitted by an exponential curve. (b) Subtraction of the exponential fit from the data decouples the dynamics from the optical and acoustic phonon modes. The acoustic phonon presents a period of  $\sim 9$  ps. (c) After subtracting the contribution of the acoustic phonon, we can merely study the coherent oscillation of the optical phonons. The frequency of each mode can be found by the Fourier transform as shown in (d). A simple model, as explained in the text, allows us to follow to decay time scale for each observed mode (e). The 5.14 THz decays at a time scale of 1 ps and the 3.07 THz mode, decays slower after 7.3 ps. . . . . 124
- 5.8 The evolution of the optical phonon modes with respect to the pump fluence. . . 125
- 5.9 (a)  $\Delta R(t)/R$  at  $1.06 \mu\text{m}$  for the pump fluence of  $0.2 \text{ mJ/cm}^2$ . The dashed red curve is the numerical simulation based on the 3-temperature model. (b) Temporal temperature evolution of the electrons (red curve), hot phonons (orange curve), and cold phonons (blue curve) after photoexcitation. The electron-phonon coupling is found to be 0.13. . . . . 125

- 5.10 Temperature dependent ARPES spectra for (a)  $d_{z^2}$  and (c)  $d_{x^2-y^2}$  band. (b) and (d) show the spectral weight evolution with respect to 130 K. These curves are obtained by subtracting the DOS at 130 K from the DOS at higher and lower temperatures. . . . . 127
- 5.11 Band dispersion for different temperatures. (a)  $d_{z^2}$  band. The solid lines show the  $E(k)$  for 130 K and 250 K, and the dashed lines are the polynomial fits. (b) Temperature-induced changes in the band. (c, d) The effect of the temperature on the  $d_{x^2-y^2}$  band. . . . . 128
- 5.12 Comparison between photo-induced and thermally induced renormalization of the linearly dispersing bands for (a)  $d_{z^2}$  and (b)  $d_{x^2-y^2}$  band. The solid lines show how the slope of the band changes while heating the sample starting from 130 K. The dashed lines shows the photoexcitation impact on the band. Around 4 ps, the electronic and lattice temperatures have converged and the renormalization of the band is equal to a temperature difference of  $\sim 25$  K which is the heat deposited by laser pulses at  $0.2 \text{ mJ/cm}^2$ . (c,d) The photoinduced changes in the density of states (dashed lines) are compared with the thermal effects (solid lines). . . . . 130
- 6.1 (a) The geometry of the tr-XRD at SLAC. (b) The Bragg reflection peak of the (116) direction for the PI phase. (c) tr-XRD measurements for a fluence of  $8 \text{ mJ/cm}^2$ , showing the pump-probe diffraction peak intensities for the (116) and (024) Bragg reflections. The solid lines are the simulations as explained in the text. (d) The calculated structure factor versus the shortest vanadium distance  $V_1 - V_4$ . The structure factor is normalized to one for the equilibrium position of  $2.744 \text{ \AA}$ . The black dots represent the minimum distance observed extracted from panel c. From reference [96]. . . . . 134
- 6.2 Time-resolved X-ray diffraction on the (116) Bragg reflection. The center of mass of the peak signal on the detector shows a shift after 4 ps, corresponding to the onset of the acoustic wave propagation. . . . . 134
- 6.3 (a) X-ray diffraction signal on the 2D detector of the XPP beamline, showing the (113) Bragg reflections from  $(V_{1-x}Cr_x)_2O_3$  ( $x = 0.011$ ) in its ground state, representative of the PI and PM phases, with the corresponding regions of interest (ROI's). No signal is present within the third ROI, in the center of the detector. (b) Diffraction signal 500 ps after photoexcitation, clearly showing a strong Bragg reflection from the third ROI which should be assigned to a novel state, not corresponding to any of the phases in the equilibrium phase diagram of  $(V_{1-x}Cr_x)_2O_3$ . 135
- 6.4 X-ray diffraction signal on the 2D detector of the SOLEIL beamline, showing the (113) Bragg reflections corresponding to the PI and PM phases for the 1.1% doped  $V_2O_3$ . . . . . 136
- 6.5 LCLS-XPP data giving the time evolution of the (113) Bragg reflection signal from the central ROI of figure 6.3 (b), corresponding to the novel transient phase. The time evolution clearly shows a marked presence of the novel phase already 300 fs after photoexcitation. (b) Intensity of the transient phase for longer time delays from pump-probe XRD experiments performed at synchrotron SOLEIL. . . . . 137
- 6.6 The energy downconversion process. . . . . 137
- 6.7 The optical path inside the TOPAS C. There are two stages of the amplification with the BBO crystals. . . . . 138

- 6.8 Time-resolved optical reflectivity measurements by pumping with  $3.6 \mu\text{m}$ . (a) dashed lines are the experimental data and the solid lines are fits to the decaying oscillations. (b) The frequency of the coherent oscillations as a function of fluence. We observe a mean frequency of 7.2 THz that is very close to the Raman frequency of 7.15 THz. (c) Time-resolved optical reflectivity measurements by pumping with 800 nm. The frequency of phonons is 7.6 THz. . . . . 140

# 1 | The physics of quantum materials

## 1.1 Introduction

Quantum materials [83] is a new term that was introduced in condensed matter physics to unify all materials in which strong electronic correlation governs physical properties of the system (e.g. Mott insulators and superconductors) and materials whose electronic properties are determined by the geometry of the electronic wave function (e.g. topological insulators). The union of these two groups is that any conventional explanation based on non-interacting constituents or Fermi liquid theory fails to describe their *emergent* properties– that is, properties that only appear by intricate interactions among many degrees of freedom, such as charge, spin, orbital, and topological nature of electrons [175] (figure 1.1). These emergent phenomena often give rise to phase diagrams accompanied by phase transitions typically with no well-defined order parameter or, if any, with an unusual complex one [38], for instance topological order.

Before getting into the two important subgroups of quantum materials, I briefly recall some fundamentals of the Fermi liquid theory.

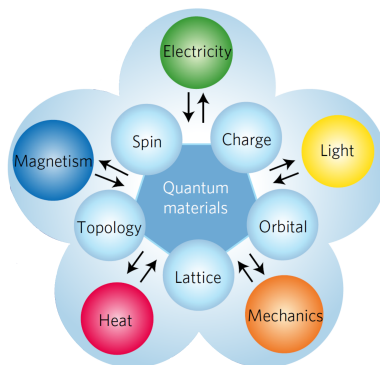


Figure 1.1: The pentagon shows various degrees of freedom of quantum materials. These entangled constituents determine the collective behavior of the system, such as magnetic and electric properties. Adopted from [175].

## 1.2 Fermi liquid theory

The simplest way towards understanding the electronic properties of a quantum material is to describe its ground state as well as the lifetime of possible excitations. We can begin by an

example: the propagation of a single electron in a many-body system can be explained by the probability amplitude that an electron added to a Bloch state with momentum  $\mathbf{k}$  at a time  $t$  will still be in the same state after a time  $|t - t'|$ . This can be mathematically described by one-particle spectral function  $A(\mathbf{k}, \omega)$  for an  $N$ -particle system:

$$A^\pm(\mathbf{k}, \omega) = \sum_m |\langle \psi_m^{N\pm 1} | c_{\mathbf{k}}^\pm | \psi_i^N \rangle|^2 \delta(\omega - E_m^{N\pm 1} + E_i^N) \quad (1.1)$$

Here,  $A^\pm(\mathbf{k}, \omega)$  is the partial spectral function for addition (+) or subtraction (-) of one particle to or from a given state. The  $|\psi_i^N\rangle$  is the wave function of the initial state with energy  $E_i^N$  and the  $|\psi_m^{N\pm 1}\rangle$  is the wave function of the final state with energy  $E_m^{N\pm 1}$ . The  $c_{\mathbf{k}}^\pm$  is the creation/annihilation operator of an electron with wavevector  $\mathbf{k}$ . Various interactions in the system for instance, electron-electron and electron-phonon correlations or impurity-scattering, lead to a correction in the single-particle spectral function that can be expressed in terms of the electron proper self-energy:  $\Sigma(\mathbf{k}, \omega) = \Sigma'(\mathbf{k}, \omega) + i\Sigma''(\mathbf{k}, \omega)$ . The self-energy is actually written as the sum of individual contributions from the mentioned interactions. Its real and imaginary parts contain all the information on the energy renormalization and lifetime of a free electron with the bare band energy  $\epsilon_k$  and momentum  $\mathbf{k}$  that propagates in a many-body system. The spectral function of an interacting system can be written in terms of the self-energy as follows:

$$A(\mathbf{k}, \omega) = \frac{-1}{\pi} \frac{\Sigma''(\mathbf{k}, \omega)}{[\omega - \epsilon_k - \Sigma'(\mathbf{k}, \omega)]^2 + [\Sigma''(\mathbf{k}, \omega)]^2} \quad (1.2)$$

In section 3.2.3, I show how ARPES extracts  $A(\mathbf{k}, \omega)$ , however the exact calculation of  $\Sigma'(\mathbf{k}, \omega)$  and  $\Sigma''(\mathbf{k}, \omega)$  that bring much information on the many-body system is an extremely difficult task. In the presence of electronic correlation, the problem can be treated by considering an *interacting Fermi-liquid* system as suggested by Landau in 1959 [95]. The basic idea behind the Fermi-liquid theory is to gradually introduce interactions to a non-interacting fermion system so that it remains at equilibrium and its ground state adiabatically transforms into the ground state of the interacting system. Within this viewpoint, the lowest-lying excitations above a metallic ground state, created by addition or removal of an electron in an interacting system, can be described by a free particle with a finite lifetime since it can be scattered out of a Bloch state by collisions with other electrons. This quasiparticle has the same charge and spin as electrons but has an enhanced effective mass. Therefore, the sharp Fermi sea is now replaced by a discontinuity at the Fermi momentum ( $k = k_F$ ) with a finite probability of finding electrons above the Fermi level even at  $T=0$ . According to this theory, the ground state of strongly interacting fermions can either be a sea of noninteracting electrons or a state with spontaneously broken symmetry, such as superconductivity, that is induced by strong interactions [134]. The spectral function for correlated systems, equation 1.2, can be divided in two parts, a coherent part with poles and an incoherent smooth part without poles:

$$A(\mathbf{k}, \omega) = Z_k \frac{\Gamma_k/\pi}{(\omega - \epsilon_k)^2 + \Gamma_k^2} + A_{incoh} \quad (1.3)$$

where  $Z_k = (1 - \partial\Sigma'/\partial\omega)^{-1}$ ,  $\epsilon_k = Z_k(\epsilon_k + \Sigma')$ , and  $\Gamma_k = Z_k|\Sigma''|$ . The  $Z_k$  accounts for the discontinuity in the Fermi-Dirac distribution mentioned earlier. The  $A_{incoh}$  accounts for the incoherent part. The picture that these complex equations illustrate is simple— the collective behavior of an interacting system can be explained by a quasiparticle with a renormalized energy  $\epsilon_k$  and mass  $m^* = \frac{Z_k}{m}$  that propagates through an incoherent surrounding that reflects the "dressing" of that quasiparticle. Different decay processes such as electron-hole, electron-plasmon and electron-

phonon interactions contribute differently to the lifetime of the quasiparticle that is inversely proportional to the width of its peak, i.e.  $\tau \propto \Gamma_k^{-1}$ . At a given temperature, the width of the peak at each wavevector is proportional to  $(k - k_F)^2$ . By increasing the temperature, the lifetime of the excitations decreases and results in a broadening of the quasiparticle peak that is proportional to  $T^2$  [146]. The Fermi liquid model of correlated electrons in metals is able to explain the  $T^2$  temperature dependence of resistivity by electron-electron interactions. It also explains the linear dependence of the electronic heat capacity to temperature [102].

The Fermi liquid theory does not posit entanglement or topology of the electronic wave function in its perturbative approach. It only states that the ground state of all arbitrarily strong interactions is in one-to-one correspondence with a non-interacting system. On the one hand, this implies that the mass of the quasiparticle should be renormalized to illogic values ( $\sim 10^4$ ) in some cases. On the other hand, the nature of the ground state of a Fermi liquid achieved by adiabatically renormalizing strong interactions might be far different from the reality. Here comes the examples from two principal subsets of quantum materials: Mott metal-to-insulator transition and topological materials which explicitly manifest the hallmarks of the Fermi liquid breakdown.

### 1.3 Strongly correlated materials: Metal to insulator transition

The electronic correlation is a measure of how much the movement of one electron is influenced by the presence of all other electrons. Concisely, it refers to all factors that influence the propagation of an electron among the sea of other electrons. Most importantly, we are interested in the case where the Coulomb repulsion between electrons leads to their spatial arrangement in such a way that the position of one electron is coupled to the position of others. The correlation also comprises the exchange interaction that arranges the spin configuration of a system.

These systems escape the Fermi liquid description and are called strongly correlated systems. They show a variety of emergent phenomena such as metal-insulator transitions, half-metallicity, charge-density waves, and so on. I focus on the first group.

Some materials show metal to insulator transition (MIT) [121]. In particular, systems like correlated transition metal oxides with partially filled  $d$ -orbitals. They have a low electronic conductivity, which varies with temperature or chemical substitution to the point that it can undergo a first order metal to insulator transition. The lack of conductivity in such compounds was first explained by De Boer and Verwey [35] in case of nickel oxide, which according to the band theory is expected to be a metal. They explained that a moving electron is attracted to the hole on the initial atom if it cannot overcome the potential barrier on another atomic site. This reduces the frequency of the electron transition from one site to another. However, a small deviation from stoichiometric composition, such as electron or hole doping, can alter the conductivity.

Mott [124] described this scenario in terms of electron-hole pair formation. In order for the material to conduct, either the activation energy in the insulating state should be greater than the pair binding energy or the density of electrons should be high enough to screen the Coulomb attraction effects. He also predicted that a cubic crystal of one electron per atom [125] with lattice parameter  $d$  is insulator if  $d$  is large (but not so large to prevent the tunneling). In this view, he explained that by applying high pressure to the system a metallic conductivity should be observed because this prevents pair formation and increases the number of free electron per site to one. A metal to insulator transition that is purely driven by electronic correlation while

maintaining the crystal symmetry is also called a Mott transition and the insulating phase is a Mott insulator. Here, the "electronic correlation" refers to the correlation between the spatial positions of electrons due to Coulomb interaction. Few years later Hubbard [71] tried to theoretically present a model that captures the essence of the Coulomb interaction in narrow energy bands. His simple and approximative theory supposes that the model system can be treated in the atomic limit— that is, an electron is "on" a specific atom. This is particularly true for the  $3d$ -orbitals as their small radius confines electrons around the nuclei of the solid and therefore the Coulomb repulsion becomes important. The Hubbard model takes into account a single-band however, a consistent description of the electronic systems requires more realistic models including orbital degrees of freedom and a generic multiband Hubbard model.

The single band Hubbard Hamiltonian can be written as:

$$H = - \sum_{ii',\sigma} c_{i\sigma}^\dagger t_{ii'} c_{i'\sigma} + \sum_{ii',jj',\sigma\sigma'} U_{ii',jj'} c_{i\sigma}^\dagger c_{i'\sigma'}^\dagger c_{j\sigma} c_{j'\sigma'} \quad (1.4)$$

The first term is the kinetic term in which  $t_{ii'}$  describes electron hopping from one lattice site  $i$  to another  $i'$ . The strength of the hopping is controlled by the effective wave function overlap of neighboring atoms (bandwidth). In the second term describing the electron-electron interaction,  $U_{ii',jj'}$  is related to the integral of the Coulomb interaction between two adjacent sites. The creation and annihilation operators for an electron on site  $i$  with spin  $\sigma$  are  $c_{i,\sigma}^\dagger$  and  $c_{i,\sigma}$ , respectively.

The solution of the above Hamiltonian is a hard task; however, some simplifications already give insight to the underlying physical phenomena to be understood. Assuming that the atoms are well separated and the overlap between neighboring orbitals is very weak,  $t_{ii'}$  can be replaced by a constant,  $t$ , for nearest neighbors and zero otherwise.  $t$  is about 1 eV for transition metal oxides. On the other hand, the screening of core electrons and  $d$ -electrons makes the Coulomb interaction between one site and its neighbors negligible. The on-site Coulomb interaction for  $3d$ -electrons is about 20 eV while for the nearest neighbor it is of order of 5 eV. Thus, it is legitimate to drop off all electron-electron interactions except the on-site one described by  $U$ . The Hubbard model is then reduced to:

$$H = -t \sum_{\langle ij \rangle} a_{i\sigma}^\dagger a_{j\sigma} + U \sum_i n_{i\uparrow} n_{i\downarrow} \quad (1.5)$$

Here,  $\langle i, j \rangle$  is the nearest neighbor interaction and  $n_{i\sigma} = a_{i\sigma}^\dagger a_{i\sigma}$  is the occupation number of the site  $i$  with spin  $\sigma$ .

Intuitively, the Hubbard model is based on purely phenomenological grounds: the bandwidth  $t$  measures the electrons tendency to minimize their kinetic energy by delocalizing. On the other hand, double occupancy of a lattice site causes an energetic penalty associated with the mutual Coulomb interaction.

In the simple case of half-filled systems ( $n=1$  for each site) with very small bandwidth, Hubbard finds the Mott insulating phase with two energy bands separated by  $U$ . The general concept of these bands for strongly correlated systems can be understood as follows: in these systems, adding or removing electrons from a given atom leaves it in an excited configuration. This excited state is scattered by not only the Coulomb repulsion of other electrons but also by different degrees of freedom inside the system such as spin or orbital momentum. This incoherent propagation of the excited states forms broad bands separated by some amount that basically describes the energy necessary to take an electron and put it on a distant atom where another electron already exists. The first band below the Fermi level containing all localized

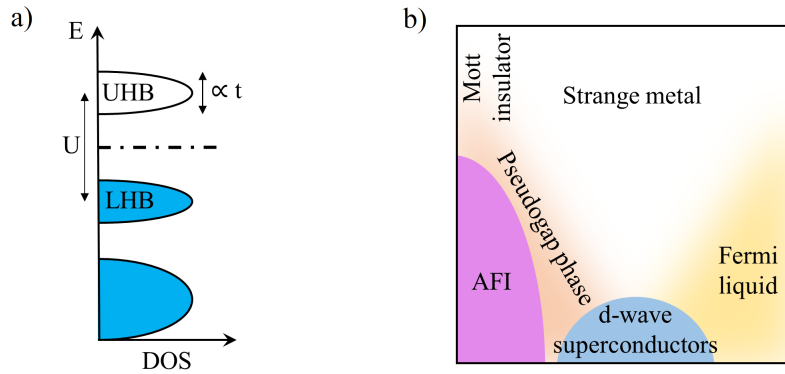


Figure 1.2: (a) Density of states of a Mott insulator. (b) Phase diagram of a generic stoichiometric high- $T_c$  cuprate superconductor.

electrons is called the lower Hubbard band (LHB) and the unoccupied band above the Fermi level corresponds to the upper Hubbard band (UHB), figure 1.2 (a).

Mott insulators are the parent compounds of stoichiometric high- $T_c$  superconducting cuprates. By adding or removing electrons to such ground state, the half-filled system experiences a competition between the hopping or Coulomb repulsion between electrons. This competition leads to a multiplicity of emergent phases as show in figure 1.2 (b).

It should be highlighted that not all MIT's are due to electron-electron interaction. A change in the crystal structure, such as Peierl's distortion, or a change in the magnetic structure at Néel temperature also leads to the gap opening [167]. The latter insulating phase is caused by long-range antiferromagnetic ordering and is called a Slater insulator. Another example is the Anderson localization of electrons due to some impurities in the system that results in a non-conductive behavior [3]. In my PhD, I only worked with materials whose phase diagram is explained by electronic correlation and they are called Mott-Hubbard materials.

The role of the magnetic ordering was not *a priori* discussed in the Hubbard model however, later Mott could derive the Néel temperature for transition metal compounds from the interplay of Coulomb interaction and bandwidth [126]. He concluded that  $T_N$  should be around 100 K. In this point, the distinction between a Slater and Mott insulator in the antiferromagnetic phase is delicate. In a Mott insulator (with  $U/t \gg 1$ ) the magnitude of the gap resulting from  $U$  does not really change across the Néel temperature. On the contrary, in a Slater insulator the system gets metallic above the  $T_N$  and the key role is played by the exchange interaction.

Despite the simplicity of the Hubbard model picture, the solutions of strongly correlated electron systems near the Mott transition has remained an endless challenge over decades. The transition involves entangled wave functions for many-body systems with different parameters such as spin and spatial degrees of freedom [83]. Various analytical or numerical methods have been proposed so far to elucidate the phase diagrams of correlated materials [7, 43, 75, 98]. In the following subsections, I briefly present different theoretical approaches that are commonly used to derive the density of states of moderately and strongly correlated materials.

### 1.3.1 Theoretical models

We have seen that the Fermi-liquid theorem is able to explain the temperature dependence of macroscopic properties, such as conductivity or magnetic susceptibility, of a weakly correlated system based on the excitation spectrum of the electrons. The density functional theory (DFT), on the other hand, is able to predict the band structure of these materials with a good approx-

imation. However, in the presence of strong electron correlation the great difficulty originates from the nonperturbative nature of the problem as well as several competing physical mechanisms. The Hubbard model then demands a dynamical approach, which is best captured by the dynamical mean-field theory (DMFT).

### 1.3.1.1 Density functional theory

In DFT [69, 89] the total energy of the interacting many-body system is written as a functional of the electron density  $\rho(\mathbf{r})$ :

$$\Gamma[\rho(\mathbf{r})] = \underbrace{T[\rho(\mathbf{r})]}_{\text{kinetic term}} + \underbrace{\int V_{cr}(\mathbf{r})\rho(\mathbf{r})d^3\mathbf{r}}_{\text{potential energy of the crystal}} + \underbrace{\frac{1}{2} \int \frac{\rho(\mathbf{r})\rho(\mathbf{r}')}{|\mathbf{r}-\mathbf{r}'|} d^3\mathbf{r}d^3\mathbf{r}'}_{\text{Hartree-Fock term}} + E_{xc}[\rho(\mathbf{r})] \quad (1.6)$$

In the last term,  $E_{xc}$  contains all information about the exchange and correlation. It has gradient expansions of electron density and needs further simplifications in order to render the DFT Hamiltonian solvable. Then, minimizing the energy of the system together with the self-consistency condition leads to a correct ground state density. Various kinds of approximations have been used to consider exchange-correlation interactions. For instance, in BaNiS<sub>2</sub>, which is a moderately correlated metal, generalized gradient approximations (GGA) [143] or hybrid functionals such as HSE (Heyd-Scuseria-Ernzerhof) [68] can be applied for the band structure calculations. I will show the results in chapter 5.

In GGA, the  $E_{xc}$  term is expressed in terms of the electron density and its first gradient. In this way, the electron-electron interaction and the total energy of the system gets more realistic with respect to the local density approximation (LDA) in which one assumes a homogeneous electron density. In GGA, the on-site Coulomb interaction of localized electrons is not correctly described. To circumvent this problem, one can treat the Coulomb interaction as a statistical mean-field of the localized electrons. This method is called GGA+U and can be used for weakly correlated *d*- or *f*-orbitals.

The HSE is a particular hybrid functional that is used as another class of approximations to the exchange-correlation energy functional in DFT and is mostly used for metallic systems [6]. It was first introduced for molecular systems but is getting more and more popular in solid state physics as well. It uses an error function screened Coulomb potential and a parameter that describes the range of interactions (whether they are short-range or long-range). The hybrid functionals are nonlocal and orbital dependent.

During my PhD, I had the opportunity of interacting with M. Casula from Paris 6 University who performed the theoretical calculations on the systems I studied. The experimental and theoretical band structure of BaNiS<sub>2</sub> and BaCoS<sub>2</sub> are presented in section 4.2 and 4.5.

### 1.3.1.2 Dynamical mean-field theory

The DMFT is based on mapping the Hubbard model onto a single-site Anderson impurity model (AIM) embedded in an effective field that is determined by self-consistency condition [50]. This mapping is exact in the limit of large lattice coordination [48, 49]. In DMFT, spatial fluctuations are supposed to be frozen and we only deal with quantum fluctuations at a given site that occur due to the interaction of the degrees of freedom at this site, e.g. spin, with an external bath. This greatly simplifies the spatial dependence of correlations. The bath is the mean-field of all degrees of freedom on other sites of the lattice and can be thought of as a reservoir of non-interacting electrons. The quantum state of one site constantly evolves in time as it absorbs or emits electrons from the reservoir with the probability amplitude of  $V_\nu$  (figure 1.3).

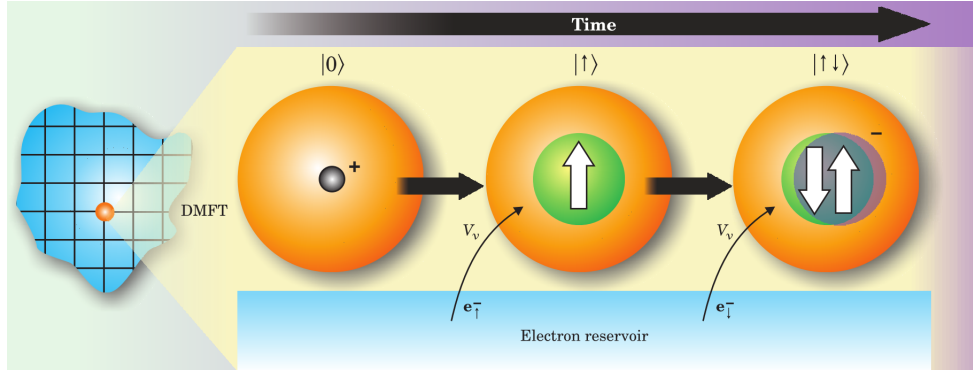


Figure 1.3: DMFT describes the interaction between one site and a bath. The quantum state of the site varies in time as electrons are emitted or absorbed by that site with the amplitude of  $V_\nu$ . From [91].

The analogy to the Anderson impurity model is now clear; one can treat the lattice site as an impurity to the conduction band that is described by the bath:

$$H_{AIM} = -\mu \sum_{\sigma} c_{0,\sigma}^\dagger c_{0,\sigma} + U n_{0\uparrow} n_{0\downarrow} + \sum_{\nu,\sigma} \varepsilon_\nu^{bath} n_{\nu,\sigma}^{bath} + \sum_{\nu,\sigma} (V_\nu c_{0,\sigma}^\dagger a_{\nu,\sigma}^{bath} + h.c) \quad (1.7)$$

The first two terms are the lattice site's Hamiltonian. The bath has energy levels of  $\varepsilon_\nu$  with occupation number  $n_{\nu,\sigma}$  for each spin. The hopping of electrons between one site and the bath is explained by the annihilation and creation operators that for the lattice site and the bath are  $(c_{\nu,\sigma}, c_{\nu,\sigma}^\dagger)$  and  $(a_{\nu,\sigma}, a_{\nu,\sigma}^\dagger)$ , respectively.

Just as DFT gives the exact density of the ground state, the impurity model gives the correct local Green function in DMFT:

$$G[\Delta(\omega)] = \sum_k (\omega - \Sigma[\Delta(\omega)] - t_k)^{-1} \quad (1.8)$$

The frequency dependence of the Green function represents the dynamical aspect of the DMFT, i.e. the quantum state of the site evolves in time. The self-energy term is  $\Sigma[\Delta(\omega)]$  and the hybridization function  $\Delta(\omega)$  is the ability of an electron to jump in or out of an atom at a time scale of  $1/\omega$ . The Fourier transform of the Hubbard hopping amplitude appears in the Green function as  $t_k$ .

In the end the DMFT energy functional,  $\Gamma[\rho(\mathbf{r}), G]$ , is written as an exact functional of the electron density and the local Green function and has a form similar to the equation 1.6. By minimizing the energy and applying the self-consistency condition, DMFT gives an explicit approximation of  $E_{xc}[\rho(\mathbf{r}), G]$  and hence, of the spectrum of strongly correlated systems. More specifically, one can study the evolution of the density of states as correlations are increased. The limits of the Hubbard model  $U \rightarrow 0$  and  $U \rightarrow \infty$  gives a metallic and insulating phase as it has been discussed before, figure 1.4. For intermediate values of  $U$ , the spectrum presents common features of both metallic and insulating phase; a quasiparticle (QP) peak at the Fermi level accompanied Hubbard bands. The width of the quasiparticle reflects the hopping amplitude of electrons. As  $U$  is enhanced, the electrons tend to get more localized. The QP peak weakens and shrinks while the spectral weight is transferred towards the lower and upper Hubbard bands. These three bands are analogous to the spectrum of the Anderson impurity model. A metal to insulator transition occurs for very large  $U$  that is able to suppress the density of states at the

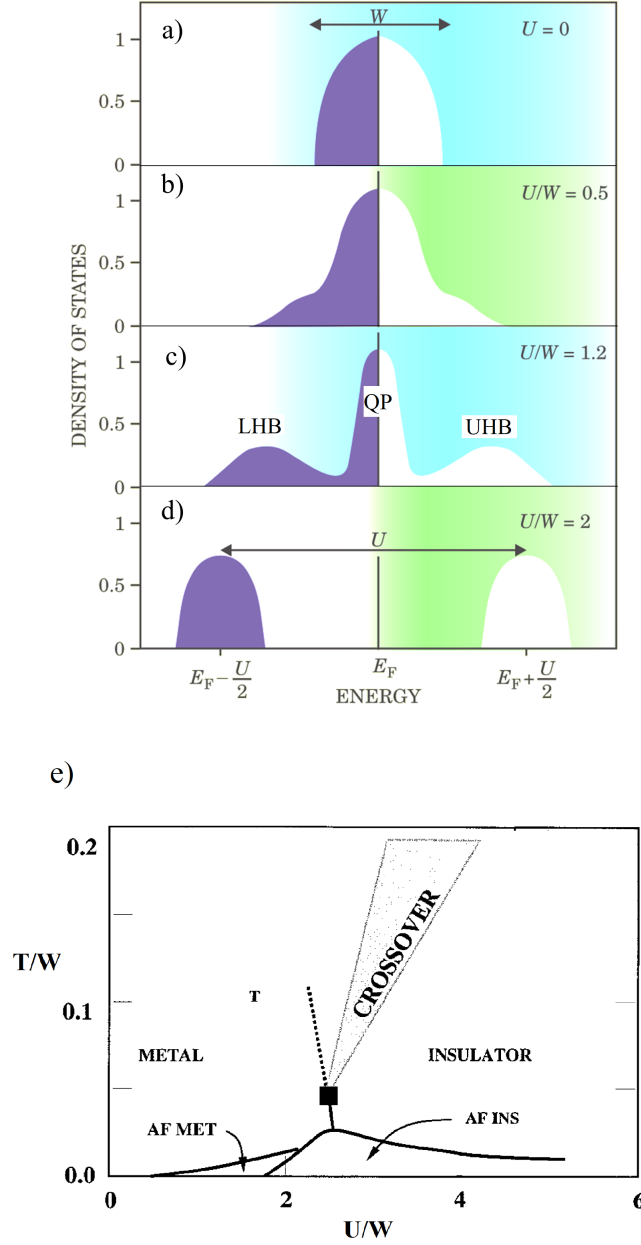


Figure 1.4: (a-d) Density of states from DMFT in strongly correlated materials with respect to the ratio of  $U$  (Coulomb repulsion) and  $W$  (bandwidth), from [91]. (e) Approximate phase diagram for the Hubbard model with nearest-neighbor and next-to-nearest-neighbor hopping  $t_2/t_1 = 1/\sqrt{3}$ . The first-order paramagnetic metal to insulator transition ends at the critical point (square). The system then goes to the crossover region. The phase diagram is calculated for a single-band model and is adopted from [50].

Fermi level and opens a gap of order  $U$  between the LHB and UHB.

DMFT also succeeded in constructing an approximate phase diagram of strongly correlated materials with respect to the ratios of  $T/W$  and  $U/W$  [50], where  $W$  is the bandwidth, figure 1.4 (e). At low temperature the systems orders antiferromagnetically (AF) for both the metallic and insulating phases. As the temperature increases the magnetic order vanishes and paramagnetic phases appear. At high temperature, the limit of metallic and insulating behavior merges to a crossover region. In this region, the QP peak of the metallic precursor dramatically smears out and in the insulating phase the spectral weight of the LHB gradually fills the gap [119]. The crossover regime can be viewed as a bad quasi-insulating behavior.

### 1.3.2 $V_2O_3$ , a prototype Mott-Hubbard material

Vanadium sesquioxide,  $(V_{1-x}M_x)_2O_3$  is a textbook example of a Mott-Hubbard system [115, 117] and a benchmark to compare different theoretical models for strongly correlated systems [120, 138]. Its phase diagram spanned in the temperature-doping space displays three phases: a paramagnetic metallic (PM), a paramagnetic insulating (PI), and an antiferromagnetic insulating (AFI) phase, figure 1.5 (a). As seen in the resistivity curve figure 1.5 (b), a first order transition from the PM to AFI phase is observed at lower temperature,  $T_N$ , accompanied a structural and magnetic order phase change. This transition corresponds to a sharp jump of about 6 orders of magnitude in the resistivity. A second first order transition is also seen at higher temperatures with no crystal symmetry breaking and is assigned to the Mott transition from the PM phase to the PI phase. Here, the resistivity change is less abrupt and is about one order of magnitude. The transition into the insulating state can be triggered by increasing temperature, increasing chemical substitution in Cr or by decreasing pressure  $P$ . For instance, for Cr-doping more than 17%, the metallic state is completely suppressed. An increase of Cr doping decreases the AFI gap and increases the PI one. In fact, the most widely studied group of vanadium sesquioxide family is the chromium-doped group [45, 60, 119]. Early studies [77, 115, 116] have shown that decreasing concentration of vanadium by  $\Delta x \sim -0.01$  is equivalent to an applied pressure of  $\Delta P \sim 4$  kbar. Alternatively, the chemical substitution with titanium corresponds to an increase of pressure.

In vanadium sesquioxide even the PM phase is characterized by strong Coulomb-correlation effects: bad metallic behavior with the resistivity of  $\rho = 2 \times 10^4 \Omega\text{cm}$  at ambient temperature [94]. A phase mixture between PI and PM phases, called the crossover regime, happens above the critical point at around 400 K [119].

#### 1.3.2.1 Crystal structure and electronic configuration

In the PI and PM phase the compound has a corundum structure and the symmetry space group is  $R\bar{3}c$  [116], figure 1.6. The unit cell structure can be viewed as the stacking of octahedra with 6 oxygens and a vanadium in the middle coordinated by oxygen ligands in a trigonally distorted octahedral fashion, figure 1.6 (a). This distortion is increased by a tilt of the  $c$  axis when crossing from the PM phase to the AFI phase. The AFI phase crystal structure is monoclinic and its symmetry group is  $I2/a$ .

In  $V_2O_3$ , the most crucial distance in order to understand the Mott transition is the vertical  $V_1$ - $V_4$  distance, which is smaller than the basal  $V_1$ - $V_2$  distance [155]. In the Mott insulating phase, the  $c$ -axis length decreases. Therefore, two consecutive octahedral groups get closer along the  $c$ -axis while the  $V_1$ - $V_4$  distance increases. The reverse occurs in the metallic phase [116], figure 1.6 (b). The sizeable change in the lattice parameter indicates an important coupling between electronic and lattice degrees of freedom. The order parameter of the Mott transition

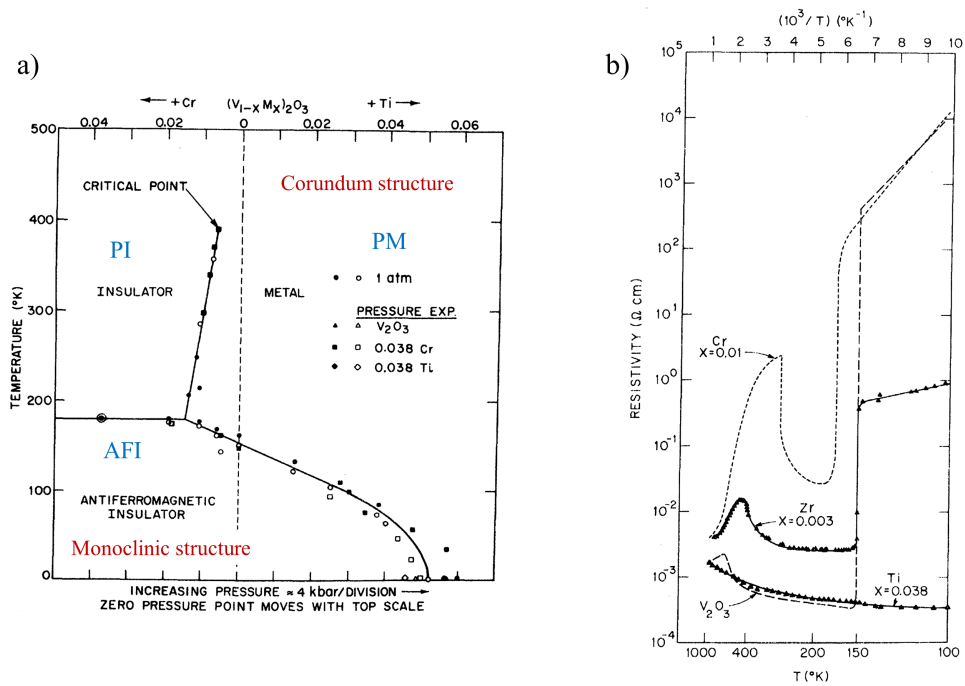


Figure 1.5: (a) Phase diagram of  $V_2O_3$  as a function of chemical substitution and temperature. (b) Resistivity perpendicular to the  $c$  axis of the crystal vs. temperature for several doped samples. From [115].

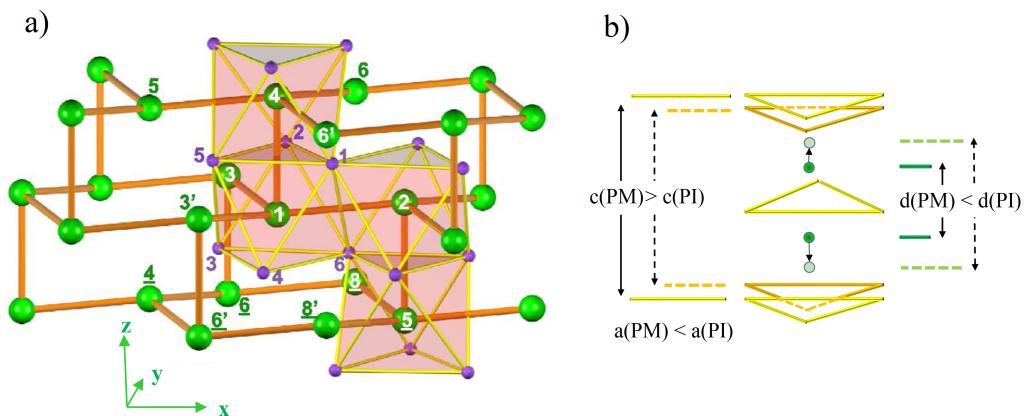


Figure 1.6: (a) Crystal structure of  $V_2O_3$  from [155] in the high-temperature paramagnetic phase. The green circles indicate the V atoms. The violet circles are oxygens. (b) Arrangement of atoms in the PI and PM phase.  $a$  and  $c$  are the units cell parameters and  $d$  is the distance between the neighboring vanadium atoms.

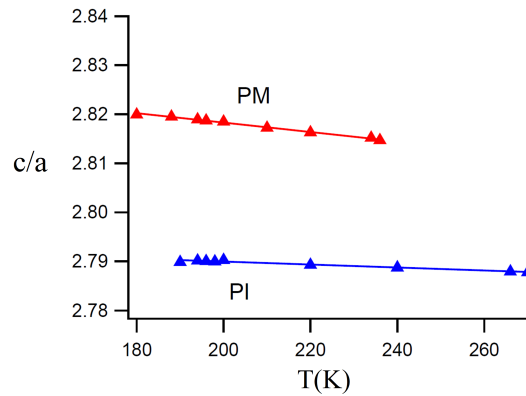


Figure 1.7: Variation of  $c/a$  during the Mott transition.

in  $V_2O_3$  compound can be defined as the  $c/a$  ratio, figure 1.7. Since the transition is a first order one, the variation of  $c/a$  has a large hysteresis with respect to the temperature and the sample shows a phase coexistence even above the critical point. The phase coexistence has been observed and confirmed by scanning photoemission microscope [104].

There have been many attempts to explain the Mott transition in  $V_2O_3$  and the spin structure of the antiferromagnetic insulating phase [23, 64, 155]. The octahedral crystal field splits the  $d$ -orbitals of vanadium atoms into the lower lying  $t_{2g}$  and the higher lying  $e_g^\sigma$  states located at 3 eV above the Fermi level [57]. Furthermore, the trigonal distortion lifts the degeneracy of the lower lying  $t_{2g}$  states and splits into a single  $a_{1g}$  and the twofold degenerate  $e_g^\pi$  states. The hybridization between the two nearest vanadium atoms,  $V_1$  and  $V_4$ , along the  $c$ -axis causes a large splitting between bonding  $a_{1g}$  and antibonding  $a_{1g}^*$  states. In spite of that, the DMFT+LDA calculations have shown the  $a_{1g}$  orbitals remains mostly unoccupied in the PI phase [64], figure 1.8, whereas the  $e_g^\pi$  orbitals are occupied by almost one electron each. In  $V_2O_3$ , the PI phase can thus be viewed as a half-filled two-band Mott insulator stabilized by the correlation-enhanced trigonal field that pushes above the Fermi energy the  $a_{1g}$  orbitals. The occupancy of the  $a_{1g}$  orbitals indeed jumps across the doping- or temperature driven Mott transition causing the opening or closure of a gap. This highlights the crucial role of the electron correlations in the MIT in  $V_2O_3$ , which is stabilized by the trigonal distortion [149], [148]. Moreover, it has been demonstrated that the on-site Coulomb energy  $U$  does not change through the MIT [45]. Therefore, the physics of the system is best described by the filling-controlled MIT. Some bulk-sensitive photoemission experiments [45, 120] have revealed the evolution of the density of states across the MIT as well different regions of the phase diagram, figure 1.9.

## 1.4 Dirac semimetals

Dirac settled a reconciliation between special relativity and quantum mechanics [36]. In condensed matter physics, the energy scales that determine the electronic properties of a system is in order of few electronvolts that is insignificant compared to the rest mass of an electron (0.511 MeV). Therefore, the relativistic quantum mechanics seems to be redundant at first glance. However, the discovery of graphene proved that even slow electrons propagating through a periodic crystal potential can give rise to relativistic fermions, with linear band dispersion, that are uniquely described by the Dirac equation. Shortly after, the revolutionary topological insulators were discovered. These materials are insulators in bulk, however their surface states display massless Dirac fermions with metallic behavior that are protected by the topology of the bulk

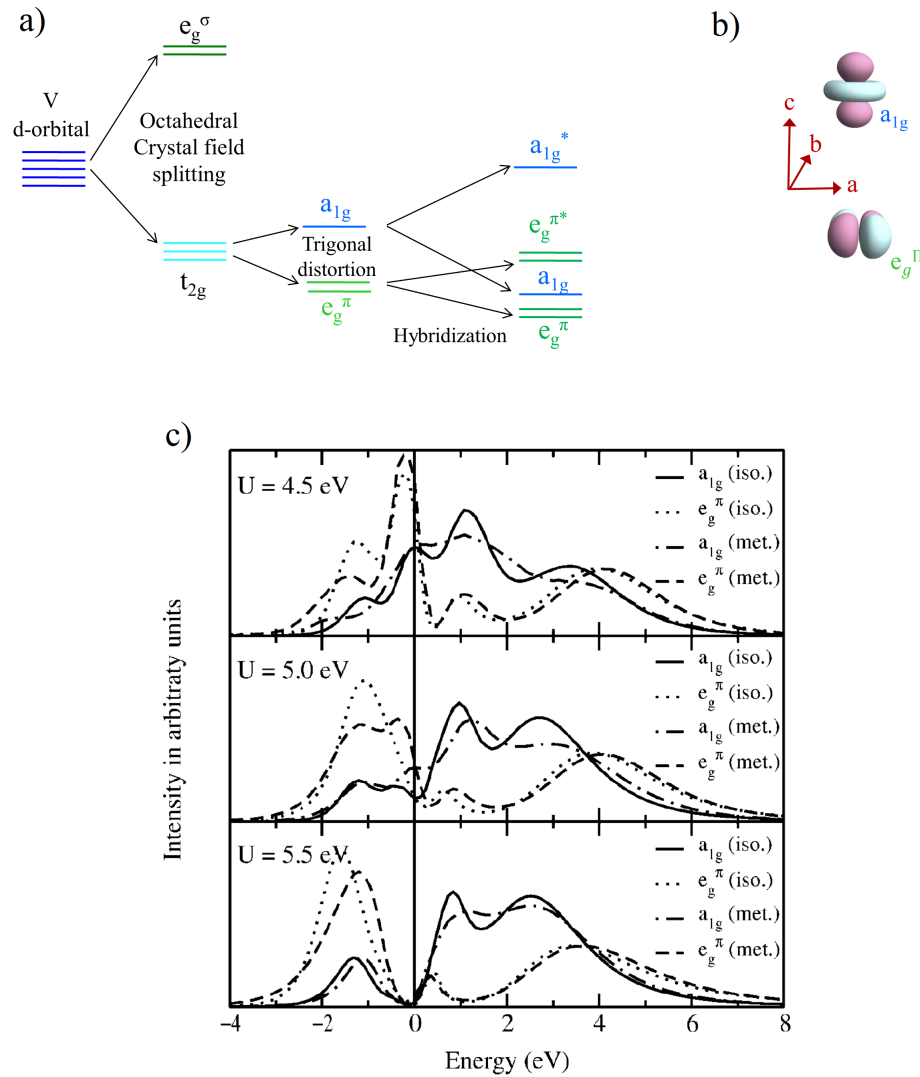


Figure 1.8: (a) Energy level splitting in  $V_2O_3$ . (b) Orbital geometry. The bonding  $a_{1g}$  orbital is along the c-axis and while the  $e_g^\pi$  orbital is in the a-b plane. (c) LDA+DMFT spectra for paramagnetic  $(V_{0.962}Cr_{0.038})_2O_3$  (iso.) and  $V_2O_3$  (met.) at  $U = 4.5, 5,$  and  $5.5$  eV, and  $T = 1000$  K [64].

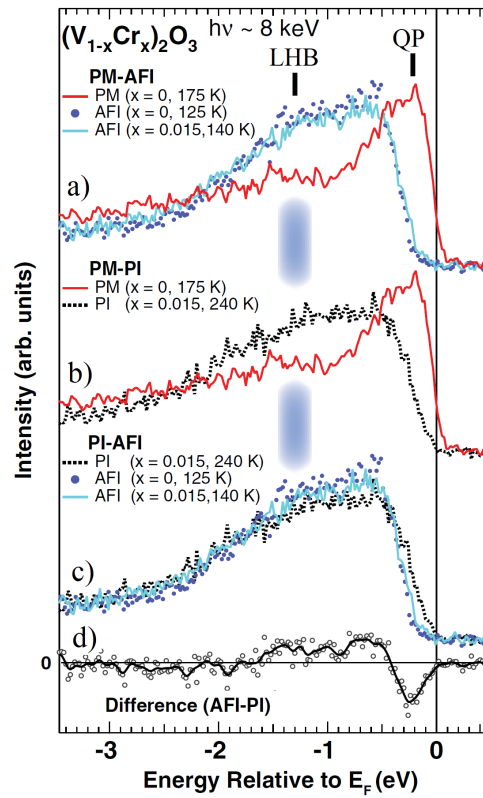


Figure 1.9: (a - c) High-resolution hard X-ray photoemission spectra of  $(V_{1-x}Cr_x)_2O_3$  ( $x=0$  and  $0.015$ ) near the Fermi level in all phases. (d) Difference between the AFI and PI spectra. The lower Hubbard band is located at the same energy for all of the studied point within the phase diagram suggesting that the parameter  $U$  remains constant. From [45].

electronic wave function. The ensuing years of intense research were accompanied by realizing topological states also in metals or semimetals, and not only in insulators. Weyl, line-node, and Dirac semimetals are examples of these novel states that have protected and robust Weyl/Dirac nodes in momentum space thanks to the interplay of the topology of wave functions and crystal space group symmetries. These novel quantum materials can be viewed as the 3D analogue of graphene but with some rich and important differences.

I start the discussion on Dirac semimetals (DSM's) by a brief reminder on topological insulators and graphene.

### 1.4.1 Topological insulators

The notion of the topology of wave functions was first introduced in condensed matter physics by the discovery of the quantum hall effect (QHE) in two-dimensional materials that in the presence of magnetic field reveal robust edge conductance. The existence of such edge states is rooted in the topology of the bulk. The following years of research widened the horizon by the emergence of topological insulators (TI) [62, 81, 82, 150]; materials with a gapped bulk state while their edge or surface has protected conducting states. The novelty of these materials is that in contrast to the QHE, the conductance occurs without an external magnetic field—that is, the time-reversal symmetry (TRS) is respected, and combined with the spin-orbit coupling (SOC), results in robust states at the boundaries of the material. A two-dimensional TI (2D TI) can be viewed as two copies of quantum hall states each for one spin direction (up or down) that leads to a one-dimensional spin-polarized current along the edges [128]. It is also called a quantum spin hall insulator. This well-defined spin-dependent direction of propagation in real space is translated into momentum-spin locking in momentum space. In the same way, a three-dimensional TI (3D TI) manifests 2D spin polarized current on its surface. The edge/surface states behave like a massless relativistic particle and are described by Dirac equations:

$$H = \hbar v \vec{\sigma} \cdot \vec{q} \quad (1.9)$$

where  $v$  is the velocity, and  $\sigma$  and  $\mathbf{q}$  present spin and momentum (relative to the Dirac point), respectively. Figure 1.10 describes the principles of a 2D and 3D TI.

The momentum-spin locking for a relativistic particle is defined as *chirality*. The chirality of a relativistic particle is right handed if its spin points in the same direction as its momentum, while its chirality is left handed if its spin points in the opposite direction. The difference between the number of right-movers and left movers defines a topological invariant. Gapless edge or surface states occur whenever the topological invariant changes across a boundary. In contrast to electronic bands in a normal metal, these states are not spin degenerate except in their crossing points. The time-reversal symmetry implies that states at momenta  $\mathbf{k}$  and  $-\mathbf{k}$  have opposite spin and thus the spin must rotate with  $\mathbf{k}$  around the Fermi surface—the electron acquires a non-trivial Berry phase while circling the Fermi level. But what is a Berry phase mathematically? How is it related to the topology of the bulk states? According to the Bloch's band theory, the electronic states within a unit cell are described by  $u_n(\mathbf{k})$ , where  $n$  is the band index and  $\mathbf{k}$  is the crystal momentum. In quantum mechanics, the Berry phase arises in a cyclic adiabatic evolution. In our case, this means when the wave function walks on a closed path around a given point in the momentum space. This particular point is the intersection of the edge/surface state and the Fermi level. The contribution of the band  $n$  to the total Berry phase is:

$$N_n = \int (\vec{\nabla} \times \vec{A}) \cdot \frac{d\vec{k}}{2\pi} \quad (1.10)$$

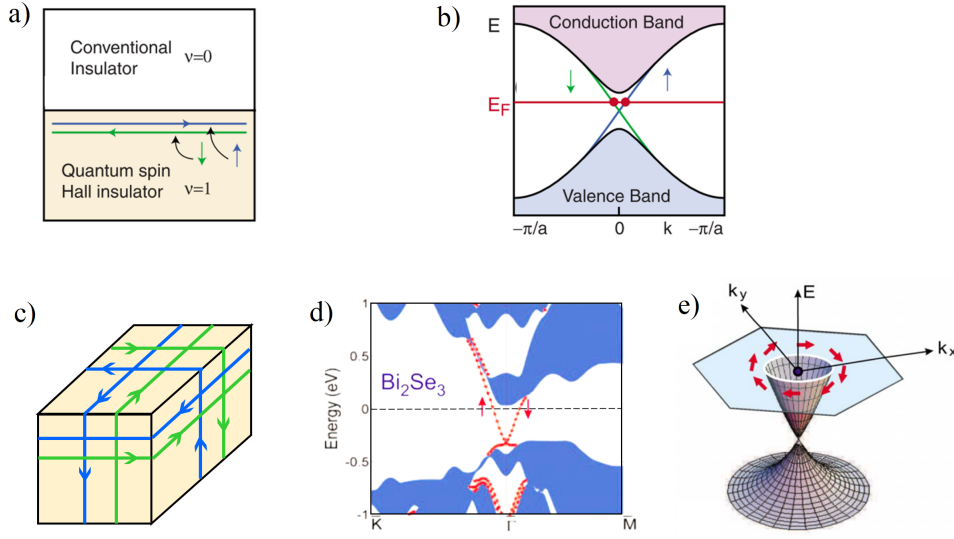


Figure 1.10: (a) Schematic figure of a 2D TI. (b) The electronic band structure presents gapless chiral edge states. (c) Current distribution on the surface of a 3D TI. (d) The electronic band structure of  $\text{Bi}_2\text{Se}_3$ . (e) Schematic of the spin-polarized Dirac-like surface-state dispersion, from [150].

Here,  $\vec{A} = -i\langle u_n(\vec{k}) | \nabla_{\mathbf{k}} | u_n(\vec{k}) \rangle$ . From the above equation one can see that the Berry flux  $\Omega(\vec{k}) = \vec{\nabla} \times \vec{A}$  behaves like a magnetic field in momentum space. However, unlike the physical magnetic field, this *Berry field* is allowed to have magnetic monopoles that, as we will see farther, are called Weyl points. I will come back to this point later.

The sum of  $N_n$  for all occupied states below the Fermi level is called the Chern number (introduced by Thouless *et al.*) and defines the topological invariant of a bulk insulator. If in addition to having TRS the lattice is also inversion symmetric then the calculation of the Chern number greatly simplifies [44]. One only needs to know the parity eigenvalue of the  $2m^{\text{th}}$  occupied energy band  $\xi_{2m}$ , at each time-reversal invariant momentum  $\Gamma_i$ . At these special points  $\mathbf{k} \equiv -\mathbf{k} \pmod{\mathbf{G}}$  where  $\mathbf{G}$  is a reciprocal lattice vector. We start by calculating the following quantity:

$$\delta_i = \prod_{m=1}^N \xi_{2m}(\Gamma_i) \quad (1.11)$$

The topological invariant  $\nu$  is then determined by:

$$(-1)^\nu = \prod_i \delta_i \quad (1.12)$$

The parity eigenvalues  $\xi_{2m}(\Gamma_i) = \pm 1$  and are tabulated in the literature. The number of time-reversal invariant momenta in 2D and 3D is four and eight, respectively.

The surface states of a 3D TI has important similarities with the Dirac cone in graphene although the origin of each one is different. In a topological insulator, the bulk is insulating while the non-trivial surface states are metallic. The absence or presence of these states depends on the topology of the full states wave function. On the contrary, the Dirac cone in graphene is a direct consequence of the electronic band structure while no non-trivial topology is involved. I dedicate few paragraphs to recall fundamentals of graphene.

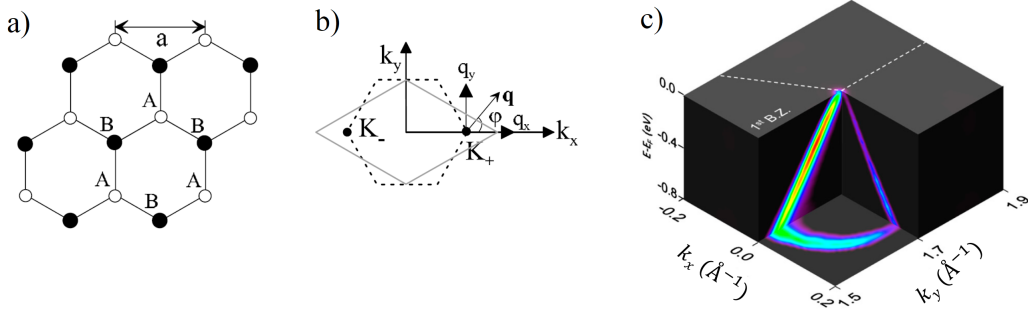


Figure 1.11: (a) Graphene lattice with sublattices A and B. (b) Hexagonal Brillouin zone. The inequivalent valleys are  $K_{\pm}$  and the wavevector of  $\mathbf{q}$  is measured from the center of the valley. (c) ARPES spectra of monolayer graphene, showing several slices through the Dirac cone, from [165].

### 1.4.2 Graphene, a prototype of Dirac materials

Since the discovery of graphene in 2004 followed by observations of the classical and quantum Hall effects [132], it has been subject of an extensive experimental and theoretical investigation that has never ceased to come up with surprising phenomena. The two-dimensional layer of carbon atoms are arranged on a honeycomb lattice that can be viewed as two interpenetrating triangular lattice A and B, figure 1.11 (a). The two sublattices are like two degrees of freedom and the electron has a probability amplitude to be on each sublattice. This resembles the case with spin one-half particle, where an electron can be in spin-up state  $|\uparrow\rangle$ , spin-down state  $|\downarrow\rangle$ , or any superposition of them. By analogy, the sublattice basis is therefore called a pseudospin. The hexagonal Brillouin zone (BZ) is shown in figure 1.11 (b). The unique electronic band structure of graphene presents conical valence and conduction bands that meet each other on the edge of the Brillouin zone at the so-called degenerate Dirac points. These six points are divided into two non-equivalent sets in the momentum space called  $K_+$  and  $K_-$  or valleys [47]. These points differ by their chirality which will be explained later. In a nominally undoped sample, the Dirac points occur exactly at the Fermi level however, by applying magnetic field or back voltage, as in the case of figure 1.12, one can tune the Dirac point position in energy [13, 131] and turn the semimetallic state to a metallic one. The existence of Dirac points near the Fermi level is responsible for many of important properties of graphene such as high electron mobility and conductivity. The valley degree of freedom is sometimes referred to as valley isospin and should not be confused with sublattice pseudospin. The eigenstates within a single valley (isospin), have different amplitudes on A or B sites that can be interpreted as pseudospins. I emphasize that the inequivalence of the two Brillouin zone corners,  $K_+$  and  $K_-$ , has nothing to do with the presence of two sublattices, A and B, in the honeycomb lattice.

The underlying interest for graphene can be concisely described as follows: First, graphene offers ballistic transport and its conductivity never drops below a minimum value [131] that corresponds to the quantum unit of conductance  $\sigma \sim e^2/h$ , figure 1.12. This minimum of conductivity is a unique and intrinsic property of electronic systems described by the Dirac equation leading to unusual spectroscopic and transport properties [24]. This implies that in 2D Dirac

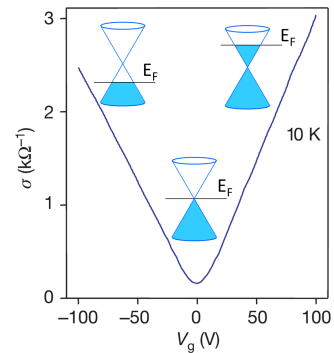


Figure 1.12: An applied voltage shifts the position of the Fermi level with respect to the Dirac point and changes the conductivity.

fermions, no localization is expected [1].

Second, the charge carriers in graphene travel as effectively massless and relativistic particles with a fixed speed of  $c^* \sim c/300$ , as it follows from the nearly linear dispersion of the bands close to the Dirac K-points [131], c.f. equation 1.9. Figure 1.11 (c) shows the electronic band structure of graphene obtained by ARPES. Graphene has four Dirac points: 2 valleys and 2 spins. The Dirac points in graphene are protected by time-reversal and inversion symmetry in a honeycomb lattice unless there is a perturbation perpendicular to the  $a$ - $b$  plane. For example, the SOC makes the Dirac fermions massive and gaps the Dirac point.

Third, graphene has many-body interactions including electron-electron and electron-phonon interactions [165]. A comprehensive knowledge of graphene is essential to understand superconductivity in carbon nanotubes [87] or graphite intercalation compound [59]. Only very recently, during the course of my thesis, superconductivity has also been surprisingly discovered in bilayer graphene under certain conditions. I will return to this later.

#### 1.4.2.1 Electronic chirality

The conical band dispersion close to the K-points as well as the pseudospin described before make it possible to extend the notion of chirality to the electronic states of graphene. Here, the projection of the pseudospin onto the direction of the wavevector  $\mathbf{q}$  defines the chirality of pseudospin. For the given  $K_+$  valley, the momentum vector reads  $\mathbf{q} = (q \cos \varphi, q \sin \varphi)$  as seen in figure 1.11 (b). The angle  $\varphi$  specifies the direction of the electronic wavevector measured from the center of the valley. On the other hand the relative phase between the wave functions on each sublattice A or B gives the pseudospin wavevector  $\sigma = (\cos \phi, \sin \phi, 0)$ . For the conduction band  $\varphi = \phi$  and for the valence band  $\varphi = \phi + \pi$ . The chiral operator  $\sigma \cdot \frac{\mathbf{q}}{q}$  then defines the chirality for each K-point. For the  $K_+$  point, the chirality is -1 (+1) for the valence (conduction) band. On the contrary, the  $K_-$  valley has the opposite sign chirality for the corresponding bands. Interaction energies are lowered when most electrons have the same chirality, just as interaction energies in ferromagnets are lowered when most particles have the same spin [47]. Therefore, this difference in chirality between positive and negative energy bands tends to protect the system from magnetic impurities and other instabilities.

#### 1.4.2.2 Superconductivity in graphene

As previously mentioned, bilayer graphene reveals zero resistance under the condition that each sheet is offset by an angle of  $\sim 1.1^\circ$  with respect to the other one [22]. In this way, the band structure shows a flat band region at the Fermi level and it implies that the electrons are completely localized in the real-space. The superconductivity has been shown to occur at 1.7 K. However, what makes it peculiar is that graphene attains the superconducting state without the need of chemical doping and only by applying small gate voltage, i.e. with one-ten-thousandth of the electron density of conventional superconductors described by production of Cooper pairs. The key is that the number of charge carriers in graphene is electrically tunable.

More generally, twisted bilayer graphene shows a phase diagram that resembles that of high-temperature cuprate superconductors [21]. Figure 1.13 (a) shows the calculated band structure for the bilayer graphene at  $\theta = 1.05^\circ$ . By applying gate voltage the position of the Fermi level changes and if it lies at the half-filling ( $n \sim -1.4 \times 10^{12} \text{ cm}^{-2}$ ) of the lower-energy band, an insulating state appears that bears similarities to a Mott insulator. Superconductivity is achieved as one dopes slightly away from the Mott-insulating state, figure 1.13 (d).

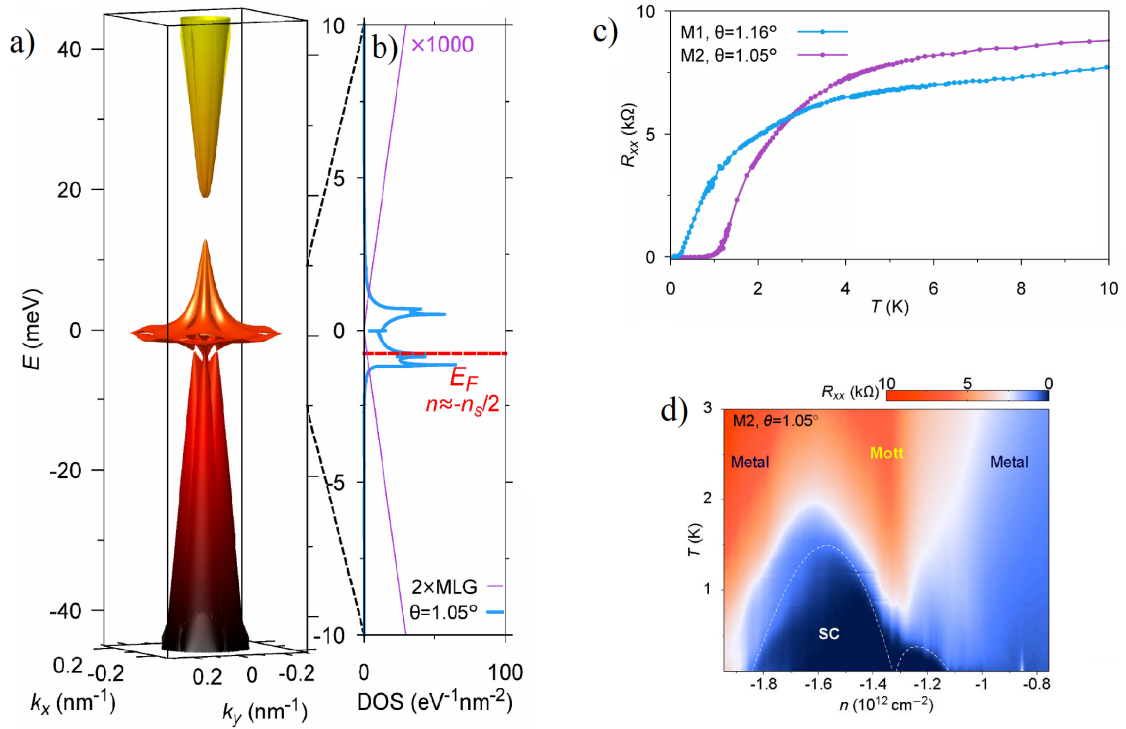


Figure 1.13: (a) The calculated band structure of twisted bilayer graphene at  $\theta = 1.05^\circ$  in the new Brillouin zone. (b) The density of states zoomed in to -10 to 10 meV. The purple lines show the DOS of two sheets of graphene without neither layer interaction nor twist angle. The red dashed line shows the Fermi energy at half-filling of the lower branch. The superconductivity is observed near this half-filled state. (c) Measured resistivity for two twisted angles. (d) The phase diagram of the bilayer graphene with angle  $1.05^\circ$ . The color scale represents the resistivity for various temperature and carrier number. From [22].

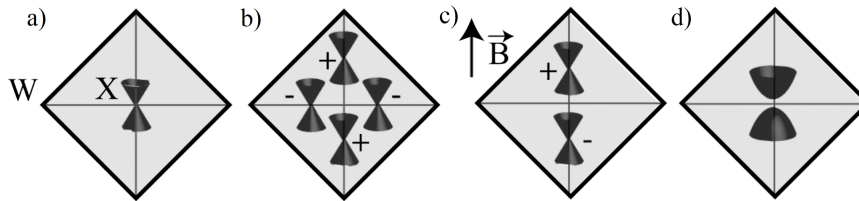


Figure 1.14: Schematics of a Dirac/Weyl semimetal phase in  $\beta$ -cristobalite BiO<sub>2</sub>. (a) The symmetry protected Dirac point occurs at three symmetry related X-points. (b) Four Weyl points migrate to the boundaries of the Brillouin zone due to the broken inversion symmetry. (c) A magnetic field breaks the TRS and results in two Weyl point. (d) Gapped phase is obtained by breaking the fourfold rotation symmetry. From [198].

### 1.4.3 Dirac and Weyl semimetals

Dirac (Weyl) semimetals [4, 180, 191] are novel states of 3D quantum materials in which valence and conduction band touch each other at discrete points of the Brillouin zone and disperse linearly in all direction around these Dirac (Weyl) points. Their low-energy physics is described by the Weyl Hamiltonian  $H_{Weyl}(\mathbf{k}) = v_{ij}k_i\sigma_j$  that can be viewed as a generalized version of the Dirac Hamiltonian. For the moment, I call the band crossing point a Weyl point and the reason will be clarified farther. With the same analogy as in topological insulators, we can define the robustness of a Weyl point at  $\mathbf{k}$  by calculating the Berry flux on a surface surrounding that point, c.f. equation 1.10. The time-reversal symmetry maps  $\mathbf{k}$  to  $-\mathbf{k}$ , and therefore reverses the momentum space magnetic field;  $\Omega(\vec{k}) = -\Omega(\vec{k})$ . In this case, a Weyl point is mapped into another Weyl point in the momentum space with the same chirality. If the inversion symmetry is additionally respected, it results in  $\Omega(-\vec{k}) = \Omega(\vec{k})$  and under this symmetry a Weyl point is mapped into another Weyl point at  $-\mathbf{k}$  with opposite chirality. The combined operation of both symmetries requires that each band is doubly degenerate for each  $\mathbf{k}$ , i.e.  $E_{n,\uparrow}(\vec{k}) = E_{n,\downarrow}(\vec{k})$ . Naturally, at the crossing point of these bands we have four-fold degenerate linearly dispersing bands. This point is now called a Dirac point that can be viewed as two copies of a Weyl node with opposite chirality and is explained by a  $4 \times 4$  Dirac Hamiltonian:

$$\begin{pmatrix} \hat{H}_{Weyl}(\vec{k}) & 0 \\ 0 & \hat{H}_{Weyl}(\vec{k})^* \end{pmatrix} \quad (1.13)$$

Here,  $\mathbf{k}$  measures momentum relative to the Dirac point and  $\hat{H}_{Weyl}(\vec{k})$  is a right-handed Weyl Hamiltonian, while  $\hat{H}_{Weyl}(\vec{k})^*$  is its left-handed (time-reversed) counterpart.

The degeneracy at the Dirac point is not topologically protected since its net Chern number is zero and residual perturbative terms in the Hamiltonian can hybridize the constituent states with different Chern number and gap the electronic bands. However, in particular situations this mixing can be forbidden by space group symmetries. Two ways have been suggested so far:

i) The Dirac point results from an unavoidable band crossing that occurs in pair along a symmetry axis. The bands should belong to different representations. In this "band-inversion" mechanism, the Dirac semimetal is not truly symmetry-protected; it is possible to uninvert the bands and annihilate the Dirac points pairwise by gradually tuning the Hamiltonian without changing the space group. The  $\text{Na}_3\text{Bi}$  is an example of such band-inversion mechanism that supports Dirac points on its six-fold symmetry axis [101, 182]. Another well-known example is  $\text{Cd}_3\text{As}_2$  [129, 183], figure 1.16 (a). In both families of compounds, the low-energy physics is controlled by a single band inversion occurring near the  $\Gamma$  point of the Brillouin zone. If the symmetries of the system is lowered, the resulting gapped phase will be a topological insulator.

ii) For system with SOC, the protection of the Dirac point is assured by nonsymmorphic symmetries<sup>1</sup> of the crystal space group, such as glide planes and screw axes, on the special  $\mathbf{k}$ -points of the Brillouin zone boundaries with four dimensional irreducible representation. This is called a "symmetry-enforced" mechanism [198, 199] and makes a single Dirac point to appear at a time-reversal invariant momentum when the conduction and valence bands touch. In this way, removing the Dirac point is not possible without an explicit breaking of the symmetry.

#### 1.4.3.1 Weyl semimetals

If either time-reversal or inversion symmetry is broken, a parent Dirac point separates into Weyl points with different chiralities and one obtains a Weyl semimetal. In a magnetic crystal, the

<sup>1</sup>Nonsymmorphic space groups are distinguished by the existence of symmetry operations that combine point group operations with translations that are a fraction of a Bravais lattice vector.

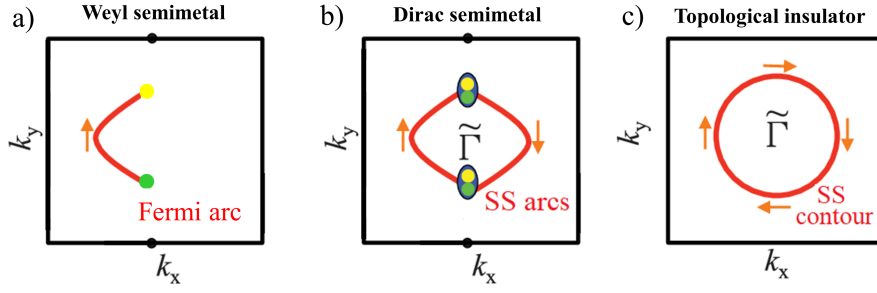


Figure 1.15: (a) Fermi arc in a 3D Weyl semimetal. (b) Pair of surface state (SS) Fermi arcs in a 3D DSM. (c) Surface states in a 3D TI.

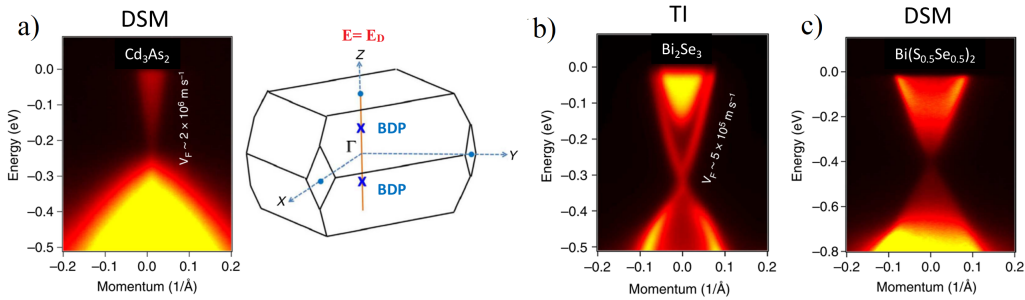


Figure 1.16: (a) ARPES spectrum of  $\text{Cd}_3\text{As}_2$ . The compound shows a very high mobility of  $\sim 10^6$   $\text{m/s}$ . The Dirac points are located at 250 meV below the Fermi level and their corresponding position in the Brillouin zone is shown in the right side. (b) Band dispersion of the topological insulator  $\text{Bi}_2\text{Se}_3$ . The surface states connect two gapped states. (c) The critical composition to achieve a DSM starting from the topological insulating phase is  $\delta = 0.5$ . Adopted from [129].

broken TRS results in two Weyl nodes with opposite Chern number [20]. On the other hand, in a non-centrosymmetric crystal the total number of Weyl points occurs as a multiple of four since the total Chern number must vanish on the Brillouin zone [192]. Figure 1.14 schematically presents a Dirac semimetal and possible ways of having a Weyl semimetal.

Weyl points are monopoles of Berry flux and are chiral due to a nontrivial topology. One strong manifestation of such topology is the emergence of spin-polarized surface states that connect two different Weyl points together. These so-called Fermi arcs are a direct consequence of the fact that Weyl nodes are sources and sinks of Berry flux [4]. The Fermi arcs can also occur in a DSM where a pair of protected surface modes connect the Weyl points embedded in the partner Dirac nodes, figure 1.15. Some ARPES measurements have revealed double Fermi arcs on  $\text{Na}_3\text{Bi}$  [189] and  $\text{Cd}_3\text{As}_2$  [197]. In contrast to 3D TIs, in 2D or 3D DSM linearly dispersing valence and conduction bands do not have spin polarization as these cases arise from the bulk itself not from the surface states. However, the spin polarization lurks in Fermi arc surface states. Before giving some detailed examples of DSMs, it is worth recalling that while surface states of a topological insulator do not have  $k_z$  dispersion due to their intrinsic 2D nature, the Dirac point of DSM disperses along the  $z$ -axis of the Brillouin zone.

### 1.4.3.2 Material consideration

The electronic systems with exotic Dirac fermions in 2D or 3D have been an active field of research in recent years. Besides their fundamental interest from theoretical and experimental point of view, their unique properties make them possible candidates for future applications

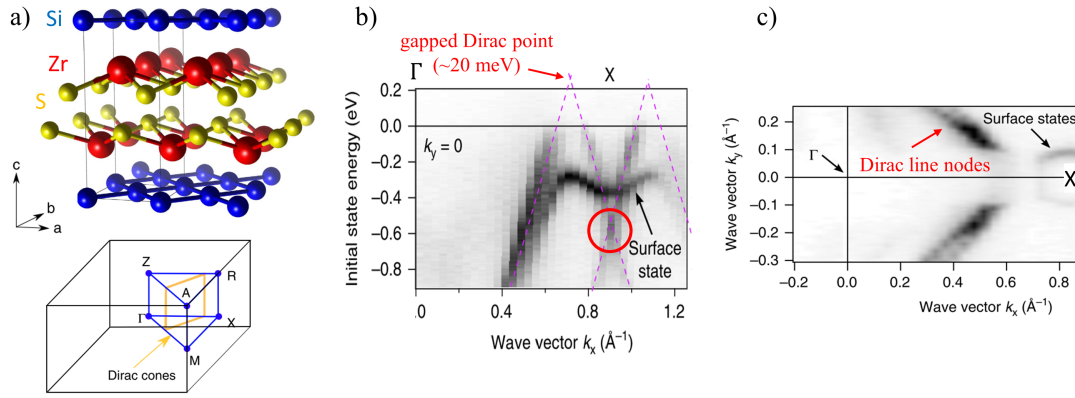


Figure 1.17: (a) Crystal structure of ZrSiS together with the Brillouin zone. The orange contour on the Brillouin zone shows the Dirac line nodes. (b) The band structure along the  $\Gamma$ X shows two Dirac cones. The one at X is protected by the crystal symmetry. (c) The iso-energy surface spectrum at the Fermi level reveals the Dirac line nodes. The Dirac node is slightly above the Fermi level. From reference [162].

in optoelectronic and fast photodiodes. Therefore, an ongoing effort in this field is to search for new materials that manifest Dirac/Weyl fermions. In addition to the crystal structure that should allow particular symmetries, two crucial ingredients are large enough band gap and band inversion at or close to the Fermi level. These criteria imply that Dirac/Weyl fermions should be the principal constituents to determine physical properties of the systems without intervention of other bands at the chemical potential. The band gap magnitude is determined by the electronegativity difference of components,  $\Delta\chi$ . A big electronegativity difference tends to localize electrons on one site and therefore the band gap increases. On the other hand, the ordering of bands is related to the strength of spin-orbit coupling. Therefore, it seems that one can lean on the ratio between Z and  $\Delta\chi$  and look for a compromise between a moderate band gap and the possibility to have band inversion.

Moreover, it has been shown that DSM appears at a phase transition between a topological insulator and a trivial one when both TRS and inversion symmetry are preserved [191]. Therefore, a straightforward way to realize a DSM is to appropriately dope the parent topological insulator with an element that respects the above-mentioned criterion ( $Z/\Delta\chi$ ) and allows a symmetry protected band inversion. Neupane *et al.* [129] showed that by the alloying of well-known topological insulator  $\text{Bi}_2\text{Se}_3$  with the critical composition (like 5% of sulfur) a DSM emerges at the phase transition, figure 1.16 (c).

### 1.4.3.3 Dirac semimetals in 2D: ZrSiS

So far, we have seen 3D topological semimetals and different mechanisms to realize them. Although the examples of these materials are growing, it seems that the realization of DSM in 2D beyond graphene is not straightforward. Young *et al.* [198] proved that in fact a nonsymmorphic symmetry of a 2D time-reversal symmetric crystal can cause the conduction and valence bands to touch and persist even in the presence of strong spin-orbit coupling. Such a symmetry protected Dirac point was also a plausible scenario in 3D. In 2D, the nonsymmorphic symmetries are screw axis, glide mirror lines and glide mirror planes (noted by  $g$ ) combined with a half-translation  $\mathbf{t}$  by a lattice vector. By lowering the symmetry, the nonsymmorphic symmetry  $\{g|\mathbf{t}\}$  still protects degeneracies along the line or in the plane of the Brillouin zone where  $g\mathbf{k} = \mathbf{k}$ . In contrast to graphene, these Dirac points cannot be gapped by SOC. If in addition the crystal

has inversion symmetry, the bands are Kramers degenerate for all  $\mathbf{k}$ . This leads to a fourfold degenerate crossing at the high symmetry points of the Brouillin zone. The authors also showed a simple model based on  $s$ -orbitals in a 2D square lattice and demonstrated the emergence of several Dirac nodes due to the combined effect of time-reversal, inversion, and nonsymmorphic symmetries of the crystal space group. The first experimental realization of 2D Dirac cones was accomplished in ZrSiS [162]. This system hosts a line of Dirac nodes at the chemical potential as shown in figure 1.17 that is slightly gapped with SOC. The line connects the midpoint of  $\Gamma M$  and  $\Gamma X$  directions. These bands show linear dispersion for an unprecedented range in binding energy ( $> 1$  eV) with a Fermi velocity of  $4.3 \text{ \AA} \cdot \text{eV}$  that is slightly smaller than that of graphene ( $6.7 \text{ \AA} \cdot \text{eV}$ ). In addition, it also reveals a 2D Dirac point below the Fermi level at the X point that is protected by the nonsymmorphic symmetry through a glide plane. This Dirac cone is generated by  $p$ -orbitals in the square sub lattice of Si and does not have any  $k_z$  dispersion as observed by photon energy dependent ARPES measurements.

#### 1.4.3.4 Massive Dirac fermions in 2D: $\text{Fe}_3\text{Sn}_2$

I now present an example of 2D Dirac fermions in a correlated semimetal that originates from the  $d$ -orbitals. The electronic band structure of the  $d$ -electron bilayer kagome metal  $\text{Fe}_3\text{Sn}_2$  shows rich spectrum of electronic excitations at/close to the Fermi level with hexagonal symmetry [196] as seen in figure 1.18 (a). This is consistent with the metallicity of the compound. Specifically, linearly dispersing bands are observed below the Fermi level at the corners of the Brillouin zone, namely K and K' points, similar to graphene. Figure 1.18 (b) shows Dirac cones at K point for the bilayer kagome structure. We observe two interpenetrating cones that are in fact caused by the bilayer structure. The cones have a mass gap of 30 meV, which correspond to massive Dirac fermions. The electronic wave functions acquire a non-trivial Berry phase around these points and result in a Berry curvature-induced Hall conductivity. This behavior is a consequence of the underlying symmetry properties of the bilayer kagome lattice in the ferromagnetic state and the atomic spin-orbit coupling. The Dirac nodes show a  $k_z$  dispersionless feature that confirm their 2D nature confined in the Fe layers.

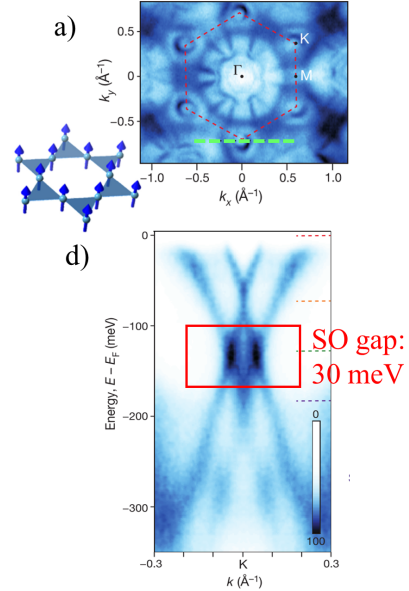


Figure 1.18: Massive Dirac fermions in  $\text{Fe}_3\text{Sn}_2$ . (a) The hexagonal BZ. (b) Doubled Dirac cone along the dashed green line in the BZ.

## 1.5 $\text{BaCo}_{1-x}\text{Ni}_x\text{S}_2$ , a moderately correlated system

$\text{BaNiS}_2$  was first grown and studied by Grey [56] and soon after the ensuing compound  $\text{BaCo}_{1-x}\text{Ni}_x\text{S}_2$  [112, 113, 172] attracted much interest due to some similarities with its contemporary counterparts high- $T_c$  cuprate superconductors [99]. The quasi two-dimensional tetragonal crystal structure of  $\text{BaCo}_{1-x}\text{Ni}_x\text{S}_2$  belongs to  $p4/nmm$  ( $D_{4h}^7$ ) space group. It consists of nonsymmorphic square-pyramidal structure with a gliding plane symmetry that relates two edge-sharing upward- and downward-pointing pyramids of  $\text{Co}_{1-x}\text{Ni}_x\text{S}_5$  together, figure 1.19 (a). The barium

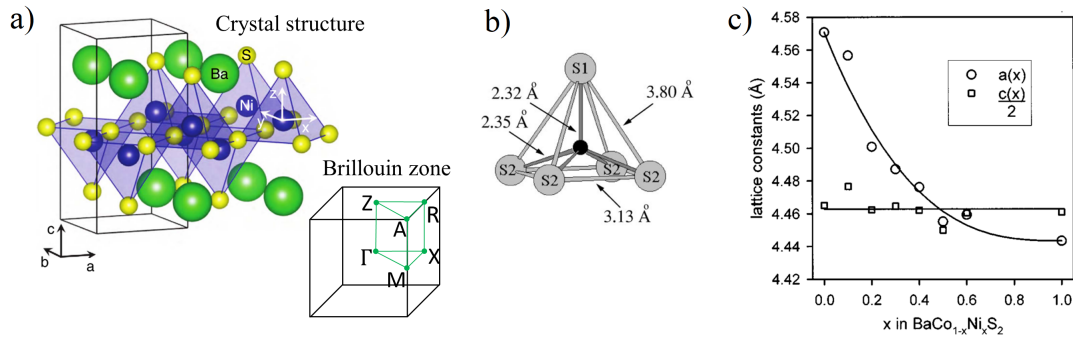


Figure 1.19: (a) Tetragonal  $P4/nmm$  structure of  $\text{BaNiS}_2$  and its corresponding Brillouin zone. (b) Interatomic distances inside the unit cell. (c) Evolution of the lattice vector sizes as a function of chemical substitution in Ni.

atoms are packed in between these pyramids. The planar Ni-S distance is 2.35 Å, and the apical distance is 2.32 Å leading to a total vertical displacement of 0.77 Å for Ni atom towards the apical sulfur [114], figure 1.19 (b). The lattice constants for  $\text{BaNiS}_2$  are  $a = 4.430$  Å and  $c = 8.893$  Å. The Co-rich compound appears to be a Mott insulator and its structure is a slight monoclinic distortion of  $\text{BaNiS}_2$  with a small change in the angle from  $90^\circ$  to  $90.45^\circ$  this is also accompanied by slight variation in the interatomic distances. Figure 1.19 (c) shows the evolution of lattice vector sizes as a function of chemical substitution [113].

The importance of  $\text{BaCo}_{1-x}\text{Ni}_x\text{S}_2$  is that it shows a metal to insulator transition from an anomalous metallic state to an antiferromagnetic insulating phase upon doping in Co ( $x_{cr} \sim 0.22$ ). The electronic and magnetic properties of the system in both phases bear similarities with their counterparts in the normal state of high- $T_c$  superconductors however, no superconductivity is observed in  $\text{BaCo}_{1-x}\text{Ni}_x\text{S}_2$  neither by temperature nor by pressure [159, 193]. To study which properties of the anomalous states are critical for realizing a high- $T_c$  superconductivity, one should naturally compare their fundamental electronic and magnetic properties to those of quasi 2D electrons in a non-Cu based compound that does not reveal superconductivity but harbors a Mott-insulating phase.

This compound also reveal another MIT at higher temperature from the paramagnetic metallic to a paramagnetic insulating phase ( $x_{cr} \sim 0.17$ ) without any structural symmetry breaking. This MIT is believed to be a Mott transition since it is merely driven by electron correlations. Yasui *et al.* [195] showed that a pressure-induced insulator to metal transition is possible starting from the antiferromagnetic insulating phase. For instance, in the case of  $\text{BaCoS}_2$  this critical pressure is  $\sim 13$  kbar. They also depicted the phase diagram as a function of  $x$ ,  $T$ , and  $p$  as shown in figure 1.20. The phase diagram is very similar to the phase diagram of  $(\text{V}_{1-x}\text{M}_x)_2\text{O}_3$ . However, in  $\text{BaCo}_{1-x}\text{Ni}_x\text{S}_2$  the MIT to the AFI phase upon doping is continuous in contrast to  $(\text{V}_{1-x}\text{M}_x)_2\text{O}_3$ . One possible explanation for this second order phase transition can be the disorder effect.

Several band structure calculations in 90's [63, 88, 114] suggested that the DOS involves several  $d$ -orbital band at or close to the Fermi level and as the binding energy increases the dominant contribution of sulfur  $3p$ -orbitals appears. Additionally, the theoretical Fermi surface predicted a more 3D nature of the band structure for  $\text{BaCo}_{1-x}\text{Ni}_x\text{S}_2$  while cuprates have rather a 2D electronic band structure. The photoemission spectroscopy of the electronic band structure for various chemical substitution [92] suggested that the MIT in  $\text{BaCo}_{1-x}\text{Ni}_x\text{S}_2$  is of bandwidth control nature, c.f. section 1.3. The relevant parameters for a model describing this compound are  $t_{pd}$  (hopping of electrons between  $d$  and  $p$  orbitals),  $U_{dd}$  (electron correlation on  $d$ -orbitals)

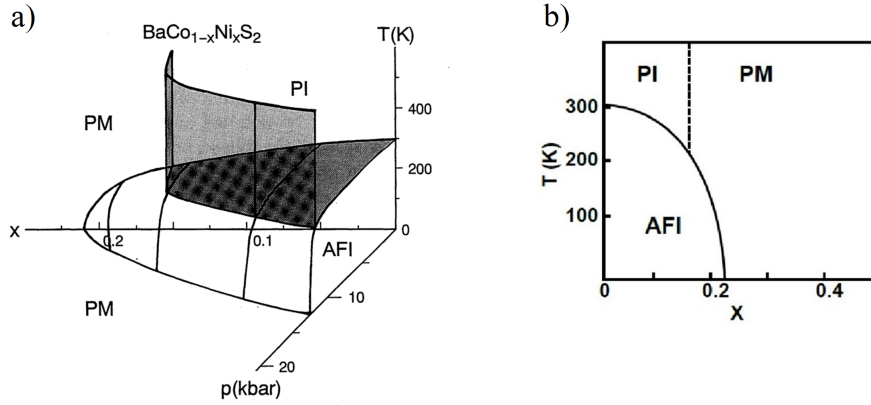


Figure 1.20: (a) Phase diagram of  $\text{BaCo}_{1-x}\text{Ni}_x\text{S}_2$  in the  $T$ - $p$ - $x$  space from [195]. (b) Phase diagram in the  $T$ - $x$  plane.

and  $\Delta$  (charge transfer energy). It was shown that the  $t_{pd}$  decreases with a decrease in Ni content while  $U_{dd}$  (3 eV) and charge transfer energy  $\Delta$  (1 eV) do not change appreciably across the phase diagram. In this way, the appropriate parameter to describe the MIT is  $U/W$ , where  $W$  is the bandwidth and is proportional to  $t_{pd}$ . A more detailed ARPES study on the metallic and insulating precursors of the MIT shed more light on the discrepancies with respect to high- $T_c$  superconductors in terms of electronic band structure [159]. For instance, the shape of the Fermi surface would exclude the possibility of nesting condition that is almost satisfied in cuprates.

$\text{BaCo}_{1-x}\text{Ni}_x\text{S}_2$  remained silent for over a decade however, some recent theoretical and experimental works put some overseen or neglected aspects of its electronic band structure in a new perspective and revived the interest for this compound. The main research has been dedicated to the insulating and metallic end members,  $\text{BaCoS}_2$  and  $\text{BaNiS}_2$ , respectively.

$\text{BaCoS}_2$  is a strongly correlated insulator that shows a magnetic transition at the Néel temperature of  $\sim 300$  K. Reproducing the experimentally observed band gap of  $\text{BaCoS}_2$  ( $\sim 500$  meV) has for long time remained a challenge for theorists due to its strong electron correlation effects. It has been proved that LDA+ $U$  calculations are only capable of reproducing the semiconducting nature of the electronic spectrum by taking into account the antiferromagnetic ordering as well as the orthorhombic distortion of the tetragonal structure [200], figure 1.21. Theoretical band structure calculation for  $\text{BaCoS}_2$  in the PI phase is pending and no experimental evidence of the band structure is available to date. In my PhD, I studied the electronic band dispersion of  $\text{BaCoS}_2$  in both AFI and PI phase and the result is presented in section 4.5. On the other hand, although many theoretical calculations existed for  $\text{BaNiS}_2$  since many years, its  $k$ -resolved band structure was only studied recently [156]. Some parallel band structure calculations by DFT method within the GGA+ $U$  framework gives a good agreement with the ARPES spectrum figure 1.22. The on-site Coulomb repulsion is indispensable due to the transition metal Ni and its intermediate filling. These calculations also confirm that the dominant contribution to the DOS close to the Fermi level comes from the Ni  $d$ -orbital. While previous works also gave the evidence for the presence of linearly dispersing bands along  $\Gamma\text{M}$  direction, Dirac fermion and topological interpretations of such features in the electronic band structure of  $\text{BaNiS}_2$  was not yet provoked at the time. Santos-Cottin *et al.* referred to the linearly dispersion bands as Dirac-like bands for the first time. They also showed that each branch is orbital polarized; one is with the out-of-plane  $d_{z^2}$  character and the other one has the in-plane  $d_{x^2-y^2}$  character with respect to the Cartesian coordinate defined along the diagonal of the  $S_4$  pyramids. The main part of my thesis was devoted to the study of these two particular bands. More specifically, we tried to

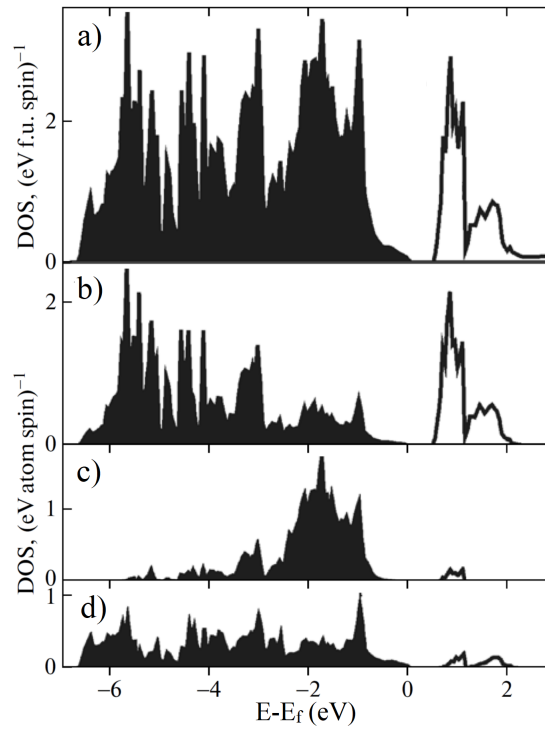


Figure 1.21: Results of the antiferromagnetic LDA +  $U$  calculation of the total and partial densities of states for  $\text{BaCoS}_2$ : (a) total density of states; (b) partial density of Co  $d$ -states; and (c, d) partial density of  $p$  states of apical and in-plane sulfur atoms, respectively. From [200].

elucidate whether the band crossing is accidental and if not, how the Dirac point is protected. In addition, all theoretical calculation so far have predicted a three-dimensional electronic nature of  $\text{BaNiS}_2$  [63, 156] in contrast to the transport measurements that suggests rather a quasi 2D electronic system. No photon-energy dependent ARPES data elucidating the  $k_z$  dispersion is available so far in the literature. However, some indirect way of Fermi surface mapping by quantum oscillations have been recently performed and will be presented in subsection 1.5.2.

I now review in the following some of interesting features of the electronic band structure properties of  $\text{BaNiS}_2$ .

### 1.5.1 Very large Rashba band splitting in $\text{BaNiS}_2$

The advent of topological insulators and topological semimetals and their potential application in spintronics was followed by an unceasing effort to search for novel materials allowing the realization of topologically non-trivial phases on their surface or bulk. As mentioned before, the SOC is the crucial parameter in these materials that adjusts the band gap as well as band ordering. An alternative way of splitting electronic bands into spin-polarized states can be the Rashba effect— if an electric field is applied perpendicular to the plane containing spin, the band splitting occurs. The Rashba effect also occurs naturally in some crystals without an external field that might result in (hidden) spin-polarized bands.

It is well known that in crystals with sufficiently low crystalline symmetry, more specifically the inversion asymmetric structures, the SOC acts as an effective magnetic field that is proportional to the crystal potential and momentum. This effective magnetic field then splits the otherwise spin-degenerate bands and results in spin-polarized bands. This is known as Rashba (or Dresselhaus) effect. However, upon the discovery of spin-polarization even in centrosymmetric



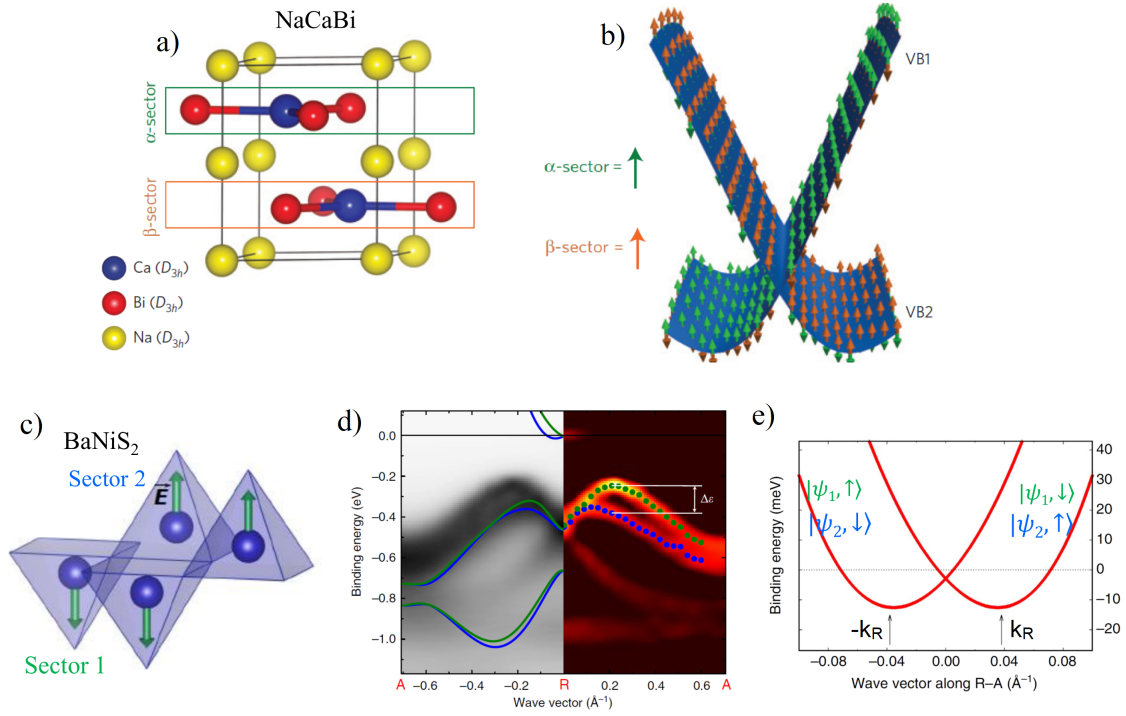


Figure 1.23: (a) Crystal structure of NaCaBi. The two separate sectors (CaBi layers) forming the inversion partners used for spin-polarization analysis are labeled by  $\alpha$  and  $\beta$ . (b) Local spin polarization is represented by green (on the  $\alpha$ -sector) and orange (on the  $\beta$ -sector) arrows for the split valence bands. From [205]. (c) Two inversion partner inside the unit cell of BaNiS<sub>2</sub> are called sector 1 and sector 2. (d) The band dispersion along RA shows a band split of 150 meV. The left panel shows the second derivative of the ARPES spectrum [156]. (e) Schematics of the conduction band splitting at R point. The contribution of the electronic wave function from each sector is shown for each sub-band.  $k_R$  shows the  $k$ -shift due to the band splitting.

nonmagnetic crystals [76, 152], the initial description of band splitting underwent a fundamental correction. Zhang *et al.* [205] demonstrated that if the site point group of an atom within a 3D crystal lacks inversion symmetry, that atom might feel a site dipole field and therefore the SOC at that site, plus the asymmetric potential surrounding it, result in a *local* Rashba effect. However, even in the absence of a polar field, the inversion asymmetry of that site is sufficient to cause degeneracy lifting. The net spin polarization of the crystal is the linear superposition of all these atomic spin-polarized state that would vanish in total if the crystal is centrosymmetric. In fact, in this case the spin polarization of each atomic site is compensated by its inversion related partner. Therefore, rather than being intrinsically zero, the spin-polarization is *hidden* by compensation. In figure 1.23 I show the example of centrosymmetric NaCaBi. The unit cell can be divided in two sectors giving asymmetric environment for each Ca atom within the CaBi planes. The valence band splitting is shown in figure 1.23 (b). We see that the two components of the band have opposite spin polarization, each spatially localized on one of the two separate sectors ( $\alpha$  or  $\beta$ ) forming the inversion partners. However, the net spin polarization is zero due to the crystal inversion symmetry.

Recently, a similar hidden spin-polarization was also demonstrated in BaNiS<sub>2</sub> both experimentally and theoretically. In fact, the gliding plane symmetry breaks the local inversion symmetry for each Ni site inside the pyramids, figure 1.23 (c). This creates a crystal field from Ni to apical sulfur as large as  $1.4 \text{ V } \text{\AA}^{-1}$  pointing in different directions for each pyramids that are

related by the inversion symmetry and are called sector 1 and sector 2. As a result, the valence band shows a band split of 150 meV at the border of the Brillouin zone at the R point as shown in figure 1.23 (d) and (e). The conduction band that only slightly crosses the Fermi level at R point shows similar splitting. However, due to its very small electron pocket at the Fermi level, it is not possible to resolve the two branches experimentally. By some chemical substitution, one can slightly fill this band and change the chemical position so that Rashba splitting becomes detectable by ARPES. Another possible way is to apply time-resolved ARPES technique and transiently populates this electron pocket and study its dispersion. In fact, pump-probe technique allows detecting the band dispersion of unoccupied states as we will see in subsection 3.4.1.

These results demonstrate that although Ni is not a heavy element, the spin-orbit coupling effect is amplified by local Rashba mechanism and leads to the hidden spin-polarized band splitting in the centrosymmetric BaNiS<sub>2</sub>.

## 1.5.2 Quantum oscillations studies

In order to study a precise Fermi surface structure of BaNiS<sub>2</sub>, some quantum oscillations measurements were performed [86]. In this technique, by controlling the strength and angle of the magnetic field, the topology of the Fermi sheets in the three-dimensional space is mapped however, the position of the electron or hole pockets cannot *a priori* be recognized in the Brillouin zone. Complementary *ab-initio* calculations are necessary to reconstruct a detailed map of the Fermi surface (FS). During my PhD, I had collaborations with the group of A. Gauzzi in Paris 6 University. The theoretical GGA+U calculations by M. Casula were not matching my photon energy dependent ARPES measurements and the main discrepancy was due to the  $k_z$  dispersion of the electronic structure (I will show the detailed result farther in subsection 4.3). Therefore, some modifications were brought to the theoretical model notably by adding a fraction of the exact nonlocal exchange to the functional. By appropriately tuning the HSE hybrid functional, c.f. paragraph 1.3.1.1, a qualitative agreement with the quantum oscillation measurements and ARPES data was achieved. This corresponds to a 7% of the exact exchange, while the screening length is kept equal to the original 0.200 Å<sup>-1</sup>. In fact, the semimetallic character of BaNiS<sub>2</sub> is responsible for an enhanced screening of the exchange operator. The importance of nonlocal effects was also investigated in iron pnictides [17, 173, 176] that are sometimes compared with BaNiS<sub>2</sub> for their intermediately filled *d*-orbitals at the Fermi level, the P4/nmm space group and the compensated semimetallic nature.

Figure 1.24 (a) shows the oscillations in the magnetoresistance as a function of magnetic field. Its Fourier transform shows few peaks and only three peaks ( $\alpha$ ,  $\beta$ , and  $\gamma$ ) are attributed to the Fermi surface. The parameters extracted for these orbits are shown in the table 1.24 (b). The experiments have suggested that the projection of the pockets that give rise to the frequency of  $\beta$  and  $\gamma$  on the  $k_x - k_y$  plane is elliptical. Further analyses have shown that in fact the  $\beta$  and  $\gamma$  orbit should belong to two different pockets while  $\alpha$  and  $\gamma$  belong to the same pocket located along the c-axis of the Brillouin zone. The  $\beta$  pocket should also occur four times on the Fermi surface to maintain compensation. The total number of electrons and holes is  $\sim 5 \times 10^{19} \text{ cm}^{-3}$ . On the other hand, the pocket at the center of the Brillouin zone is rather quasi 2D while the  $\beta$  pocket has a conical dispersion along the  $k_z$ . Theoretically, these features are best reproduced by applying the HSE functional. Figure 1.24 (c) shows the calculated Fermi surface for GGA+U ( $U=3 \text{ eV}$ ) and HSE 7% exchange interaction. The position of each orbit observed in the quantum oscillation measurements are recognized and shown by arrows. The  $\gamma$  orbit in the quantum oscillations is an electron pocket while the  $\beta$  orbit is a hole-like pocket located at the midpoint of the  $\Gamma M$  direction.

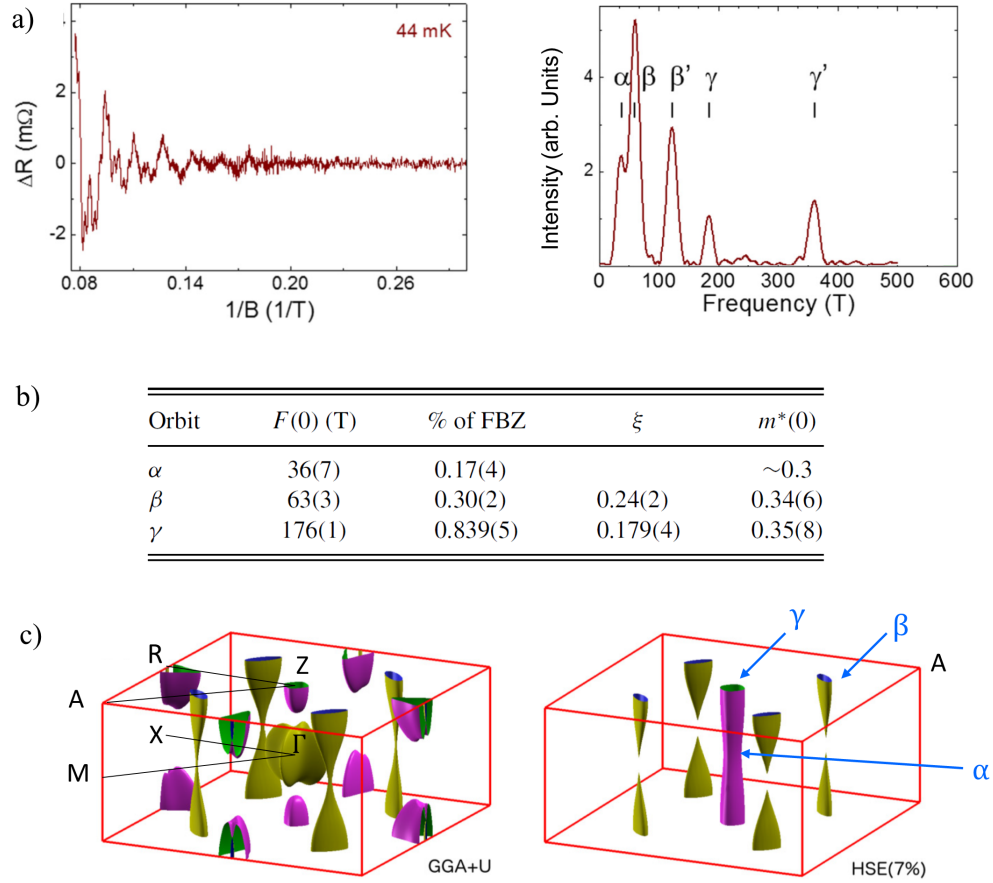


Figure 1.24: (a) Left panel: oscillating part of the longitudinal magnetoresistance  $\Delta R$ . Right panel: Fourier transform of the oscillations. (b) Parameters relevant to the three detected orbits projected in the  $k_x - k_y$  plane. The cross section areas are given in percentage of the first Brillouin zone area. The ratio between the big and small axis of the elliptical pocket is labeled by  $\xi$  and  $m^*$  shows the effective mass. (c) Calculated Fermi surface. The high symmetry direction are shown in the right panel. The  $\gamma$  and  $\beta$  pockets are of electron and hole nature, respectively. From [86].

### 1.5.3 Similarities of $\text{BaCo}_{1-x}\text{Ni}_x\text{S}_2$ with iron pnictides

As mentioned above,  $\text{BaCo}_{1-x}\text{Ni}_x\text{S}_2$  bears resemblances with a new family of high- $T_c$  superconductors, the iron pnictides. The discovery of iron-based superconductors [80] has sparked off a growing interest in studying interacting multiband systems. Before finishing this chapter, a brief reminder on salient features of iron pnictides will be pedagogical.

In contrast to the high- $T_c$  superconducting cuprates, whose parent compounds are Mott insulators, in pnictides the superconducting state originate from a spin density wave state (SDW). Moreover, the strength of correlations in pnictides remains moderate in their entire phase diagram. The quasi 2D crystal structure of pnictides consists of iron-pnictogen planes (Fe - As, P) with a charge reservoir layer in between. The normal and superconducting states have a tetragonal structure while doping can induce an orthorhombic crystal structure accompanied by magnetic ordering. All the families of pnictides are semimetals, with several small hole and electron pockets at the Fermi level with  $d$ -orbital character. Explaining physical properties of these compounds as well as the origin of the superconductivity demands an inclusive theory taking into account spin density wave fluctuations, moderate correlations, and multi-orbital situation.

$\text{BaAs}_2\text{Fe}_2$  is a widely studied example of pnictides. It becomes superconductor either by hole doping (replacing barium atoms with potassium), or electron doping (for instance replacing iron with cobalt). The crystal structure and the phase diagram of the electron-doped compound is shown in figure 1.25 (a) and (b). The optimum superconducting transition temperatures are not reached until the long-range structural and magnetic transitions are both completely suppressed. Figure 1.25 (c-e) shows the band structure and Fermi surface of  $\text{BaFe}_{1.85}\text{Co}_{0.15}\text{As}_2$ . The hole and electron pockets with  $d$ -orbital nature are observed at  $\Gamma$  and M points, respectively [16, 108]. On the other hand, thanks to the well-defined orbital character of the bands close to the Fermi level, by appropriately selecting the polarization of the incident light, one is able to discern bands with different  $d$ -orbital components [16, 108]. I describe how it is possible in subsection 3.2.4.

In iron-based superconductors, common upward and downward shifts of the electron and hole bands, respectively, relative to band structure calculations are often found. Therefore, a shrinking of the FS with respect to the theoretical predictions is frequently observed in ARPES or quantum oscillation measurements [106, 135, 174]. This FS shrinking was first attributed to electronic correlation effects and especially inter-band scattering that results in the nesting of the wavevector observed on the FS of the iron-based compounds [17, 173]. However, it has been shown after that non-local self-energy modifications could greatly enhance the agreement between the theory and experiments.

It is thus logical to compare  $\text{BaCo}_{1-x}\text{Ni}_x\text{S}_2$  with iron pnictides as both compounds offer moderately correlated multi  $d$ -orbital systems that is best explained theoretically by non-local  $k$ -dependent self-energy.

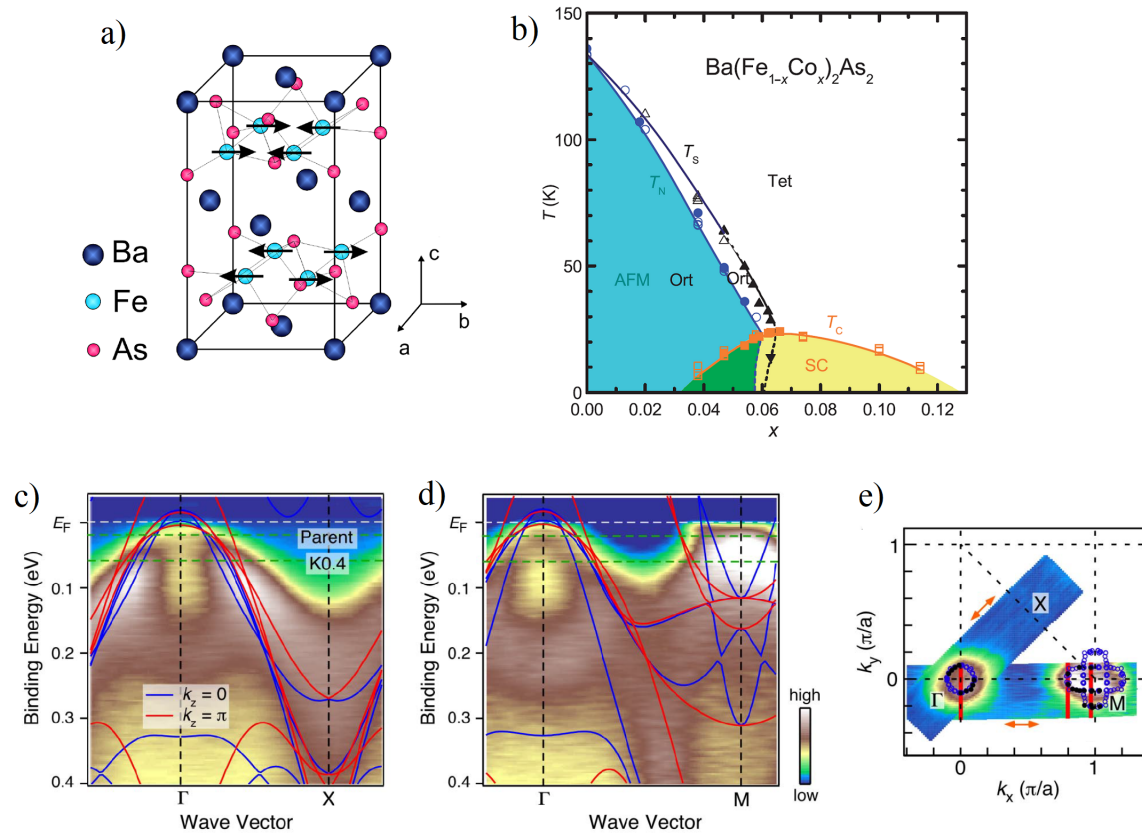


Figure 1.25: (a) Crystallographic structure and (b) phase diagram of  $\text{BaFe}_2\text{As}_2$ . (c,d) ARPES intensity plots of  $\text{BaFe}_{1.85}\text{Co}_{0.15}\text{As}_2$  ( $T_c = 25.5$  K) as a function of wavevector and binding energy measured at 8 K along the  $\Gamma$ X and the  $\Gamma$ M together with the band dispersion from the first-principle calculations for  $k_z=0$  and  $k_z=\pi$ . (e) The Fermi surface shows a small electron and hole pocket. From reference [173].



## 2 | Time-resolved studies of quantum materials

### 2.1 Introduction

The notion of time-resolved experiments in an ultrafast fashion was first introduced in chemistry; the act of initiating (pumping) and recording snapshots (probing) of chemical reactions with a femtosecond time resolution [203]. On this time scale, the vibration of atoms or molecules is "frozen out" and one is able to observe the complete evolution of an event stimulated by an ultrashort pulse. The same idea soon pervaded to physics but with another perspective.

In fact, the discovery of strong correlation in transition metal oxides evoked much intellectual and technological interest. However, the subtle interplay among their atomic structure, charge, spin, and orbital dynamics, c.f. section 1.1, was far complex to yield any fundamental understanding both from theoretical and experimental point of view. Among fundamental issues is, for instance, to determine the coupling strength among different degrees of freedom as well as the hierarchy of important couplings. In any experiment performed at equilibrium, all of these degrees change equally and simultaneously and one can only gain a time-integrated insight of the entire process. The key to tackle this problem is the application of ultrafast pump-probe techniques that transiently decouples different degrees of freedom by an ultrafast pulsed stimulus, and lets us observe the reaction that appears in others within an ultrashort time interval. The study of these interactions and competitions between the relevant degrees of freedom gives insight into the macroscopic functionality of correlated materials. Particularly, femtosecond laser pulses act only on the electrons and set them to an out-of-equilibrium distribution inexplicable by the Fermi-Dirac distribution. The ensuing dynamics is followed by evacuating the excess of energy to the lattice via various processes and the rate at which this relaxation occurs is related to the coupling constants.

On the other hand, on the importance of quantum materials Orenstien says "*it is precisely in such system—where complexity rules— that the most interesting and technologically important properties might emerge*", [134]. In fact, the phase diagram of strongly correlated systems shows multiplicity of nearly degenerate ground states that some often lurk in slightly higher free energy inaccessible via adiabatic thermal pathways. Femtosecond laser pulses might act as an additional parameter to the control of the phase diagram different from thermodynamic parameters like temperature and pressure. They derive the material out of

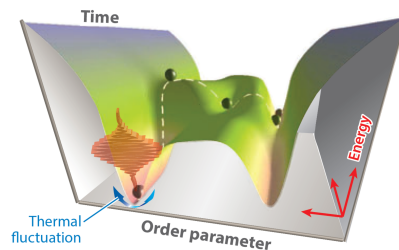


Figure 2.1: Pathway for photoinduced phase transition along the dynamical free-energy landscape from [204].

equilibrium in an ultrafast fashion and competing interactions might unveil and stabilize hidden metastable phases, figure 2.1. This idea gives the opportunity of ultrafast control and manipulation of materials. However, one needs to learn about the optimal excitation pathways that can be, for instance, interband transitions or IR active phonons, to dynamically drive a phase transition in an efficient way. The role of the time-resolved spectroscopy is to precisely quantify the amount and the duration of the photoinduced modifications achieved by different pathways.

The importance of time-resolved experiments on quantum materials is not only limited to strongly correlated materials. Topological materials reveal many interesting phenomena upon photoexcitation. For instance, their bulk and robust surface states can generate different ultrafast response [58, 168]. More interestingly, it has been demonstrated that it is also possible to manipulate their topological order and Berry phases only by applying appropriate light pulses. Recently, the discovery of Dirac/Weyl semimetals have also shown their potential for optoelectronic applications or fast photodetectors thanks to their very high mobility [103, 184]. Anyhow, before exploring the applications, a complete knowledge of a material's (sub-) picosecond response to an optical excitation such as relaxation dynamics of photoexcited carriers and their coupling with lattice should be acquired.

In this chapter, I first describe some general aspects of out-of-equilibrium dynamics by introducing relaxation processes as well as simple models to simulate the dynamics and extract some important parameters from that. Then I give some examples of the time-resolved studies on strongly correlated materials such as oxides of vanadium, showing the formation of photoinduced phases and their similar dynamics. Then I present some time-resolved reflectivity measurements on iron pnictide  $\text{BaFe}_2\text{As}_2$ . I also present few works on Dirac materials starting from graphene and extending to Dirac semimetals. While extensive studies have been carried out on numerous correlated materials, the time-resolved domain is relatively young for Dirac/Weyl semimetals and is yet to be explored experimentally as well as theoretically. Specifically, the study of photoinduced topological phase transitions offers one of the most exciting challenges for the field.

## 2.2 Time-resolved studies: general considerations

### 2.2.1 Electron excitation and relaxation processes

A photon can be absorbed by electrons via two processes: interband and intraband transitions. The first one describes the transition of the electron from one band to another. This transition is possible in metals as well as in semiconductors or Mott insulators (since the photon energy used for a pump-probe experiment is usually of the order of 1.5 eV). On the other hand, the intraband transition defines an optical transition inside the same band and mostly occurs in metals. The excitation of electrons occurs on a sub femtosecond timescale, and therefore can be viewed as instantaneous compared to the pump pulse temporal length ( $\sim 50 - 100$  fs). The out-of-equilibrium excited electrons quickly thermalize by scattering and Auger-like processes and this creates a density of hot electrons above the Fermi level. The thermalization implies that the temperature of the electrons becomes well-defined by a Fermi-Dirac distribution. In a non-correlated system, the electron-electron thermalization occurs in few tenth of femtosecond. On this timescale, the electrons are practically disentangled from the lattice up to the time they reach the maximum temperature determined by their specific heat and the pump power. The electrons then quickly cascade down to the regions close to the Fermi level by evacuating their excess of energy through different processes, for instance by emission of optical phonons. The rate at which this relaxation occurs depends on the density of states of phonons accessible by

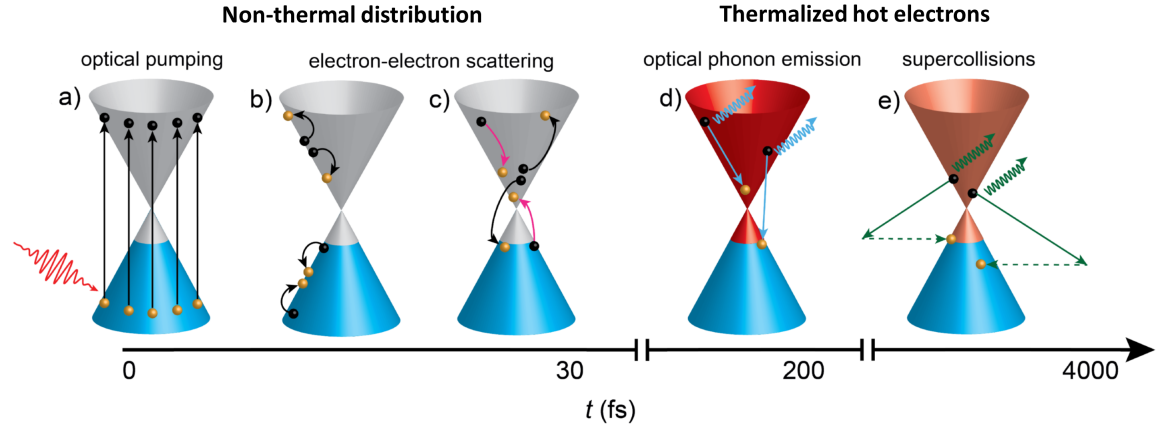


Figure 2.2: Timeline of electron dynamics on the Dirac cone in graphene: (a) At time zero electrons (black spheres) and holes (yellow spheres) are generated by 1.5 eV pump pulses (straight arrows). (b)-(c) Within 30 fs the excited electrons and holes undergo scattering processes (b) within and (c) between the bands by Auger recombination (black curled arrows) and electron-electron scattering (magenta arrows). This leads to a thermalized hot electron distribution. (d)-(f) The decay dynamics occurs within 200 fs by (d) emission of optical phonons (blue wiggled arrows), which is followed by (e) slower supercollisions involving acoustic phonons (green wiggled arrows) and impurities. The image is taken from [178].

excited electrons as well as the coupling strength between the electrons and phonons. The latter is called the electron-phonon coupling constant and is of paramount importance in the study of strongly correlated materials. It is well known that the fundamental principle for the conventional superconductivity is the strong electron-phonon interaction that results in the formation of Cooper pairs [30]. Once the electrons and phonons have reached the same temperature, the relaxation is accompanied by the emission of acoustic phonons that evacuate the energy from the photoexcited region through the entire sample and slightly heat it up. Note that during the entire process of the relaxation, the scattering with impurities can also aid the relaxation, which is often referred to as supercollision. The thermalization of the sample with the external environment occurs at a very long timescale, for instance hundreds of nanoseconds or microseconds. In the end, the final recombination of the electrons to their initial state is achieved. Figure 2.2 illustrates the above-mentioned picture of the electron dynamics in a pedagogical way for the case of graphene. I explain the ultrafast dynamics of graphene in subsection 2.4.1.

Mathematically, the dynamics of the excited electron is captured by two simple models: two-temperature and three-temperature model that I explain in the following.

## 2.2.2 Two-temperature model

The phenomenological two-temperature model (2TM) was first introduced by Allen [2]. This model describes the electronic dynamics after excitation with femtosecond laser pulses and applies to metals and conventional metallic superconductors. He suggested that  $\lambda$  in the Eliashberg generalization of BCS theory can be measured using by time-resolved techniques that at the time was mostly limited to the time-resolved optical reflectivity experiments. The first systematic application of this model to metallic superconductors was done in 1990 [15] who reported the electron-phonon coupling constant of 0.08 for Cu and a very big value of 1.45 for Pb.

The idea behind the 2TM is simple. At first approximation, it considers that the temperature is well defined for the electrons at each instant, i.e. they always follow a Fermi-Dirac distribution.

In addition, the electrons and the lattice are two thermalized interacting bath with a coupling constant between them that describes the energy transfer rate between the two and determines the rapidity of the relaxation. The lattice, on the other hand, is described by the Bose-Einstein distribution. The model neglects any diffusion driven by spatial inhomogeneities as well as any acceleration due to internal electric field, and assumes that no other collision processes, except electron-phonon scattering, is possible. Within this framework, the rate equations for the temperature of electrons  $T_e$  and that of the lattice  $T_l$  will be simplified as follows:

$$\frac{\partial T_e}{\partial t} = \gamma_T(T_l - T_e) + \frac{P(t)}{C_e} \quad (2.1a)$$

$$\frac{\partial T_l}{\partial t} = \frac{\gamma_T C_e}{C_l}(T_e - T_l) \quad (2.1b)$$

where  $C_e = \gamma T_e$  and  $C_l$  are the electronic and lattice heat capacities, respectively and  $P(t)$  is the laser pulse temporal profile. The mean energy of phonon is given by  $\langle \hbar\omega \rangle$ . These equations imply that the electronic temperature evolution follows an exponential decay with time-constant equal to  $\gamma_T^{-1}$  that is given by:

$$\gamma_T = \left( \frac{3\hbar\lambda\langle\omega^2\rangle}{\pi k_B T_e} \right) \left( 1 - \frac{\hbar^2\langle\omega^4\rangle}{12\langle\omega^2\rangle k_B^2 T_e T_l} + \dots \right) \quad (2.2)$$

This equation is obtained by a Taylor expansion in the high temperature limit— that is, when both  $T_e$  and  $T_l$  are much higher than the phonon energy. The second term in the parenthesis is a first thermal correction factor that, along with higher order terms, is negligible in most of the experiments.

I now add a little paragraph to describe how the absorbed laser power  $P(t)$  [J/cm<sup>3</sup>s] is calculated. We have:

$$P(t) = \frac{E}{V\tau} \frac{2\sqrt{\ln(2)}}{\sqrt{\pi}} e^{-4\ln 2 \frac{t^2}{\tau^2}} \quad (2.3)$$

where  $E$  is the mean pump energy and is obtained from the pump power, repetition rate, and the reflectivity of the sample at the pump wavelength.  $\tau$  is the pulse temporal FWHM and  $V$  is the volume in which the energy is deposited. This volume can be assumed to be a cylinder with area equal to the pump pulse size (FWHM<sub>d</sub>) and height equal to the penetration depth of the pulse. Therefore it is written as  $V = \pi(FHWM_d/2)^2\alpha^{-1}$  where  $\alpha$  is the absorption coefficient.

By solving the rate equations, one can eventually estimate the electron-phonon coupling strength  $\lambda$ . In paragraph 3.4.3.3, I will show how this is possible by aid of time-resolved reflectivity measurements. The pump fluence typically applied in pump-probe experiments is  $\sim 1$  mJ/cm<sup>2</sup>. The electronic maximum temperature is about thousands of kelvin and the relaxation occurs from hundreds of femtoseconds to few picoseconds. The bigger the electron-phonon coupling constant, the faster the decay dynamics takes place. The lattice heats up to about 20 K once the electrons have completely relaxed their energy to the lattice.

In the end, it is worth mentioning that in the 2TM the  $T_e$  and  $T_l$  are always higher than the initial equilibrium temperature  $T_0$  because the heat diffusion effect is not taken into account.

### 2.2.3 Three-temperature model

The 2TM implies that the relaxation occurs with only one timescale that is related to the mean energy of all phonons to which electrons are coupled. However, some time-resolved experiments

on high-temperature superconductors such as  $\text{Bi}_2\text{Sr}_2\text{CaCu}_2\text{O}_{8+\delta}$  suggest a decay dynamic with two time constants [145]. The dynamics consists of a fast decay ( $\sim 110$  fs) with a subsequent energy bottleneck ( $\sim 2$  ps) suggesting a strong anisotropy of the electron-phonon interaction. This phenomenon can be interpreted as follows: the hot electrons start to relax by first getting coupled to a subset of strongly coupled phonons whose temperature is indicated by  $T_p$ . These phonons are also called *hot* phonons and constitute the fraction  $f$  of the total phonon density. After some time, the electrons and hot phonons are thermalized and the phonon-phonon anharmonic scattering takes over the dynamics. This scattering occurs between the strongly coupled phonons and the nearly non-interacting subset of phonons. To keep a similar terminology, we can call the latter subset *cold* phonons that can be viewed as the lattice at temperature  $T_l$  and comprises  $1-f$  modes. With this approach, the rate equations involve three components:  $T_e$ ,  $T_p$ , and  $T_l$ . The corresponding equations for  $T_p$  and  $T_l$  describe how these subsystems are heated up by the energy that is lost in the electronic system. We have:

$$\frac{\partial T_e}{\partial t} = \frac{P(t)}{C_e} - \frac{3\lambda_1\Omega_0^3}{\hbar\pi k_B^2} \frac{n_e - n_p}{T_e} - \frac{3\lambda_2\Omega_0^3}{\hbar\pi k_B^2} \frac{n_e - n_l}{T_e} \quad (2.4a)$$

$$\frac{\partial T_p}{\partial t} = \frac{C_e}{C_p} \frac{3\lambda_1\Omega_0^3}{\hbar\pi k_B^2} \frac{n_e - n_p}{T_e} - \frac{T_p - T_l}{\tau_B} \quad (2.4b)$$

$$\frac{\partial T_l}{\partial t} = \frac{C_e}{C_l} \frac{3\lambda_2\Omega_0^3}{\hbar\pi k_B^2} \frac{n_e - n_l}{T_e} + \frac{C_p}{C_l} \frac{T_p - T_l}{\tau_B} - \frac{T_l}{\tau_c} \quad (2.4c)$$

where  $C_p$  and  $C_l$  are the heat capacity of the hot and cold phonons, respectively. The distribution of electrons and hot phonons is given by  $n_j = (e^{\Omega_0/k_B T_j} - 1)^{-1}$  with  $j = e, p$ . The electrons and hot phonons are coupled to each other by  $\lambda_1$  and the electron-phonon scattering with the  $1-f$  lattice modes that are more weakly coupled contributes to the temporal evolution of  $T_e$  with the coupling  $\lambda_2$ . It should be mentioned that in the original model introduced in [145] the coupling between the electrons and cold phonons was supposed to be negligible, and therefore was not taken into account. The reason I add this term to the 3TM is that I will need it to better describe my data in subsection 5.3.2. The decay time  $\tau_\beta$  describes the anharmonic decay of hot phonons and the relaxation of lattice due to diffusion takes place with a very long time constant  $\tau_c$ . Note that on the contrary to the 2TM, in the derivation of the 3TM it is supposed that all phonons have the same energy  $\Omega_0$  which correspond to a delta function in the phonon spectrum. The specific heat of hot phonons and cold phonons are  $C_p = 3f\Omega_0 \frac{\partial n_p}{\partial T_p}$  and  $C_l = 3(1-f)\Omega_0 \frac{\partial n_p}{\partial T_p}$ , respectively. The total specific heat is given by  $C_{tot} = C_l + C_p$  and is found in the literature. On the other hand,  $C_p$  is easily calculated as mentioned above but must be multiplied by a factor of proportionality so that when  $f \rightarrow 1$ ,  $C_p$  satisfies  $C_p \rightarrow C_{tot}$ . In the end, the cold phonon specific heat  $C_l$  is deduced.

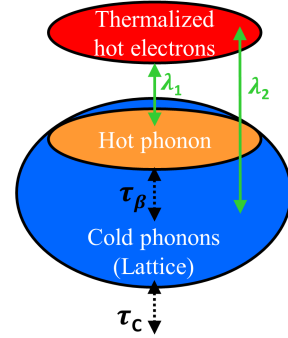


Figure 2.3: Sketch of the 3TM. Electron are coupled to hot and cold phonons with  $\lambda_1$  and  $\lambda_2$ , respectively. Dashed black arrows show the decay time constants.

### 2.2.4 Choice of the pump pulse wavelength

So far, some general aspects of the ultrafast electron dynamics has been highlighted. Another important (and crucial) factor determining the fate of the electrons undergoing photoexcitation, is the pump wavelength. If the energy of the pump is higher than the band gap of the solid: it excites all bands and no particular optical transition is triggered. During this process, the electron-hole will scatter and all coherence of the light is lost. Therefore, it is called incoherent pumping and has been vastly studied in many materials over decades. Among main motivations for this type of experiments is, for instance, to study the electronic band structure of unoccupied states and to find the coupling constants. In this way, it is also possible to transiently stabilize new states of strongly correlated systems as Mott insulators with small Mott gap. In subsection 2.3.1, I give some examples.

Recently, the study of coherent pumping has attracted much more interest. The idea is to perturb the material without losing the coherence of light and this is possible in two ways: either by stimulating a resonant optical transition between two electronic bands, or pumping with wavelengths below the band gap with mid-infrared (MIR) or terahertz (THz) pulses. In the latter case, the pump can be resonant with a phonon mode [54, 204] and therefore, one induces collective oscillations of the lattice corresponding to a given mode and observes the effects of the electronic properties of the systems. It is also possible that the pump pulse is not resonant with any electronic transitions or collective mode. Even though light is not doing intraband transition, the electron in the solid will still feel the periodic perturbation due to the light. Coherent pumping has opened a whole new domain in ultrafast physics to be explored further over the next years. The novelty of this technique lies on the unique possibility that it offers to manipulate the topology of the electronic wave function by light. I very briefly give an example of such effort in subsection 2.4.3.

## 2.3 Out-of-equilibrium studies of (strongly) correlated materials

### 2.3.1 Instantaneous gap collapse in vanadium oxides

Some oxides of vanadium, for instance  $\text{VO}_2$  and  $\text{V}_2\text{O}_3$ , present MIT driven by enhanced electron-electron repulsion that its origin is often unclear: it can be either the lattice distortion or the electron localization on the atomic sites. This chicken and egg dilemma has been answered by a combination of time-resolved techniques.

$\text{VO}_2$  has a monoclinic insulating phase at low temperature ( $T < 340$  K) while at higher temperature it is a rutile metal. Cavalleri *et al.* were the first ones to show a photoinduced phase transition of the insulating phase towards a transient metallic phase [26]. They later suggested that this transition could not be explained by a mere electronic effect. Actually it appears due to the coherent structural motion as observed in the time-resolved reflectivity measurements, highlighting the dominance of the lattice over the electrons during the phase transition [25]. Few years later, the application of the time-resolved photoemission spectroscopy (tr-PES) shed new light on the dynamics of the electrons [185]. Wegkamp *et al.* observed that the gap of the insulating phase collapses immediately with the arrival of the femtosecond pulses, figure 2.4 (a), and there is no *bottleneck* due to the lattice [185]. They showed that the transient phase reached by photoexcitation is different from the equilibrium metallic phase and it corresponds to a monoclinic metal. The hot carriers relaxation in this novel phase takes 200 fs and then the system evolves to the rutile metallic phase due to the heat delivered to the systems by

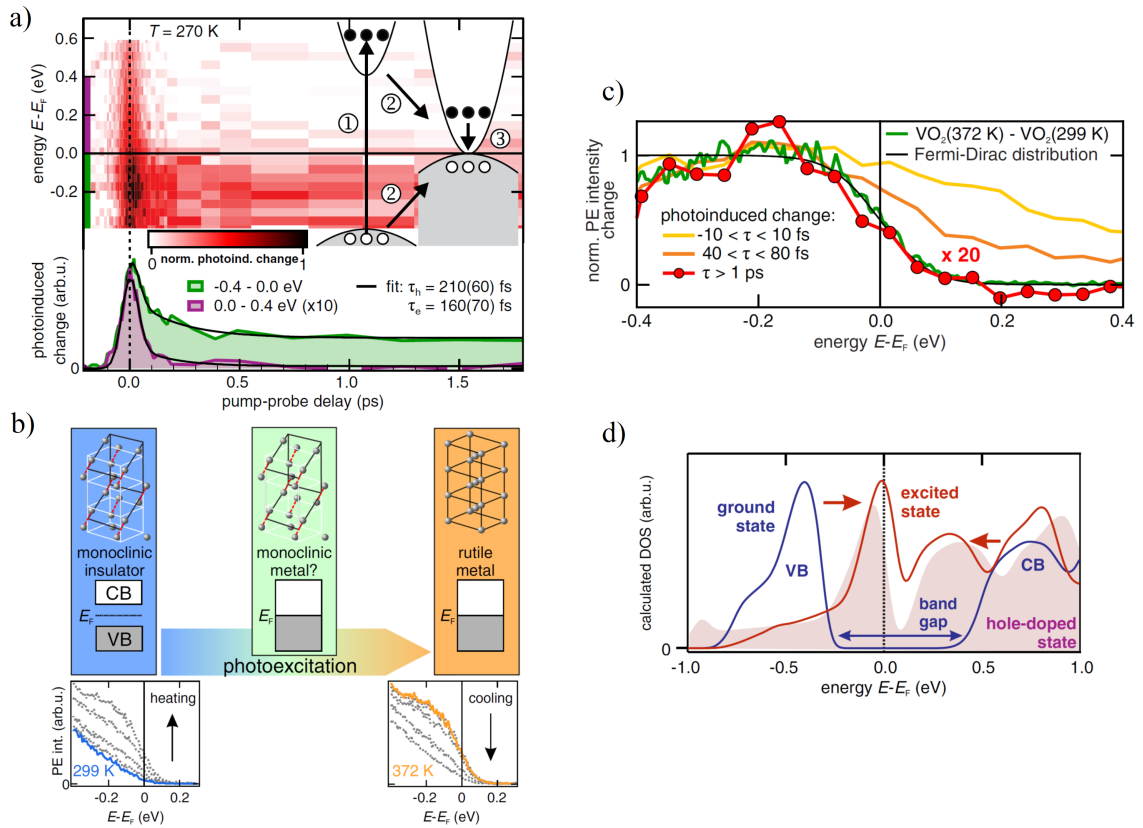


Figure 2.4: Ultrafast transient phase in  $\text{VO}_2$  (from [185]). (a) Time-resolved density of states. The dynamics of the excited electrons and holes are shown below the spectrum. (b) By photoexcitation the monoclinic insulator phase passes through a non-thermal monoclinic metallic phase and then eventually evolves to the rutile phase. The evolution of the DOS as a function of temperature are shown. (c) Comparison between the photoinduced and thermally induced phases. (d) Theoretical DOS for the equilibrium phase (blue curve) and the non-equilibrium phase (red curve). The latter is obtained by introducing a dynamical screened Coulomb interaction to the self-energy. The shaded curve corresponds to the DOS of the rutile phase.

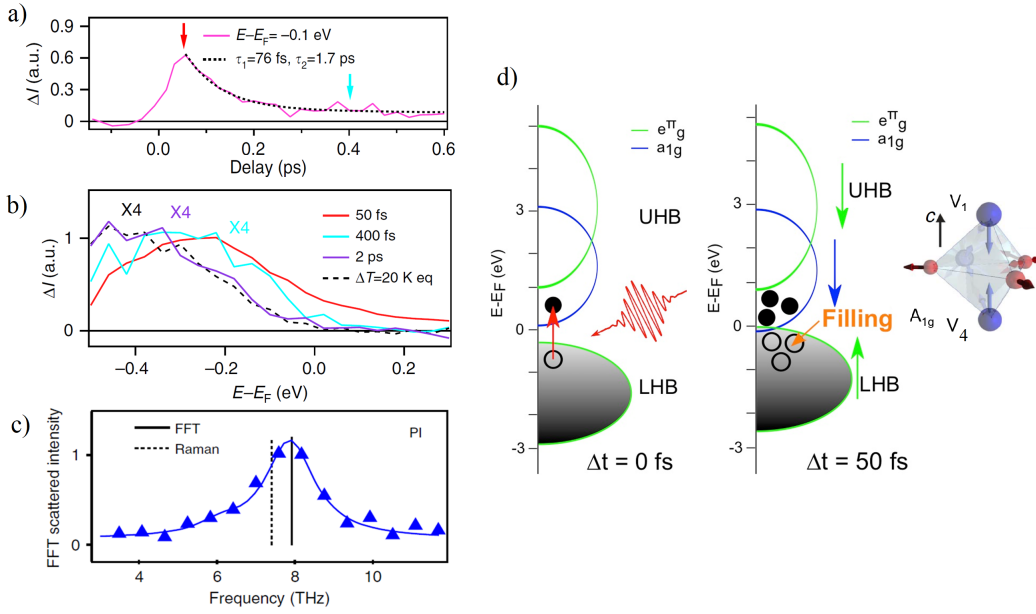


Figure 2.5: Ultrafast transient phase in  $V_2O_3$  (from [96]). (a) Dynamics of the in-gap states. (b) The transient metallic state is non-thermal with a lifetime of 1.7 ps. (c) Comparison of the  $A_{1g}$  frequency at equilibrium and out-of-equilibrium. (d) Schematics of the photoinduced gap filling process.

laser pulses. The latter is a pure thermal effect. Once the heat is evacuated from the lattice, the system retrieves its insulating phase (hundreds of nanoseconds). Figure 2.4 (c) shows the density of states for different time delays proving the non-thermal nature of the transient phase for less than 1 ps.

The interpretation of this phenomenon was supported by theoretical calculations explaining the extremely important role of the occupancy number of the localized d-orbitals that affects the screened Coulomb interaction. The photoexcitation is accompanied by a depletion of the V 3d valence band that increases the screening, modifies the electronic correlations, and results in an instantaneous metallization of the system, figure 2.4 (d).

Vanadium sesquioxide,  $V_2O_3$ , is different from  $VO_2$  in that its high temperature phase is insulating for the Cr-doped compound. Inspired by the above-mentioned studies on  $VO_2$  as well as by the particular electronic configuration of  $V_2O_3$ , c.f. paragraph 1.3.2.1, one would naturally ask what happens to the Mott insulating phase of  $V_2O_3$  after photoexcitation. By combining different pump-probe techniques, Lantz *et al.* [96] presented a comprehensive study on 2.8% Cr-doped sample and pure  $V_2O_3$  that belong to the paramagnetic insulating (PI) and paramagnetic metallic (PM) phases, respectively. In the tr-PES experiments, they observed an ultrafast formation of a transient metallic phase in the PI phase and an ultrafast loss of coherence in the PM phase. The dynamics of the in-gap states of the PI phase suggests two time scales, figure 2.5 (a), 76 fs and 1.7 ps. By comparing the evolution of the DOS after photoexcitation and upon heating, figure 2.5 (b), the fast component of the dynamics can be assigned to the hot electron relaxation after photoexcitation and clearly indicates a strong electron-phonon coupling. The second slower time constant can be viewed as the lifetime of the transient metallic state. Only after 2 ps, the system has retrieved its thermal equilibrium that corresponds to a rise in the temperature to 20 K further caused by the laser pulses. On the other hand, some parallel mea-

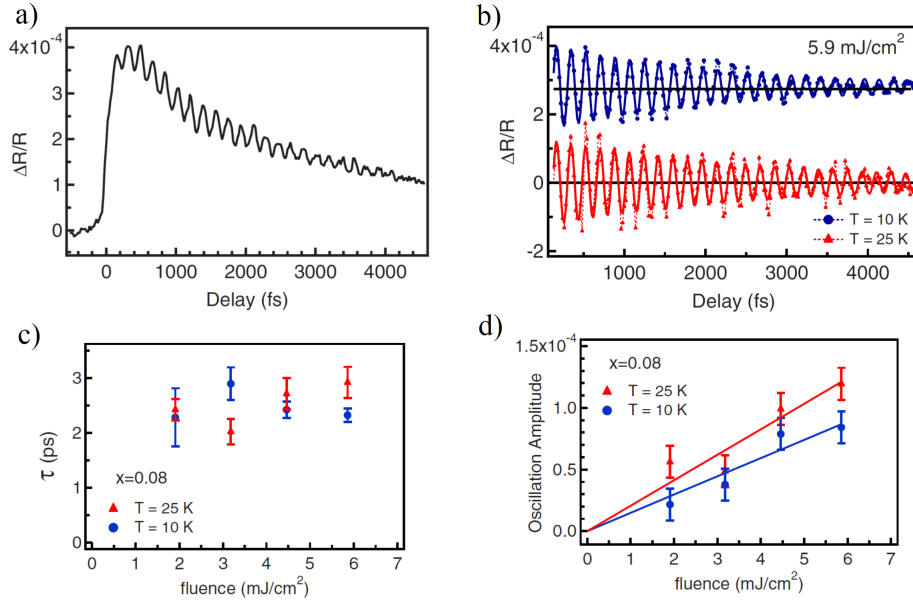


Figure 2.6: Time-resolved reflectivity studies on  $\text{Ba}(\text{Fe}_{1-x}\text{Co}_x)_2\text{As}_2$ . (a) Spectrum at 10 K showing  $A_{1g}$  mode. (b) Coherent optical lattice oscillation of the superconducting and metallic phases at 10 and 25 K. Damping time (c) and amplitude (d) as a function of the pump fluence. From [107].

Measurements with time-resolved optical reflectivity revealed the fully symmetric  $A_{1g}$  mode after pumping with 800 nm. Surprisingly, the mode displayed a significant blue-shift with respect to the equilibrium frequency for both PI and PM phases, figure 2.5 (c). This photoinduced blue shift is very rare, as one would naturally expect a red shift due to the heating effect of the ultrashort laser pulses. Such a blue-shift—a phonon hardening, is certainly non-thermal in nature. In fact, the ultrafast metallization observed in the tr-PES and the hardening of phonon are very close to what is expected from reducing the shortest distance between the vanadium atoms. On the other hand, as the electronic structure is actually very sensitive to the trigonal distortion, a relaxation of the in-gap states should also be accompanied by a relaxation of the lattice. These results can be explained within a theoretical framework; indeed, in  $\text{V}_2\text{O}_3$  the crucial role is played by the fact that the unoccupied  $a_{1g}$  electronic state is a bonding orbital which lies along the  $c$ -axis. By pumping the system, we photoexcite the electrons to this bonding orbital which transiently changes the specific filling of the orbitals close to the Fermi level. Hartree-Fock model is sufficient to describe this gap collapse and the loss of coherence in the PM phase by the number of  $a_{1g}$  orbital filling. The strong electron-phonon interaction should lead to a subsequent non-thermal lattice modification mainly by the reduction of the vanadium distance along the  $c$ -axis that stabilizes the non-thermal state for about 2 ps.

The common features between both oxides of vanadium are now clear. The (Mott) gap filling is triggered merely by electronic excitation and is accompanied by the formation of a non-thermal metallic phase that is stabilized by a lattice distortion.

For the case of  $\text{V}_2\text{O}_3$ , neither tr-PES nor tr-reflectivity is sensitive to the dynamics of the lattice directly. However, some time-resolved X-ray diffraction measurements can disclose the answer. I leave the discussion here and I will come back to it in section 6.1.

### 2.3.2 Coherent optical phonons in iron pnictide superconductors

The mechanism behind the high- $T_c$  superconductivity has remained a subject of debate over years and the complexity arise from multiplicity of competing phases in the proximity of the superconducting phase. The role of different degrees of freedom, for instance coherent phonons, in mediating the phase transitions is the underlying question towards better understanding. Time-resolved studies provides a direct way for observing lattice vibrations as a response to an ultrafast stimulus. In this view, Mansart *et al.* [107] studied the time-resolved reflectivity changes of the iron pnictide  $\text{Ba}(\text{Fe}_{1-x}\text{Co}_x)_2\text{As}_2$  with  $x=0.08$  both below and above the  $T_c$  (24 K). Figure 2.6 (a) presents the spectrum at 10 K. The decaying behavior is accompanied by coherent oscillations. The oscillation frequency is 5.56 THz that corresponds to the fully symmetric  $A_{1g}$  optical mode. The amplitude and decay time of these phonons as a function of fluence is presented in figure 2.6 (c) and (d) for both high temperature and low temperature phases. The damping time of the oscillations remains the same for all fluences and both phases. As expected, the phonon amplitude varies linearly with the excitation fluence, but with a slightly smaller slope with respect to the metallic phase. The smaller slope below  $T_c$  can possibly be related to the breaking of superconducting pairs induced by the pump pulse.

In the end the authors concluded that the fact that neither the damping time nor the phonon frequency change between the two phases indicates that the fully symmetric mode is not involved in the superconducting phase transition. However, as the wavevector of the  $A_{1g}$  is close to the center of the Brillouin zone, the role of other phonons remains unclear and deserves further studies.

## 2.4 Out-of equilibrium studies of Dirac fermions

### 2.4.1 Dirac carrier relaxation in graphene

Any application of the ultra-high-mobility materials with Dirac-like dispersion in future devices, demands investigating the relaxation dynamics of photoexcited carriers. An interesting question that can be addressed is whether it is possible to have carrier multiplication—that is, the generation of more than one electron-hole pair per absorbed photon and this is only possible if these pairs can be efficiently separated before they lose energy and merge to the same distribution [78, 186]. In fact, carrier multiplication (CM) after photo-excitation can occur only if impact ionization dominates over other competing relaxation channels such as Auger heating or emission of phonons. The ultrafast dynamics of excited carriers in graphene was studied by means of time-resolved ARPES [78] by pumping with infrared 1.5 eV pulses and probing the system with 33.2 eV pulses. Figure 2.7 (a) shows the ARPES difference spectra for several positive delays minus the negative delay<sup>1</sup> signal. The asymmetry in the intensity of the bands below the Fermi level is due to the interference effects studies in [127]. The excited electrons above the Fermi level are shown in red and the holes in blue. The excited states follow a double exponential decay involving two time constants 150 fs and 3 ps that can be assigned to relaxation via optical phonons and acoustic phonons (or supercollisions), respectively. The excited electrons retrieve their Fermi-Dirac distribution at a time scale less than the pump duration via strong Coulomb scattered processes, meaning that the electronic temperature is well-defined at any time. The authors applied the 3TM, Figure 2.7 (b), and extracted the coupling with hot phonons and lattice equal 0.033 and 0.010, respectively. They also showed that the  $\text{CM} > 1$  could only occur

<sup>1</sup>Roughly speaking, the negative delay means that the probe pulse is not yet seeing the effect of the pump pulse. It arrives before any photoinduced has occurred.

by a high pump photon energy or a very low fluence that is beyond the favorable experimental condition for a pump-probe experiment. Figure 2.2 shows different channel of relaxation of excited electrons. The CM is defined as the ratio between the time-dependent photoinduced carrier density ( $n_l$ ) above the Fermi level, and the number of electron-hole generated by the pump pulse ( $n$ ) right after complete absorption of the pump power. Figure 2.7 (c) shows that the CM is always below 1. Another work by Gierz *et al.* [55] on hole-doped graphene using MIR pulses has also proved the absence of efficient carrier multiplication. They show that THz lasing is only possible within very short interval of time after MIR excitation ( $\sim 100$  fs) where the density of states can be explained by a Fermi-Dirac plus a Bose-Einstein distribution. However, the short lifetime of electron-hole pairs demonstrates that graphene is not suitable for efficient light harvesting, at least in the present excitation regime.

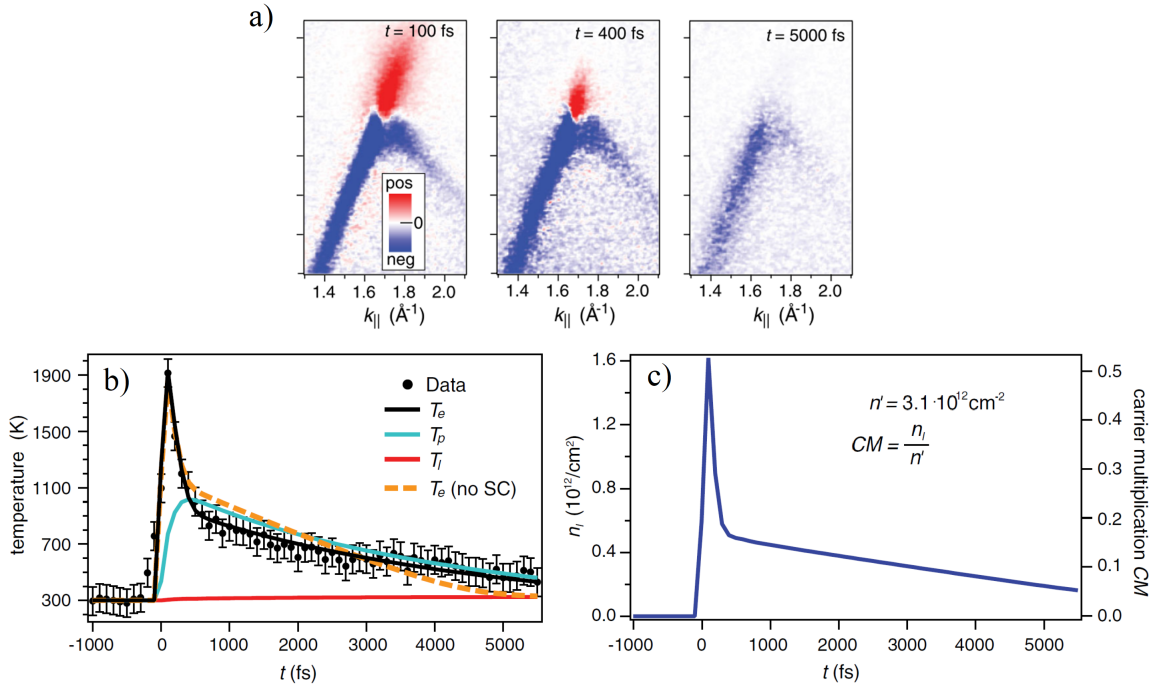


Figure 2.7: (a) ARPES difference spectra. The red signal shows the excited electrons above the Fermi level. (b) The evolution of the temperatures obtained by the 3TM. (c) The carrier multiplication and number of photoinduced Dirac carriers are shown as a function of time. From [78].

### 2.4.2 Dynamics of the Weyl semimetal $\text{MoTe}_2$

$\text{MoTe}_2$  has been proposed as a type II Weyl semimetal hosting tilted Dirac cones at its low temperature noncentrosymmetric phase while at high temperatures ( $T > 257.5$  K) the gap opens and results in a trivial phase. However, this prediction had no experimental support due to the fact that the Weyl point lies above the Fermi level, inaccessible via equilibrium-state experiments. By means of time-resolved ARPES Crepaldi *et al.* [31] probed the unoccupied states and unveiled the Weyl semimetal nature of the low temperature phase, figure 2.8 (a). They also showed that the dynamics of the gapped state is slowed down with respect to the gapless phase, figure 2.8 (d) and (e). This slower dynamics cannot be purely explained by the electron-phonon coupling since both phases have the same phonon dispersion. In fact, in the trivial phase the local gap between the valence band and the conduction band is a bottleneck for the relaxation of electrons optically excited in the conduction band. On the contrary, the relaxation time in the gapless type-

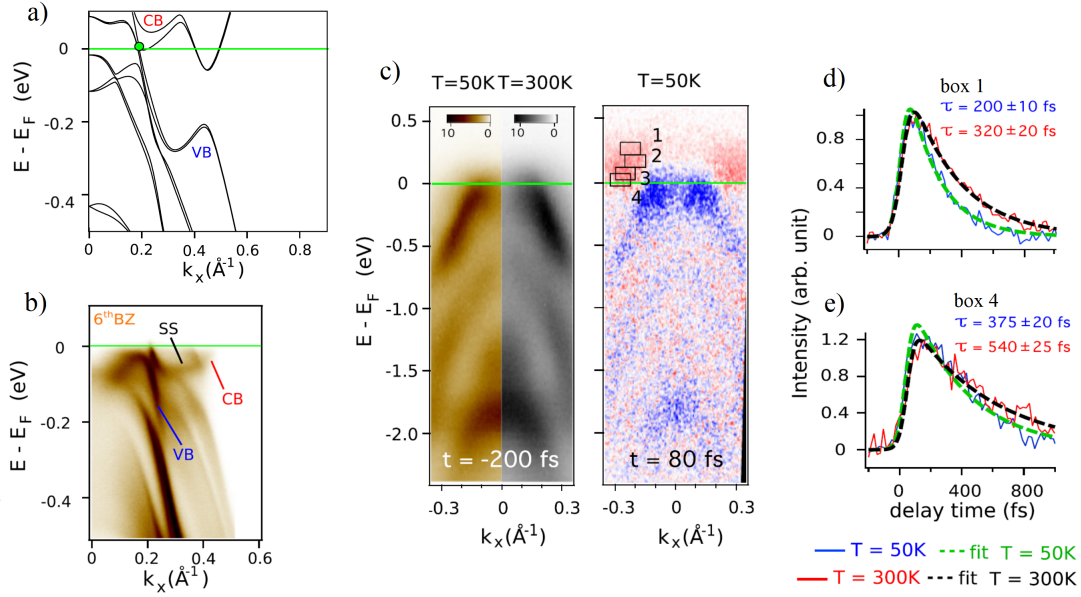


Figure 2.8: (a) The theoretical band dispersion of  $\text{MoTe}_2$ . The Weyl node is shown in green. (b) Experimental band dispersion. (c) Left panel: Band dispersion along  $\Gamma X$  for low (brown) and high (grey) temperatures before optical excitation. Right panel: Effect of optical excitation at Weyl semimetal phase at 50 K. The dynamics of the excited states corresponding to boxes 1 and 4 are shown in (d) and (e) respectively. The fit to the data shows a slower dynamics for the gapped phase at 300 K. From [31].

II Weyl phase of  $\text{MoTe}_2$ , reflects the enhanced interband scattering from the conduction band to the valence band mediated by electron-electron scattering along the Weyl cone. The same effect of the small band gap has also been studied on the Dirac fermions of the bilayer graphene [177], suggesting a slower dynamics with respect to the monolayer graphene due to less efficient electron-phonon scattering in the presence of a gap close to the Fermi level.

### 2.4.3 Broken time-reversal symmetry and Floquet states

A straightforward paradigm that comes to mind for manipulating topological properties of Dirac semimetals, is to add magnetic impurities to the system or to slightly dope it with another element to make it a trivial or non-trivial insulator, c.f. paragraph 1.4.3.2. However, these methods demand chemically manipulating the system that can be time-consuming and less precise. It has been demonstrated both experimentally and theoretically that ultrafast pulses can be a smart alternative choice towards this goal. As an example, by coherent pumping with linear polarization below the band gap of the topological insulator  $\text{Bi}_2\text{Se}_3$ , the photon-dressed surface electrons produce Floquet-Bloch<sup>2</sup> states that exhibit momentum-dependent band gaps within the Brillouin zone at avoided crossings [105, 181]. These Floquet-Bloch states can be viewed as replicates of interpenetrated Dirac cones with anisotropic band gaps. For instance, band crossings along the  $k_y$  are gapped while there is no gap along the  $k_x$ , figure 2.9 top panel. The linearly polarized light does not break the time-reversal symmetry; it only perturbs electrons periodically. Therefore, the Dirac point remains protected and gapless. However, the circularly polarized MIR light

<sup>2</sup>Electrons in a periodic potential in solids gives Bloch bands. In the same way, if they feel a periodic potential in time, i.e. an AC electric field, the periodicity in momentum turns into a periodicity in energy, i.e.  $\epsilon$  turns into  $\epsilon + n\hbar\omega$  and these are called Floquet states. In a solid the combination of spatial and temporal periodicity results in Floquet-Bloch states. Note that the photon energy should be below the absorption threshold of the material.

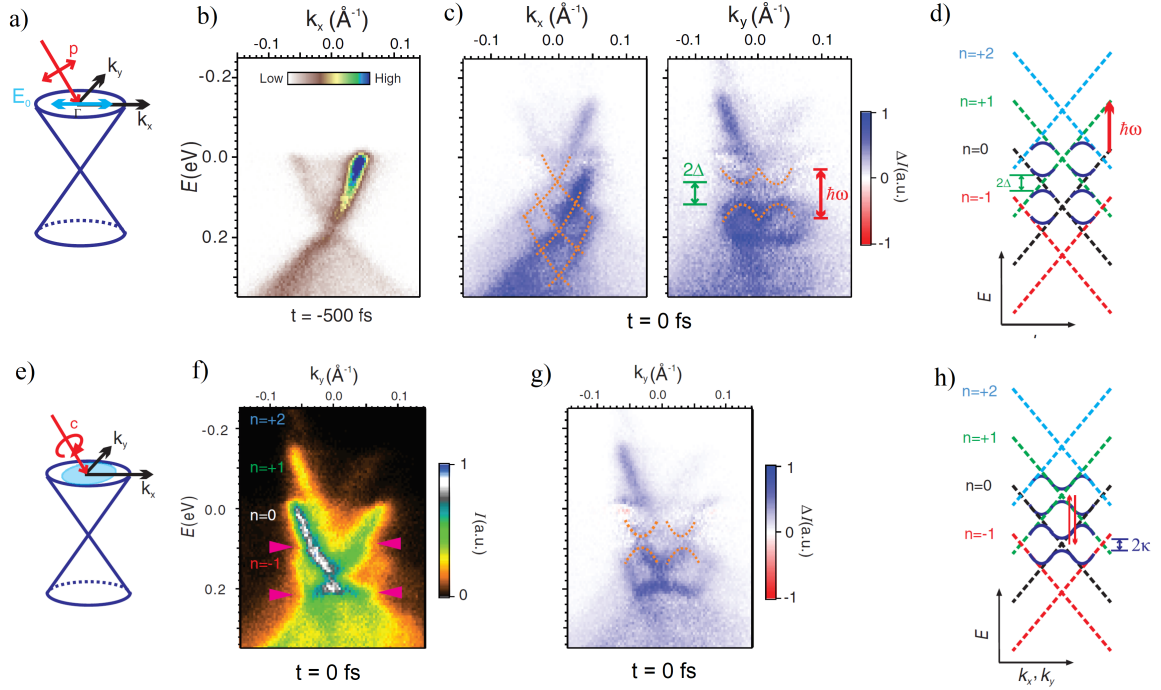


Figure 2.9: Schematics of the bands subjected to the AC electric field of the MIR pulses at  $10 \mu\text{m}$  (from [181]). (a) With linear polarization of light the surface states at a negative delay are shown in (b). (c) The spectrum at the negative delay is subtracted from the spectra at time zero for two different directions in order to highlight the photoinduced effects. Dashed orange lines are guides to the eye. (d) Sketch of the Floquet states of different order as induced by the MIR excitation. The numbers show the band index of the states. Band gaps occur at several momenta due to the hybridization between the states. (e) The projection of the CPL electric field on the surface plane (light blue) is elliptical. (f) ARPES spectrum at time zero. (g) Photoinduced effects at the arrival of the pump pulse. (h) Band gaps occur at several momenta however, the band gap that is induced by the TRS breaking is at the Dirac point,  $2\kappa \sim 50 \text{ meV}$ .

can be used as an ultrafast tool to break the time-reversal symmetry and therefore, to open the band gap at the otherwise protected Dirac point. This gap along with other avoided gaps at the band crossing remain isotropic within the Brillouin zone (figure 2.9 bottom panel).

In the same spirit, one might expect to generate a 3D Weyl semimetal from a Dirac semimetal by subjecting it to a periodic TRS breaking field, i.e. circularly polarized light (CPL). The frequency of the CPL should be much less than or comparable to the bandwidth of the parent DSM. It has been theoretically proved [19, 72] that in this way, the Dirac fermions in a DSM can indeed split into Weyl fermions. The work was done for the case of  $\text{Na}_3\text{Bi}$  but the same approach can be generalized to any DSM. The starting point is to introduce the coupling to a time-dependent external gauge field by Peierls substitution in equation 1.13, so that  $\mathbf{k} \rightarrow \mathbf{k} - \mathbf{A}(t)$ , where  $\mathbf{A}(t)$  is the time-dependent vector potential of the applied CPL. For instance,  $\mathbf{A}(t) = A_0(0, \cos(\omega t), \sin(\omega t))$  for polarization in the y-z plane.  $\omega$  is the frequency of the light. This approach only takes into account the electric field of the laser pulse and neglects its magnetic component. The resulting time-dependent Hamiltonian  $H(t) = H(\mathbf{k} - \mathbf{A}(t))$  describing the dynamics of the driven model system reduces to:

$$\begin{pmatrix} \hat{H}_{Weyl}(\vec{k}) + \frac{(V_F A_0)^2}{\omega} \sigma_x & 0 \\ 0 & \hat{H}_{Weyl}(\vec{k})^* - \frac{(V_F A_0)^2}{\omega} \sigma_x \end{pmatrix} \quad (2.5)$$

where  $V_F$  is the Fermi velocity. The effective gauge field acts only on the x-component of the wavevector and results in the splitting of the 4-fold degenerate Dirac points to two non-equilibrium transient states, called Weyl-Floquet states. These states are located at  $\pm(V_F A_0)^2/\omega$  along the  $k_x$  direction with respect to the original Dirac point, figure 2.9. It has been also shown that the number, location, and nature of the Weyl nodes are tunable within the Brillouin zone by amplitude and frequency of the CPL [19].

We have already seen that any explicit symmetry breaking of the DSM opens the gap and results in a topologically non-trivial state. One way is, for instance, to break the inversion symmetry by applying strain on the sample. Hübener showed that by shining this state with femtosecond CPL with enough intensity, the Floquet-Weyl semimetal phase is restored. To conclude, circularly polarized light may be used to alternatively switch between Weyl semimetal, Dirac semimetal and topological insulator states.

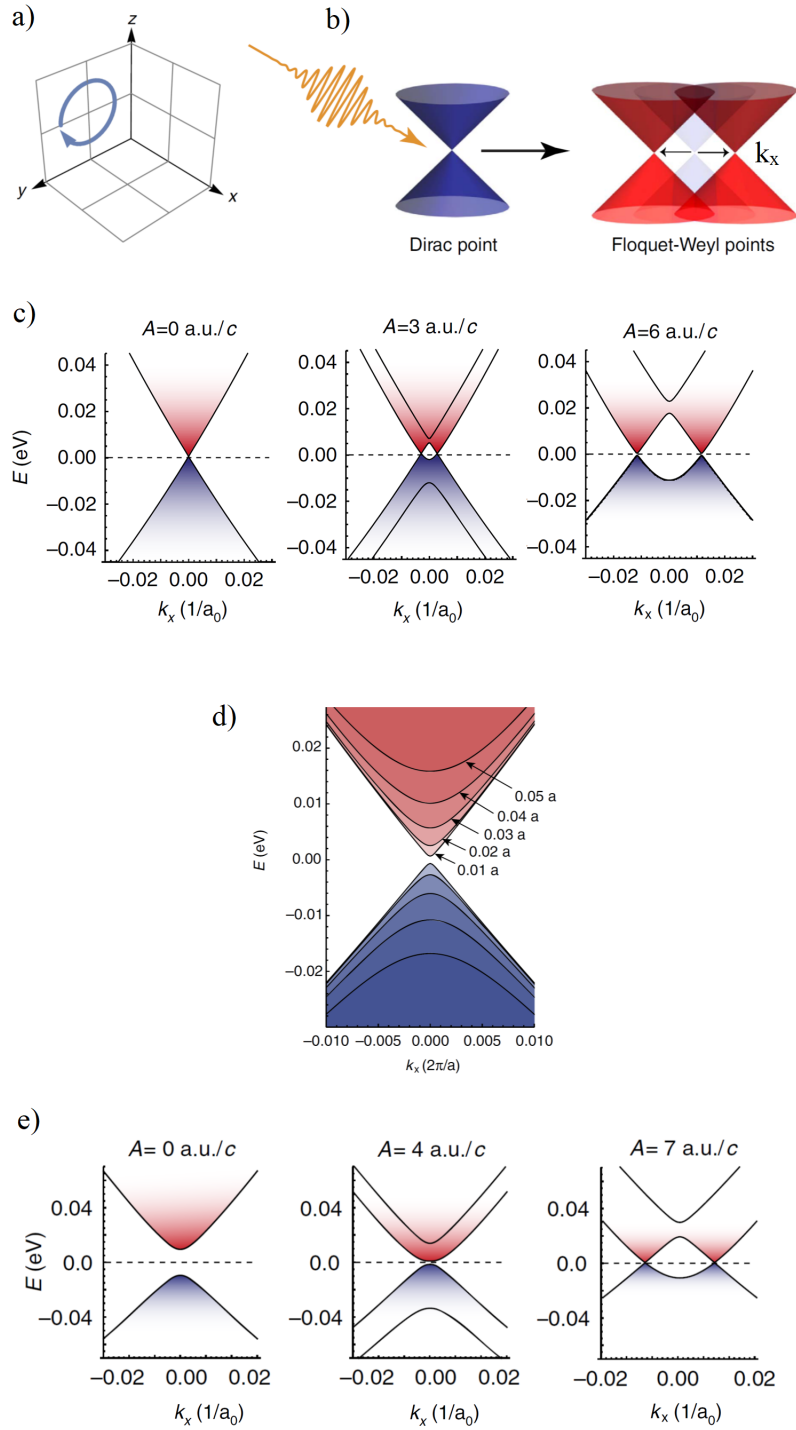


Figure 2.10: Engineering the non-trivial states in  $\text{Na}_3\text{Bi}$ . (a) CPL in the  $y$ - $z$  plane. (b) The Dirac cone splits along the  $k_x$  direction at the Fermi level, resulting in a Floquet-Weyl semimetal. (c) The separation of the transient states can be tuned by the amplitude of the incident light. (d) The lattice distortion along the  $a$ -axis of the unit cell induced by strain makes the Dirac fermions massive and opens the gap. By applying femtosecond CPL, one is able to close the band gap. (e) If intensity of light is above the threshold, Floquet-Weyl states with different chirality appear. From [72].



# 3 | Experimental methods

## 3.1 Introduction

The observation, classification and description of materials on a quantum mechanical basis indispensably demands understanding their electronic properties as well as the relevant and dominant couplings among their different degrees of freedom. The previous chapter was thoroughly devoted to highlight how to reveal and possibly to manipulate these intricate couplings. In this chapter, I describe how this effort is technically possible.

Photons or accelerated particles such as neutrons or electrons are widely used to perform experiments on quantum materials. I focus on the photon-based techniques. Setups that apply a monochromatic or continuous photon beam reveal structure and electronic properties of materials at equilibrium. If the beam is replaced by ultrashort pulses and another pulse is also added to the experiment, it will be possible to study the dynamics of the system in a pump-probe fashion. Here, the pulse duration and the energy of the second pulse enables one to selectively follow the dynamics of a specific component, study how fast it relaxes, and which dominant process causes the relaxation to occur. In a generic experiment, the choice of photon energy determines first, what part of the sample is studied (the surface or the bulk) and second, which component is observed, e.g. electrons and/or lattice. For instance, UV pulses are mostly sensitive to the surface and they probe the electrons while X-rays provide information on the bulk structure of the material and they probe the atomic positions into the elementary cell.

In this chapter, I present the experimental techniques that I used during my PhD project to study the equilibrium and out-of-equilibrium properties of the correlated materials  $\text{BaCo}_{1-x}\text{Ni}_x\text{S}_2$  and  $(\text{V}_{1-x}\text{Cr}_x)_2\text{O}_3$ . Several techniques measuring the equilibrium state of solids are presented. In parallel, I explain the pump-probe configuration of these techniques as well as the information they provide to us.

## 3.2 Angle-resolved photoelectron spectroscopy

The electrons band structure and dynamics determines most of the physical properties of a system. Therefore, the indispensable building block towards understanding condensed matter physics is to observe electrons in their quantum states and more specifically, how they interact among themselves. A straightforward way is to detect electrons via photoelectric effect.

The photoelectric effect was first discovered by Hertz [67] when he observed that ultraviolet light caused the ejection of electrons from the surface of a metal. This was later explained by the quantum mechanical nature of light by Einstein in 1905 [39]. He explained that an electron can absorb a photon incident to the sample and escape from the material with a maximum kinetic energy  $E_{kin} = h\nu - \phi$ . Here  $\nu$  is the photon frequency and  $\phi$  is the material work function that measures the potential barrier at the surface preventing the valence electrons from escaping.

The photoelectric work function is typically around 4 - 5 eV for most of materials.

Photoemission spectroscopy, also known as photoelectron spectroscopy, is a general term that refers to all techniques based on the application of the photoelectric effect. It was first employed by a Swedish scientist Kai Siegbahn in 1957 who performed the X-ray photoemission spectroscopy to study the electron binding energies of a copper sample [130].

**Angle-resolved photoelectron spectroscopy (ARPES)** is a unique experimental technique that offers the possibility to simultaneously detect the kinetic energy and angular distribution of the photoemitted electrons from a sample illuminated with a beam of monochromatized radiation supplied by a gas-discharge lamp, laser pulses, or synchrotron radiation. An electron inside the solid absorbs energy and (negligible) momentum from the incoming photon and is ejected in vacuum. In recent decades, the advent of state-of-the-art electron energy and momentum analyzers as well as high energy resolution and polarization control of the exciting light lead to the precise two-dimensional energy-momentum mapping of the photoelectrons in the reciprocal space ( $k$ -space). Therefore, accurate information about the quantum states of electrons inside a solid and the dispersion of filled electronic bands is acquired.

The following sections are devoted entirely to a detailed explanation of ARPES that, as we have seen, starts from the simple idea of the photoelectric effect and extends to much rich and fundamental knowledge of quantum materials. The discussions are mostly inspired by Hüfner's photoelectric spectroscopy [73], and Damascelli's review article [34].

### 3.2.1 General description

The energetics of the photoemission process and the geometry of an ARPES experiment are shown in figures 3.1. The kinetic energy of the electron is  $E_{kin}$  and its emission angle is read from the polar angle  $\theta$  and azimuthal angle  $\varphi$ .

An ARPES electron energy analyzer, figure 3.1 (b), collects outgoing photoelectrons at a given emission angle within a finite acceptance angle and energy resolution and then bins them according to their momentum and kinetic energy. The analyzer generally consists of three parts: i) an electrostatic lens that sorts the electrons according to their ejection angle; ii) a hemispherical energy analyzer [111] that sorts the electrons by their kinetic energy; and iii) a 2D detector, which reads the emission angle and kinetic energy for each photoelectron. Since the ARPES technique measures only at one angle, the full band structure is obtained either by rotating the sample around its surface normal or by changing the analyzer's angle. This depends on the setup configuration.

By using conservation laws, one can extract information about the electrons prior to the photoemission process. Conservation of energy and momentum are:

$$E_{kin} = h\nu - E_B - \phi \quad (3.1a)$$

$$\mathbf{k}_f - \mathbf{k}_i = \mathbf{k}_{h\nu} \quad (3.1b)$$

where  $E_B$  is the bending energy,  $\mathbf{k}_{h\nu}$  is the photon wavevector, and  $\mathbf{k}_f$  and  $\mathbf{k}_i$  are the electron final and initial wavevector, respectively. The modulus of the photoelectron momentum in vacuum  $K$ , is related to  $E_{kin}$  by  $K = \sqrt{2mE_{kin}}/\hbar$ . The components of  $K$  parallel and perpendicular

to the sample surface are obtained from the polar and azimuthal emission angles  $\theta$  and  $\varphi$  by:

$$K_x = \frac{1}{\hbar} \sqrt{2mE_{kin}} \sin \theta \cos \varphi, \quad (3.2a)$$

$$K_y = \frac{1}{\hbar} \sqrt{2mE_{kin}} \sin \theta \sin \varphi, \quad (3.2b)$$

$$K_z = \frac{1}{\hbar} \sqrt{2mE_{kin}} \cos \theta, \quad (3.2c)$$

Now, we can determine the energy-momentum relation  $E(\mathbf{k})$  inside the sample. As the photon energy used in ARPES experiments is typically low ( $\hbar\nu < 100$  eV), the photon momentum is perfectly negligible in comparison with the Brillouin zone size which is of order of  $\sim 1 \text{ \AA}^{-1}$ . Therefore, we can consider the excitation of a bulk electron as being vertical in  $\mathbf{k}$ -space, i.e.  $\mathbf{k}_i = \mathbf{k}_f$ . When this electron reaches the surface, the translational symmetry in  $x-y$  plane is preserved thus,  $k_{\parallel} = K_{\parallel}$ . However, due to a sudden potential change along the  $z$  axis, the symmetry in this direction is broken and  $k_{\perp}$  is no longer conserved. The parallel and perpendicular components of the momentum with respect to the sample surface are given by:

$$k_{\parallel} = K_{\parallel}, \quad (3.3a)$$

$$k_{\perp} = \frac{1}{\hbar} \sqrt{2m(E_{kin} \cos^2 \theta + V_0)} \quad (3.3b)$$

The parameter  $V_0$  is the inner potential that corresponds to the energy of the bottom of the valence band referenced to the vacuum level and is normally unknown for most materials. This means that even if one has the possibility to measure all parallel components of the photoelectrons momentum, a complete knowledge on the crystal wavevector remains challenging. Nonetheless, for (quasi) two-dimensional systems the dispersion along the  $z$ -axis is negligible and the uncertainty in  $\mathbf{k}$  due to the perpendicular component is less relevant. In these systems, the electronic dispersion is almost determined by  $k_{\parallel}$  as in the case of 2D copper oxide superconductors or  $\text{BaNiS}_2$  (that is studied in details in chapter 4). By measuring the width of the photoelectron peaks in such systems, one can determine the lifetime of the photoexcited electrons that contains rich information on the nature as well as on the strength of many-body correlations. For three-dimensional systems, on the other hand, absolute band mapping requires a series of band dispersion measurements with different incident photon energies. In this way, one is able to deduce the  $V_0$  from the periodicity of the Fermi surface and eventually to determine  $k_{\perp}$ .

### 3.2.2 Photoemission intensity

The quantitative analysis of the photoemission spectroscopy data is often performed under the assumption of the *independent-particle* picture and the *sudden* approximation. The sudden approximation is widely used in many-body calculations of photoemission spectra for interacting electron systems and is more conveniently applicable to electrons with high kinetic energy<sup>1</sup>. This approximation implies that there is no post-collisional interaction between a photoelectron and the remaining system. In this regard, the photoemission process can be described by three sequential and independent steps:

1. Optical excitation of the electron to a bulk final state
2. Travel of the excited electron toward the surface

---

<sup>1</sup>Less energetic electrons undergo more collisions before being ejected from the surface.

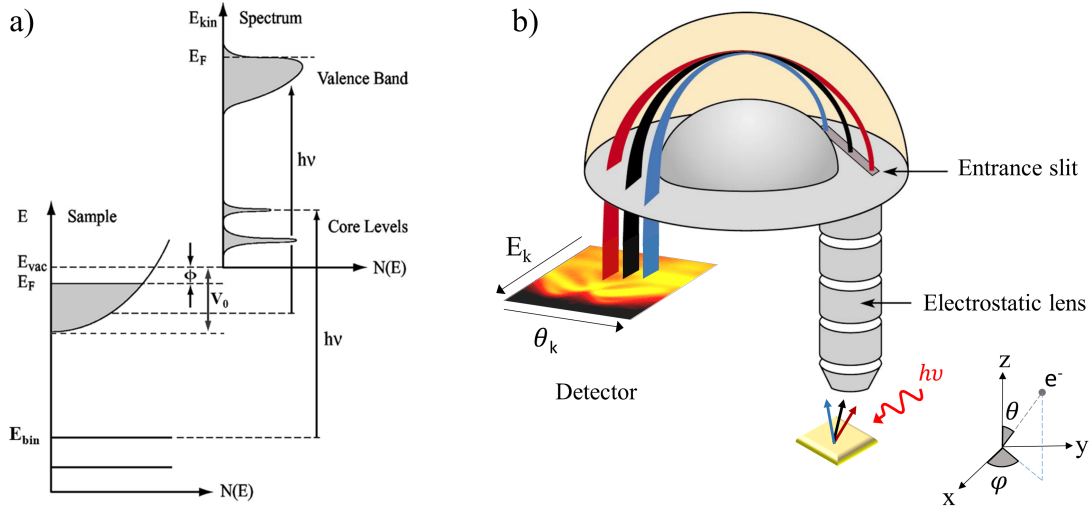


Figure 3.1: (a) The electron energy distribution (from [33]) produced by the incoming photons, and measured as a function of the kinetic energy  $E_{kin}$  of the photoelectrons. The left diagram shows the density of states of the solid in terms of the binding energy. The Fermi level corresponds to the zero binding energy. (b) Representation of the hemispherical photoelectron analyzer and the geometry of the experiment.

### 3. Transfer of the photoelectron into the vacuum through the surface potential barrier

Step 1 describes the intrinsic electronic structure of the material. Step 2 is explained by the effective mean free path of electrons inside a sample and will be described in subsection 3.2.5. It is proportional to the probability that the excited electron reaches the surface without scattering. The inelastic-scattering processes give rise to a continuous background in the spectra and is usually ignored or subtracted. Step 3, which describes the escape of the electron to the vacuum, depends on the energy of the excited electron and the material work function  $\phi$ . Specifically, the perpendicular component of its momentum needs to be larger than the work function and the binding energy:

$$\frac{\hbar^2 k_{\perp}^2}{2m} \geq E_B + \phi \quad (3.4)$$

The total photoemission intensity is proportional to the product of the probability of the above-mentioned steps. The probability of the first step, namely the optical transition probability  $W_{f,i}$  between an initial  $N$ -electron ground state  $\psi_i$ , and a final state  $\psi_f$  is given by Fermi's golden rule:

$$W_{f,i} = \frac{2\pi}{\hbar} |\langle \psi_f^N | H_{int} | \psi_i^N \rangle|^2 \delta(E_f^N - E_i^N - h\nu), \quad (3.5a)$$

$$H_{int} = \frac{e}{mc} (\mathbf{A} \cdot \mathbf{p}) \quad (3.5b)$$

where  $e$ ,  $m$  and  $c$  are the elementary charge, the electron mass and the speed of light in vacuum, respectively, and  $E_f^N = E_f^{N-1} + E_{kin}$  and  $E_i^N = E_i^{N-1} - E_{bin}^k$  are the final and initial state energies of the  $N$ -particle system. The interaction of light and electron is written within the dipole approximation—that is, there is no spatial dependence when considering its effect on the classical motion of an electron bound to an atom. Here,  $\mathbf{p}$  is the momentum operator and  $\mathbf{A}$ , is the electromagnetic vector potential. The interacting Hamiltonian  $H_{int}$  is treated as a perturbation to the system. Equation 3.5a implies that for an electron to be photoemitted into

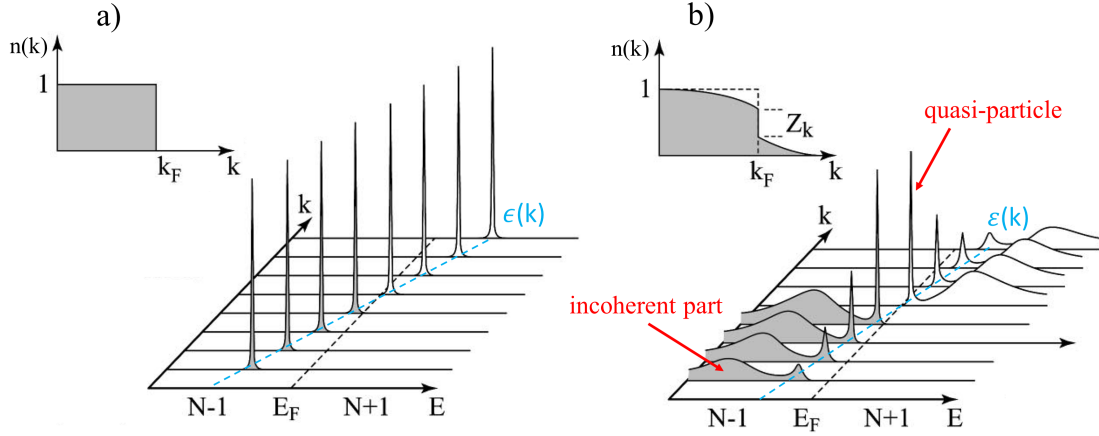


Figure 3.2: Spectral function and Fermi distribution of an electronic system with (a), and without interaction (b). The figure is inspired from [34].

vacuum, not only there must be a non-vanishing overlap between the amplitude of initial and final states, but also the energy and momentum conservation laws should be respected.

The sudden approximation allows us to factorize the wave functions into a traveling photoelectron  $\phi^k$ , and  $(N-1)$ -electrons left-behind  $\psi^{N-1}$ :

$$\psi_{i/f}^N = A \phi_{i/f}^k \psi_{i/f}^{N-1} \quad (3.6)$$

where  $A$  is a factor that antisymmetries the electronic wave function. Although this factorization greatly simplifies the equations, it is not trivial because during the photoemission process the system will relax. We can now write down the total intensity  $I$  of a photoemission peak as a sum over all possible initial and final states:

$$I = \sum_{f,i} W_{f,i} \propto \sum_{f,i} |M_{f,i}^k|^2 \sum_{m,i} |C_{m,i}|^2 \delta(E_{kin} + E_m^{N-1} - E_i^N - h\nu) \quad (3.7)$$

In the above equation, the experimental resolution and the continuous background due to the inelastically scattered electrons are not taken into account. These effects can be treated later while analyzing the experimental data. Here,  $M_{f,i}^k \equiv \langle \phi_f^k | H_{int} | \phi_i^k \rangle$  is called the matrix element and describes the interaction of a traveling photoelectron and light. The term  $C_{m,i}$  equals  $\langle \psi_{m,f}^{N-1} | \psi_i^{N-1} \rangle$  and its amplitude  $|C_{m,i}|^2$  describes the probability that after removing one electron, the  $(N-1)$ -particle system goes into an excited state  $m$ .

For a free-electron system for *only* one particular  $m$ , the  $C_{m,i}$  is not zero. Because in this case,  $\psi^{N-1}$  remains an eigenfunction of the system and is orthogonal to all other states. As a result, the ARPES data is accompanied by a set of delta function peaks whose position in the  $E$ - $k$  plane constructs the band dispersion of the studied sample. In a correlated system, however, the removal of an electron changes the interaction potential and the remaining  $N-1$  electrons are no longer an eigenfunction of the system but rather a superposition of all eigenfunctions of the system. This means that  $\psi_i$  has a finite overlap with some of  $\psi_{m,f}$  wave functions and  $|C_{m,i}|^2$  will be non-zero for many of the excited quantum states. Consequently, one principal quasi-particle peak is observed accompanied by several satellite peaks. Figure 3.2 schematically explains the mentioned ARPES spectra features. Next section is dedicated to a mathematical description of these features.

### 3.2.3 One-particle spectral function

The spectral function  $A^\pm(\mathbf{k}, \omega)$  describes the evolution of an N-particle system after adding (+) or removing (-) one particle and was thoroughly discussed in section 1.2. Experimentally, the spectral function can be measured by inverse photoemission or by ARPES, respectively and is related to the sum of  $|C_{m,i}|^2$  for all possible final states in equation 3.7. Therefore, we can re-write the photoemission intensity as:

$$I(\mathbf{k}, \omega) = I_0(\mathbf{k}, \nu, \mathbf{A})f(\omega)A(\mathbf{k}, \omega) \quad (3.8)$$

where  $f(\omega)$  is the Fermi-Dirac function and  $I_0(\mathbf{k}, \nu, \mathbf{A})$  is proportional to the square of the one electron matrix element and will be discussed in subsection 3.2.4. I should emphasize that the proportionality of the photoelectron intensity to the spectral function is a direct consequence of the sudden approximation. However, it is no longer valid for very low photoelectron kinetic energy. For the sake of simplicity, the  $A^-(\mathbf{k}, \omega)$  is replaced by  $A(\mathbf{k}, \omega)$ . Equation 3.7 implies that for a non-interacting system, where  $A(\mathbf{k}, \omega) = \delta(\mathbf{k}, \omega)$ , the ARPES spectrum will have a single peak at each binding energy at each binding energy  $\epsilon_k$  and therefore, there is a sharp Fermi surface. However, for an interacting system treated by the Fermi-liquid formalism, the ARPES spectrum consists of a quasiparticle peak and an incoherent part. The physical description of each part was given in section 1.2.

### 3.2.4 Matrix elements and light polarization

The last point to discuss about the photoemission intensity is the matrix element ( $M_{f,i}^k$  in equation 3.7). While the spectral function defines general features of an ARPES spectrum arising from intrinsic interactions inside a system, the matrix elements determine the intensity of the peaks according to some external parameters such as photon energy and experimental geometry. The photon energy dependence results from the atomic photoionization cross section for photoemission experiments that decreases while photon energy increases although not necessarily in a monotonic fashion.

In order to clarify the effect of the experimental geometry, we can rewrite the matrix elements as  $\langle \phi_f^k | \varepsilon \cdot \mathbf{x} | \phi_i^k \rangle$ , where  $\varepsilon$  is a unit vector along the polarization direction of light, and  $\mathbf{x}$  is the electron position operator. The integration of the function over all possible states is done perpendicular to the mirror plane, where the detector is located to collect electrons in their final states. In order to have a non-vanishing photoemission intensity due to the integral, the integrand must not be odd under the reflection with respect to the mirror plane.

The ejected electron in vacuum is a free electron with the wave function  $e^{i\mathbf{k}\cdot\mathbf{r}}$ , which is an even parity function<sup>2</sup>. Therefore,  $\varepsilon \cdot \mathbf{x} | \phi_i^k \rangle$  should not be odd. The odd polarization is when the electric field,  $E_p$ , is perpendicular to the mirror plane and lies on the surface of the sample while the even polarization lies on the mirror plane,  $E_s$ . Figure 3.3 illustrates the geometry of the experiment. In the figure, the positive (negative) sign is an even (odd) orbital symmetry. For a generic initial state of a given symmetry, the light polarization resulting in an even matrix element should have an equal symmetry with respect to the mirror plane, otherwise the photoemission intensity will be suppressed.

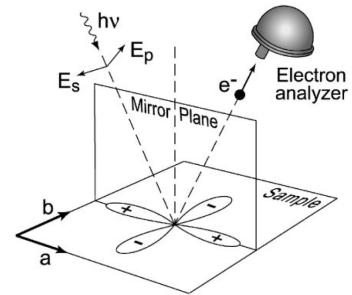


Figure 3.3: Symmetry of orbitals in the photoemission process [33].

<sup>2</sup>Its momentum and wavefronts are in the mirror plane and orthogonal to it, respectively.

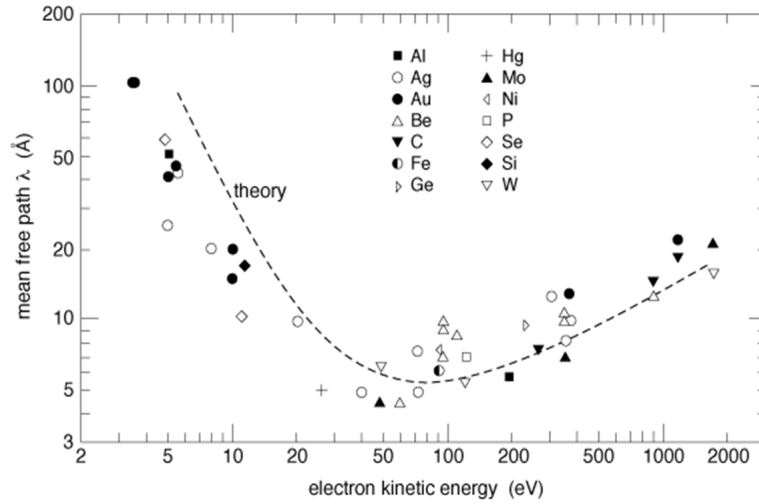


Figure 3.4: Mean free path of electrons from [164].

To conclude, the ARPES spectrum reflects the symmetry of the electronic bands and a detailed electronic band structure of a specimen is acquired by varying the polarization of the incident beam.

### 3.2.5 Surface sensitivity and angular resolution

During the photoelectron process, only the photoelectrons who propagate elastically toward the surface of the solid will conserve the memory of their initial states in the crystal. In fact, consecutive collisions of the photoelectrons among themselves, with phonons or the crystal impurities decrease their kinetic energy. These inelastically scattered electrons are called secondary photoelectrons and contribute to the exponential loss of intensity with the depth beneath the surface:

$$I(z) \propto I_0 e^{-z/(\lambda \cos \theta)} \quad (3.9)$$

where  $I_0$ ,  $z$ ,  $\lambda$  and  $\theta$  are the initial beam intensity, the direction of propagation of the beam, the wavelength of the beam and the angle at which the beam heats the sample surface, respectively.

The inelastic collision probability depends on the distance that the electrons travel towards the surface as well as their kinetic energy. Figure 3.4 illustrates the elastic mean free path of electrons as a function of their kinetic energy. It has a minimum of about 5 Å, i.e. several atomic layers, for 20-100 eV that is the interval of energy typically used in ARPES measurements. This implies that ARPES signal comes mostly from the surface. In general, ARPES experiments are highly sensitive to the surface of materials. Therefore, surfaces have to be carefully prepared, i.e. without defect at the atomic scales and cleaved *in situ* in an ultra-high vacuum (UHV) chamber in order for the electron to propagate in vacuum without any energy loss and also to keep the surface clean during the experiment.

The momentum resolution, on the other hand, depends on the incident photon energy as can be derived from equation 3.2:

$$\Delta k_{\parallel} \propto \sqrt{E_{kin}} \cos \theta \Delta \theta \quad (3.10)$$

with  $\Delta \theta$  being the finite acceptance angle of the electron analyzer. Momentum resolution will be better at lower photon energy, and for large polar angles  $\theta$ . The latter implies that one can eventually improve the momentum resolution by extending the measurements to momenta

farther from the first Brillouin zone.

In general, before performing a photoemission experiment, one should carefully choose the appropriate photon energy according to the experimental needs. For low energies ( $E < 10$  eV), the probed depth is larger and the momentum resolution is better while only a small part of the Brillouin zone can be detected. For energies higher than 200 eV the probing depth increases and the core levels might be accessible. However, the momentum resolution gets poorer.

In the following section, I described the light sources where I performed the ARPES experiments.

### 3.3 Synchrotron light sources

Recent decades have witnessed the emergence of third generation synchrotron light sources providing light from infrared to hard X-rays with extremely high brightness of about  $\sim 10^{20}$  photons/s/mm<sup>2</sup>/mrad<sup>2</sup>/0.1% bandwidth. Tunability in wide range of energy, variable polarization of light and very high brightness, have opened a wide range of new characterization methods for various research purposes, from infrared spectroscopy to protein crystallography.

Figure 3.5 shows the scheme of a synchrotron. The electrons are produced, grouped in some electron bunches and are gradually accelerated in a linear accelerator. Then they enter in the booster where they acquire almost 99% of speed of light. The majority of 3<sup>rd</sup> generation sources operate with the electron beam energy in the range of 2 to 4 GeV. Once the high-energy electron beam has been generated, it is directed into auxiliary components such as bending magnets and insertion devices (undulators or wigglers [18]) in storage rings in which they circulate and produce synchrotron radiation without gaining further energy. Beamlines are built tangentially to the electron beam orbit of the storage ring and capture the radiation emitted from bending magnets, wigglers or undulators. Each beamline has specific optical elements that depend on the experimental methods they use. The optical devices include crystal mirrors to guide light through the end station, monochromators to select the desired wavelength, and slits and attenuators to cut the unwanted wavelengths and decrease the beam intensity.

During my PhD, I had the opportunity to work with synchrotron facilities to perform ARPES in the ultra-violet (UV) range as well as some time-resolved X-ray diffraction experiments by soft X-rays which will be explained in paragraph 3.4.2.5.

The combination of increasing number of third generation synchrotron beamlines operating in the UV range and great technical progress of hemispherical photoelectron analyzers to attain meV energy resolution makes synchrotrons the unrivaled facilities for performing ARPES experiments. The possibility of focusing the beam to a sub-micron scale by either Schwarzschild objectives or zone plates adds the spatial resolution to the privileges of synchrotron sources in the field of photoemission spectroscopy. In particular, this makes it possible to obtain much information on the electronic structure of nano-sized structure.

The Spectromicroscopy beamline and Advanced Photoelectric Effect beamline at synchrotron Elettra in Italy are discussed below for their unique properties for photoemission spectroscopy.

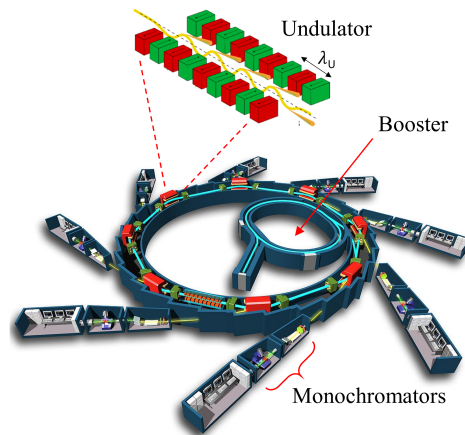


Figure 3.5: Synchrotron facility.

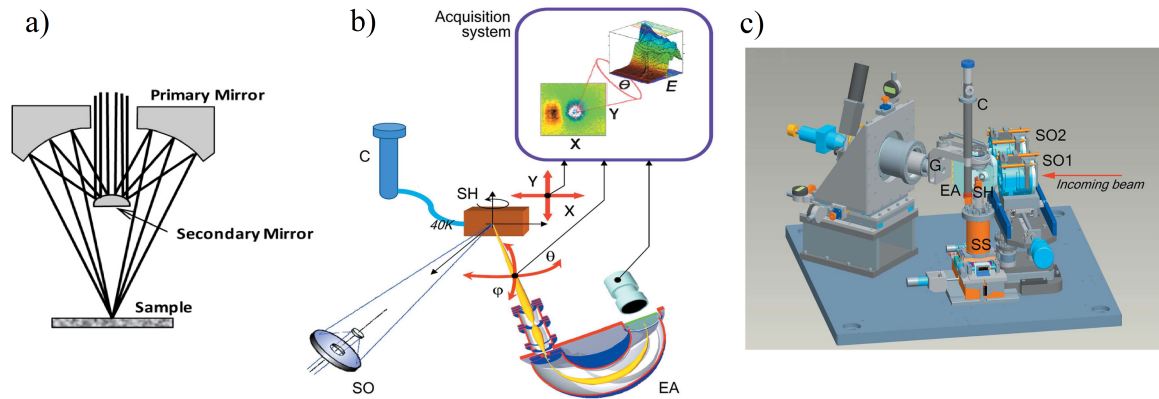


Figure 3.6: Instruments at the Spectromicroscopy beamline. (a) Schwarzschild objective. (b) The geometry of the experiment from [37]. For the ARPES mode the analyzer angles change while for the surface cartography the position of the sample is scanned. (c) The beamline has two SO's. One for the 27 eV and the other for the 74 eV beam.

### 3.3.1 Spectromicroscopy beamline

The Spectromicroscopy beamline [5, 37] is one of the unique beamlines to run a scanning photoemission microscope. The source of light is a classic undulator and consists of 36 periods of 12.5 cm, for a total length of 4.5 m. The end station hosts two exchangeable multilayer-coated Schwarzschild objectives (SO) designed to focus the radiation at 27 eV and 74 eV to a small spot. It also has an internal movable hemispherical electron energy analyzer that can perform polar and azimuthal angular scans in ultrahigh vacuum (UHV). The beamline is designed to perform photoemission experiments with high spatial resolution with spot size of  $\sim 600$  nm. The energy and momentum resolutions are  $\sim 33$  meV and  $\pm 0.03 \text{ \AA}^{-1}$ , respectively.

The beamline is based on three spherical grating monochromators that can rotate one with respect to each other to produce different photon energies. The largest energy range covered by one of the gratings is 20 - 310 eV. The microscope is based on a Schwarzschild objective, figure 3.6 (a). Such a device consists of two spherical mirrors: one is the convex primary and the other is the concave secondary mirror. High reflectivity of the Schwarzschild objective at fixed photon energy is obtained by using periodic multilayer coatings that for 27 and 74 eV are Sc/Si and Mo/Si, respectively. The sample is placed at the focus of the Schwarzschild objective.

We have the possibility to perform two different types of measurement on the Spectromicroscopy beamline. First, it is possible to acquire a detailed ARPES map from a small illuminated area of the sample by gradually moving the analyzer so that the entire Brillouin zone is covered. The acceptance angle of the analyzer in this case is  $1.4^\circ$  and the momentum resolution at the Fermi level for 27 eV photons is  $\pm 0.03 \text{ \AA}^{-1}$ . Second, we can also acquire images by fixing the analyzer and scanning the sample position perpendicular to the direction of the incoming radiation. This gives a map of the sample surface with the contrast arising from the photoemission spectrum features of each probed region. In this configuration the analyzer operates in the wide-angle mode with  $8^\circ$  acceptance angle since the k-resolution matters less. Figure 3.6 (b) illustrates the setup for spectroscopy and microscopy experiments.

One of the big advantages of the SO is that it can be operated in the visible as well as in the X-ray region. In the optical microscope configuration it can be used to observe the sample with a field of view of the order of 300 - 400  $\mu\text{m}$  by the synchrotron white light beam. This gives an overview of the sample features in order to look for the best position to be probed by the beam.

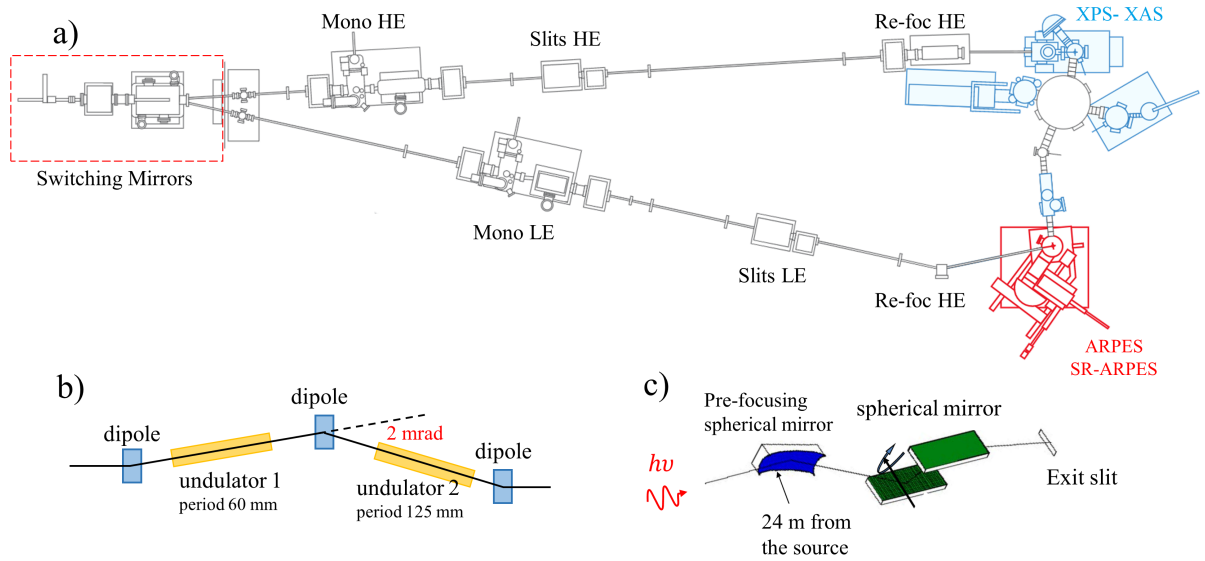


Figure 3.7: (a) Instruments at APE beamline. (b) Undulators for the HE and LE beamlines. (c) Monochromator section. It is based on twin plane grating-spherical mirror assemblies.

### 3.3.2 Advanced Photoelectric Effect experiment beamline

In this section, I briefly describe the principles of the Advanced Photoelectric Effect (APE) beamline at synchrotron Elettra [9, 136], devoted to spectroscopy and magnetometry of materials whose fundamental properties are determined by strong electron and spin correlations. The beamline hosts two independent branches: 1) The low-energy (LE) branch performing high resolution ARPES and Fermi surface mapping with near- and far-UV photon energies between 10 and 100 eV. 2) The high-energy (HE) end station mainly dedicated to the study of low dimensional magnetic systems using photon energies from 140 to 1500 eV. The HE branch is employed for soft X-rays spectroscopy techniques such as X-ray absorption (XAS), X-ray magnetic dichroism (XMCD, XMLD) and X-ray photoelectron spectroscopy (XPS). Figure 3.7 (a) represents the APE beamline scheme.

Two variable-polarization undulators in zig-zag configuration generate two independent photon beams at 2 mrad angle in the horizontal plane, figure 3.7 (b). One insertion device emits in the UV energy range; the second one emits in the soft X-ray range. The HE and LE beams travel in a single UHV tube until reaching the spherical mirror that deviates the beams to their corresponding branch. In each line, the desired photon energy and polarization is obtained by appropriately adjusting the vertical gap and longitudinal phase between the top and bottom magnetic arrays of the monochromators.

All experiments presented in this manuscript were performed on the APE-LE beamline. In this beamline three plane gratings 700, 1200, and 1600 l/mm cover the energy ranges of 9 - 25, 25 - 40, and 40 - 100 eV, respectively. The beam is focused to  $\sim 50 \times 100 \mu\text{m}^2$  by a spherical and a toroidal mirror. All the optic elements of the LE branch are made of pure silicon with no coating. Therefore, the intensity of the beam has a sharp decrease at Si 2p edge around 90 eV photon energy. The overall energy resolution is around 10 meV, while the angular resolution is  $< 0.2^\circ$ . The VG-Scienta DA30 electron energy analyzer situated at the beamline end station operates in deflection mode in the direction perpendicular to the analyzer slit and photoelectrons are collected over  $30^\circ$  angular range for a given sample alignment. This development allows detailed k-space mapping of the full Brillouin zone at fixed sample/beam geometry while providing higher time

efficiency in data acquisition. The fix geometry of the experiment is specifically beneficial for studying small samples and surface domains with almost constant matrix elements.

### 3.4 Pump-probe techniques

When femtosecond pump pulses deliver energy to a system, the excited electrons will recover their equilibrium quantum state by dissipating their excess of energy via interaction with other electrons at a femtosecond timescale, followed by subsequent collisions with the incoherent and coherent lattice vibrations, which can last for few hundreds of femtoseconds up to several picoseconds, c.f. section 2.2.1.

Experimentally, an out-of-equilibrium population of electrons is created by femtosecond optical pulses that transiently decouple the electrons from the lattice. By appropriately selecting the timescale at which one probes the photoexcited system, one can follow the time-resolved dynamics of separate degrees of freedom ensued from the electronic excitation. The probe pulse comes at a controllable delay after the pump and builds up a chronological series of images describing the photoinduced events, figure 3.8. The temporal resolution is defined by the pump and probe pulse width, as well as by the sampling accuracy determined by the precision of the delay line step.

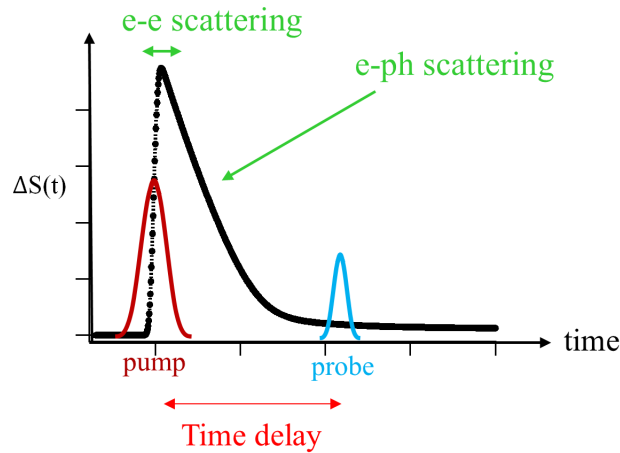


Figure 3.8: Schematic of a time-resolved experiment. The pump pulse arrives at time zero and initiates a dynamics in the system. The probe pulse comes after a controllable delay and maps out the photoinduced changes of the signal,  $\Delta S(t)$ .

In addition to the time scale, the wavelength of the probe should be correctly chosen according to the degree of freedom one wish to study. An UV pulse, for instance, monitors the temporal evolution of the electrons, while X-rays mainly reveal the lattice dynamics. In the course of my PhD, I worked with different pump-probe techniques. The techniques that I applied comprise time-resolved ARPES, time-resolved X-ray diffraction, and time-resolved optical spectroscopy.

It should be mentioned that an important parameter in pump-probe experiments is the repetition rate of the laser pulses, which should be balanced between the data acquisition time and the unfavorable residual heat delivered to the system.

### 3.4.1 Time-resolved ARPES

#### 3.4.1.1 Laser-based photoemission spectroscopy

While synchrotron light sources are typically employed for ARPES with tunable photon energy ranging from near-UV to soft X-rays, the very narrow bandwidths (often less than 1 meV [85]) of laser pulses make them suitable for photoemission spectroscopy with very high energy resolution. This provides some complementary and more detailed information on the electronic band structure.

On the other hand, ultrashort pulses constitute the crucial part of pump-probe techniques as will be described in the next subsection. The short wavelength of probe pulse required for the photoemission process can be obtained by different frequency up-conversion techniques. The most common one is the frequency doubling or frequency mixing method by expanding the frequency of the pump laser to some higher orders. The maximum photon energy obtained by non-linear optics is 6.994 eV [133] and as follows, only  $0.5 \text{ \AA}^{-1}$  of the reciprocal space can be probed in the normal photoemission angle. The advantages of working at low photon energies are essentially a higher sensitivity to bulk states [90, 153] and a higher resolution in  $k_{\parallel}$ , as it has been mentioned in subsection 3.2.5. In spite of that, probing the entire Brillouin zone with laser-based setups, demands complex sample/beam geometry which is often unreachable for most manipulators.

It is worth mentioning that in recent years, a growing number of groups have been investigating on how to perform photoemission spectroscopy with femtosecond or sub-femtosecond pulses using high harmonic generation (HHG) from irradiated noble gases [32, 166]. This technique requires kHz infrared (IR) pulsed lasers with mJ energies in order to reach intensity of about  $10^{14} \text{ W/cm}^2$  necessary for high-energy emission. Under this condition, the non-linear interaction between the IR laser and the gas ionizes atoms, with their Coulomb barrier suppressed below the ground state energy level during the interaction [161] and converts IR radiation into higher order radiation (above fifth harmonic), ranging from extreme UV to soft X-rays. It has been recently demonstrated that the HHG can also be derived from a UV laser [147]. In this way, the generated femtosecond pulse is in the range of 10 - 60 eV and gives access to the entire Brillouin zone. In spite of that, the relatively low photon flux (typically  $< 10^{10}$  photons/s) increases the time required for data acquisition and makes an ARPES experiment based on HHG a lengthy or often impractical task. Research on photoemission with HHG has been very active in the past few years.

#### 3.4.1.2 Time-resolved ARPES

In laser-based photoemission spectroscopy, the femtosecond duration of laser pulses makes them a unique and unparalleled tool that can be used as an ultrafast energy pump source to create excited electrons as well as a probe source to study the photoinduced changes in the electronic structure in time domain. This property greatly overtakes the use of conventional synchrotrons or radiation sources such as gas-discharge lamps for pump-probe techniques as they only offer pulsed beams with duration of about 100 ps or a continuous radiation, respectively.

Time-resolved ARPES (tr-ARPES), as the names indicates, is the study of the electronic structure in a time- and  $k$ -resolved fashion. A femtosecond pulse, mainly an IR pulse of wavelength 800 nm (photon energy 1.55 eV), prompts electrons close to the Fermi level to some unoccupied states. In the meantime, a UV pulse maps and follows the band structure after the arrival of the pump pulse. A tr-ARPES experiment demands several requirements: the probe pulse energy should be larger than the material work function and its photon flux should be high enough

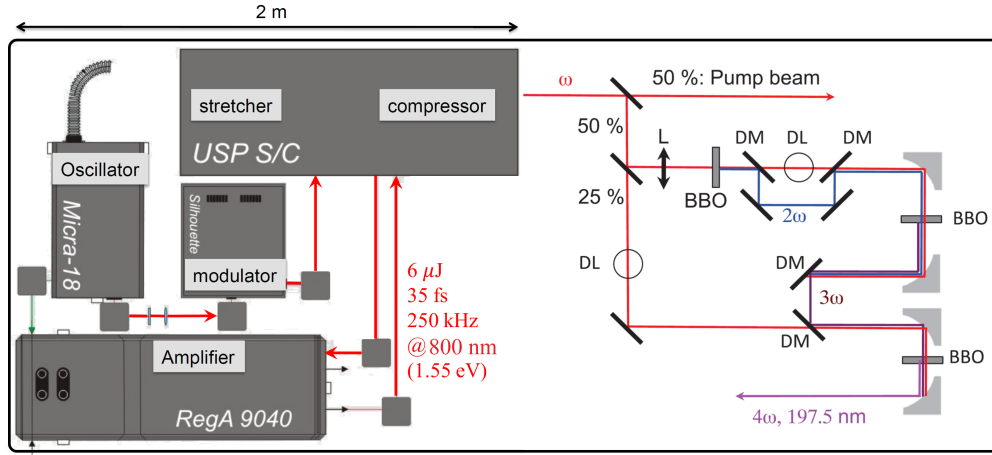


Figure 3.9: The fourth harmonic generation by frequency mixing.  $L$ : lens with  $f=20\text{cm}$ ,  $DM$ : dichroic mirror;  $DL$ : delay line. The off axis parabolas have  $f=5\text{-}10\text{ cm}$  focal length depending on their location. The frequency mixing setup uses 50% of the laser energy that is  $3\ \mu\text{J}$ .

( $\sim 10^{12}$  photon/s) for significant statistics in an appropriate time interval. However, the considerable high density of photoelectrons at the surface of the sample produced by femtosecond pulses can result in a large space charge field [65, 139], which broadens and distorts the electronic bands.

The combination of photon flux and repetition rate of pulses should be carefully selected in order to avoid the space charge effect while maintaining satisfactory statistics.

During my PhD, I performed a series of laser-based ARPES and tr-ARPES experiments on  $\text{BaNiS}_2$  with the femtoARPES setup which is explained in the following.

### 3.4.1.3 FemtoARPES setup

The FemtoARPES is a tr-ARPES setup situated in synchrotron SOLEIL. It is a collaboration among the LSI (École Polytechnique), the LPS, (Université Paris-sud), and Synchrotron SOLEIL. Detailed information on the setup can be found in [42].

A commercial Ti:Sapphire laser system (RegA Coherent) delivers  $6\ \mu\text{J}$  per pulse with 35 fs duration at full width half maximum (FWHM) at 250 kHz repetition rate. The laser wavelength can be tuned between 780 nm and 820 nm. A beam splitter selects 50% of the energy which is used for the fourth harmonic generation while the rest remains intact in energy and is sent to a separate optical path to be further used as the IR pump pulse. The wavelength of 800 nm (1.55 eV) is chosen as the fundamental beam for fourth harmonic generation, leading to wavelengths as short as 197 nm (6.28 eV). The schematics of our fourth harmonic generation setups is shown in figure 3.9.

Femtosecond 6.28 eV laser probe pulses are obtained by cascade frequency mixing in non-linear  $\beta\text{-BaB}_2\text{O}_4$  (BBO) crystals. First the fundamental pulse is doubled by second harmonic generation on 1-mm thick BBO crystal, then the third harmonic is created by mixing the second harmonic plus the fundamental through a  $50\ \mu\text{m}$  crystal. Finally, the fourth harmonic at 6.28 eV with bandwidth of 1.34 nm FWHM (corresponding to a 55 fs time resolution) is produced by the third harmonic and the fundamental at a  $20\ \mu\text{m}$  BBO crystal. The overall temporal and energy resolution of the experiment considering the pump and the probe pulse is 70 fs and 60 meV, respectively. The spot size of the 1.55 eV pump pulse is about  $200 \times 200\ \mu\text{m}^2$  and the 6.28 eV pulse is about  $60 \times 60\ \mu\text{m}^2$ . The larger spot size of the pump pulse ensures that the probed

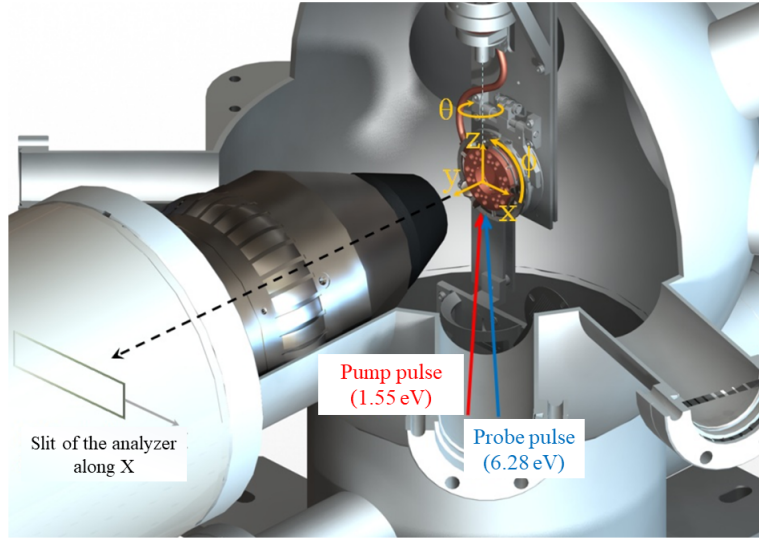


Figure 3.10: Experimental chamber of the FemtoARPES setup.

area of the sample is homogeneously excited. The probe and pump beams propagate in a nearly collinear geometry with only  $1^\circ$  between them, which is low enough for maintaining a high temporal resolution.

A high UV photon flux as much as  $10^{14}$  photon/s can be attained that is comparable to synchrotron light flux. The polarization of the light pulses can also be tuned horizontally or vertically. The experimental chamber of the setup is represented in figure 3.10. The beam enters the UHV chamber through a  $\text{MgF}_2$  window. A cryostat is connected to the manipulator so that the sample can be cooled down to 35 K using liquid helium and 130 K using liquid nitrogen. The sample can also be heated to 1100 K. Therefore, this setup allows us to perform experiments at any sample temperature ranging from 35 to 1100 K.

Although the portion of the Brillouin zone accessible with 6.28 eV photon energy is limited (about 10%), it is still sufficient to study the low-energy band structure close to the Fermi level for selective areas of the momentum space. The photoemitted electrons are analyzed by a commercial hemispherical electron analyzer (Phoibos 150, Specs) providing angular resolution down to  $0.05^\circ$ .

I performed a series of standard laser-based-ARPES and tr-ARPES experiments on the femtoARPES setup. As long as one performs ARPES experiments without concern about the time resolution, the pulse duration of the UV pulses and consequently the energy resolution can be tuned according to the user's expectations. To do so, the BBO crystal generating the fourth harmonic can be replaced by a thicker 1 mm one, reducing the energy resolution down to about 20 meV.

## 3.4.2 Time-resolved X-ray diffraction

### 3.4.2.1 X-ray diffraction

X-ray diffraction (XRD) is based on studying the scattered intensity of an X-ray beam hitting a sample as a function of the incident and scattered angles and photon energy. The diffracted beam reveals information about the crystal structure, chemical composition, and physical properties of bulk crystals or thin films. The Bragg's law describes the condition that the angle between the incident and scattered beam should satisfy so that a constructive interference from a given

family of crystallographic planes occurs:

$$2d_{h,k,l} \sin \theta = n\lambda \quad (3.11)$$

where  $\theta$  is the angle between the X-rays and the crystallographic planes,  $\lambda$  is the wavelength of the X-rays, and  $d_{h,k,l}$  is the interplanar distance between the crystallographic planes described by Miller indices  $[h,k,l]$  and is determined by reciprocal space vector  $\mathbf{a}^*$ ,  $\mathbf{b}^*$ , and  $\mathbf{c}^*$ :

$$d_{h,k,l} = \frac{2\pi}{|\mathbf{h}\mathbf{a}^* + \mathbf{k}\mathbf{b}^* + \mathbf{l}\mathbf{c}^*|} \quad (3.12)$$

The Laue equation reformulates the Bragg's law in terms of the momentum transfer. It states that the momentum transfer from a crystal to X-rays (scattering vector) should belong to the reciprocal space and represents the normal to the  $(h,k,l)$  plane, i.e.  $\mathbf{k}_f - \mathbf{k}_i = \mathbf{Q}_{h,k,l}$ . For an elastic scattering  $|\mathbf{k}_i| = |\mathbf{k}_f|$ . Therefore, the requirement for constructive interference in a diffraction experiment means that in the reciprocal space (or equivalently in the momentum space), the vectorial difference between the final and initial X-ray wavevector must be equal to a vector of the reciprocal space of the crystal.

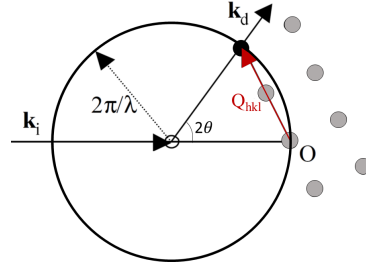


Figure 3.11: Ewald's sphere. The center of the reciprocal space is shown with O.

A geometric interpretation of the diffraction conditions was proposed by P. Ewald: Let us consider a given incident wavevector  $\mathbf{k}_i$ . For simplicity, we consider that the wavevectors space has the same orientation as the reciprocal lattice of the sample. The condition  $|\mathbf{k}_i| = |\mathbf{k}_f|$  implies that, if we take the same origin for the incident and outgoing X-ray wavevectors, the ensemble of all possible outgoing wavevectors form a sphere, obtained just by rotation of  $\mathbf{k}_f$  in the whole solid angle. This sphere is called Ewald's sphere. Now, we notice that the Laue condition corresponds simply to the points of the reciprocal lattice  $(h, k, l)$  that fall on the surface of the sphere, as it can be seen in figure 3.11. Therefore, only these points can generate a constructive interference and give rise to a diffracted beam. Each one of these points correspond to a diffraction peak from a family of crystallographic planes  $(h, k, l)$ . The strength of this approach is that we convert the problem of knowing which diffraction peaks are accessible, into a simple geometrical problem.

Typically, X-ray crystallography consists in determining the average atomic positions by measuring the position and the intensity of all Bragg peaks at different scattering vectors. The intensity of an X-ray diffraction (XRD) peak with the scattering vector  $\mathbf{Q}_{h,k,l}$  is related to the atomic structure of the unit cell via the structure factor:

$$F(Q) = \sum f_j e^{-i\mathbf{Q}_{h,k,l} \cdot \mathbf{r}_j} e^{-W_j} \quad (3.13)$$

The index  $j$  runs over all basis atoms,  $f_j$  is the atom scattering form factor which is related to the local density of electrons,  $\mathbf{r}_j$  is the average position of a basis atom  $j$  inside the unit cell, and the Debye-Waller factor  $e^{-W_j}$  represents the attenuation of the peak due to deviation of an atom  $j$  in the crystal lattice from its average position. Crystallography tables, for instance Bilbao crystallographic server, give the atomic position (Wyckoff positions) for different space groups.

Quantitative analysis of the intensity can be done by considering the kinematic theory of diffraction, which basically assumes that the X-ray beam undergoes a single scattering and in this

way the scattering potential of the crystal lattice can be treated as a perturbation and eventually the scattered X-ray intensity can be written as:  $I \propto |F(Q)|^2$ . By considering an isotropic atomic position variance  $\langle u^2 \rangle$ , the Debye-Waller factor can be simplified to  $W_j = \frac{q^2 \langle u^2 \rangle}{6}$  [79], where  $q = |\mathbf{Q}_{h,k,l}|$ . In the thermal equilibrium,  $\sqrt{\langle u^2 \rangle}$  is related to the temperature of the system by the equipartition theorem and is usually about 0.05 to 0.1 Å.

By applying the above-mentioned formulas to the intensity of the Bragg peaks, the full reconstruction of a crystal unit cell is finally achieved. In the following, I explain the ultrafast XRD in a pump-probe configuration

### 3.4.2.2 Time-resolved X-ray diffraction

After photoexcitation by the pump pulse, the out-of-equilibrium energetic electron population retrieves its equilibrium quantum state by evacuating the excessive energy by coupling first to the electrons and then with the lattice vibrations. However, in the meantime the interatomic forces are modified due to the excitation of a large fraction (10% or more) of the valence electrons to the conduction band [170]. This can induce changes in the lattice that in turn might collaborate or compete with other degrees of freedom in the dynamics of the system [137, 144]. A comprehensive study of the lattice dynamics demands diffraction-based techniques as well as a femtosecond time resolution so that any photoinduced changes provoked by the ultrafast excitation of electrons can be precisely captured [122, 163]. Time-resolved X-ray diffraction (tr-XRD) is the most direct technique to study lattice dynamics by measuring the relative changes that occur in the Bragg peaks upon photoexcitation [26, 74, 79, 96, 97]. In a tr-XRD experiment, any change of the lattice parameters results in a shift in the Bragg peaks angles. In addition, a change of the intensity is either due to the Debye-Waller factor or due to a change of the structure factor while the symmetry of the crystal is maintained. Another particular example is a structural phase transition changing the crystal symmetry that results in the appearance/disappearance of some Bragg peaks [29].

In tr-XRD experiments, the pump pulse is usually a femtosecond laser pulses centered at 1.55 eV. One should carefully match the penetration lengths of the IR laser and X-rays since X-rays can probe the bulk while IR pulses create excitations close to the surface of the sample. By shining the sample with nearly grazing angle X-rays and normal incidence laser pulses, and adjusting the corresponding beam spot sizes, one can make sure that the signal comes from a homogeneously excited region. As easy as this solution might seem to be, it is hard to be applied experimentally. First, in order to detect a Bragg peak in grazing incidence, the angle between the surface direction and the observed peak has to be larger than the angle  $\theta$  from the Bragg's law. Second, the X-ray spot size should be sufficiently small so that even in the grazing incidence it still remains smaller than the pump pulse. Because of the geometrical projection, the size of the X-ray spot also influences the temporal resolution, which deteriorates as spot size increases.

X-ray probe pulses can either be the synchrotron pulsed beam or X-ray free electron laser beam providing a picosecond and femtosecond time resolution, respectively. The advantages and beam properties of each facility are described in the following paragraphs.

Our team performed a series of tr-XRD on pure and Cr-doped  $V_2O_3$  samples at the Linac Coherent Light Source at Stanford linear accelerator. In parallel, I could perform some complementary time-resolved measurements at Synchrotron SOLEIL.

### 3.4.2.3 X-ray free electron laser

Despite all advantages of 3<sup>rd</sup> generation synchrotron facilities, as it has been mentioned in section 3.3, they encounter limitations as long as very intense sub-picosecond pulses are desired

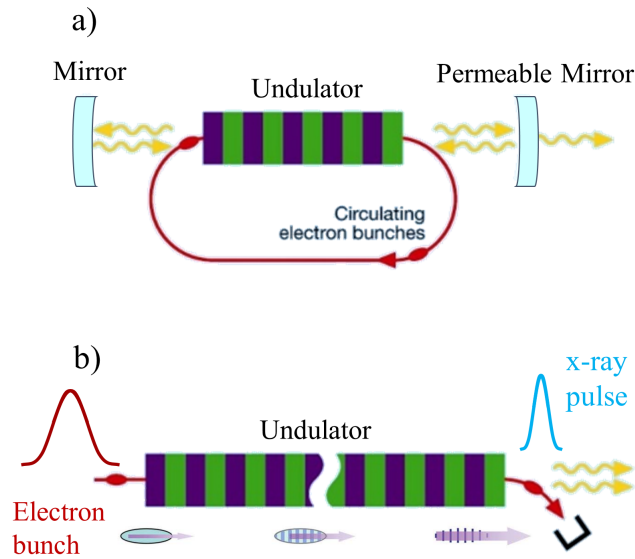


Figure 3.12: (a) Low-gain FEL. (b) SASE FEL. The interaction of light and electrons orders the electrons with a periodicity equal to the X-ray radiation wavelength.

for specific time-resolved experiments to study the dynamics at atomic and molecular scale [46]. The picoseconds-long X-ray pulses produce blurred images of atoms and molecules in motion. X-ray free electron lasers (XFEL) that are referred to as 4<sup>th</sup> generation light sources, open the horizon to this ultra-small and ultrafast world. A detailed description of the free electron lasers can be found in [41, 70, 110, 141, 142] as well as in many other publications and a growing number of the relevant research.

The main components of a free electron laser (FEL) are an accelerator providing a bunched relativistic electron beam and an undulator magnet. The physics of FEL is based on the interesting phenomenon of self-organization of an electron bunch in a relativistic beam, known as the free-electron laser collective instability [140].

The FEL ultrashort and extremely coherent radiation is produced in the same manner as a laser however, the active laser medium and the energy pump are replaced by relativistic free electron beam in the vacuum itself. Therefore, in contrast to lasers, no atomic or molecular state is involved. The pump source is the large kinetic energy of the electrons and stimulated emission occurs by the energy transfer from higher to lower kinetic energies under the action of an already existing nearly monochromatic radiation field produced by the electrons themselves in the undulator. The energy exchange depends on the undulator properties as well as the density and the distance between the electrons inside the bunch. The interaction of light and electrons eventually orders an electron beam with a random electron position distribution to a cluster with regular periodicity equal to the radiation wavelength, i.e.  $\sim 1 \text{ \AA}$ . The electrons are therefore closer to each other within a wavelength, their electromagnetic fields superimpose in phase, and the total radiation field has a large amplitude. Just like an optical laser, a cavity then lets the electron do many trajectory inside the cavity and this continuous process reinforces the electron to bunch even in a more effective way and results in the intensity to scale quadratically with the number of electrons. This is called a low-gained FEL, figure 3.12 (a).

A free electron laser producing the extreme-UV and X-ray regime is called an XFEL. As most optics are highly transparent to X-rays, the cavity should be replaced by a more efficient solution; a high laser gain has to be achieved in a single passage. Therefore, the electron path

length should be extended by a multitude of undulators on the way. The principle of Self-Amplified Spontaneous Emission (SASE) allows the production of intense and coherent light at sub-nanometer wavelengths, figure 3.12 (b). The key is that the collective instability is now triggered by an external electromagnetic field. For instance, one can use the spontaneous undulator radiation in the first section of a long undulator magnet as seed radiation in the main part of the undulator. This self-amplification of spontaneous emission process results in exponential growth of the intensity along the undulator. The exponential growth saturates when all the electrons are well ordered inside a bunch.

As the emission of spontaneous undulator radiation is a stochastic process, the SASE radiation has the properties of chaotic light [11]. It suffers from shot-to-shot fluctuations in energy, duration, spatial profile, temporal profile and intensity. The origin of these fluctuations is that the section in which the spontaneous radiation is produced may comprise typically hundreds of undulator periods corresponding to a bandwidth of  $\sim 1\%$ . Moreover, the longitudinal position at which an electron emits its radiation will vary from particle to particle. The radiation that is emitted first undergo a high exponential amplification, while radiation starting at a later position will be lower on the gain curve.

The XFEL beam fluctuations can significantly complicate the pump-probe experiments. They give rise to a time jitter between the arrival time of X-rays and pump laser pulses as well as instabilities in the beam position. These effects should be carefully corrected in post-data analysis in order to have physically meaningful results.

#### 3.4.2.4 XPP beamline at Linac Coherent Light Source

I now explain the X-ray pump-probe (XPP) beamline at the Linac Coherent Light Source (LCLS) in Stanford, figure 3.13. A detailed description of the LCLS and the beamline can be found in [40] and [28], respectively. The X-ray pump-probe instrument has achieved femtosecond time-resolution by the X-ray free-electron laser source. To maximize the range of phenomena that can be studied, the pump and probe energy and temporal resolution are tuned according to the experimental case. Optical fs laser pulses at 800 nm, 400 nm, or 266 nm create a non-equilibrium state of matter and fs X-ray pulses study atomic-scale structural dynamics generated by ultrafast excitations. X-ray pulses covers a photon energy range of 4 to 24 keV.

The repetition rate of pump-probe experiments at the XPP beamline can be tuned from 120 Hz to 1 Hz. The minimum X-ray spot size is about  $2 \mu\text{m}$  (as a result of the finite SASE bandwidth and optics imperfections). A custom-built diffractometer provides various degrees of freedom together and the detector positioning is provided by a robotic arm that can be located up to about 1.5 m from the sample.

As mentioned previously, the SASE beam has some intrinsic fluctuations. The XPP beamline is equipped with various diagnostic tools in order to correctly record all beam parameters of the X-ray and optical laser pulses for post data analysis. The readout electronics require a large single shot dynamic range because of the pulsed nature of the FEL. Several intensity position monitors (IPM) are installed at various locations along the instrument for pulse-to-pulse intensity normalization [66]. The IPM has four photodiodes, arranged in quadrants. It measures the x and y coordinates of the beam from the relative intensity of the four diodes while the sum measures the intensity of each single shot.

A very important parameter while doing time-resolved experiments with FEL's, is the time jitter that comes from shot-to-shot variations in the electron bunch arrival time. The time jitter is a result of fluctuations in the electron bunch energy and consequently their flight time through the undulators [160]. This challenges an accurate synchronization between X-rays and optical

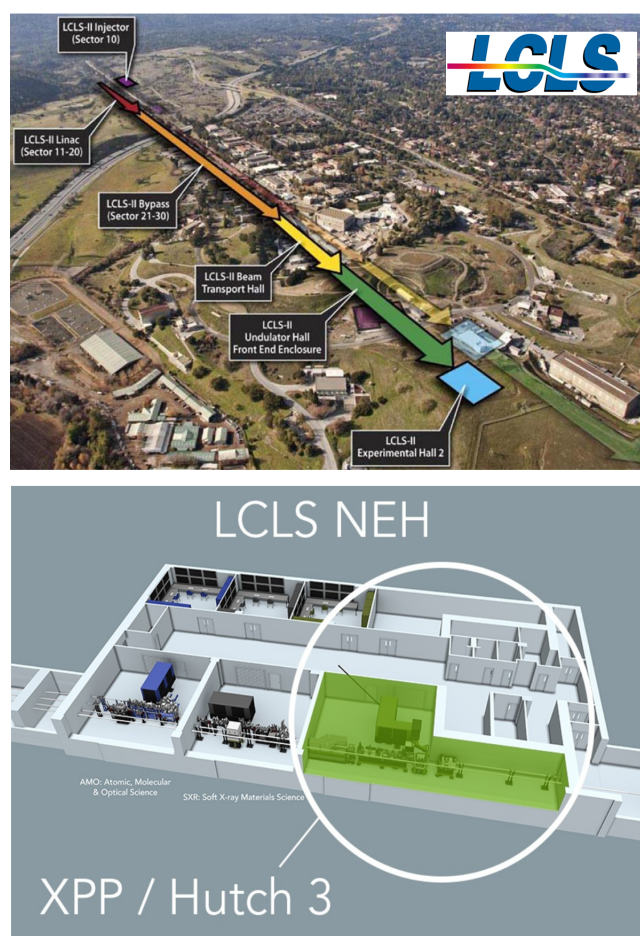


Figure 3.13: LCLS XFEL and XPP beamline.

laser pulses and in turn restricts the time resolution. At the LCLS, the maximum arrival time jitter is  $\pm 100$  fs. At the XPP beamline the timing tool monitors measure the relative arrival time between the pump and probe pulses and their corrections lead to a sub-10 fs r.m.s. resolution in the hard X-ray regime [61].

The images are acquired by the 140 kpixel CSPAD-140k detector [10] with a readout speed matched to the LCLS repetition rate (120 Hz). The temperature of the sample can be controlled by a nitrogen cryoblower.

### 3.4.2.5 Cristal beamline at synchrotron SOLEIL

I also performed some complementary tr-XRD experiments on the Cristal beamline at synchrotron SOLEIL. This beamline allows to perform tr-XRD with picosecond time resolution, which is enough for many types of investigations and more generally to gain a general insight on the dynamics of the system at ps time-resolution.

Depending on the synchrotron function mode, different time resolution and photon flux are obtained. For instance in the single bunch filling mode, one pure electron pocket circles around the storage ring at a bunch current of 20 mA and the time resolution is about 70 ps. On the other hand, the hybrid multibunch mode has 301 bunches of electrons circulating in the storage ring, 300 fill 3/4 of the ring and 1 is isolated in the middle of the remaining 1/4. The time resolution of this mode is 4.7 ps that can be reduced to 1 ps by the low-alpha hybrid mode. In this mode, the momentum compaction factor is modified to smaller values and the spatial lengths of the electron bunches are decreased. This gives rise to shorter emission pulses in time and therefore a higher time resolution.

In the Cristal beamline, the pump source is an optical 1.55 eV laser operating at 1 kHz. In the low-alpha hybrid mode, we block the multibunch X-rays and take advantage of the X-rays from the single electron bunch. We also tune the frequency of the data acquisition to 2 kHz. Therefore, one X-ray pulse is used for the reference image while the other studies the structural dynamics after a given delay from the laser pump pulse. Figure 3.14 presents different synchrotron filling modes together with the time structure of each, and the cristal beamline.

The zero delay is done roughly with a fast photodiode, and the spatial overlap is done using a fluorescent paper. A 6-circle diffractometer and an XPAD detector with two degrees of freedom in angle, allow precisely identifying the  $\theta$  of a Bragg peak. The XPAD detector can be gated with the frequency of the single bunch pulse so that the irrelevant signal from the multibunch be blocked.

The sample temperature is controlled using a nitrogen cryoblower.

## 3.4.3 Time-resolved optical spectroscopy

### 3.4.3.1 Motivation

Before explaining the interest of pump-probe optical reflectivity measurements, it is important to recall few aspects of optical properties in the equilibrium state [187] and how they are eventually related to the electronic band structure of a material. I devote few lines to remind some useful relations between the optical reflectivity and other relevant parameters.

The optical conductivity is a complex value, i.e.  $\sigma(\omega) = \sigma_1(\omega) + i\sigma_2(\omega)$ , and is not a straightforward experimental observable. It is principally deduced from the dielectric function  $\sigma(\omega) = i\frac{\omega}{4\pi}(\epsilon(\omega) - 1)$ . Experimentally, the dielectric function is in turn derived from the reflectivity, as at normal incidence the following equations hold:

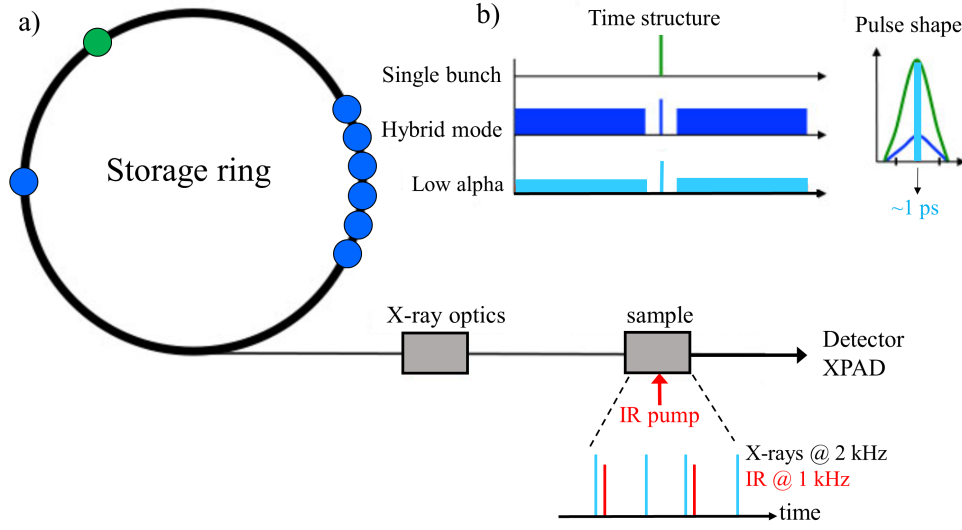


Figure 3.14: Diagram of the synchrotron. (a) Storage ring and the Cristal beamline. The X-rays arrive at 2 kHz (in the low-alpha mode) and the system is pumped at 1 kHz. (b) Time structure of different synchrotron filling modes. The low-alpha mode has the minimum time resolution.

$$R(\omega) = \left| \frac{1 - \sqrt{\epsilon(\omega)}}{1 + \sqrt{\epsilon(\omega)}} \right|^2 \quad (3.14)$$

However, what is measured experimentally and we call it reflectivity is the amplitude of the reflectivity coefficient  $r(\omega) \exp[i\theta(\omega)]$ —that is,  $R(\omega) = r^2(\omega)$ , while no information on the phase  $\theta(\omega)$  is obtained directly. All the parameters defined so far are complex values and causality implies that the imaginary and real parts are related to each other by the Kramers-Kronig integrals. Once the reflectivity  $R(\omega)$  is correctly found, other parameters are extracted subsequently. The key point is to measure  $R(\omega)$  over a wide range of frequency in order to accurately solve the Kramers-Kronig integrals:

$$\theta(\omega) = \frac{-2}{\pi} \int_0^\infty \frac{\ln r(\omega') - \ln r(\omega)}{\omega'^2 - \omega^2} d\omega' \quad (3.15a)$$

$$\ln r(\omega) = \frac{2}{\pi} \int_0^\infty \frac{\omega' \theta(\omega') - \omega \theta(\omega)}{\omega'^2 - \omega^2} d\omega' \quad (3.15b)$$

Starting merely from measuring the amplitude of reflectivity coefficient, one is eventually able to deduce the real and imaginary part of the dielectric function:

$$\epsilon_1(\omega) = \frac{(1 - r^2(\omega))^2 - 4r^2(\omega) \sin^2 \theta(\omega)}{1 + r^2(\omega) - 2\sqrt{r^2(\omega) \cos^2 \theta(\omega)}} \quad (3.16a)$$

$$\epsilon_2(\omega) = \frac{4(1 - r^2(\omega))\sqrt{r^2(\omega) \sin^2 \theta(\omega)}}{1 + r^2(\omega) - 2\sqrt{r^2(\omega) \cos^2 \theta(\omega)}} \quad (3.16b)$$

Mathematical approach to derive the above-mentioned equations are found in [187].

These explanations clarify that corresponding to the structure in the reflectivity, there will be structure observed in the real and imaginary parts of the dielectric function. On the other hand, the equilibrium electronic band structure are identified by detailed features in the reflectivity

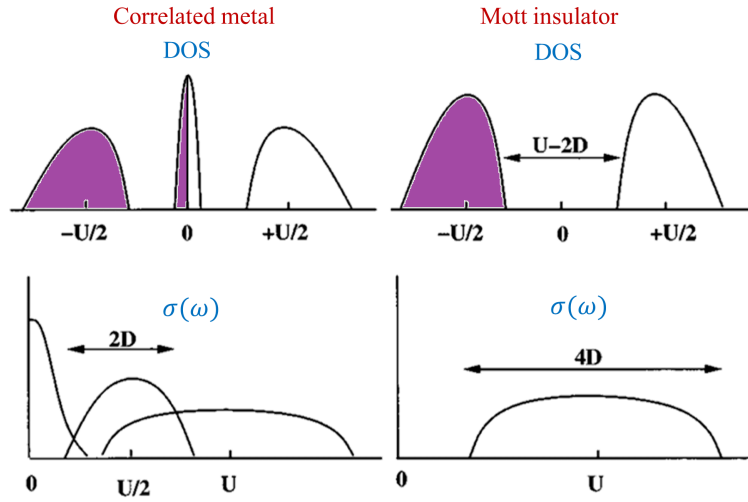


Figure 3.15: Top panel: schematic DOS for the half-filled Hubbard model for a metallic and an insulating state. Bottom panel: The optical conductivity spectra for the corresponding states.

data that result from interband and intraband transitions or near edge absorption. Therefore, the optical response of a material is intrinsically coupled to its density of states [154, 171] as schematically explained in figure 3.15. For instance, the optical conductivity of a Mott insulator presents a broad peak with the width of  $U - 2D$  centered at the frequency of  $U$ , where  $U$  is the on-site Coulomb repulsion and  $D$  is the half-filled width of the Hubbard bands. The single peak of the optical conductivity corresponds to the optical transitions from the lower to the upper Hubbard band. For the case of a correlated metal, the low-temperature optical conductivity is composed of three main parts: *i*) A narrow low-frequency peak that is due to transitions within the quasiparticle resonance and its width is proportional to the temperature. It is important to note that as the coherence of the quasiparticle is related to the temperature, this narrow peak is always present as long as the temperature is below a critical temperature at which the coherence is lost. *ii*) An incoherent feature of width  $2D$  at frequencies of order  $U/2$  due to transitions between the Hubbard bands and the coherent quasiparticle peak. *iii*) A broad feature around the frequency of  $U$  that emerges by transitions between the two Hubbard bands.

The interest of studying the optical response of a material can now be extended to the out-of-equilibrium domain. In fact, the photoexcitation induces an ultrafast redistribution of the electrons and therefore yields in a transient change in the optical properties of the systems such as reflectivity. The starting point for reconstructing the out-of-equilibrium band structure is to probe the system with a femtosecond pulse that contains a wide range of frequencies, such as white light. Alternatively, this can be achieved by manually changing the wavelength of the probe however, this is can be time-consuming and inaccurate due to some alignment issues.

The ultrafast dynamics of the optical response also unveils some aspects of paramount importance that are inaccessible via equilibrium techniques. For instance the coherent oscillations of phonons and electron-phonon coupling strength which is explained in the following paragraphs.

### 3.4.3.2 Coherent oscillations of optical phonons

After photoexcitation the energy distributions of the carriers evolve dynamically and this will modify the reflectivity of the sample. Generally, the photoinduced change of reflectivity is small and is the order of  $10^{-3}$  to  $10^{-6}$ . Moreover, photoexcitation stimulates in-phase oscillation of

phonons around their metastable position in the photoexcited region of the sample. The in-phase periodic motion of atoms, which can be due to acoustic or optical phonons, modifies the optical medium of a propagating electromagnetic wave in turn. In general, the optical response to an ultrafast light stimulus comprises an oscillatory decaying response. The oscillations are the real time manifestation of the atomic motion and the decay corresponds to the electron-phonon coupling strength. The optical phonon excitation by an ultrashort pulse can be explained within two theoretical frameworks: Impulsive Stimulated Raman Scattering (ISRS) [190] and Displacive Excitation of Coherent Phonon (DECP) [202]. In both theories, the problem is simplified by an analogy to a simple harmonic oscillator that is excited by an impulsive driving force,  $F(t)$ :

$$\ddot{Q} + 2\gamma\dot{Q} + \omega_0^2 Q = \frac{F(t)}{m} \quad (3.17)$$

where  $Q$  is the phonon normal coordinate,  $m$  is the reduced mass of the oscillator,  $\gamma$  and  $\omega_0$  are the vibrational damping constant and frequency of the excited phonon, respectively. In the ISRS, the underlying assumption is that the large bandwidth of a femtosecond laser pulse contains many frequencies so that the difference between some frequencies is resonant with a Raman active phonon mode of the medium. Such phonon mode can therefore be excited coherently if the pump pulse duration is shorter than the vibration period. This clarifies the terminology of the stimulated Raman scattering. On the other hand, this model also assumes that the polarizability of materials depends on the interatomic distance through the normal coordinates  $Q$ .

The driving force within this context is written as:

$$F(t) = \frac{1}{2} N \left( \frac{\delta\alpha}{\delta Q} \right)_0 \mathbf{E}\mathbf{E} \quad (3.18)$$

with  $N$  being the density of oscillators,  $\alpha$  the differential polarizability tensor, and  $\mathbf{E}$  the electric field. In this way, the solution of the equation of motion has a sinusoidal form, i.e. it presents a vibrational wave whose wavevector is in the direction of light propagation with an amplitude proportional to the laser intensity:

$$Q(z > 0, t > 0) = Q_0 e^{-\gamma(t - \frac{nz}{c})} \sin(\omega_0(t - \frac{nz}{c})) \quad (3.19)$$

where the phonon amplitude  $Q_0$  is proportional to the force  $F$ ,  $n$  is the real part of the refractive index,  $z$  is the direction of propagation of the beam and  $c$  is the speed of light in vacuum. This model implies that all phonon modes can be observed regardless of the laser power as long as the pulse is short enough to contain proper frequency differences. However, one can selectively observe a single mode by choosing appropriately the probe light polarization. Nonetheless, most of metals and semimetals only reveal Raman-active modes of  $A_1$  symmetry in pump-probe experiments, although they show modes of different symmetries in spontaneous and resonant Raman scattering. The ISRS theory cannot explain this phenomenon.

The DECP theory describes the detection of only modes of  $A_1$  symmetry. The theory is based on the fact that  $A_1$  displacement modes do not lower the symmetry of the crystal and thus, it is improbable to stimulate displacements of any symmetry other than  $A_1$  in an optical pump-probe experiment. One may rather expect to observe other modes upon electronic photoexcitation if the material is close to a structural phase transition with that specific symmetry in the ground state. In this model, the oscillations in the transient reflectivity result purely from a change in the  $A_1$  coordinate,  $Q(t)$ . The pump pulse instantaneously increases the electronic temperature by some  $\Delta T_e$  and populates the conduction band with a density of hot electrons,  $n(t)$ . The electron-phonon interaction will then also generate an increase of the lattice temperature by

some  $\Delta T_i$ . All these quantities will modify the reflectivity of the sample. We start by writing the changes in the reflectivity by its partial derivatives:

$$\frac{\Delta R(t)}{R} = \frac{1}{R} \left[ \left( \frac{\partial R}{\partial n} \right) n(t) + \left( \frac{\partial R}{\partial T_e} \right) \Delta T_e + \left( \frac{\partial R}{\partial T_l} \right) \Delta T_l + \left( \frac{\partial R}{\partial Q} \right) Q(t) \right] \quad (3.20)$$

The model postulates that  $Q_0(t)$ , the equilibrium coordinate of  $A_1$ , is linearly dependent on  $n(t)$  and a rate equation describes the dynamics of  $n(t)$  as:

$$\dot{n}(t) = \rho P(t) - \beta n(t) \quad (3.21)$$

$P(t)$  is the energy in the exciting pulse per unit area per unit time and  $\beta$  is the decay time constant because of electron-hole recombination. The constant  $\rho$  is given by:

$$\rho = f \frac{2n_{Im}}{\hbar c} (1 - R)$$

where  $f$  is the fraction of photoexcited electrons,  $n_{Im}$  is the imaginary part of the refractive index and  $R$  is the unperturbed reflectivity of the sample. The excited electrons incite a sudden change of the equilibrium nuclear coordinates that is accompanied by an oscillatory movement. The equation of motion is therefore re-written:

$$\ddot{Q}(t) = -\omega_0^2(Q(t) - Q_0(t)) - 2\gamma\dot{Q}(t) \quad (3.22)$$

with the driving force being replaced by  $\omega_0^2 Q(t)$ . The frequency of the  $A_1$  mode is supposed to be constant and not affected by electronic excitation. In the end, the quasi-equilibrium position of atoms is proved to be a decaying oscillating exponential:

$$Q(t) \propto \int_0^{\text{inf}} g(t - \tau) [e^{-\beta\tau} - e^{-\gamma\tau} (\cos(\Omega\tau) - \frac{\beta - \gamma}{\Omega} \sin(\Omega\tau))] d\tau \quad (3.23)$$

where  $g(t)$  is a normalized pulse shape function and  $\Omega = \sqrt{\omega_0^2 - \gamma^2}$ .

While in the ISRS theory the coherent oscillations were a consequence of the hypothesis of the model, the DECP theory already includes them in the initial supposition and reproduces the ultrafast optical response upon photoexcitation, c.f. equation 3.20. The ISRS theory has been successfully applied to describe the excitation of coherent phonon modes in transparent materials, whereas the DECP theory can better describe the coherent phonon excitation in absorbing materials.

### 3.4.3.3 Extracting the electron-phonon coupling constant

By the above-mentioned semi-phenomenological models, the fundamental aspects of transient changes in reflectivity are described in terms of coherent oscillation of phonons and their decay in time. I now explain how it is possible to deduce electron-phonon coupling constant and other relevant parameters to the electronic dynamics by means of time-resolved optical spectroscopy.

In pump-probe techniques, the pump-induced changes in the electronic and lattice temperatures affect the optical response of the material in time and this in turn depends on the electronic band structure of the material. In subsections 2.2.2 and 2.2.3, I described the two and three-temperature models that simulate the electrons and lattice temperatures after applying an ultrashort pump pulse.

In the context of the two-temperatures model, the induced change in the reflectivity depends linearly on  $\Delta T_e$  and  $\Delta T_l$  so that  $\frac{\Delta R(t)}{R} = c_1 \cdot \Delta T_e + c_2 \cdot \Delta T_l$  where  $T_e$  and  $T_l$  are given by equation 2.1.

By the three-temperature model the lattice was described more accurately in terms of hot phonons and cold phonons to which electrons are coupled by  $\lambda_1$  and  $\lambda_2$  constants, respectively. On the other hand, the hot phonons and cold phonons consist of a fraction  $f$  and  $1-f$  of the total phonons. In this way, the transient reflectivity is written as:

$$\frac{\Delta R}{R} = c_1 \cdot \Delta T_e + c_2 (f \Delta T_p + (1 - f) \Delta T_l) \quad (3.24)$$

The fitting procedure using this equation coupled to the three-temperatures model, allows one to find the experimental phonon frequency as well as the electron-phonon coupling constant(s).

In the following paragraphs, I explain two different techniques of pump-probe optical spectroscopy: single color reflectivity and supercontinuum reflectivity measurements. These two techniques are complementary and each provides advantages unique to its own.

#### 3.4.3.4 Pump and probe experiments with tunable wavelength

The main motivation for doing single color time-resolved optical spectroscopy is to extract mean energy of the optical phonons and the coupling constants. On the other hand, the tunability of the wavelength allows us to pump electrons to the region of interest in the band structure, for instance very close to the band gap of a Mott insulating or a superconducting state. The possibility of independently tuning the pump wavelength significantly extends the range of accessible excitations in matter. Similarly, an appropriate choice of the probe pulse makes it possible to only focus on the dynamics of a given part of the band structure.

The setup located in salle Argent at the Laboratoire d'Optique Appliquée (LOA) provides the possibility to continuously tune the wavelength of light by Optical Parametric Amplifier (OPA). The OPA is pumped by the fundamental harmonic of Ti:Sapphire laser at 800 nm and 0.5 mJ per pulse at the repetition rate of 1 kHz. The optical parametric amplification involves a non-linear process and principally produces two pulses called signal and idler whose energy can be tuned continuously and interchangeably. A detailed explanation of the OPA is given in section 6.3. The wavelength range obtained is 1.2 - 2.6  $\mu\text{m}$ . However, an extra difference frequency generation (DFG) modulator inside the cavity provides photons with energy equal to the difference energy between the signal and idler and makes it possible to obtain photon energies in the range of 2.6 - 20  $\mu\text{m}$ .

This setup gives us two possibilities for the pump-probe experiment according to the experimental needs. *i)* Before the entrance of the OPA we can divide the optical path of the 800 nm in two parts, so that we use one part as pump (probe) while the output of the OPA (either signal or DFG mid-infrared pulse) is used as probe (pump). *ii)* Another way is to use the signal and the DFG for the pump and probe interchangeably. During my PhD I worked principally on the  $\text{V}_2\text{O}_3$  samples with the first configuration which is schematically described in figure 3.16. The probe pulse is 800 nm and the pump pulse is the DFG mid-infrared (MIR) light. The MIR pulse allows us to pump very close to the Fermi level and to study the photoinduced effects.

The detection of the time-resolved  $\frac{\Delta R}{R}$  signal is based on a photodiode connected to a lock-in amplifier. This procedure requires the use of an optical chopper, in order to modify the repetition rate at which the sample is pumped with respect to the repetition rate at which it is probed. The most straightforward modulation for the pump is to set it to 50% of the laser repetition rate. The modulation of the pump is thus 500 Hz, while the probe pulse has a repetition rate of 1 kHz. The lock-In amplifier extracts only the signal that has a frequency equal to the one set by an external reference, which in our case is the repetition rate of the pump. In this fashion, we directly measure the changes in the reflectivity  $\Delta R$  due to the pump pulse. In order to calculate

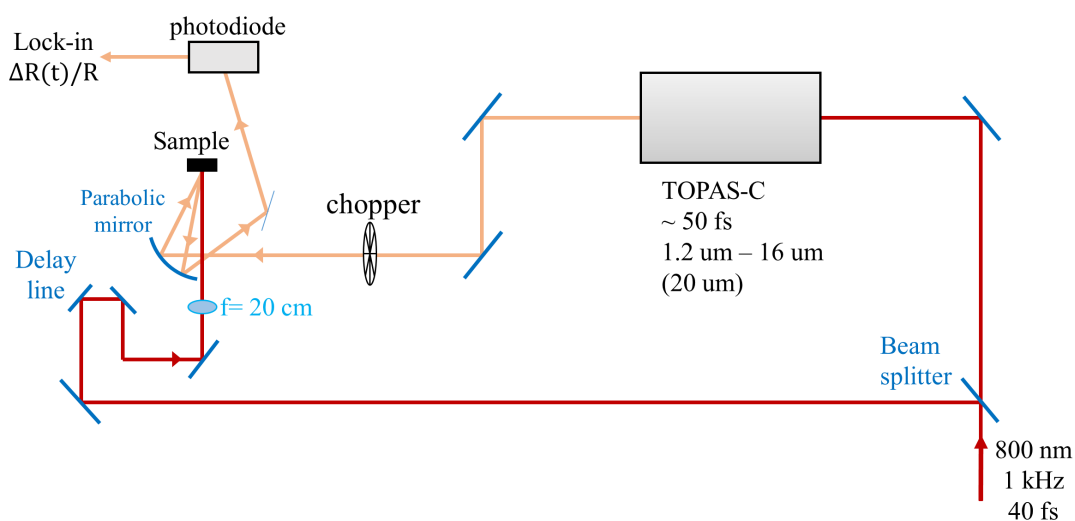


Figure 3.16: The time-resolved reflectivity setup at LOA with 800 nm as probe and MIR as pump.

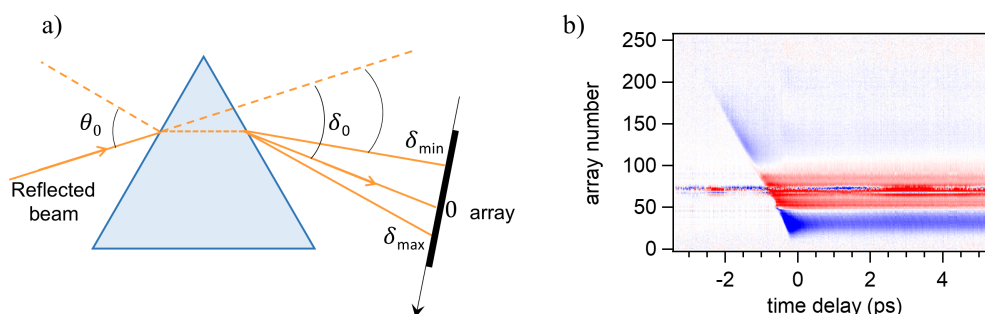


Figure 3.17: (a) Dispersion of the reflected white-light pulse through the prism onto the linear array sensor. The calibration procedure for the system consists in the assignment of a wavelength to every pixel of the array. (b) Time- and spectrum- resolved reflectivity.

the relative change with respect to the equilibrium reflectivity  $R$ , the reference value is measured at 1 kHz, which is typically of the order of few tens of  $mV$ . The experiment can be run with the pump-probe delay steps of 6 fs or longer. The acquisition time depends on the integration time set on the lock-in amplifier. Typically, a time-resolved spectrum for a range of 2 ps takes about 5 minutes. This acquisition system has a sensitivity of around  $10^{-4}$ , which is the state-of-the-art at 1 kHz repetition rate.

### 3.4.3.5 Time-resolved optical spectroscopy with broadband probe

As explained in paragraph 3.4.3.1, to get a comprehensive view on the photoinduced changes of the band structures, the optical response in a large enough frequency spectrum should be studied. For this purpose, the new generation of optical parametric amplifiers makes available the femtosecond pulses from far-UV to far-infrared regions.

The pump-probe reflectivity setup in the T-Rex beamline at the Fermi accelerator provides a broadband pulse (supercontinuum) to be served as probe and the conventional 800 nm as pump pulse. The laser is a Ti:Sapphire that delivers 800 nm pulses with 5  $\mu J$  per pulse and 80 fs bandwidth at a repetition rate of 250 kHz. The supercontinuum in the range of 460 nm to 1.57  $\mu m$  is acquired by pumping a sapphire plate. This wide energy spectrum is focalized on the

sample and the reflected white light beam is then dispersed by a prism towards a linear array of photodiode sensor, figure 3.17 (a). The wide energy spectrum of the probe makes it possible to simultaneously study the photoinduced changes of reflectivity for different wavelengths at a fixed delay. Therefore, by spanning the appropriate time delay range, a two-dimensional map is acquired. One axis contains 256 points that resolves the spectrum in energy and the other axis is the time delay. The intensity of each point then corresponds to the  $\frac{\Delta R(\lambda, t)}{R}$ . Figure 3.17 (b) shows an example of a 2D time- and spectral- resolved intensity map. The observed linear temporal structure as a function of wavelength is related to the linear and positive chirp that depends on the material through which the supercontinuum is generated, e.g. the sapphire crystal. In order to have a correct interpretation of data, one has to rectify these irrelevant features due to the probe pulse temporal profile.

The setup in T-Rex also has an open-cycle liquid Nitrogen/ liquid Helium cryostat and allows studying solids in a temperature range of 4 to 325 K.



# 4 | Electronic band structure of BaNiS<sub>2</sub> and BaCoS<sub>2</sub>

## 4.1 Introduction

In this chapter, I present the full electronic band structure of BaNiS<sub>2</sub> acquired by photon energy-, polarization-, and temperature- dependent ARPES measurements. My experimental results give evidence that BaNiS<sub>2</sub> is a correlated semimetal that has two-dimensional linearly dispersing bands. It is also demonstrated theoretically by our collaborators that these bands can be described with a Dirac Hamiltonian.

Next, I present the hitherto missing electronic band structure of the Mott-insulator BaCoS<sub>2</sub> in both its magnetic and non-magnetic phases. The band dispersion shows similarities and discrepancies with BaNiS<sub>2</sub>. Some DMFT calculations, performed for the first time by M. Casula, show good agreement with the ARPES data.

## 4.2 Correlated Dirac fermions in BaNiS<sub>2</sub>

### 4.2.1 Introduction

The topological classification of materials has been one of the major breakthroughs in condensed matter theory [4, 14, 62, 150]. It provides a robust framework to explain and predict remarkable material properties, such as the quantum spin Hall effect and low-energy relativistic behavior, by means of band structure analysis. A key ingredient of this framework is the band inversion, which can be associated with a parity twist of the Bloch states along a path through the inversion point in the reciprocal ( $\mathbf{k}$ -) space. Under crystal symmetries protection, the band inversion leads to an allowed crossing point. Whenever inversion and time reversal symmetries are also fulfilled, the allowed band crossing generates a Dirac cone [101, 182, 198, 199], c.f. subsection 1.4.3. Thus, Dirac states can emerge at the boundary between trivial (i.e. non-inverted) and topological insulators with inverted bandgaps [191].

However, in Dirac semimetals the cones with opposite chirality can annihilate each other unless additional crystal symmetries are provided as we have seen in paragraph 1.4.3.1. For instance, one possible way is when the robustness is assured by crystal symmetry when two bands with distinct 2D representations are inverted and cross each other [129, 182, 183]. In this case, the gapless nodes appear along the high-symmetry lines [27, 101]. In these systems, the SOC renders the Dirac fermions massive and opens the gap. However, in a 2D crystal the nonsymmorphic symmetry can stabilize a Dirac node that cannot be gapped by SOC. In paragraph 1.4.3.3 I showed the experimental evidence of two-dimensional Dirac cones in the square lattice of ZrSiS [162] that are located at the high symmetry X and R points and are protected by glide plane

symmetry regardless of the SOC strength. On the other hand, the discovery of the massive Dirac fermions on the 2D kagome lattice of ferromagnetic  $\text{Fe}_3\text{Sn}_2$  [196] widened the horizon of topological materials. The novelty of this material is that it presents Dirac cones that are subject to electronic correlation as well as exchange interaction, and are mainly composed of  $d$ -orbitals while the Dirac cone in most of the materials studied so far typically results from  $p$ -orbitals or hybridization of  $s$ - and  $p$ -orbitals. The search for novel materials that present *interaction-induced* Dirac fermions has attracted growing interest and has been very active recently.

Here, I present a systematic study of the electronic band structure of  $\text{BaNiS}_2$  by means of ARPES and first-principles calculations. I performed the ARPES experiments and the theory part is done by our collaborators from the University of Paris 6 and SISSA in Trieste, notably M. Casula, A. Amaricci, and M. Fabrizio.

Our results give evidence of the presence of Dirac cones made of nickel  $d$ -orbitals, where the band inversion mechanism is provided by a strong hybridization of the  $d$ -orbitals with the ligand  $p$ -orbitals of sulfur atoms, favored by the nonsymmorphic symmetry of the lattice. By using a minimal tight-binding model derived from first principles calculations, it is proved that this band inversion mechanism is very general. In the case of  $\text{BaNiS}_2$ , it gives rise to Dirac cones located at the Fermi level and widely extended in energy.

Owing to the quasi-bidimensional nature of  $\text{BaNiS}_2$ , the accidental band crossings assisted by the  $p-d$  hybridization generate Dirac line nodes that lie on the  $\sigma_d$  reflection planes and fully stretch along the  $k_z$  direction, therefore piercing the whole Brillouin zone. By symmetry, there are 4 replica of line nodes, one for each quadrant. This is quite different from other topological node-line semimetals known to date, i.e.  $\text{Cu}_3\text{NPd}$  [84],  $\text{Ca}_3\text{P}_2$  [188], and  $\text{ZrSiS}$  [162], where the nodal lines are circles developing around high-symmetry points, and not straight lines like in the present case.

A relevant feature of the Dirac fermions found in  $\text{BaNiS}_2$  is their strong  $d$ -orbital character. This can host strong correlation effects, a rare situation among the Dirac semimetals that have been experimentally established. As explained in section 1.5,  $\text{BaNiS}_2$  attracted interest in the different context of a Mott metal-to-insulator transition (MIT) observed in the substituted  $\text{BaCo}_{1-x}\text{Ni}_x\text{S}_2$  compound at a critical doping level of  $x_{cr} \sim 0.22$  [92, 112]. This MIT is of particular interest because it is exclusively driven by electron-electron correlation and the unconventional precursor phases make it similar to the case of High- $T_c$  superconductors like cuprates. We have also seen in subsection 1.5.3 that this system is also very similar to high- $T_c$  iron pnictide for multiple reasons except that  $\text{BaCo}_{1-x}\text{Ni}_x\text{S}_2$  does not show any superconductivity.

Therefore, the present finding of Dirac cones puts  $\text{BaNiS}_2$  in a novel perspective, for  $\text{BaNiS}_2$  appears to be a unique system which combines Dirac and Mott physics. For instance, one can envisage that the strength of the electron-electron correlations controlled by the Co/Ni substitution may be used to effectively tune the Dirac bands. This may give rise to novel electronic states not studied before. This opportunity is not possible in weakly correlated Dirac materials, where novel electronic phases such as superconductivity are achieved only by radically altering the crystal structure, e.g. by twisting bilayers of graphene [21, 22].

In order to investigate the electronic properties of  $\text{BaNiS}_2$  that arise from such peculiar gapless nodes, I first present in subsection 4.2.2 the results of a systematic ARPES study complemented by an *ab initio* electronic structure investigation, both giving evidence of the Dirac cones. Then, I show the role of the crystal space group, crystal field and orbital symmetries in the creation of the band inversion near the Fermi level in subsection 4.2.3. Third, I present the theoretical

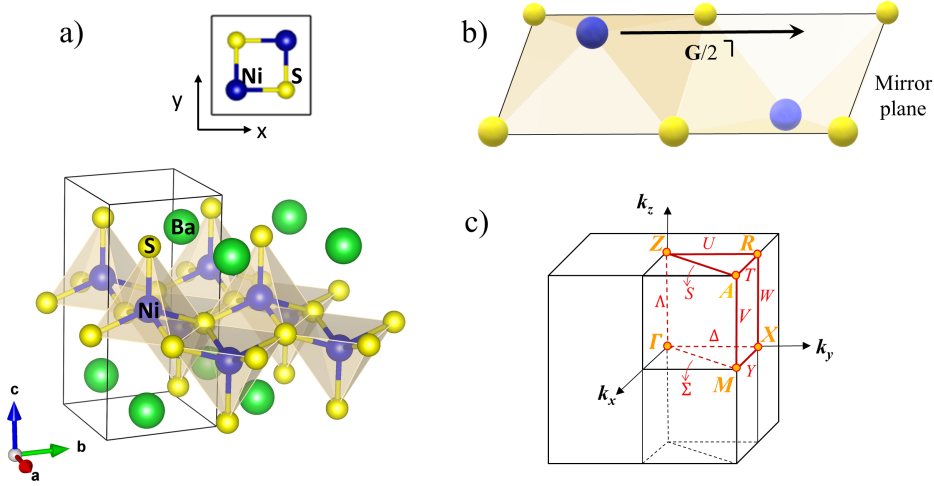


Figure 4.1: (a) Crystal structure of  $\text{BaNiS}_2$ . Blue, yellow and green spheres represent the Ni, S and Ba atoms, respectively. The tetragonal unit cell is indicated by black solid lines. The lattice parameters are  $a = 4.44 \text{ \AA}$  and  $c = 8.93 \text{ \AA}$ [56]. On the top the projection of the unit cell in the  $xy$  plane, containing two Ni atoms is shown. (b) Gliding plane symmetry relating the Ni atoms inside the unit cell. (c) First Brillouin zone, and high-symmetry directions.

description of the experimental results in subsection 4.2.4. Specifically, starting from the *ab initio* description of the band structure, successive simplified tight-binding Hamiltonians are introduced which capture the essential properties of the system. This simplified treatment shows that the band structure near the gapless nodes is accurately described by an effective Dirac-like Hamiltonian similar to that of graphene. Our findings reveals novel possibilities for the conception new Dirac materials with correlated  $d$  orbitals.

## 4.2.2 Results

### 4.2.2.1 ARPES measurements

In order to shed light on the detailed electronic band structure of  $\text{BaNiS}_2$ , I performed synchrotron-ARPES on high-purity single crystals synthesized by a self-flux method and characterized by X-ray diffraction. The measurements were performed at the Advanced Photoelectric Effect (APE) beamline at synchrotron Elettra, c.f. subsection 3.3.2, at 70 K with linearly  $p$ -polarized beam of 70 eV. Single crystals of  $\text{BaNiS}_2$  were cleaved *in-situ* within the  $ab$  plane with a top-post under UHV conditions (base pressure better than  $10^{-11}$  mbar). The data were collected at the end station with a VG-DA30 Scienta hemispherical analyzer that provides high-resolution two-dimensional  $k$ -space mapping while the sample geometry is fixed. The total measured energy resolution (analyzer, temperature, photon energy) is  $\sim 15$  meV and the angular resolution is better than  $0.2^\circ$ .

In figure 4.2 (a) I represent a three dimensional ARPES map of the Brillouin zone whose shape and high-symmetry  $k$ -points are shown in figure 4.1 (c). The top surface shows the constant energy contour at the Fermi level accompanied by the band dispersion spectra along the high symmetry directions  $\Gamma M$ ,  $\Gamma X$ , and  $XM$  on the sides of the cube. We clearly observe the linearly dispersing bands along the  $\Gamma M$  that create a gapless node at the Fermi level. The Fermi surface reveals two pairs of such Dirac-like crossings related to each other by the time-reversal symmetry and by the  $C_2$  operation symmetry of the  $C_{2v}$  little group of the  $k$ -vectors belonging to the  $\Gamma M$  direction. We also observe a small electron pocket centered at  $\Gamma$ . The small Fermi

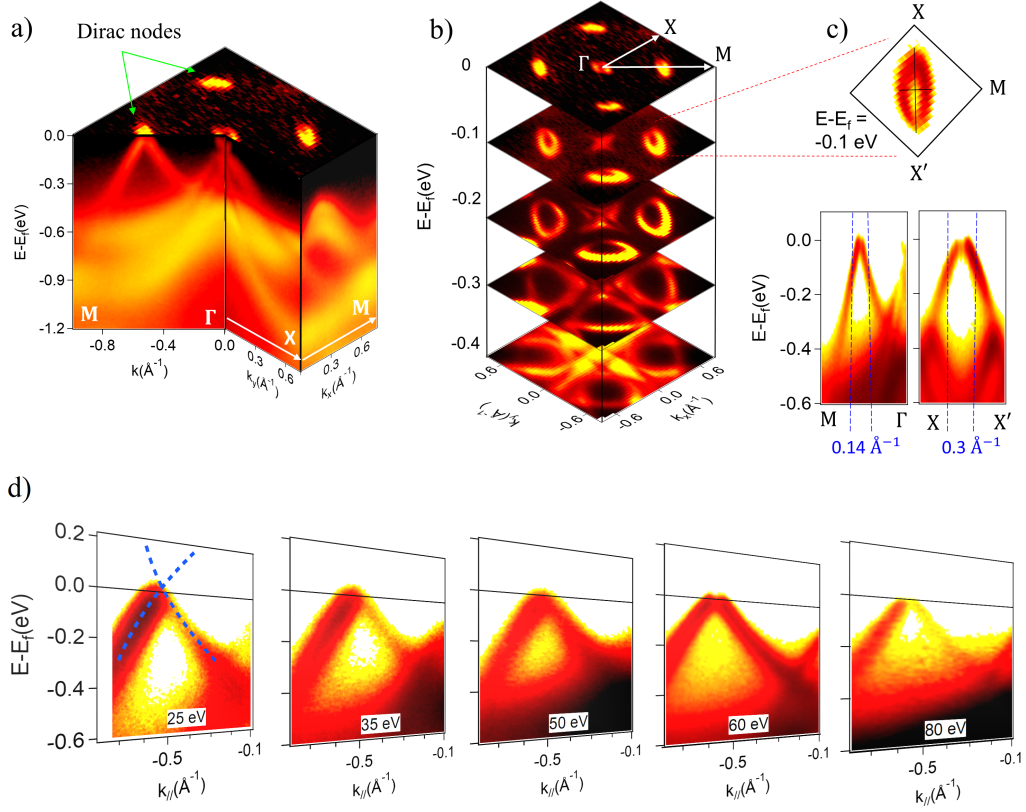


Figure 4.2: Experimental electronic band structure of BaNiS<sub>2</sub>. (a) A three-dimensional ARPES map acquired with 70 eV photon energy. The top surface shows the Fermi surface and the sides of the cube present the band dispersion along the high symmetry directions depicted with the white arrows. The linearly dispersing bands along the  $\Gamma M$  cross each other at the Fermi level, creating four Dirac nodes on the Fermi surface. (b) Stacking plots of constant-energy contours show the band structure evolution with respect to the binding energy. Particularly, we observe the ellipse-shaped section of the linearly dispersing bands on the  $k_x - k_y$  plane that loses symmetry as the binding energy increases. (c) Elliptical section of the Dirac cone for the binding energy of 100 meV. The band dispersion along the small and big axis of the ellipse are also shown. (d) The ARPES yield along the  $\Gamma M$  direction with different photon energies for the region where bands are linearly dispersed. The dashed blue lines are the guide to the eyes along the linearly dispersing bands.

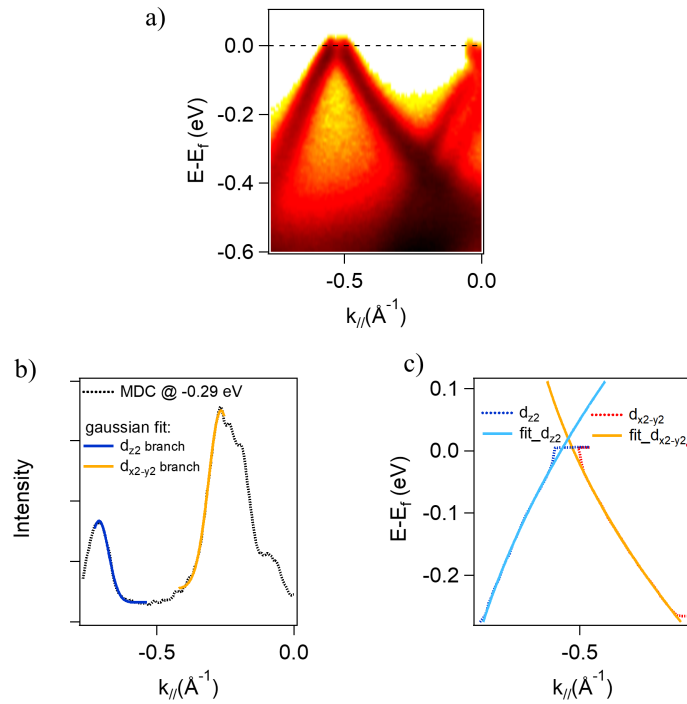


Figure 4.3: (a) The Dirac cone as obtained by 60 eV of photon energy. (b) MDC at the binding energy of 0.29 eV. The photoemission peaks of the  $d_{z^2}$  and  $d_{x^2-y^2}$  bands are fitted by a Gaussian function and a linear background and are shown in blue and orange curves, respectively. (c) The continuity of the bands above the Fermi level are obtained by fitting the reconstructed band dispersion for each band with a polynomial function. The crossing point of the fits gives the position of the Dirac point.

surface emanates from the rich electron correlations leading to the semi-metallic properties of BaNiS<sub>2</sub> [86, 156]. I present in figure 4.2 (b), the evolution of the bands with respect to the binding energy in the constant energy contours in the  $k_x - k_y$  planes. We observe that the electron pocket at  $\Gamma$  disappears at binding energy  $\sim -0.14$  eV and then evolves into a growing star-shaped dispersion as the binding energy increases. On the other hand, the linearly dispersing bands along  $\Gamma M$  remain isolated up to about -0.5 eV. In contrast to graphene, these bands create an elliptical section on the constant energy maps close to the Fermi level. In figure 4.2 (c), I show the elliptical shape of the Dirac cone for the binding energy of 0.1 eV. The big and small axis of the ellipse lie along the  $\Gamma M$  and  $XX'$  directions and their sizes are 0.14 and  $0.3 \text{ \AA}^{-1}$ , respectively. The band dispersion along the axis of the ellipse are also shown. However, as the binding energy increases the sections of the Dirac cone with respect to binding energy gradually lose their symmetry until they reach the border of the Brillouin zone and interfere with other bands. This asymmetric aspect also comes from the originally tilted nature of the Dirac cone which will be discussed after. Henceforth, I mainly focus on the linearly dispersing bands. In order to elucidate the  $k_z$  dispersion character of their electronic band structure, I performed a series of photon energy dependent measurements from 25 eV to 80 eV ensuring a complete span of the Brillouin zone. The full electronic band dispersion with respect to photon energy is discussed in section 4.3.

Figure 4.2 (d) shows the ARPES yield acquired with different photon energies. We notice slight variations in the intensity of the bands that can be explained by matrix element effects. In order to obtain the position of the Dirac point in the binding energy and momentum, I used the following method: I have sliced the ARPES yield for each binding energy into momentum distribution curves (MDC's). Figure 4.3 (a) and (b) show the Dirac cone at 60 eV and the MDC at -0.29 eV below the Fermi level, respectively. The photoemission intensity peak for each branch of the Dirac cone— that is, the  $d_{z^2}$  and  $d_{x^2-y^2}$  band, was fitted by a Gaussian with a linear background as show in the figure. The centers of the fit for all binding energies then give the reconstructed band dispersion,  $E(k)$ , for each band. In order to obtain the continuity of the bands above the Fermi level, I fitted each reconstructed band by a polynomial fit as shown in figure 4.3 (c). The crossing of these fits for the  $d_{z^2}$  and  $d_{x^2-y^2}$  bands gives the position of the Dirac point. For instance, in this case Dirac point is located at 20 meV above the Fermi level and at wavevector  $-0.52 \text{ \AA}^{-1}$ . Table 4.1 shows the Dirac point position for different photon energies:

$h\nu$ (eV)	E (meV)	$k_{//}(\text{\AA}^{-1})$
25	20	-0.52
35	19	-0.51
45	17	-0.50
50	21	-0.49
60	20	-0.52
70	20	-0.52
80	17	-0.52

Table 4.1: The position of the Dirac cone in energy and momentum with respect to the photon energy. The Dirac point always occurs around 20 meV above the Fermi level and does not disperse in the momentum space within the experimental resolution.

The ARPES data reveals no dispersion of linear bands within the experimental resolution. The Dirac point always occurs at about 20 meV above the Fermi level and its position in the  $k_x - k_y$  plane is almost constant. Furthermore, the velocity of the bands does not change for

different  $k_z$ . These dispersionless features strongly indicate a 2D nature for the Dirac cone in the square lattice of  $\text{BaNiS}_2$ . I found that the Fermi velocity for two branches of the linearly dispersing bands along the  $\Gamma\text{M}$  direction is about  $2 \text{ eV}\cdot\text{\AA}$ .

#### 4.2.2.2 *ab initio* electronic band structure calculations and polarization-resolved band structure

The band structure calculations were performed in the density functional theory (DFT) framework by a modified hybrid Heyd-Scuseria-Ernzerhof (HSE) functional with an optimized 7% of exact exchange, while keeping the regular screening length  $\lambda \approx 4.8 \text{ \AA}$  in the exchange potential [68, 93].

I briefly describe the DFT *ab-initio* calculations that our theorist collaborators carried out: they used the QUANTUM ESPRESSO package [51, 53] for the calculations. The geometry of the cell and the internal coordinates are taken from experiment [56]. The core electrons of the Ni, Ba, and S atoms are replaced by norm-conserving pseudopotentials. The Ni pseudopotential is fully relativistic, with 10 valence electrons ( $4s^2 3d^8$ ) and nonlinear core corrections. The Ba pseudopotential includes the semicore states, while the S pseudopotential has  $3s^2 3p^4$  in-valence electrons. They employed a  $8 \times 8 \times 8$  electron-momentum grid and a Methfessel-Paxton smearing of 0.01 Ry for the  $k$ -point integration. The plane-waves cutoff is 60 Ry for the wave function. The non-local exchange terms of the HSE functional are computed through the fast implementation of the exact Fock energy [51], based on the adaptively compressed exchange scheme [100]. In the non-local Fock operator evaluation, the integration over the  $q$ -points is downsampled on a  $8 \times 8 \times 2$  grid. A half-a-grid shift in the  $z$  direction was applied to minimize the number of nonequivalent momenta in the  $k + q$  grid. They performed a Wannier interpolation of the *ab initio* bands, by means of the WANNIER90 code [123], to accurately resolve the band structure, chemical potential, and Fermi surface.

The advantage of introducing the hybrid functionals is that they are nonlocal and orbital dependent. They effectively take into account static non-local correlations of screened-exchange type, proven to be relevant to correctly reproduce quantum oscillations data [86]. Nickel spin-orbit (SO) interactions were included, whose importance has been demonstrated in  $\text{BaNiS}_2$  [156]. Figure 4.4 (a) shows the comparison between calculations and the ARPES data acquired at 70 eV of photon energy. It shows a quite good agreement, particularly at  $k_z = 0$ . The location and the shape of the Dirac cones are well reproduced along the  $\Gamma\text{M}$  and  $\text{ZA}$  directions. The asymmetric (tilted) nature of the cones, already mentioned in the ARPES Section, is highlighted by the *ab initio* band structure.

The HSE results allow one to analyze the nature of the Dirac cones, in particular their orbital character, and to extract the tight-binding parameters for a model low-energy Hamiltonian. In accordance with recent calculations done in the so-called DFT+U framework [156], we can ascribe the electronic states close to the Fermi level mainly to Ni  $3d$ -orbital hybridized with  $3p$  orbitals of sulfur atoms.

With the aim of clarifying the multi-orbital nature of the bands experimentally, I performed a series of polarization dependent laser-based ARPES experiments. The measurements were performed at the FemtoARPES setup, c.f. paragraph 3.4.1.3. By using a thick  $\beta\text{-BaB}_2\text{O}_4$  (BBO) crystal (1 mm) the total effective energy resolution was ultimately reduced to 20 meV. The intensity of the UV pulses was decreased to approximately 1000 photons/pulse in order to avoid space charge effects from femtosecond laser pulses during our measurement [65]. The base temperature of the experiments was 130 K.

As explained in subsection 3.2.4, thanks to different parities of the  $d$ -orbitals with respect to

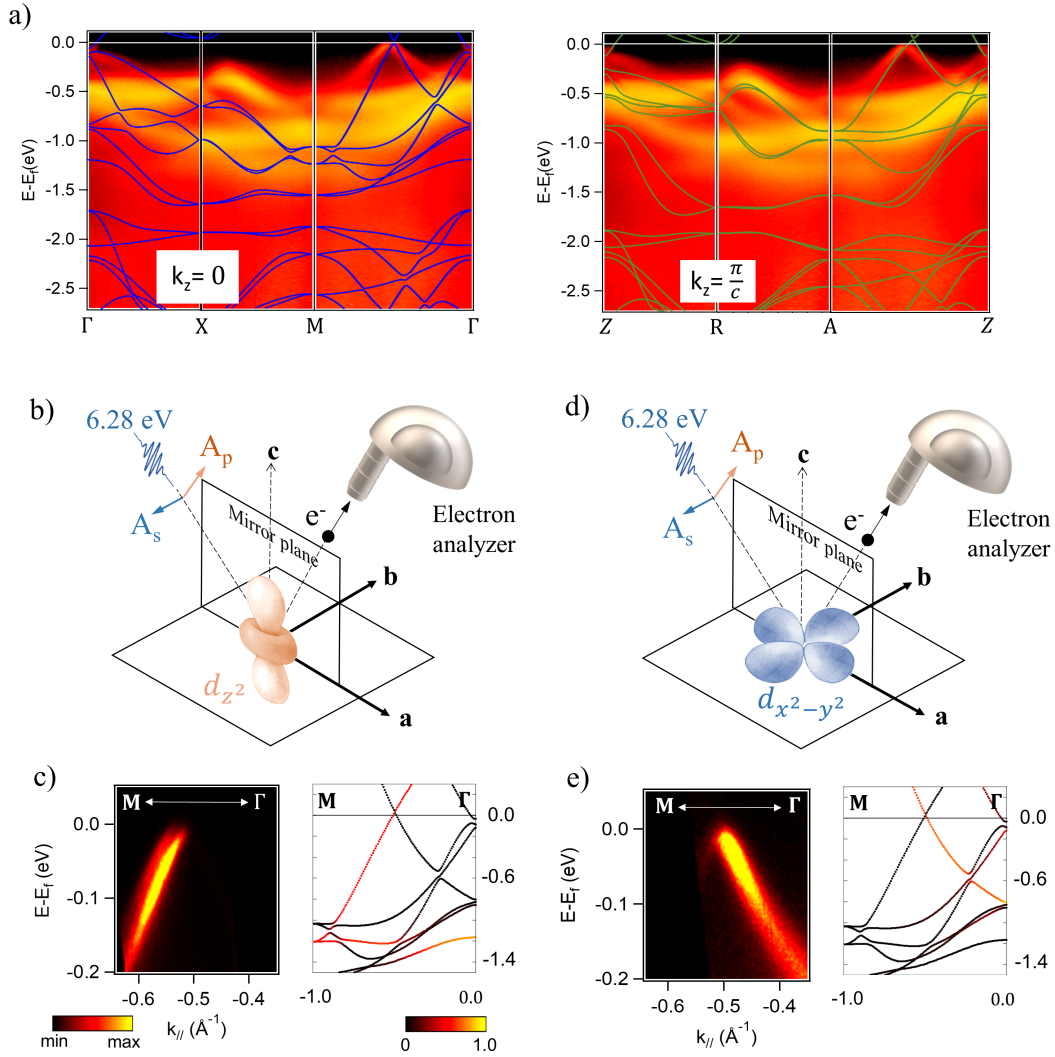


Figure 4.4: Band structure calculations and  $d$ -orbital character of the Dirac bands revealed by laser-based ARPES. (a) Comparison between the electronic band structure calculations with the HSE method and the experimental data acquired with 70 eV of photon energy. (b) Mirror plane emission of the  $d_{z^2}$  band. (c) P-polarized photon with the electric field indicated as  $A_p$  allows the detection of the out-of-plane  $d_{z^2}$  band. The right hand side figure shows the orbital-resolved band structure. (d) Mirror plane emission of the  $d_{x^2-y^2}$  band. (e) s-polarized photon with the electric field indicated as  $A_s$  reveals only the band dispersion of the in-plane  $d_{x^2-y^2}$  band. The color scale of the calculations indicates the relative weight of the given  $d$ -orbital component for the studied bands.

the scattering plane of the experiment, see figure 4.4 (b) and (d), the out-of-plane  $d_{z^2}$  and the in-plane  $d_{x^2-y^2}$  states are observable with  $p$  and  $s$  polarization of the incident light, respectively. The results in figure 4.4 (c) and (e) confirm the well-defined character of the Dirac bands close to the Fermi level, also by direct comparison with the orbital resolved band structure. These results show that it is logical to try to derive the Hamiltonian that is based on the contribution of two  $d$ -orbital components as explained in the following subsection.

### 4.2.3 Symmetry analysis of the Dirac bands

As reported in figure 4.1, the crystal structure of BaNiS<sub>2</sub> is made of square-lattice layers of staggered edge-sharing NiS<sub>5</sub> pyramids pointing along the out-of-plane [001]  $c$ -axis direction [113]. The Ni atoms are located inside the S pyramids along their axis. They feel a square-pyramidal crystal field which splits the atomic  $d$ -shell into levels that are, in descending energy order:  $d_{x^2-y^2}$ ,  $d_{z^2}$ ,  $d_{xy}$ , and  $(d_{xz}, d_{yz})$ , the latter two being degenerate. Since the Ni is in a  $3d^8 4s^0$  electronic configuration, we expect that all  $d$  orbitals are filled except for the two topmost energy levels  $d_{x^2-y^2}$  and  $d_{z^2}$ , each one nearly half filled, if the Hund's exchange overwhelms the crystal field splitting between them.

The puckering of the BaNiS<sub>2</sub> layers gives rise to a tetragonal non-symmorphic  $P4/nmm$  symmetry characterized by a horizontal gliding plane which generates two Ni (and apical S) positions at  $(1/4, 1/4, z)$  and  $(3/4, 3/4, -z)$ , separated by a fractional  $\mathbf{f}=(1/2, 1/2, 0)$  translation in the plane, figure 4.1 (b). The two Ni are at the Wyckoff position  $2c$ , also position of the M point, while the two planar S are at the position  $2a$ , which is also the Wyckoff position of the  $\Gamma$  point.

As one can see from figure 4.5 (a), at the M point the energy hierarchy of the atomic orbitals follows closely the crystal field splitting. Moreover, as the little group has four 2D irreducible representations, the states originating from the same orbitals of the two inequivalent Ni must be degenerate. The topmost level of the  $p-d$  manifold is of  $E_{M1}$  symmetry, and is made by the two  $d_{x^2-y^2}$  orbitals, while the doublet generated by the  $d_{z^2}$  orbitals transforms as the irreducible representation (irrep)  $E_{M2}$ . The latter lies below  $E_{M1}$  and is in between  $E_{M3}$  and  $E_{M4}$  irreps, made of linear combinations of the  $(d_{xz}, d_{yz})$  orbitals, one set for each inequivalent Ni.

On the contrary, the levels stacking at the  $\Gamma$  point, whose little point group is isomorphic to  $D_{4h}$ , is quite different from that predicted by the crystal field. This uncommon behaviour stems from the sizeable hybridization of Ni- $d$  orbitals with the S- $p$  ligands. Because of the nonsymmorphic symmetry, each Bloch eigenfunction at  $\Gamma$  can be either even or odd upon exchanging the inequivalent Ni and S within each unit cell. Even and odd combinations of the same  $d$ -orbitals belonging to inequivalent Ni atoms split in energy since they hybridize differently with the the ligands. For instance, the even combination of the  $d_{x^2-y^2}$  Ni-orbitals is weakly hybridized with the lower energy  $p_z$ -orbitals of the planar S, since the two Ni are one above and the other below the basal plane, whereas the odd combination is non-bonding. As a result, the even combination, of symmetry  $B_{1g}$ , shifts up in energy with respect to the odd one, of symmetry  $B_{2u}$ . Seemingly, the  $A_{2u}$  odd combination of  $d_{z^2}$  hybridizes substantially with the  $p_z$  orbitals of both planar and apical S, and thus is pushed up in energy well above not only the even combination, of symmetry  $A_{1g}$ , but also above the  $d_{x^2-y^2}$  even and odd combinations, thus reversing the crystal field order (figure 4.5 (b)).

Because the irreps at the A and Z  $\mathbf{k}$ -points are equivalent to those at the M and  $\Gamma$  ones [179], respectively, the orbital hierarchy found at M must be preserved along the MA direction, and that at  $\Gamma$  along the  $\Gamma Z$  direction. This implies that along the path  $(0, 0, v) \rightarrow (1/2, 1/2, v)$  for any  $v$ , there must be a band inversion between bands with predominant  $d_{z^2}$  and those with  $d_{x^2-y^2}$

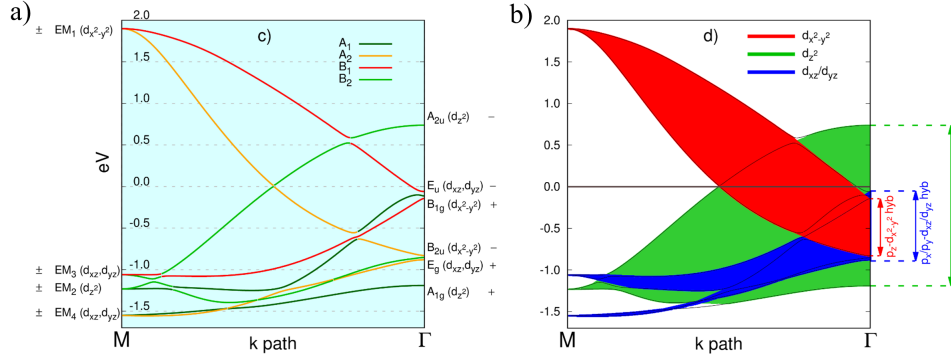


Figure 4.5: Band structure calculations and band symmetries along the  $M\Gamma$  direction. (a) Band symmetries along the  $M\Gamma$  direction. At the right (left) -hand side of the panel, the symmetries at  $\Gamma$  ( $M$ ) is shown, while the symmetries in between follow the irreps of the  $C_{2v}$  point group, represented by the color code in the key. The outer  $+/-$  signs indicate the parity of the respective Bloch wave functions at the beginning and at the end of the  $k$ -path. (b) Evolution of the energy splitting between even and odd combinations of  $d$  orbitals along  $M\Gamma$ . The red (dark-green) vertical arrows indicate the splitting between the  $d_{x^2-y^2}$  ( $d_{z^2}$ ) bands at  $\Gamma$  due to the hybridization with the ligand  $p_z$  orbitals. The blue arrow is the splitting of  $d_{xz}/d_{yz}$  bands at  $\Gamma$  due to their hybridization with the  $p_x/p_y$  orbitals.

characters. Remarkably, the band crossing is allowed in this case without SOC, and leads to two Dirac points, one right at the Fermi energy for  $k_z = 0$ . Indeed, the crossing bands transform like different irreps of the little group, which is isomorphic to  $C_{2v}$  for a  $k$ -point  $(u, u, v)$  with  $v = 0, 1/2$ , and to  $C_s$  with  $v \in ]0, 1/2[$ . Figure 4.5 (a) shows the bands around the Fermi energy and along  $\Gamma M$ , each labeled according to the irreps of the corresponding little groups. In the next subsection, I show the orbital character of those bands, which highlights the major role played by the ligands.

From a parity analysis of the band structure (the parity sign for each band at the two time-reversal inversion momenta points  $M$  and  $\Gamma$  is reported in figure. 4.5 (b)), it turns out that  $BaNiS_2$  is close to being a weak  $Z_2$  topological insulator, thanks to the inverted bandgap occurring at  $\Gamma$  between the  $E_u$  and the  $B_{1g}$  states, carrying opposite parities. Both bands are however slightly below the Fermi level, and the system is thus metallic with a small Fermi pocket centered at  $\Gamma$ , as found also in ARPES. It is interesting to note that the inverted bandgap at  $\Gamma$  is very sensitive to the electronic correlations. The HSE functional pushes up the  $B_{1g}$  state with respect to the GGA results, by reducing the inverted band gap, which then closes along the  $\Gamma Z$ .

Previous theoretical calculations [63, 92, 113, 156] already suggested that all the Ni ( $3d$ )-orbital components contribute to the density of states near/at the Fermi level and that they are strongly hybridized with the S( $3p$ ) orbitals. However, to the best of our knowledge, the presence of linearly dispersing bands with unavoided crossing at the Fermi level was not noted before. Remarkably, the unavoided crossing occurs along a symmetry line and not at high-symmetry points as, for instance, in the case of the prototype system graphene.

#### 4.2.4 Effective Dirac Hamiltonian

In order to derive a minimal 2D model for the Dirac cones, Wannier orbitals from the HSE band structure for the full  $p$ - $d$  manifold were generated. The resulting tight-binding Hamiltonian features 22 atomic orbitals. The  $p$  orbitals belonging to the apical sulfurs and the  $d$ -orbitals not contributing to the Dirac bands are easily removed from this Hamiltonian, and all out-of-plane

hoppings are set to zero. However, care must be taken for the remaining in-plane sulfur atoms which are nearest neighbors of the Ni sites. As such, these S atoms favor the electron hopping between Ni atoms aligned in the Ni-S-Ni direction. We shall see that the strong Ni-S hybridization is key to shape the linear dispersion of the Dirac bands, while the gapless nodes are protected by the different  $d_{z^2}$  and  $d_{x^2-y^2}$  symmetries, as discussed above. A further simplification of the tight-binding model is achieved by reducing the unit cell from a 2-Ni sites to a single Ni. Note that among the remaining orbitals, only the  $p_z$  ones are odd with respect to the reflection through the  $x$ - $y$  plane. By exploiting the nonsymmorphic symmetry of the crystal space group, we can introduce a gauged set of atomic orbitals ( $\{\tilde{p}_i\}_{i=x,y,z}$  and  $\{\tilde{d}_j\}_{j=z^2,x^2-y^2}$ ), which differs from the physical set only for the  $\tilde{p}_z$  orbital, defined such that  $\tilde{p}_z(i_x, i_y) = (-1)^{i_x+i_y} p_z(i_x, i_y)$ , where  $i_x, i_y$  are indices of the underlying Bravais square lattice. Once the Hamiltonian in the 1-Ni unit cell with gauged orbitals is derived, one easily finds that upfolding its band structure yields the one of the full 2-Ni nonsymmorphic unit cell. Thus, we end up with an equivalent  $5 \times 5$  Hamiltonian, in a bipartite square lattice containing 1-Ni and 1-S sites and nearest neighbor hoppings, much simpler to handle. For convenience, we will henceforth work in a reference frame obtained upon rotating the  $x$ - $y$  plane by  $45^\circ$  around the  $z$ -axis, so that  $d_{x^2-y^2} \rightarrow d_{xy}$ , and Ni-Ni directions are along either the  $x$  or  $y$  of new axis. This Hamiltonian reads:

$$\begin{aligned}
H(\mathbf{k}) = & \sum_{i=x,y,z} E_i n_{i\mathbf{k}} + \sum_{a=z^2,xy} E_a n_{a\mathbf{k}} \\
& + \sum_{\substack{\sigma, a=z^2,xy \\ i=x,y,z}} v_{i,a}(\mathbf{k}) \left( d_{a\mathbf{k}\sigma}^\dagger p_{i\mathbf{k}\sigma} + H.c. \right), \tag{4.1}
\end{aligned}$$

where  $\mathbf{k} = (k_x, k_y)$ ,  $n_{a\mathbf{k}}$  and  $n_{i\mathbf{k}}$  the occupation numbers in moment space. The non-zero hybridization amplitudes are:

$$\begin{aligned}
v_{z,xy}(\mathbf{k}) &= t_{z,xy} \sin \frac{k_x}{2} \sin \frac{k_y}{2}, \\
v_{z,z^2}(\mathbf{k}) &= t_{z,z^2} \cos \frac{k_x}{2} \cos \frac{k_y}{2}, \\
v_{x,xy}(\mathbf{k}) &= t_{x,xy} \left( \sin \frac{k_x}{2} \cos \frac{k_y}{2} + \sin \frac{k_y}{2} \cos \frac{k_x}{2} \right), \\
v_{y,xy}(\mathbf{k}) &= t_{x,xy} \left( \sin \frac{k_x}{2} \cos \frac{k_y}{2} - \sin \frac{k_y}{2} \cos \frac{k_x}{2} \right), \\
v_{x,z^2}(\mathbf{k}) &= t_{x,z^2} \left( \sin \frac{k_x}{2} \cos \frac{k_y}{2} + \sin \frac{k_y}{2} \cos \frac{k_x}{2} \right), \\
v_{y,z^2}(\mathbf{k}) &= -t_{x,z^2} \left( \sin \frac{k_x}{2} \cos \frac{k_y}{2} - \sin \frac{k_y}{2} \cos \frac{k_x}{2} \right). \tag{4.2}
\end{aligned}$$

The model parameters are compatible with the spatial symmetries and implicitly depend on  $k_z$ . Their values are reported in table 4.2.

Denoting with  $E_d, E_p$  the on-site energies of the  $d$ - and the  $p$ -orbitals, we find that the charge transfer energy is positive  $E_d - E_p > 0$ . Thus, assuming that the  $p$ -orbitals lie well below the Fermi level, we can integrate them out to obtain a Hamiltonian which effectively describe the

Hopping element	eV
$E_x/E_y$	6.33
$E_z$	6.85
$E_{z^2}$	7.48
$E_{x^2-y^2}$	7.54
$t_{z,xy}$	-1.48
$t_{z,z^2}$	-2.32
$t_{x,xy}$	1.76
$t_{x,z^2}$	0.22

Table 4.2: Tight-binding coefficients used in the low-energy  $5 \times 5$  Hamiltonian, as derived from a Wannier fitting of the ab initio HSE band structure.

physics of  $d$ -orbitals near the Fermi level:

$$\begin{aligned}
H^d(\mathbf{k}) = & \sum_{a=z^2,xy} [\tilde{E}_a - t_a(\cos k_x + \cos k_y) \\
& - t'_a \cos k_x \cos k_y] n_{a\mathbf{k}} \\
& + \sum_{\substack{a,b=z^2,xy \\ a \neq b, \sigma}} t_{ab} \left( d_{a\mathbf{k}\sigma}^\dagger d_{b\mathbf{k}\sigma} + H.c. \right), \tag{4.3}
\end{aligned}$$

where the hopping amplitudes are defined according to the following chain of relations:  $t_1 = t_{z^2} = 4t_{z^2,z}^2/E_z$ ,  $t_2 = -t_{xy} = 4t_{xy,z}^2/E_z$ ,  $t_3 = 4t_{z^2,x}^2/E_x = 4t_{z^2,y}^2/E_y$ ,  $t_4 = 4t_{xy,x}^2/E_x = 4t_{xy,y}^2/E_y$ ,  $t'_{z^2} = t_1 - t_3$ ,  $t'_{xy} = t_2 - t_4$ ,  $t_{z^2,xy} = t_{xy,z^2} = \sqrt{t_1 t_3} - \sqrt{t_2 t_4}$  and  $E_{z^2} = E_{z^2} - t_1 - t_3$ ,  $E_{xy} = E_{xy} - t_2 - t_4$ .

We note that the hybridization among the two  $d$ -orbitals vanishes along  $\Gamma X$  and along  $\Gamma Y$ , as dictated by symmetry. Moreover, along, e.g.,  $\Gamma X$ , the  $d_{z^2}$ -dispersion decreases monotonically ( $t_{z^2} > 0$ ), contrary to that of the  $d_{xy}$  component ( $t_{xy} < 0$ ). Along the two lines, the system then admits band crossing points at  $\mathbf{k}^* = (\pm k^*, 0)$ ,  $(0, \pm k^*)$ . The position  $k^* > 0$  of such points is defined by the solution of the equation:  $\cos k^* = \frac{(\tilde{E}_{z^2} - \tilde{E}_{xy}) - (t_1 + t_2)}{2t_1 - t_3 + t_4}$ .

Finally, a Dirac Hamiltonian is obtained by expanding around such gapless points  $\mathbf{k}^*$ , i.e.  $\mathbf{k} = \mathbf{k}^* + \mathbf{q}$  to the linear order in  $\mathbf{q}$  and making use of  $SU(2)$  invariance:

$$H_{Dirac}(\mathbf{q}) \simeq \hat{h}_0 q_x I + \hat{h}_x q_x \sigma_x + \hat{h}_y q_y \sigma_y \tag{4.4}$$

in which the Hamiltonian coefficients are defined as  $\hat{h}_0 = -\frac{1}{2}(2t_1 + 2t_2 - t_3 - t_4) \sin k^*$ ,  $\hat{h}_x = (\sqrt{t_1 t_2} - \sqrt{t_3 t_4}) \sin k^*$ ,  $\hat{h}_y = -\frac{1}{2}(2t_1 - 2t_2 - t_3 + t_4) \sin k^*$ , where  $I$  is the identity, and  $\sigma_{i=x,y,z}$  are the Pauli matrices. The opposite node at  $\mathbf{k} = (-k^*, 0)$  has opposite chirality. The two other nodes at  $\mathbf{k} = (0, \pm k^*)$  are obtained by mirror symmetry. Note that Eq. 4.4 shows a nontrivial  $k$ -dependence in the  $I$  component, which implies an elliptical shape of the Dirac cone (see figure 4.6 (d)). This result matches the experimental observation discussed in the previous subsection. To highlight this feature, we compared in figure 4.6 (a)-(b) the experimental and theoretical constant energy contour near the Fermi level. The theoretical result obtained with the effective Dirac model perfectly agrees with the ARPES data (see also figure 4.2 (b) and (c)).

Finally, in figure 4.6 (c) we compare the linear Dirac dispersion with the one obtained within the  $5 \times 5$  model introduced in Eq. 4.1. This calculation highlights the elliptical shape loss of the Dirac cone at energies of 0.5 eV away from the Fermi level. The bending of the electronic dispersion qualitatively matches the widening of the pockets experimentally observed in figure 4.2 (b).

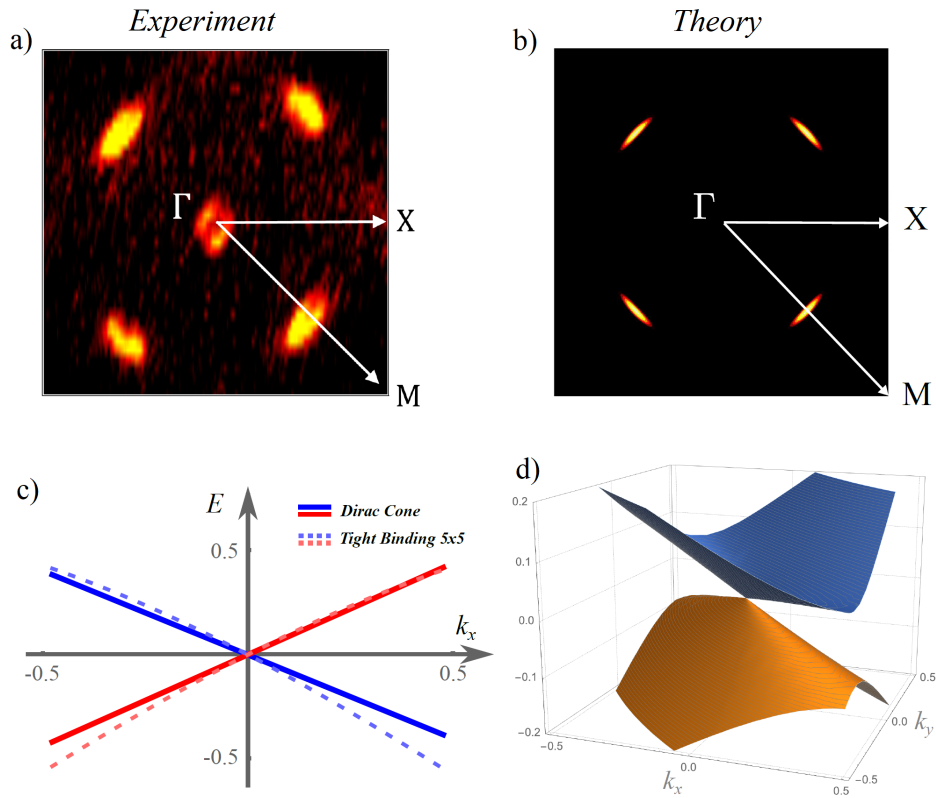


Figure 4.6: (a)-(b) Constant energy contour near the Fermi level as obtained experimentally (left) and from the effective Dirac model (Eq. 4.4). The comparison highlights the agreement between theory and experiment. The effective model explains the presence of elliptically shaped Dirac cones, as observed in ARPES measurements, along  $\Gamma M$  direction. (c) Electronic dispersion near the Fermi level from the  $5 \times 5$  Hamiltonian (Eq. 4.1) and the linearized effective Dirac model in Eq. 4.4. This is in qualitative agreement with the widening of the energy pockets observed in ARPES data (see figure 4.2 (b)). (d) Elliptical shape of the Dirac cones.

### 4.2.5 Discussion

In this work, by means of band structure theory and ARPES experiments, we have studied the electronic Dirac states hosted in the bulk  $\text{BaNiS}_2$  semimetal. These states have several remarkable features. First, they are made of correlated  $d$  orbitals, strongly hybridized with the ligand  $p$  states. Secondly, they are lying at, or very close to, the Fermi level, therefore participating in the low-energy electronic properties of the material. Finally, they are not pinned at high-symmetry points of the BZ, but at the mid point along the  $\Gamma\text{M}$  direction.

We demonstrated that the Dirac points existence, as well as their location, crucially depend on the hybridization strength between the  $d$  and  $p$  states. The hybridization with the ligands yields band inversions, the necessary condition for the Dirac points occurrence. These symmetry protected topological contacts are set by the time-reversal, inversion, and  $C_{2v}$  symmetries of the tetragonal  $P4/nmm$  space group. This implies a fourfold degeneracy of the states, which yields two pairs of cones. Their alignment with the Fermi level is a consequence of two additional conditions which are met in  $\text{BaNiS}_2$ , namely the energy  $d$ -levels hierarchy, and the atomic  $d$ -orbitals filling. The former is provided by the square-pyramidal crystal field splitting, implying that the two topmost energy levels in the  $d$  manifold are of  $z^2$  and  $x^2 - y^2$  symmetries. The latter condition is given by the Ni electronic configuration, which leaves the  $d_{z^2}$  and  $d_{x^2-y^2}$  states with integer partial occupation:  $2n(d_{z^2}) + 2n(d_{x^2-y^2}) = 4$ , by counting both Ni in the unit cell, while the other  $d$  states are completely filled. Therefore, the  $C_{2v}$ -allowed crossing between the corresponding  $d_{z^2}$  and  $d_{x^2-y^2}$  bands must happen at the Fermi level, if there are no other Fermi pockets around. This condition is nearly satisfied in the  $\text{BaNiS}_2$  semimetal, which shows only a very small cylindrical electron pocket centered along the  $\Gamma\text{M}$  direction, populated by electrons much less mobile than the Dirac ones[157]. It turns out that the Dirac points are weakly dispersive along the  $k_z$  direction, with the Fermi level in the  $[0 - 25]$  meV ( $[0 - 75]$  meV) range from the crossing point energy, according to ARPES (HSE), as reported in figure 4.2 (d). This leads to the formation of Dirac nodal lines.

Thanks to the nonsymmorphic symmetry, the the symmetry protected topological contacts are robust against the non-negligible on-site Coulomb interaction present in the system. In principle, were the Hubbard repulsion strong enough, it could prevent the Dirac cones formation by the opening of a Mott gap, in the  $2d_{z^2} = 2$ ,  $2d_{x^2-y^2} = 2$  half-filled situation. However, the non-symmorphic operations imply a double degeneracy of the bands at M. This gives  $2d_{z^2}(\mathbf{k} = M) = 4$ , and breaks the filling condition for a Mott insulator.

Our findings point to  $\text{BaNiS}_2$  as a unique experimental and theoretical playground where to study Dirac fermions, and exploit their properties. The tunability of the Dirac points, due to the subtle interplay with the orbital  $p - d$  hybridization, is just one of the possibilities. For instance, the Dirac cones wandering [52] could be realized by chemical substitution in the  $\text{BaNi}_{1-x}\text{Co}_x\text{S}_2$  system, where the cobalt doping makes the compound more correlated, by changing the chemical potential level and reshuffling the atomic orbitals [158]. This could pave the way to exploring the physics of strongly correlated Dirac fermions in a controlled environment. Controlling the shape and position of the Dirac cones should also be viable under pressure. A non hydrostatic pressure distorts the underlying square lattice, thus breaking one of the symmetries that protect the fourfold occurrence of the Dirac nodal lines. Opening a gap by an external electromagnetic field is another possibility. Non-trivial phases could then be triggered by external conditions, thanks to the proximity of the material to a topological insulator.

In the realm of topological materials,  $\text{BaNiS}_2$  sheds light on the ingredients one needs to put together to synthesize new compounds. We suggest that the following three conditions must be met in order to have  $d$ -electron Dirac states near the Fermi level: i) a  $d_{z^2} - d_{x^2-y^2}$  manifold

isolated from the other  $d$  states, with band inversion through hybridization with the ligands; ii) the  $C_{2v}$  symmetry along some  $k$ -points line to protect the crossing point; iii) the  $n(d) = 8$  filling to pin the symmetry protected topological contacts around the Fermi level. This situation can be realized for instance in octahedral or square pyramidal arrangements of ligands around the transition metal center, crystallizing in a tetragonal or orthorhombic space group. These are fundamental hints to explore the existence of new Dirac compounds, and they could open future opportunities to deepen our knowledge of tunable topological phases.

### 4.3 $k_z$ dispersion

In subsection 1.5.2, I presented the Fermi surface of  $\text{BaNiS}_2$  acquired by means quantum oscillations. This technique only indirectly gives the topology of the Fermi surface and the exact reconstruction of the shape demands parallel theoretical work. Therefore, a precise  $k_z$  dispersion is a hard task particularly in the case of complex materials of which  $\text{BaNiS}_2$  is an example.

In order to elucidate the hitherto missing  $k_z$  dispersion character of the electronic band structure, I performed a series of photon energy dependent measurements as I partially presented the results in subsection 4.2.2. Figure 4.7 (a) shows ARPES spectra along the  $\Gamma M$  direction for different photon energies. We discern an overall variation of the intensity due to the matrix elements effect. However, a close look to the data shows that while the linearly dispersing bands are not dispersing (this was thoroughly discussed in subsection 4.2.2), the rest of the bands below the Fermi level show non-negligible  $k_z$  dispersion. For instance, the spectrum at 70 eV shows different features under the Dirac cone in the energy range of -0.5 to -1 eV while the lower photon energy counterpart shows only one band in the same region. On the other hand, these bands show periodic behavior with respect to the photon energy. The DFT calculations with the HSE nonlocal exchange interaction for both  $k_z = 0$  and  $k_z = \frac{\pi}{c}$  are compared to the experiment in figure 4.7 (b). The overall agreement is good however, one can easily distinguish some differences. It seems that the spectrum at 25 eV is close to  $k_z = 0$  while the spectrum at 70 eV shares more similar features with the calculated bands for  $k_z = \frac{\pi}{c}$ .

I also show the ARPES intensity map for the iso-energy contours corresponding to the Fermi level for different photon energies, figure 4.7 (c). We observe that while the relative intensity of the pockets crossing the Fermi level changes, no sizable difference in the form is present. We observe the  $\alpha$  ( $\gamma$ ) electron pocket in the center of the Brillouin zone and the  $\beta$  hole pocket along the  $\Gamma M$  direction. These results show that the quantum oscillations experiments showed a good agreement to the real Fermi surface. However, in contrast to the quantum oscillations measurements, our data unveil the electron pocket at the X (R) point that is shown by an oval contour on the figure. This pocket barely crosses the Fermi level and is split in two due to Rashba effect, c.f. subsection 1.5.2; however, it is not possible to detect the split experimentally.

To conclude, the bands at the Fermi level show a 2D  $k_z$  dispersion while at slightly higher binding energies the  $k_z$  dispersion is more important. These findings are in good agreement with the layered quasi two-dimensional crystal of  $\text{BaNiS}_2$ .

### 4.4 Temperature dependence of the density of states

The electronic properties of a correlated material change as function of thermodynamics parameters as explained in section 1.3.  $\text{BaNiS}_2$  is a moderately correlated metal so it is important to understand how the electronic band structure responds to temperature variations. This evolution would also help to theoretically adjust relevant parameters such as Coulomb interaction and

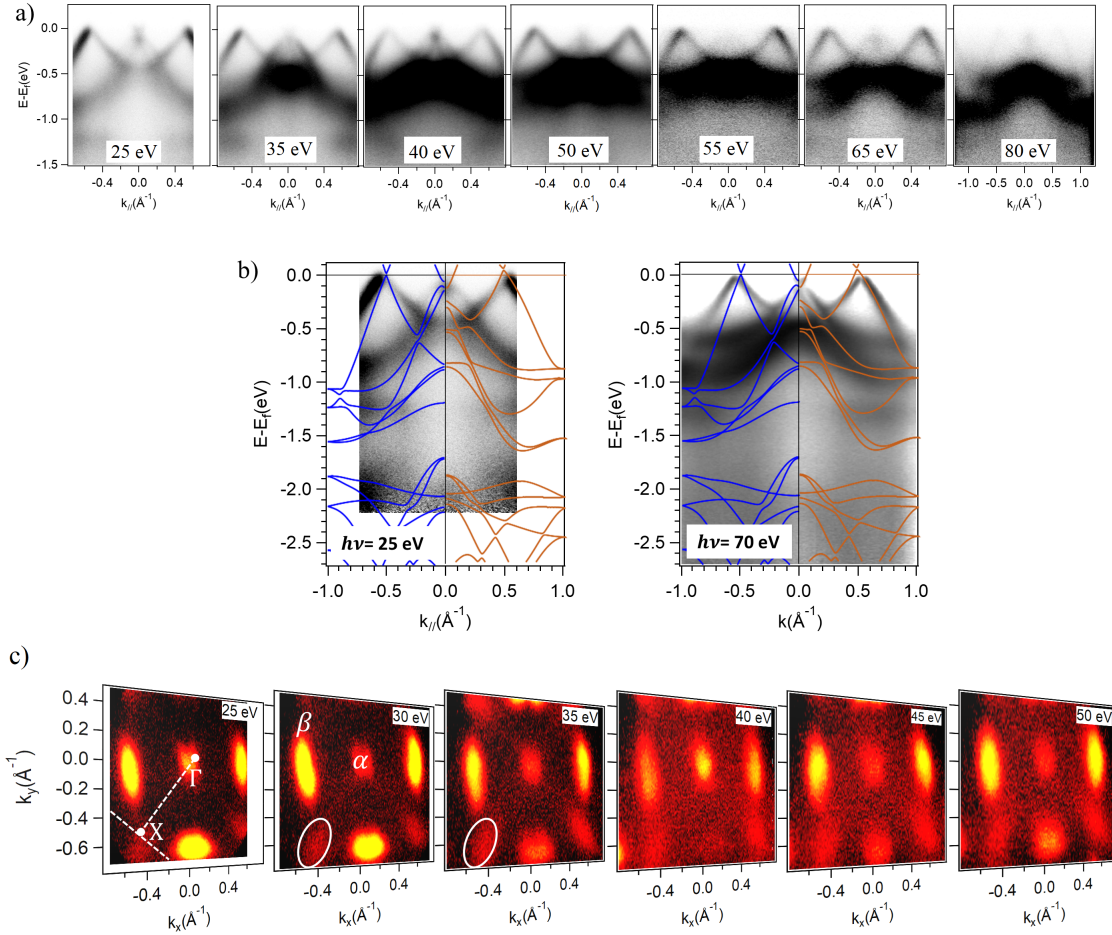


Figure 4.7:  $k_z$  dispersion of the electronic band dispersion. (a) ARPES yield along the  $\Gamma M$  high symmetry direction for different photon energy. Dirac bands do not show a significant  $k_z$  dispersion while other bands below the Fermi level have rather a 3D character. (b) Comparison with HSE (7%) method. The blue spectra shows the band dispersion for  $k_z = 0$  and the orange shows the bands for  $k_z = \pi/c$ . The left and right panels are acquired with 25 eV and 70 eV of photon energy, respectively. (c) Iso-energy contours at the Fermi level for different photon energies. The  $\alpha$  and  $\beta$  pockets are shown. In addition, the Rashba split pocket at X point is also observed and is shown by an oval contour. The data suggest that the electronic band structure at the Fermi level have a quasi 2D nature.

hopping terms.

Some preliminary temperature dependent ARPES measurements were performed at the Spectromicroscopy beamline, c.f. subsection 3.3.1, by 74 eV of photon energy. The use of high photon energy allows studying the bands in a relatively large interval of binding energy. Figure 4.8 (a) shows the  $d_{x^2-y^2}$  band along the  $\Gamma\text{M}$  direction as well the integration window to study the spectral weight evolution as a function of temperature. At low temperature (147 K), a sharp quasiparticle peak crosses the Fermi level. However, by increasing the temperature its intensity drops while it gradually broadens and transfers the spectral weight towards the band at -0.5 eV, figure 4.8 (b). This behavior can be explained as follows:

In contrary to a normal metal (with no interaction) where heating only smears out the Fermi-Dirac distribution, in a solid with strong interactions heating results in a non-trivial change in the density of states. First of all as I described in section 1.2, increasing the temperature of a Fermi liquid results in a broadening of the quasiparticle peak that scales with  $T^2$ . This is due to a general loss of the coherence of electrons due to scattering with, for instance, phonons. On the other hand, in a correlated material in which the orbital occupancy, Coulomb interaction, and itinerant nature of electrons are competing in parallel, a change in the temperature is definitely accompanied by a change in the density of states of electrons. The main reason is that heating affects the orbital overlap and tendency of electrons to get more delocalized (or localized). As a consequence the ratio  $U/t$  changes, c.f. paragraph 1.3.1.2. This phenomenon is shown both theoretically and experimentally for the case of  $\text{V}_2\text{O}_3$  in references [118] and [120] where heating lowers the QP peak and pushes the spectral weight towards the higher binding energies. Figure 4.8 (c) schematically describes the spectral weight transfer from the quasiparticle peak towards the incoherent part (lower Hubbard band) of the spectrum for a simple case of single band Hubbard model upon heating

The density of states of  $\text{BaNiS}_2$  nicely shows a similar behavior with respect to temperature. The fact that the width of the peak increases with temperature implies the Fermi liquid behavior. In addition, the spectral weight transfer between the bands indicates that electronic correlation is important. However, it should be emphasized that  $\text{BaNiS}_2$  is a multiband system and the definition of the QP and LHB is not straightforward for it. Without the loss of generality I address the sharp peak close to the Fermi level as the QP peak while the band at -0.5 eV should not be confused with a LHB.

These results show that the DOS of  $\text{BaNiS}_2$  evolves as a function of temperature. The interesting question is whether the electronic band dispersion changes as well. In section 5.4, I show that changing the temperature has interesting and non-trivial consequences on the Dirac cone of  $\text{BaNiS}_2$ .

## 4.5 Electronic band structure of $\text{BaCoS}_2$

As mentioned in subsection 1.4.3, if both time-reversal and inversion symmetries are simultaneously respected, a Dirac semimetal occurs straightforwardly at the phase transition between a topological insulator and a trivial one. We proved that  $\text{BaNiS}_2$  is a two-dimensional DSM with two pairs of  $d$ -orbital Dirac nodes protected by gliding plane symmetry. The question naturally arises as to whether other neighbors of  $\text{BaNiS}_2$  in the phase diagram of  $\text{BaCo}_{1-x}\text{Ni}_x\text{S}_2$  can possibly comprise topological states, and if any, how these states evolve across the phase diagram and what the role of  $d$ -orbitals is. Hitherto, the electronic band structure of  $\text{BaCo}_{1-x}\text{Ni}_x\text{S}_2$  has never been addressed for its potential topological properties; it has been rather considered as a correlated system with some similarities to the high temperature superconductors. On other hand, the ARPES data is missing for different parts of the phase diagram especially for  $\text{BaCoS}_2$

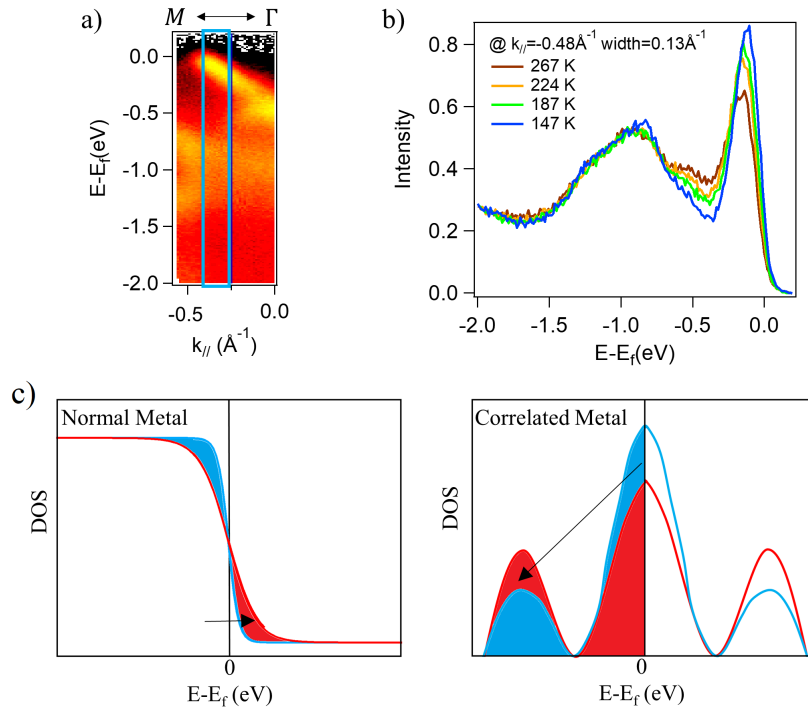


Figure 4.8: Temperature dependent density of states. (a) The blue contour shows the integration window of the spectral function. (b) The density of states for different temperatures. (c) Comparison between the spectral weight transfer upon heating for a normal metal and a correlated metal. The density of states at high and low temperatures are shown in red and blue, respectively.

that is the Mott insulating extreme of the phase diagram and its electronic properties cannot be captured by the Fermi liquid description [86]. The band structure of this compound has also remained challenging for *ab-initio* calculations due to its strong electron correlations. Therefore, I studied the band structure of BaCoS<sub>2</sub> in both its antiferromagnetic and paramagnetic insulating phases (AFI and PI phases). I present the results in the following subsection.

### 4.5.1 ARPES measurements

I performed a series of ARPES experiments on BaCoS<sub>2</sub> at the Spectromicroscopy beamline. This compound is more three-dimensional with respect to BaNiS<sub>2</sub>, and therefore harder to cleave and obtain a flat surface. The sub-micron beam of the beamline is particularly convenient to find best flat region on the surface of the sample after cleaving. The experiments were performed with 74 eV photon energy at 110 K (AFI phase) and 300 K (PI phase, very close to the Néel temperature). No significant difference between the spectra at low and high temperature was observed except that at the PI phase the overall quality and intensity of the bands were poorer. Therefore, I present here the data on the AFI phase.

Figure 4.9 (a) shows the iso-energy surface at -1.23 eV below the Fermi level at 110 K. The borders of the Brillouin zone as well as the high symmetry directions are drawn on the figure. The electronic band dispersion along these direction are shown in the top panel in figure 4.9 (b). In contrast to BaNiS<sub>2</sub>, bands are broad and rather of poor quality. This can be related to the significant electronic correlation in BaCoS<sub>2</sub>. On the other hand, the atomic cross-section of Co 3d orbital is less than Ni 3d state [92] leading to an overall lower intensity of BaCoS<sub>2</sub> spectrum. The band gap at the AFI phase is about 500 meV.

The theoretical DMFT calculations for the PI phase and at  $k_z = 0$  done by M. Casula are also shown for comparison below the ARPES data. Before, the DMFT calculations were only performed on  $\text{BaCoS}_2$  to study the pressure-induced insulator-to-metal transition [201] starting from the AFI phase, and all other theoretical methods failed to reproduce the insulating nature of  $\text{BaCoS}_2$  in its normal AFI state. We observe an overall agreement between the real band structure and calculations however, some discrepancies are also noticeable. For instance, at the M point the theory predicts that there is a dispersing band at  $E - E_f = 0.5$  eV while it is absent in the ARPES data. In addition, it is not possible to identify different bands in the ARPES spectra.

The density of states of  $\text{BaCoS}_2$  for both temperatures are shown in figure 4.9 (c) and are compared with the DMFT calculation performed on the PI phase. There are two bands located in  $0 < E - E_f < 2$  eV that are well reproduced by the theory. However, for higher binding energies we observe that the theoretical bands are slightly shifted with respect to the real band structure. On the other hand, as we see from the figures, the theory predicts the in-gap states at the Fermi level for the PI phase that is possibly responsible for the large (but not diverging) resistivity of  $\text{BaCoS}_2$ . These states disappear below the Néel temperature and a gap opens due to a long-range spin order. However, the experimental data does not show any evidence of these states. I consistently observe a band gap of 500 meV for both phases. By comparing the experimental density of states of the AFI and PI phases, we observe a spectral weight transfer between the bands and a slight gap filling while heating and approaching the magnetic transition as shown in the inset.

In the end, I give a detailed comparison between the spectra of  $\text{BaCoS}_2$  and  $\text{BaNiS}_2$  in figure 4.10. This allows us to distinguish similar salient features in the electronic band structure of both phases. The guide to the eyes are depicted by dashed lines and are numbered for each high symmetry direction in order to make the comparison of the corresponding bands in  $\text{BaCoS}_2$  and  $\text{BaNiS}_2$  easier. We observe a general shift of the bands to higher binding energies in  $\text{BaCoS}_2$ . Moreover, the bands are more separated in binding energy with respect to  $\text{BaNiS}_2$ . We see that the electron pocket at the  $\Gamma$  point has disappeared since Co has one electron less than Ni. Notably, we distinguish the remnants of the Dirac cone of  $\text{BaNiS}_2$  along the  $\Gamma\text{M}$  direction on the insulating phase; the gap of order of 1 eV has opened and the linearly dispersing bands are deformed. It is obvious that  $\text{BaCoS}_2$  does not show any topological aspect. However, the fact that it becomes metallic under pressure [194, 195] and that in the normal state it presents a gaped Dirac cone rise the question as to whether the pressure-induced metallic phase can possibly be a Dirac semimetal. Answering this question demands some precise optical measurements under pressure.

I would like to mention that we also tried to measure the band structure of  $\text{BaCoS}_2$  with 27 eV in order to study the  $k_z$  dispersion of the band structure however, the poor signal at this photon energy made the comparison impossible.

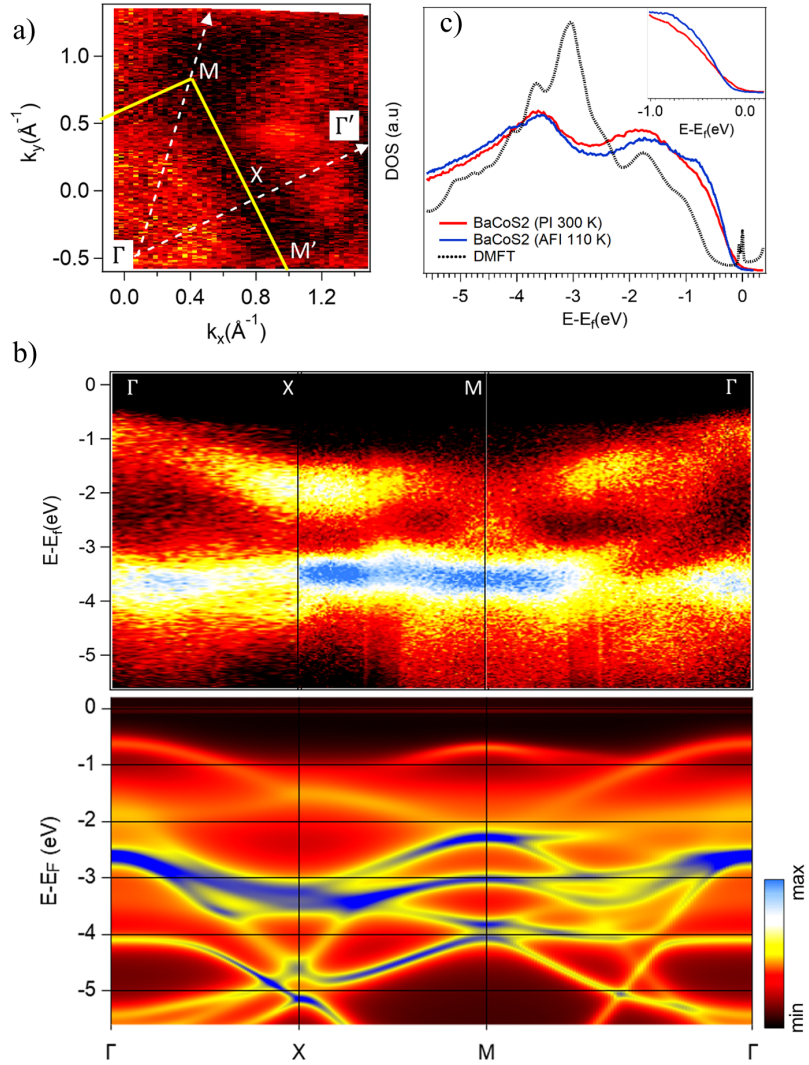


Figure 4.9: (a) Iso-energy surface of BaCoS<sub>2</sub> at  $E-E_f = -1.23$  eV. The border of the Brillouin zone is shown with a yellow contour and the high symmetry directions are shown with white arrows. (b) Top panel: A series of ARPES spectra along the high symmetry directions for the PI phase. Bottom panel: The DMFT calculations of the band structure. (c) The density of states of BaCoS<sub>2</sub> in the AFI phase ( $T=110$  K) and PI phase ( $T=300$  K) compared with the DMFT calculation. The inset is a zoom to the DOS for the AFI and PI phases.

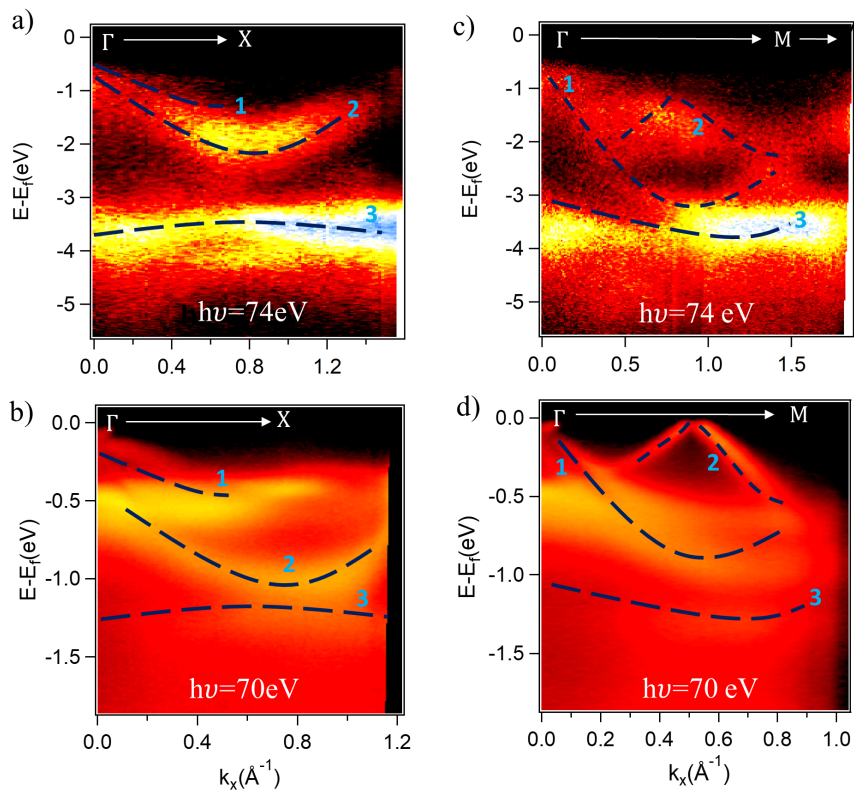


Figure 4.10: Comparison between  $\text{BaCoS}_2$  (top panel) and  $\text{BaNiS}_2$  (bottom panel). The dashed lines are guide to the eyes. (a) and (b) Along the  $\Gamma X$  direction the band number 2 and 3 get closer to each other at  $\sim 0.8 \text{ \AA}^{-1}$ . (c) and (d) A remnant of the Dirac cone in  $\text{BaNiS}_2$  (band number 2) can be detected on the band dispersion of  $\text{BaCoS}_2$ .



# 5 | Out-of-equilibrium electron dynamics of Dirac carriers

## 5.1 Introduction

In this chapter, I present the out-of-equilibrium electron dynamics of  $\text{BaNiS}_2$  studied by means of time resolved-ARPES and time-resolved optical reflectivity techniques. In the previous chapter I showed that the rich equilibrium state of  $\text{BaNiS}_2$  has a twofold importance; first, it presents enhanced electron-electron correlation and second, it hosts massless Dirac fermions as a result of entangled interplay of the crystal symmetry and topology of the electron wave function. Therefore, it is very intriguing to decouple the electrons from other degrees of freedom by driving the system out-of-equilibrium and to study the consequence on the Dirac cone or electronic correlations. Importantly, we are inspired by the idea of manipulating the Dirac cone in  $\text{BaNiS}_2$  by transiently depopulating the orbitals that are responsible for the formation of the Dirac fermions close to the Fermi level and photoexciting them to other orbitals. It is also interesting to observe the possible effect of the electric field, c.f. subsection 2.4.3, on the Dirac cone.

## 5.2 Time-resolved ARPES

With the aim of following the hot Dirac carrier dynamics in  $\text{BaNiS}_2$ , I performed some time-resolved ARPES experiments. A clean surface of  $\text{BaNiS}_2$  normally lasts less than 12 hours after cleavage. On the other hand, in order to avoid multi-photon process I had to work with relatively low pump fluences.

The well defined orbital character of the linearly dispersing bands along the  $\Gamma\text{M}$  direction (see paragraph 4.2.2.2), allowed me to selectively follow the dynamics of each branch by suitable polarization of the probe light. Figure 5.1 (a) and (c) show the reference images of the  $d_{z^2}$  and  $d_{x^2-y^2}$  bands without pump. For these experiments I used a thin BBO crystal ( $20 \mu\text{m}$ ) for the fourth harmonic generation to maintain a good time resolution, however the energy resolution is less than the orbital-resolved bands that I introduced previously. The experiments were performed at 130 K with the pump fluence of  $0.2 \text{ mJ/cm}^2$ . The polarization of the pump pulse is always set at  $s$  because it penetrates farther in the bulk of the sample. This assures that the probe pulse sees a homogeneously pumped area. Figure 5.1 (b) and (d) show a series of difference tr-ARPES spectra. In each spectrum, the ARPES yield at a negative delay is subtracted from the one at a given positive delay. The negative delay corresponds to when the probe pulse arrives before the pump pulse— that is, when no photoexcitation has taken place yet. In our case, the negative delay is  $-1 \text{ ps}$ . The red and blue signals in the tr-ARPES difference images correspond to the gain and loss of signal, respectively. The chemical potential does not shift when photoexciting the system, so the gain of the signal above the Fermi level is uniquely

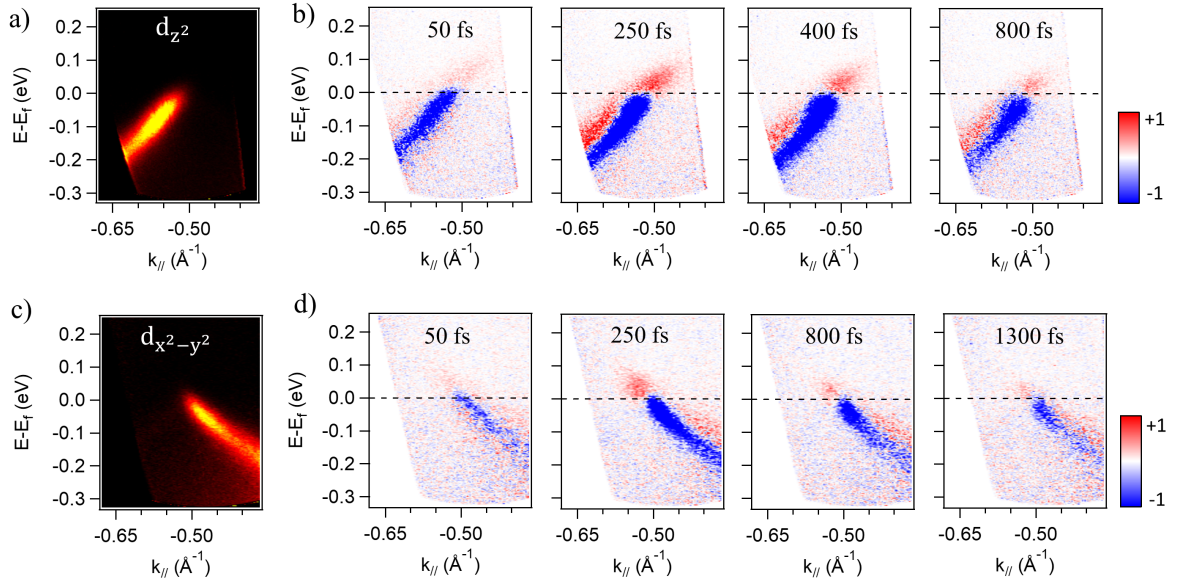


Figure 5.1: (a) ARPES reference image for the out-of-plane  $d_{z^2}$  band. (b) Difference tr-ARPES images before and after photoexcitation. The red and blue signal show gain and loss of signal, respectively. A non-rigid shift of the band below the Fermi level is observed upon photoexcitation. (c, d) Evolution of the in-plane  $d_{x^2-y^2}$  band for different time delays.

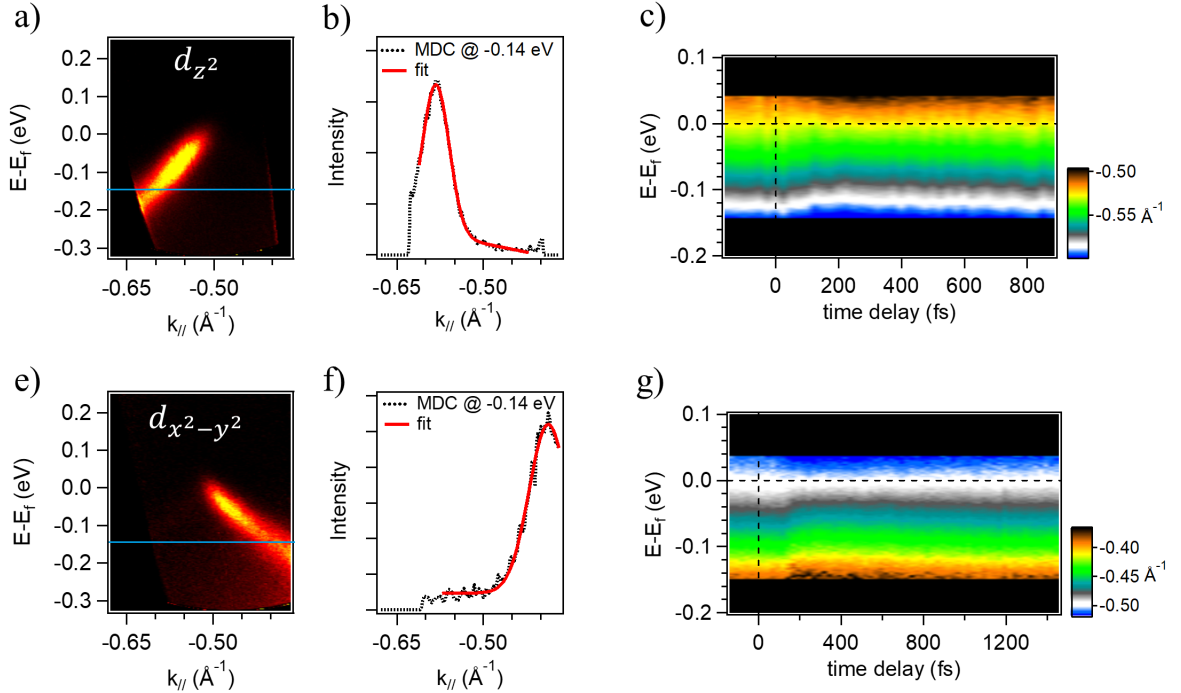


Figure 5.2: Time-resolved dynamics of the shape of the bands. (a)  $d_{z^2}$  band. (b) The MDC at  $E-E_f = -0.14$  eV that is shown by a blue line in the ARPES image. The red curve shows the fit with a Gaussian function and a linear base line. The center of the Gaussian shows the wavevector for each binding energy. In this way, the band dispersion can be reconstructed for each time delay. (c) Stacking of the reconstructed band dispersion for all delays. The intensity at each point shows the position of the wavevector for that point in the  $E-t$  plane. The bottom panel shows the same procedure for the  $d_{x^2-y^2}$  band.

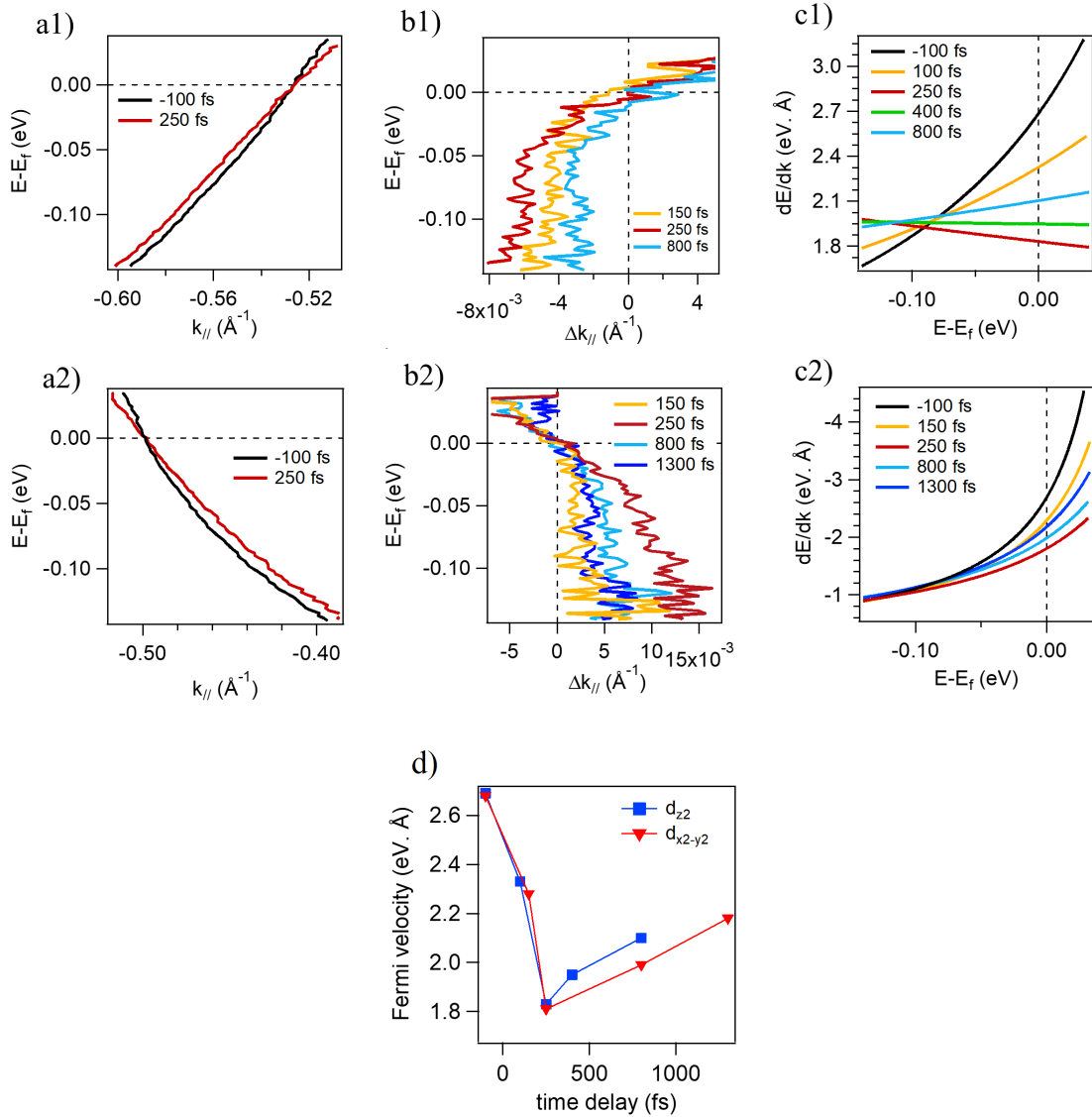


Figure 5.3: Dynamics of the Dirac cone. (a1)  $d_{z^2}$  band: the reconstructed band dispersion,  $E(k)$ , before and after arrival of the pump pulse. This is obtained by a vertical line profile from figure 5.2 (c). The band crossings at the Fermi level does not show any shift and remains still for all time delays. (b1) The photoinduced renormalization of the band for different time delays. (c1)  $dE/dk$  curves. Figures a2 - c2 show the same study on the  $d_{x^2-y^2}$  band. (d) Evolution of the Fermi velocity for both bands. The Fermi velocity decreases up to 250 fs.

attributed to the presence of excited hot electrons in the previously unoccupied states.

Now, if for instance we focus on figure 5.1 (b), we observe that at 50 fs after the arrival of the pump pulse some electrons from higher binding energies are excited to the states in the continuity of the  $d_{z^2}$  band above the Fermi level while the electrons of this band are excited to  $\sim 1.5$  eV above the Fermi level that is inaccessible in the energy window of our experiment. These electrons scatter with each other, lose their energy, and cascade down to lower energy states in the conduction band. At around 250 fs, the number of the excited electrons close to the Fermi level reaches its maximum. These excited electrons then gradually lose their energy and relax back to their initial equilibrium states by different relaxation channels such as emitting optical and acoustic phonons, c.f. paragraph 2.2.1. If we integrate all states above the Fermi level, the decaying dynamics suggests two time scales, 0.4 ps and 1 ps, as shown in figure 5.4 (b). The physical interpretation of these time scales will be discussed later.

Coming back to figure 5.1 (b) and (d), we also interestingly observe some red signal below the Fermi level along with the blue signal. This red signal unveils a photo-induced renormalization of the band while the blue signal shows not only the left behind holes from the excited electrons but also the position of the band before photoexcitation. These images give the impression of a non-rigid (k-dependent) and time-dependent shift of the bands. In order to study the chronological evolution of the band dispersion  $E(k,t)$ , I have sliced the ARPES yield for each time delay into momentum distribution curves (MDC's). The procedure is the same as introduced in paragraph 4.2.2.1, i.e. the photoemission intensity peak was fitted by a Gaussian with a linear background, figure 5.2 (b). This gives the  $E(k)$  for one time delay. By stacking all of the  $E(k)$  curves a 2D map is acquired in the energy and time-delay plane and the intensity of each point shows the wavevector position, figure 5.2 (c) and (g).

Figure 5.3 (a1) shows the example of the reconstructed shape of the  $d_{z^2}$  band before (-100 fs) and after (250 fs) the arrival of the pump pulse. Figure 5.3 (a2) shows the same for the  $d_{x^2-y^2}$  band. We obviously observe a k-dependent shift of the bands, more interestingly the farther from the Fermi momentum  $k_F$ , the more important is the change in the wavevector. We significantly observe that the position of the  $k_F$  at the Fermi level does not show any shift and remains still for all time delays. This can be further clarified by studying the renormalization of the bands for different time delays as shown in figure 5.3 (b1) and (b2). These curves are obtained by subtracting the  $E(k)$  curves at the negative delay from the  $E(k)$  curves at positive delays. Therefore, each curve corresponds to a given time delay and shows the shift in the wavevector for each binding energy. We observe that the slope of each band decreases upon photoexcitation, reaches its maximum around 250 fs (red curves) and then gradually recovers to the equilibrium normalization. Please note that the continuity of the linearly dispersing bands was maximally populated at 250 fs that seems to be correlated with largest renormalization of the band. At this point, it is important to show how the velocity of the band changes with respect to the time delay. For this purpose, I first fitted the  $E(k)$  curves by a polynomial function, c.f. paragraph 4.2.2.1. Hence, I studied the temporal evolution of the band velocity via  $dE(k)/dk$  curves as shown in Figure 5.3 (c1) and (c2). In the end, I also show the evolution of the Fermi velocity for both bands in figure 5.3 (d). The Fermi velocity reaches a minimum value at 250 fs. The dynamics of the Fermi velocity is almost the same for both in-plane and out-of-plane bands.

In order to better visualize the Dirac cone deformation upon photoexcitation with pump pulses, I combined separate studies on the  $d_{z^2}$  and  $d_{x^2-y^2}$ , figure 5.4 (a). In the equilibrium, the Dirac node is located at 20 meV above the Fermi level and at  $k_{\parallel} = 0.52 \text{ \AA}^{-1}$ . The Dirac cone reacts to the pump by getting wider however, the band crossing points at the Fermi level remains intact. This implies that the Dirac node slightly shifts closer to the Fermi level. I show in figure 5.4 (c)

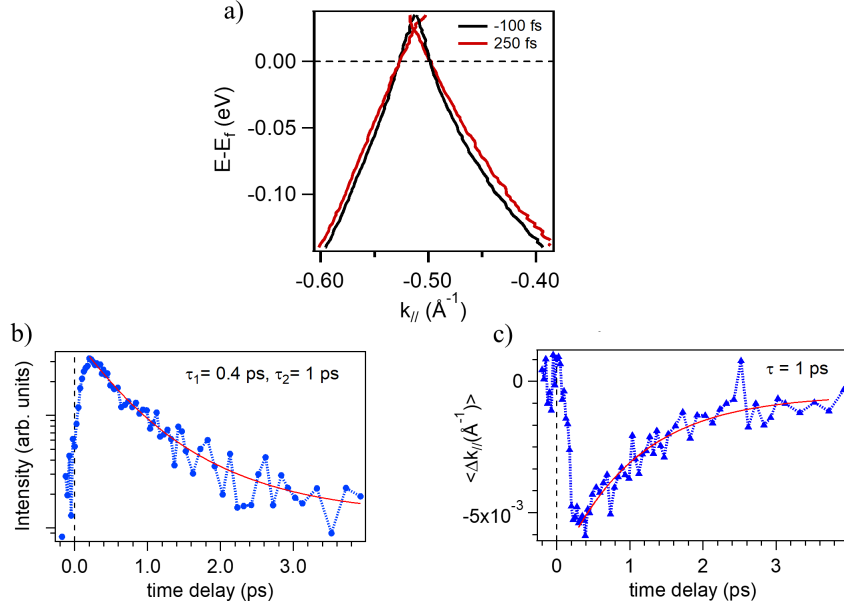


Figure 5.4: (a) By combining previous studies, I show how the Dirac cone evolves upon photoexcitation. (b) The dynamics of the excited states above the Fermi level. (c) The averaged shift of the band shows a dynamics of 1 ps starting from 250 fs.

the average shift of the wavevector  $\langle \Delta k \rangle$ , for the states below the Fermi level within 100 meV. The decay toward the equilibrium occurs with a single time constant of 1 ps.

I would like to add some words on the dynamics of the Dirac point. In view of precisely revealing the dynamics of the location of the Dirac point in the energy-momentum space, I also performed experiments with a mixed polarization of the probe pulse, i.e. an intermediate polarization between  $s$  and  $p$ . The experimental conditions are the same as before. Figure 5.5 (a) shows the ARPES image for a negative delay and figure 5.5 (b) shows the image at 250 fs when the states above the Fermi level are maximally populated. Please note that even a saturated logarithmic color scale does not allow a clear visualization of the continuity of the linearly dispersing bands. In fact, it is not possible to draw a clear conclusion on the position of the Dirac cone with respect to time delay. Moreover, it is also not possible to increase the pump fluence to excite more electrons because of multi-photon emission.

In this section, we observed that deformation of the Dirac cone is triggered shortly after the impulsive injection of energy merely into the electrons. One important issue that is frequently addressed in ultrafast dynamics studies, is to which extent a photoinduced effect is different from a purely thermal effect. Moreover, the importance of this difference is directly related to the strength of electron-phonon coupling. In view of decoupling the thermal and photoinduced effects on the ultrafast renormalization of the Dirac cone, I performed some time-resolved optical reflectivity experiments on  $\text{BaNiS}_2$  as it is the most direct technique that allows us to estimate the electron-phonon coupling constant. In parallel, I also studied the evolution of the linearly dispersing bands upon heating by means of high-resolution laser-based ARPES.

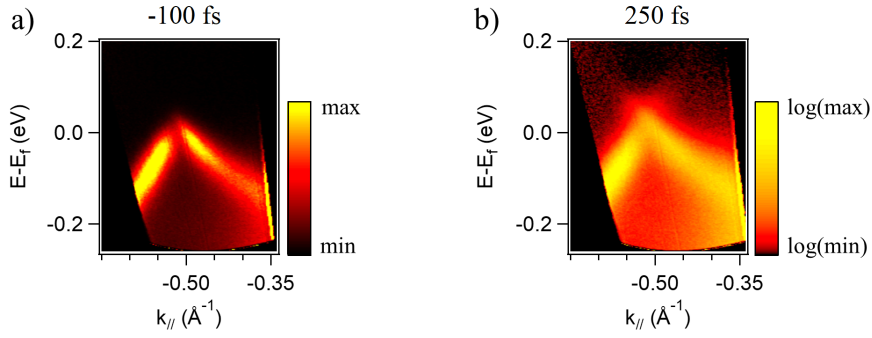


Figure 5.5: Dirac cone of  $\text{BaNiS}_2$  studied by 6.28 eV as the probe pulse. The polarization of the light is not well defined so that both branches are observed. (a) Negative delay image. (b) 250 fs after the arrival of the pump pulse. The color scale is maximally saturated in the logarithmic scale in order to better visualize the excited states above the Fermi level.

## 5.3 Time-resolved optical spectroscopy

### 5.3.1 Observation of coherent optical phonons in $\text{BaNiS}_2$

The time-resolved optical spectroscopy measurements were done at the T-Rex beamline (see paragraph 3.4.3.5) at the base temperature of 80 K and with different fluences of the pump pulse. Figure 5.6 (a) shows the time- and spectrum- resolved optical response of  $\text{BaNiS}_2$  upon photoexciting with  $4 \text{ mJ/cm}^2$ . The 2D spectrum acquired in the experiments covers wavelengths from 400 nm up to  $1.5 \mu\text{m}$ . The spectrum reveals a decay dynamics accompanied by oscillations of coherent optical phonons. Figure 5.6 (b) shows the photoinduced changes in the reflectivity for several wavelengths. Each curve corresponds to a horizontal line profile in the continuum spectrum. The curves are normalized with respect to their maximum in order to better visualize the relaxation dynamics differences. We observe that the decay time is different for each wavelength since they probe different part of the joint density of states<sup>1</sup> by different optical transitions. On the other hand, the maximum of the reflectivity changes occurs at around 250 fs consistently with the tr-ARPES data.

In order to study the frequency of phonons, I chose the reflectivity at 996 nm, figure 5.7 (a). The frequency of optical and acoustic phonons does not depend on the wavelength of the probe. However, some wavelengths can have better optical efficiency allowing for better detection of phonons. The subtraction of an exponential fit from the raw data allows to decouple the oscillations from the decaying part of the spectrum as shown in figure 5.7 (b). In this curve, we can observe a combined effect of optical phonons accompanied by an acoustic wave that propagates in the material with a longer period. The period of the acoustic wave is found to be 9 ps. By subtracting its contribution, we can now focus only on the optical phonon modes as shown in figure 5.7 (c). At first glance, the spectrum reveals two phonon modes. The Fourier transform of these optical oscillations, figure 5.7 (d), presents two optical modes with frequencies of 3.07 and 5.14 THz. The latter is assigned to the fully symmetric  $A_{1g}$  mode as compared to reported value found in the literature for doped samples [169].

The lifetime of each mode can be obtained by fitting the oscillations with two damped harmonic oscillators with the amplitude and phase of  $A_j$  and  $\varphi_j$ , respectively:

<sup>1</sup>The joint density of states in optical calculations refers to the density of states of interband transitions in optical absorption phenomenon.

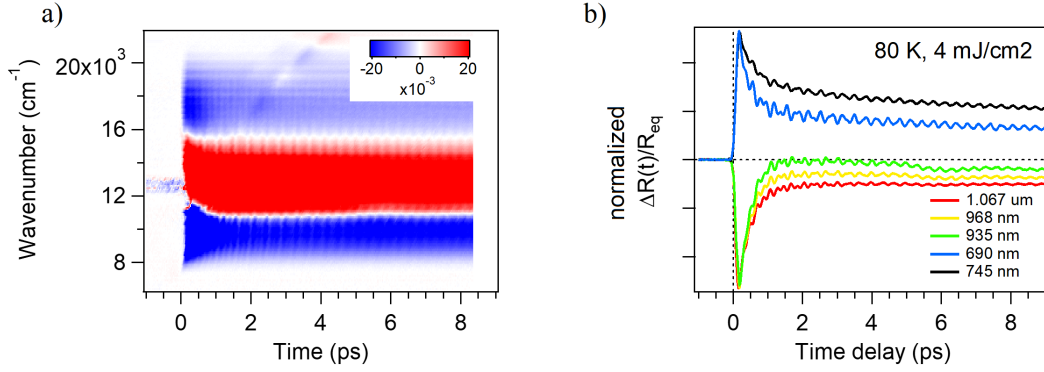


Figure 5.6: (a) Spectrum- and time-resolved reflectivity of  $\text{BaNiS}_2$  with the fluence of  $4 \text{ mJ/cm}^2$ . (b) Photoinduced reflectivity changes for several wavelengths obtained by horizontal line profiles in the continuum spectrum.

$$I(t) = A_1 * \sin(2\pi f_1 t + \varphi_1) * \exp(-t/\tau_1) + A_2 * \sin(2\pi f_2 t + \varphi_2) * \exp(-t/\tau_2) \quad (5.1)$$

In this equation,  $f_j$  is the frequency and  $\tau_j$  is the time decay constant for each mode, respectively. Figure 5.7 (e) shows the fit. We obtain a fast decay time of 1 ps for 5.14 THz  $A_{1g}$  mode and a slower constant of 7.3 ps for the mode at 3.07 THz. I also performed the experiment for different fluences: 0.2, 0.8, 2, and  $4 \text{ mJ/cm}^2$  (figure 5.8). The frequencies do not show a clear dependence on the fluence. However, at the high fluence of  $4 \text{ mJ/cm}^2$  there is a drop of the frequency that is probably due to accumulated heat effect of the pump pulses.

### 5.3.2 Electron-phonon coupling constant

In order to get a wider insight on the dynamics of the Dirac cone, I also performed some time-resolved optical reflectivity experiments with the same fluence as we applied for the tr-ARPES measurements, i.e.  $0.2 \text{ mJ/cm}^2$ . Figure 5.9 (a) shows the  $\Delta R(t)/R$  for  $1.06 \mu\text{m}$  after pump excitation. The optical phonons are not very clear due to low pump energy excitation. This signal is fitted by the 3-temperature model (3TM), c.f. subsection 2.2.3, as explained below.

In the previous subsection, I showed the frequency of the optical phonon modes for different fluences. This gives us a good estimate of the mean frequency of the phonons to which excited electrons get coupled after photoexcitation. By solving the 3TM, I can derive the values of the coupling constant between the electrons and hot phonons (that is traditionally called the electron-phonon coupling constant) as well as between the electrons and cold phonons. These parameters are shown by  $\lambda_1$  and  $\lambda_2$ , respectively. Here, I should mention that the basic assumption behind the 3TM was that there is only one phonon mode at frequency  $\Omega_0$ , while here  $\text{BaNiS}_2$  obviously presents two modes. To be accurate mathematically, it means that one has to add another rate equation to the 3TM that accounts for the second optical mode. Nonetheless, this might result in overfitting and not necessarily correct set of parameters. To avoid this problem, it seems logical to take the average of the phonons energy. The heat capacity of the lattice and electrons are found in [157] and the thermal diffusion along the z-axis is not relevant in our case due to the quasi 2D nature of  $\text{BaNiS}_2$ . I present in the following table the experimental parameters to be introduced in the 3TM model:

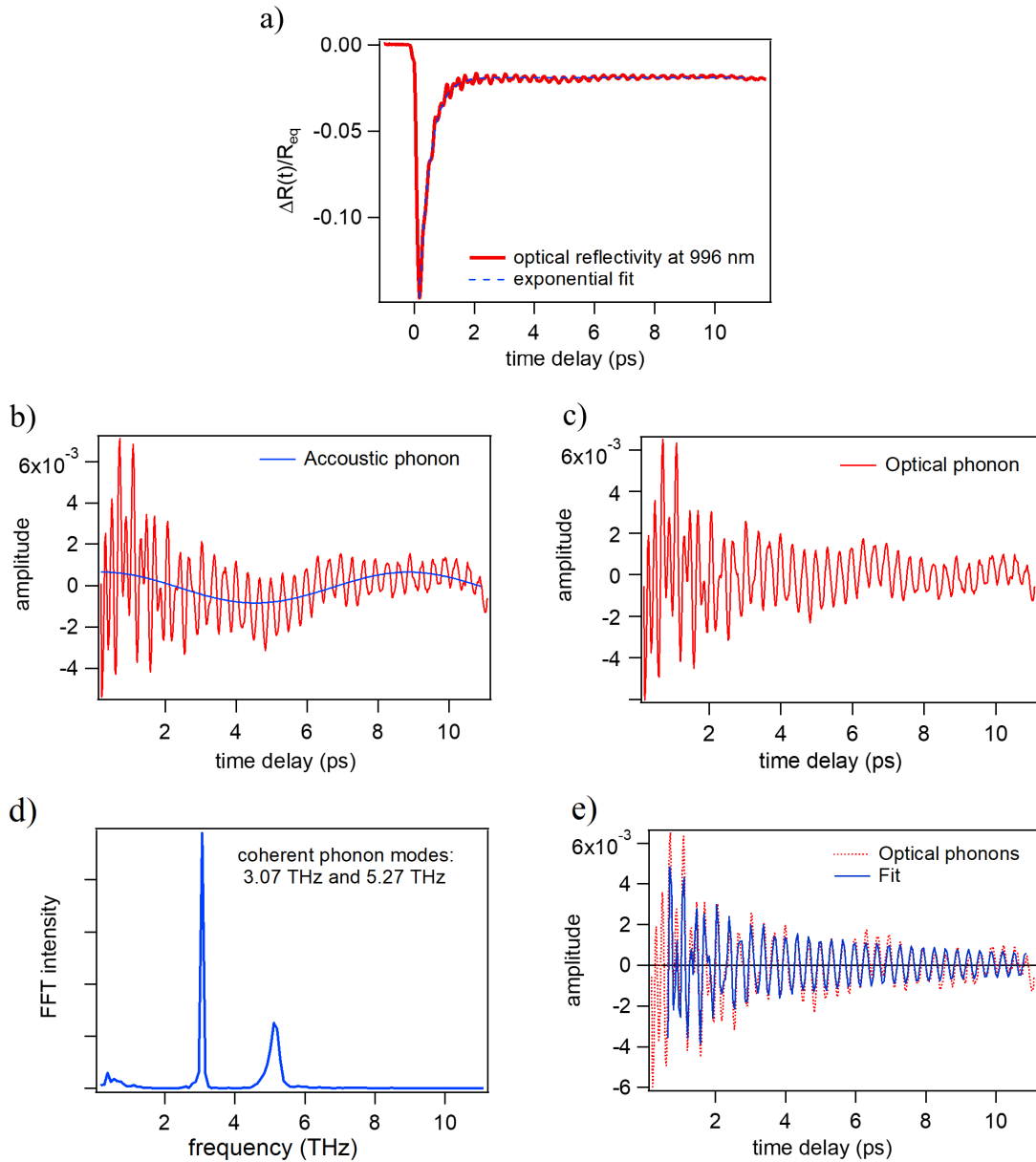


Figure 5.7: (a) Time-resolved changes in the reflectivity of 996 nm. The raw data was fitted by an exponential curve. (b) Subtraction of the exponential fit from the data decouples the dynamics from the optical and acoustic phonon modes. The acoustic phonon presents a period of  $\sim 9$  ps. (c) After subtracting the contribution of the acoustic phonon, we can merely study the coherent oscillation of the optical phonons. The frequency of each mode can be found by the Fourier transform as shown in (d). A simple model, as explained in the text, allows us to follow to decay time scale for each observed mode (e). The 5.14 THz decays at a time scale of 1 ps and the 3.07 THz mode, decays slower after 7.3 ps.

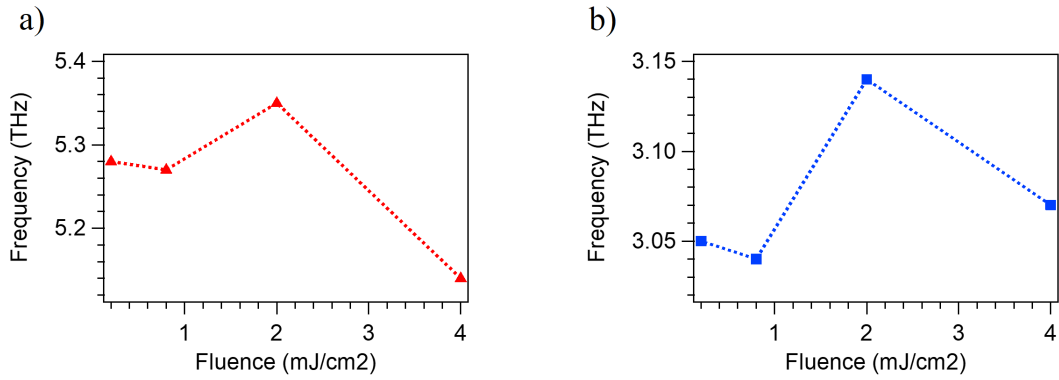


Figure 5.8: The evolution of the optical phonon modes with respect to the pump fluence.

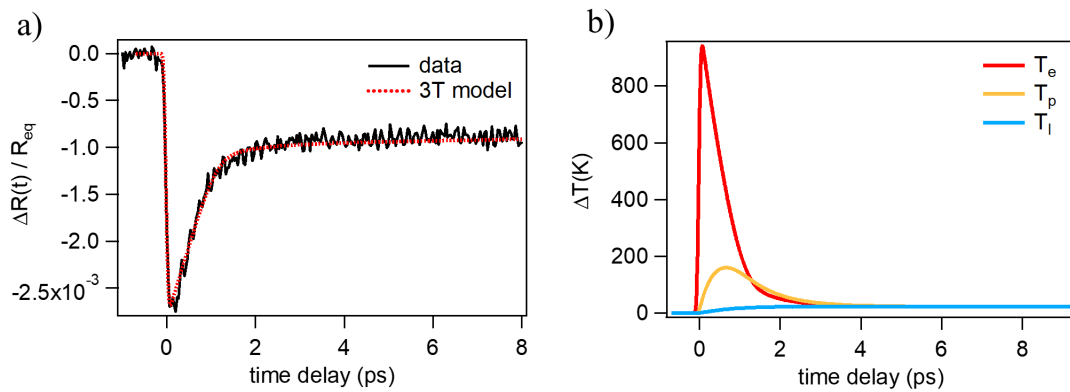


Figure 5.9: (a)  $\Delta R(t)/R$  at  $1.06 \mu\text{m}$  for the pump fluence of  $0.2 \text{ mJ/cm}^2$ . The dashed red curve is the numerical simulation based on the 3-temperature model. (b) Temporal temperature evolution of the electrons (red curve), hot phonons (orange curve), and cold phonons (blue curve) after photoexcitation. The electron-phonon coupling is found to be 0.13.

pump fluence(mJ/cm <sup>2</sup> )	FWHM <sub>t</sub> (fs)	FWHM <sub>d</sub> (μm)	γ <sub>e</sub> (J/mol.K <sup>2</sup> )	α (cm <sup>-1</sup> )	T (K)
0.2	80	170	0.00215	1.87×10 <sup>5</sup>	80

Table 5.1: The experimental parameters in the time-resolved reflectivity measurements.

where FWHM<sub>t</sub> and FWHM<sub>d</sub> are the laser temporal and spatial width, respectively. γ<sub>e</sub> is the linear heat capacity coefficient of the electrons and α is the absorption coefficient of BaNiS<sub>2</sub> at 800 nm.

We can now study the temperature evolution of different degrees of freedom as shown in figure 5.9 (b) based on the 3TM. The change of the reflectivity is then calculated according to equation 3.24. We notice a good agreement between the experiment and theory. The relevant parameters used to simulate the transient reflectivity changes are given below:

Ω <sub>0</sub> (eV)	λ <sub>1</sub>	f	τ <sub>β</sub> (ps)	τ <sub>c</sub> (ps)	λ <sub>2</sub>
0.017	0.13	0.05	1	100	0.09

Table 5.2: Averaged phonon energy, electron-phonon coupling constant, fraction of strongly coupled phonons, anharmonic decay of hot phonons, heat diffusion time constant from the surface to the bulk, and coupling strength of the electrons to cold phonons as obtained by three temperature model simulations.

I find the average phonon energy of 0.017 eV (4.11 THz) that is very close to the average frequency of the observed optical modes for 0.2 mJ/cm<sup>2</sup>. The electron-phonon coupling constant λ<sub>1</sub> is equal to 0.13 that is a moderate coupling constant. We also observe that the anharmonic decay of hot phonon occurs at a time scale of 1 ps and eventually the dissipation of heat from the surface towards the bulk takes about 100 ps. The anharmonic decay time constant recalls the time constant that we have encountered in the time-resolved ARPES studies in the previous section: the hot carriers relax with a time constant of 400 fs and 1 ps.

We can now give an interpretation for each of these timescales. The first constant can be viewed as the time that takes for the out-of-equilibrium electrons to get coupled to the hot phonons and to evacuate part of their energy through them. After that, the hot phonons dissipate their energy by scattering with other lattice modes (cold phonons) with the anharmonic decay timescale of 1 ps. Moreover, the Dirac cone renormalization also takes place within 1 ps, c.f. figure 5.4 (c). These results imply that the relaxation of the Dirac cone and the anharmonic decay of phonons are related to each other.

In order to complete our understanding of the dynamics of the Dirac cone upon photoexcitation, it is now important to study the temperature dependent behavior of the equilibrium band structure.

## 5.4 Photoinduced vs. thermal effects

The 3TM applied to our data also suggests that the electronic and lattice temperatures converge for time delays longer than 3 ps after photoexcitation with 0.2 mJ/cm<sup>2</sup>, figure 5.9 (b). This *a priori* rules out the doubt that the Dirac cone renormalization at a sub-picosecond time scale could be explained as a thermal effect. To further clarify this point and to disentangle the photoexcitation effects from the thermal ones, I did a series of temperature-dependent ARPES experiments for each branch of the Dirac cone in the temperature range of 40 K to 260 K. The

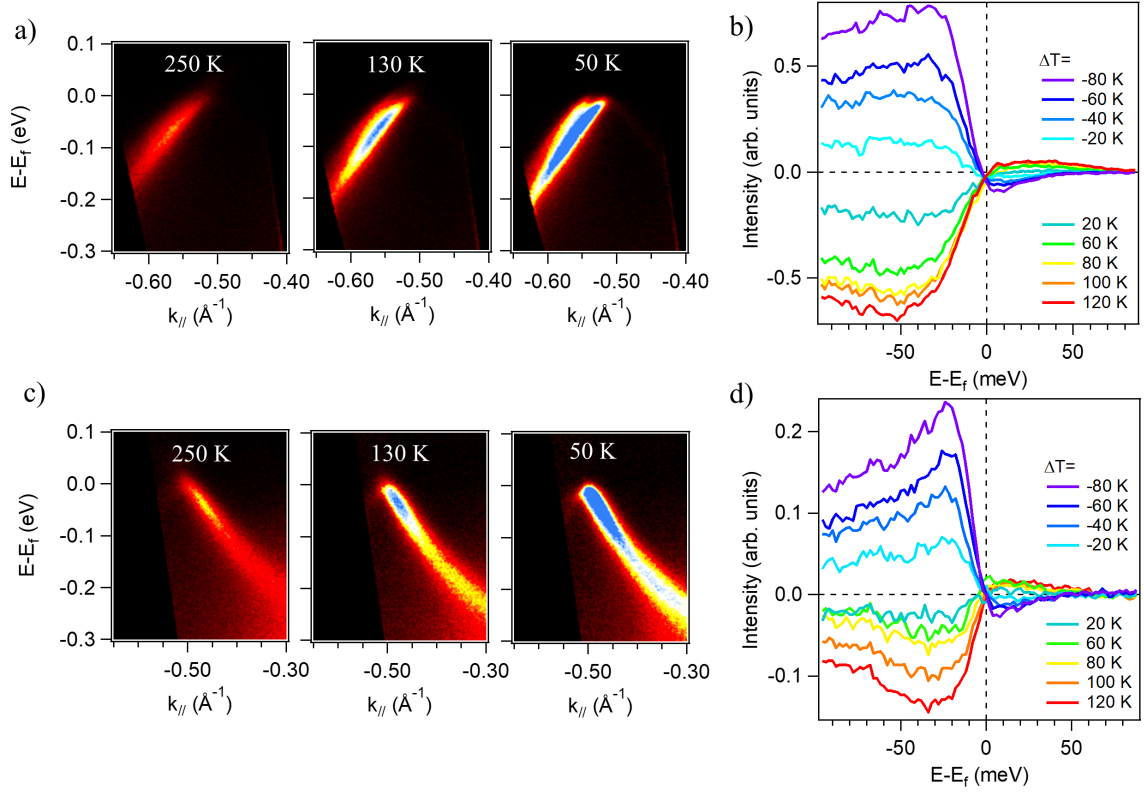


Figure 5.10: Temperature dependent ARPES spectra for (a)  $d_{z^2}$  and (c)  $d_{x^2-y^2}$  band. (b) and (d) show the spectral weight evolution with respect to 130 K. These curves are obtained by subtracting the DOS at 130 K from the DOS at higher and lower temperatures.

experiments were performed with the high-resolution laser based-ARPES setup as explained before.

In figure 5.10 (a) and (c), we see that by increasing the temperature, the intensity of the spectra increases due to the overall increase of the quasiparticle weight. Although with the photon energy of 6.28 eV we have a limited window in the binding energy, we remember from section 4.4 that the spectral weight transfer with respect to temperature actually comes from the higher binding energies. Since the time-resolved ARPES measurements were all performed at the base temperature of 130 K, I study the evolution of the density of states (DOS) with respect to this temperature. In order to do that, I take the DOS of each band for all temperatures and then I subtract the DOS at 130 K from them. The results are shown in figure 5.10 (b) and (d).  $\Delta T$  shows the temperature difference with respect to 130 K. We clearly observe the quasi particle weight gain (loss) while decreasing (increasing) the temperature. These temperature difference spectra are farther compared with the photoinduced changes in the DOS.

Now, I show the evolution of the band structure with respect to temperature. By the same routine as introduced before, I reconstruct the band dispersion of the  $d_{z^2}$  and  $d_{x^2-y^2}$  bands for different temperatures and the results are shown in figure 5.11 (a) and (c), respectively. I chose the polynomial fit of the  $E(k)$  curve at 130 K, and I subtracted it from other curves at higher temperatures. This gives the temperature-induced renormalization of the bands— that is, the change in the wavevector position for each binding energy while varying the temperature. Figure 5.11 (b) and (d) correspond to this effect for a  $\Delta T=120$  K ( $T_f=250$  K). A non-rigid shift in wavevector is observed similar to the time-resolved experiments. Moreover, the bands do not

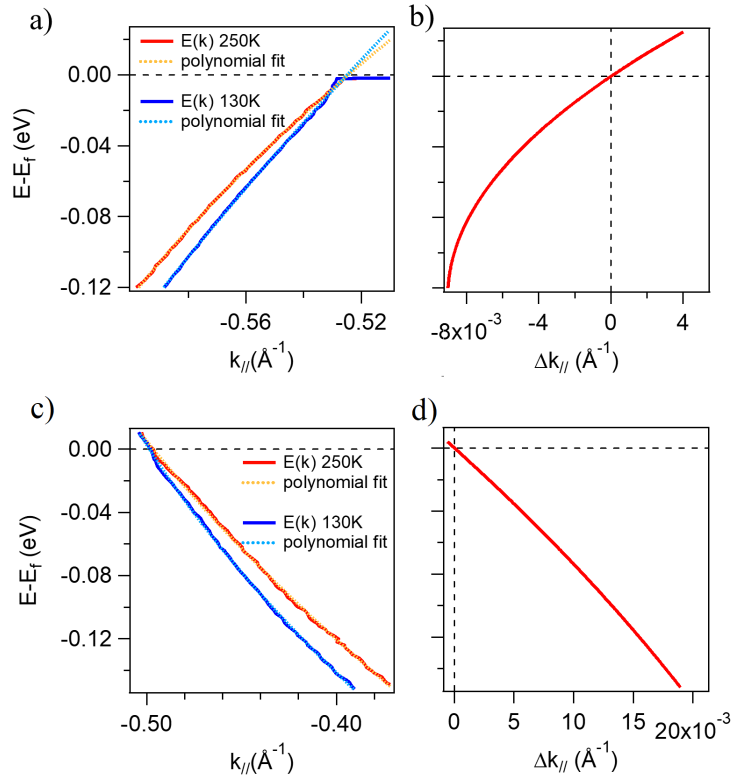


Figure 5.11: Band dispersion for different temperatures. (a)  $d_{z^2}$  band. The solid lines show the  $E(k)$  for 130 K and 250 K, and the dashed lines are the polynomial fits. (b) Temperature-induced changes in the band. (c, d) The effect of the temperature on the  $d_{x^2-y^2}$  band.

show a clear shift at the  $k_F$ . The non-rigid shift of the bands with respect to temperature has already been observed in other systems, in particular in iron-pnictides [17, 109]. However, those compounds reveal some changes in the position of the  $k_F$  due to the interband interactions that makes thermal excitations among the narrow bands possible.

At this point, we have enough ingredients from both time-resolved ARPES and temperature dependent ARPES studies. In figure 5.12, I present a comprehensive comparison between the thermal and photo-induced effects that are shown by solid lines and dashed lines, respectively. The  $\Delta T$  shows the increase of the temperature starting from 130 K and the  $\Delta t$  shows the time delay after the arrival of the pump pulse. In figure 5.12 (a) and (b), we notice that photoexcitation and heating induce qualitatively similar behavior of the Dirac cone however, only at time delays longer than 4 ps (for fluence of  $0.2 \text{ mJ/cm}^2$ ) do they produce quantitatively the same effect. However, the roots that end up in the same effect are different. The evolution of the density of states shows that upon photoexcitation, the electrons are excited to the unoccupied states above the Fermi level while with heating, the electrons close to the Fermi level are transferred to the incoherent part of the spectrum (higher binding energies). The temperature effects due to photoexcitation can be explained with the support of the 3TM, figure 5.9 (b). For instance, this model showed that at about 800 fs, we should have  $\Delta T_e \sim 300 \text{ K}$  and  $\Delta T_l \sim 100 \text{ K}$ . We clearly see that none of the thermally induced band shifts creates the same effect as photoexcitation for this time delay. However, at 4 ps the electronic and lattice temperatures have converged and the

renormalization of the band is equal to a temperature raise of  $\sim 25$  K which corresponds to the heat deposited by laser pulses at  $0.2 \text{ mJ/cm}^2$ .

I also compare the photoinduced changes in the density of states (solid lines) with the thermal effects, figure 5.12 (c) and (d). The density of states at 130 K has been subtracted from its counterpart at different temperatures and the result is shown in the set of solid-line curves. We consistently observe that at about 4 ps the excited states have relaxed and the systems heats up to  $\sim 25$  K further while before this time scale, it is not straightforward to define an electronic temperature.

Here, it is worth mentioning that the traditional way of determining the temperature of excited electrons during the relaxation process, is to adjust a Fermi-Dirac distribution to the spectral function and to deduce the temperature. This procedure remains correct as long as the density of states does not change with temperature. For instance, for linearly dispersing bands in non-correlated materials, this method has been widely used [58, 78, 177]. On the contrary, this routine cannot be applied to correlated materials since the density of states itself changes with respect to temperature [17, 96, 109, 144]. BaNiS<sub>2</sub> falls in this category and its temperature-dependent density of states was presented in section 4.4. By heating, the spectral weight close to the Fermi level is transferred to higher binding energies while with photoexcitation the electrons are excited into the states above the Fermi level making it *a priori* difficult to assign a temperature to the electrons. However, by leaning on some simple phenomenological models, as in our case the 3TM, one can gain some insight about the ultrafast temperature evolution of the system.

## 5.5 Discussion

With the above-mentioned coherent results, it is thus logical to think that the non-thermal dynamics of the Dirac cone renormalization upon photoexcitation is initiated purely by an electronic effect that is then stabilized by the coherent optical phonons thanks to the moderate electron-phonon coupling constant ( $\lambda = 0.13$ ). The decay of these excited phonons is accompanied by the relaxation of the Dirac cone towards a thermal state that depends on the applied pump fluence.

The non-rigid time-dependent shift of the bands was also observed in others systems. For instance, the photoexcited Bi<sub>2</sub>Sr<sub>2</sub>CaCu<sub>2</sub>O<sub>2+ $\delta$</sub>  above the  $T_c$ , shows ultrafast changes in the occupied electronic band structure notably at the Fermi momentum [151]. The authors attributed the general photoinduced modification of the band structure to a light-induced change in the electronic interaction underlying the dressing of the quasiparticles. The fact that the velocity of the band increases (the effective mass decreases) in this cuprate superconductor for a few tens of femtoseconds is suggestive of a reduction of the electronic correlation that is purely driven by electron excitation and does not involve any optical phonon. The change in the  $k_F$  was also explained by an effective photodoping due to particle-hole asymmetry. Another example is the photoinduced changes of the electronic band structure in bismuth [137]. The bands show a k-dependent shift towards higher binding energies because of the reduced ion core screening induced by a sudden injection of high energy into electrons. In this case, the non-rigid shift is a result of strong electron-phonon interplay.

The physical interpretation of the band renormalization in BaNiS<sub>2</sub> demands taking into account two important aspects: electronic correlation and Dirac semimetallic state of BaNiS<sub>2</sub>. First, I take into account the electronic correlation in a very simple way and argue that as simple as the explanation of the photoinduced effects might seem to be, it is indeed contradictory. In fact, by photoexciting the Dirac carriers we transiently depopulate the *d*-orbitals at/close to the

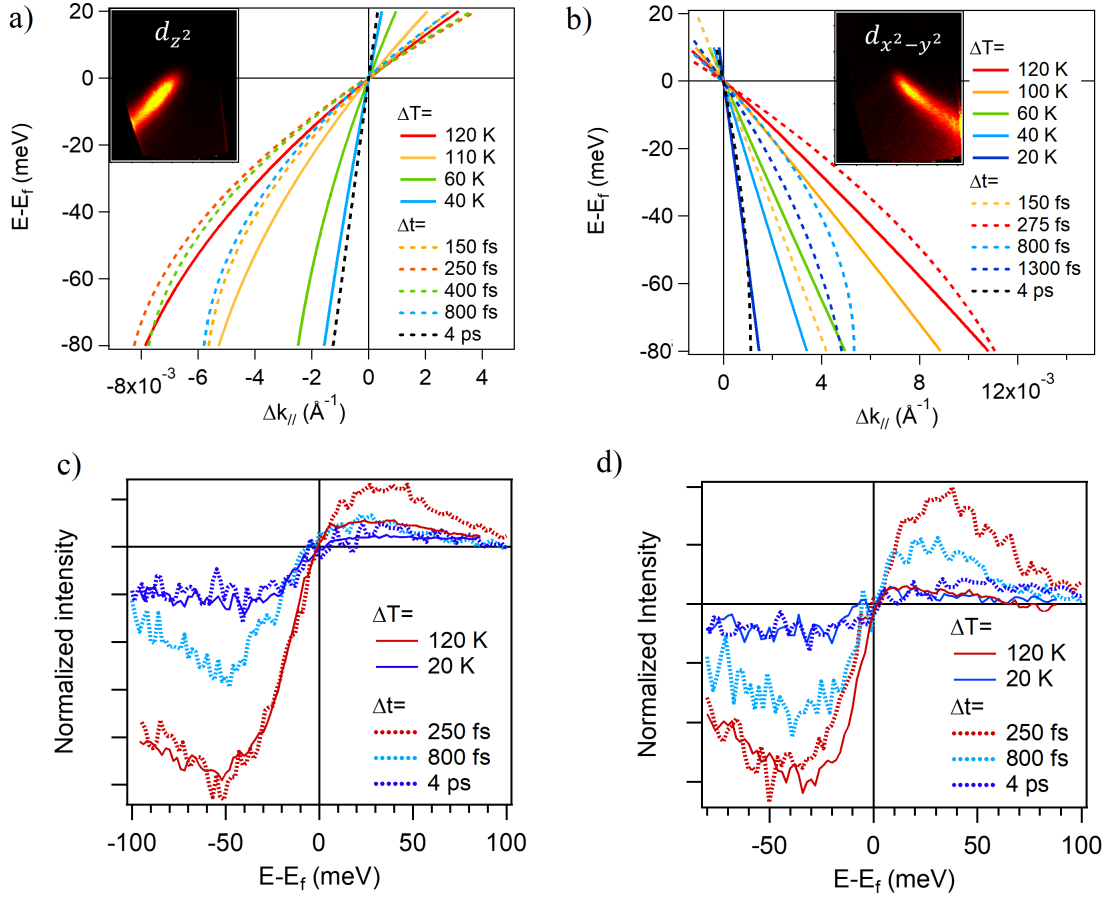


Figure 5.12: Comparison between photo-induced and thermally induced renormalization of the linearly dispersing bands for (a)  $d_{z^2}$  and (b)  $d_{x^2-y^2}$  band. The solid lines show how the slope of the band changes while heating the sample starting from 130 K. The dashed lines shows the photoexcitation impact on the band. Around 4 ps, the electronic and lattice temperatures have converged and the renormalization of the band is equal to a temperature difference of  $\sim 25$  K which is the heat deposited by laser pulses at  $0.2 \text{ mJ/cm}^2$ . (c,d) The photoinduced changes in the density of states (dashed lines) are compared with the thermal effects (solid lines).

Fermi level and the electrons get more delocalized due to the ultrafast injection of energy to them. Therefore, the Coulomb screening increases and the electronic correlation should reduce and one expects that the velocity of the band increases. However, we exactly observe the reverse effect, suggesting that photoexcitation should increase the localization of the electrons by putting them to a particular orbital with enhanced correlation effects. This hypothesis seems to be impossible as  $\text{BaNiS}_2$  is a multiband semimetal with non-localized states below or above the Fermi level. At this point, the protection of the Dirac cone can be one underlying reason to the change of the band dispersion. Another possible scenario can be that by photoexciting the electrons close to the Fermi level, the hybridization of the  $d$  and  $p$  orbitals is modified in an ultrafast way that consequently affects the renormalization of the bands. We have seen in section 4.2 that the strength of this hybridization controls the location of the band crossing as well as the shape of the band. On the other hand, the effect of the electric field on topological insulators has been shown both experimentally and theoretically however, it has remained only theoretically predicted on DSM's with no experimental witness presented so far. I also speculate that the observed ultrafast dynamics of the Dirac cone is related to the electric field of the pump pulse. In particular, we have observed that the  $k_F$  acts as a fixed point around which the slope of the band changes. Therefore, when the slope of the band decreases, the Dirac node is slightly pushed towards the Fermi level. Would it be possible to open the gap by applying stronger pump pulses? In order to describe this effect within a theoretical framework, I have the support of the theorists in SISSA and Paris 6 University and it is part of our ongoing collaborative project.



# 6 | Ultrafast electron and lattice dynamics of $(V_{1-x}Cr_x)_2O_3$

## 6.1 Time-resolved X-ray diffraction

In this section, I complete discussion outlined in subsection 2.3.1 on the time-resolved diffraction part of the article in ref [96].

In order to verify our interpretation on the nature of the transient phonon blue-shift in the photoexcited  $V_2O_3$ , I participated in a series of time-resolved X-ray diffraction (tr-XRD) experiments with sub-ps time resolution at the X-ray pump probe (XPP) end-station of the Linac Coherent Light Source (c.f. paragraph 3.4.2.4). The incidence angle for the 8 keV X-ray beam was 0.6 degrees, while for the optical laser beam it was 12 degrees: this geometry is illustrated in figure 6.1 (a) and allows matching the penetration depths and retaining a temporal resolution of the order of 200 fs. The fluence of the pump pulse is  $8 \text{ mJ/cm}^2$  that is higher than the one applied for the time-resolved photoelectron spectroscopy (tr-PES) at  $1.8 \text{ mJ/cm}^2$ . The reason is that the probing depth of X-rays is much higher than PES so one needs to create higher density of photoexcited electrons uniformly inside the sample. This can be safely done since the photoexcited signal varies linearly with respect to the fluence as it was verified for the tr-PES experiments. I was principally involved in the data analysis of the tr-XRD experiments. The data analysis demanded much care as different issues coming from the SASE instability should have been correctly removed from the signal. The main issues were related to instabilities in the X-ray pulse pointing and intensity as well as the time jitter, c.f. paragraph 3.4.2.3.

Figure 6.1 (b) shows the Bragg reflection peak of the 2.8% Cr-doped  $V_2O_3$  for the (116) direction without pump. The position of the peak does not change up to 4 ps (when the lattice parameters start being modified by the onset of the acoustic wave, c.f. figure 6.2) however, it shows a time-dependent variation of intensity as shown in figure 6.1 (c) for both (116) and (024) direction. If we assume that the symmetry of the crystal stays the same, as confirmed by the fact that only  $A_{1g}$  mode was observed in the time-resolved reflectivity measurements, the diffracted intensity can be simulated by a change of the vanadium Wyckoff position  $Z_v$  and a Debye-Waller factor (c.f. paragraph 3.4.2.3).

The change of the oxygen Wyckoff position affects the peak intensity less than 0.02% for the (116) and about 1% for the (024) peak. On the other hand, the Debye-Waller factor is also only responsible for 0.1% of the intensity change before 4 ps. The distance of the nearest vanadium atoms is given by the relation  $d(V_1-V_4) = (2Z_V - 0.5)c$ , where  $c$  is the lattice constant. The (116) and (024) structure factors vary in opposite directions with  $Z_V$  as shown in figure 6.1 (d). We find that for the insulating phase,  $d(V_1-V_4)$  goes from  $2.744 \text{ \AA}$  to a minimum value of  $2.71 \text{ \AA}$  well before 1 ps. This minimum value is actually very close to the vanadium atoms distance in the paramagnetic metallic phase, i.e.  $2.69 \text{ \AA}$ . This result elucidates the photoinduced

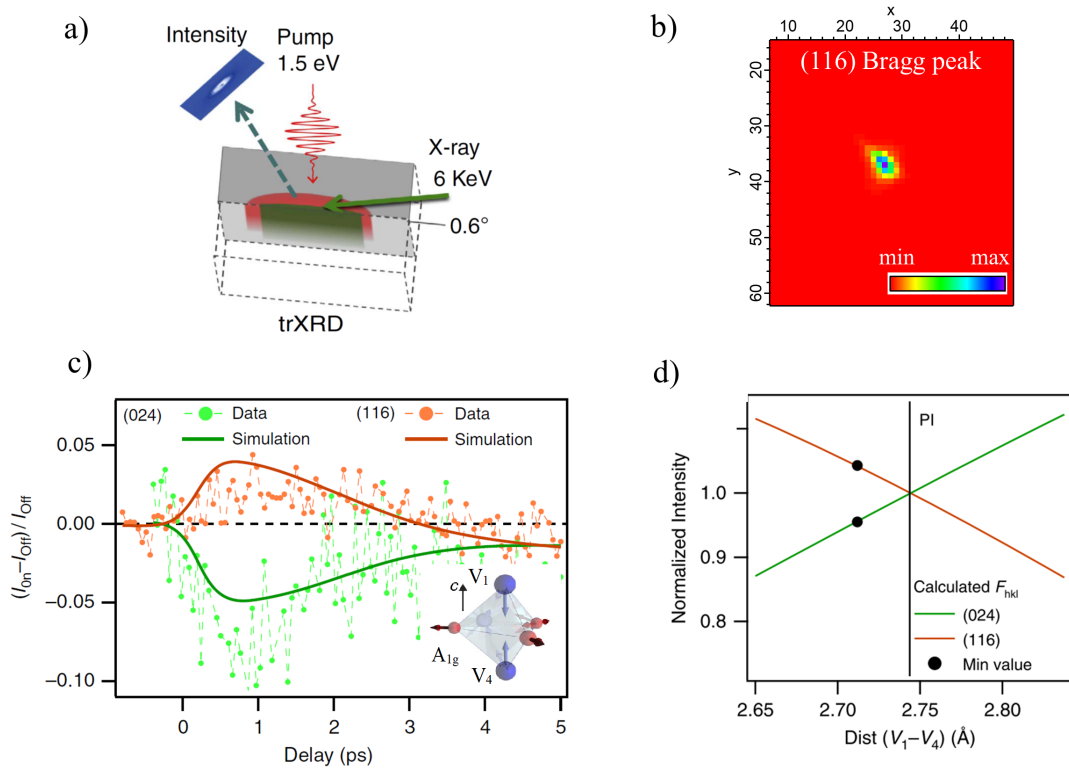


Figure 6.1: (a) The geometry of the trXRD at SLAC. (b) The Bragg reflection peak of the (116) direction for the PI phase. (c) tr-XRD measurements for a fluence of  $8 \text{ mJ/cm}^2$ , showing the pump-probe diffraction peak intensities for the (116) and (024) Bragg reflections. The solid lines are the simulations as explained in the text. (d) The calculated structure factor versus the shortest vanadium distance  $V_1 - V_4$ . The structure factor is normalized to one for the equilibrium position of  $2.744 \text{ \AA}$ . The black dots represent the minimum distance observed extracted from panel c. From reference [96].

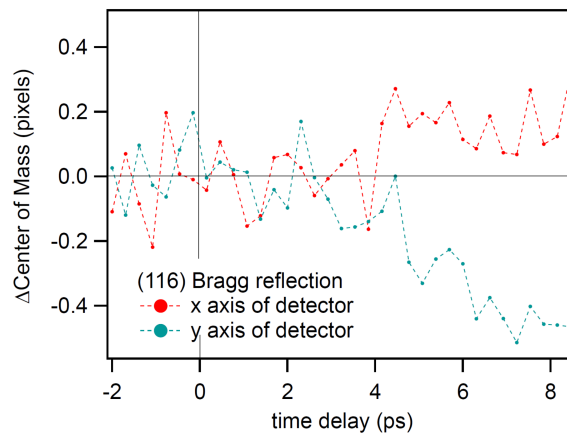


Figure 6.2: Time-resolved X-ray diffraction on the (116) Bragg reflection. The center of mass of the peak signal on the detector shows a shift after 4 ps, corresponding to the onset of the acoustic wave propagation.

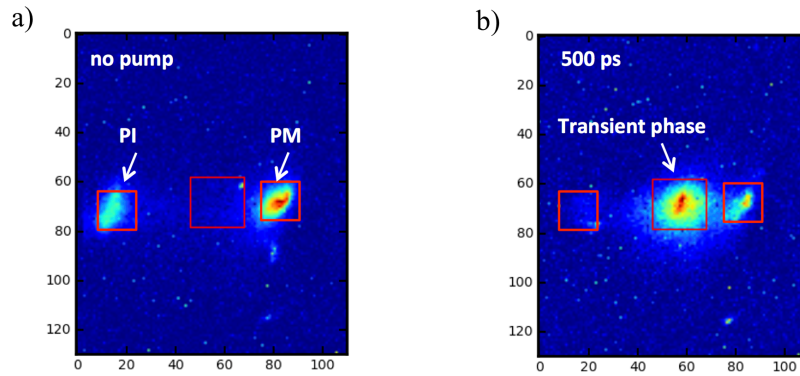


Figure 6.3: (a) X-ray diffraction signal on the 2D detector of the XPP beamline, showing the (113) Bragg reflections from  $(V_{1-x}Cr_x)_2O_3$  ( $x=0.011$ ) in its ground state, representative of the PI and PM phases, with the corresponding regions of interest (ROI's). No signal is present within the third ROI, in the center of the detector. (b) Diffraction signal 500 ps after photoexcitation, clearly showing a strong Bragg reflection from the third ROI which should be assigned to a novel state, not corresponding to any of the phases in the equilibrium phase diagram of  $(V_{1-x}Cr_x)_2O_3$ .

hardening of the lattice.

The above-mentioned simulation does not account for the dynamics after 4 ps. Due to the onset of the acoustic phonons, the changes in structure factor are no longer sufficient to explain the experimental curves as the Bragg peak position also starts changing and going out of the Ewald's sphere.

To conclude, we clearly observe that the onset of the structure distortion occurs after few hundreds of fs but before 1 ps. Then it takes about 2 ps in order for the lattice hardening to retrieve its equilibrium state. On the other hand, by means of tr-PES it was observed that the dynamics of the electrons unveils an abrupt onset of the in-gap states for the PI phase and the ultrafast quasiparticle quenching for the PM phase. These states are instantaneously observed upon photoexcitation and live for about 2 ps. A comparison between the dynamics of the electrons and the lattice implies that, once the electronic band structure is modified, the lattice follows the dynamics of the electrons thanks to the important electron-phonon coupling strength. The relaxation of the excited electrons is accompanied by the relaxation of the lattice hardening.

## 6.2 Ultrafast photoinduced phase transition

A unique feature of vanadium sesquioxide compared to other materials is that for Cr concentrations around  $x=0.011$ ,  $(V_{1-x}Cr_x)_2O_3$  goes through a metal-to-insulator transition by increasing the temperature from 200 K to 300 K. This is counter intuitive since it means that the higher energy electrons rather get more localized. This sparks off the idea that by an impulsive ejection of energy to the electrons, it might be possible to induce and stabilize an unprecedented metal-to-insulator transition (PM  $\rightarrow$  PI).<sup>1</sup> During the same run at LCLS, as previously mentioned, some preliminary experiments were performed towards realizing this goal.

First, the Bragg peak was studied as a function of temperature. By cooling the sample, the PM phase Bragg peak is observed while at high temperature only the PI phase appears. A promising

<sup>1</sup>Here, I might recall the photoinduced insulator-to-metal phase transition of  $VO_2$ . After the relaxation of the transient metallic state, the system relaxes to a thermal phase with higher temperature. The final thermal state for  $VO_2$  corresponds to the rutile metallic phase.

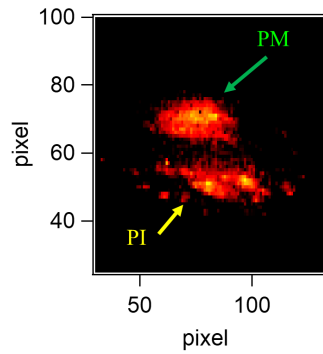


Figure 6.4: X-ray diffraction signal on the 2D detector of the SOLEIL beamline, showing the (113) Bragg reflections corresponding to the PI and PM phases for the 1.1% doped  $V_2O_3$ .

regime, is the coexistence regime close to the phase transition at  $T \sim 200$  K as it allows us to simultaneously observe the interplay between the dynamics of the PM and PI phase, figure 6.3 (a). The pump fluence was set at  $10 \text{ mJ/cm}^2$ . We notice an extremely fast appearance of a novel, non-thermal phase in between the two peaks after photoexcitation, figure 6.3 (b). By integrating the intensity of this new peak, we can track its dynamics. Its onset takes place well before 1 ps; already after only 300 fs there is a visible signal coming from it that lasts for longer time delays, figure 6.5 (a).

In order to get a clear insight on the dynamics of this transient phase, I performed some complementary pump-probe experiments on longer time scales at the Cristal beamline in synchrotron SOLEIL. The experimental condition was the same as in the LCLS. However due to the larger beam spot of X-rays, the Bragg peaks were not small and well defined, figure 6.4. I was able to consistently observe again the transient phase forming between the PM and PI phase for the specific  $x=0.011$  doping level, and to study its dynamics on longer time scales, as resumed in figure 6.5 (b): the transient phase grows up to around 1 ns, then decreases until it vanishes at around  $10 \mu\text{s}$ . The available data unambiguously demonstrate the very fast onset of this novel phase, already at sub-ps time scales, and its transient nature (the system comes back to equilibrium before the following pump pulse). In order to get a clear understanding of the physical nature of this transient phase, it is essential to collect more information on its behavior, by changing the relevant thermodynamic and optical parameters affecting its formation and evolution and it is part of the ongoing project of our group.

### 6.3 Time-resolved mid-infrared optical spectroscopy

In  $V_2O_3$ , the pump pulse of 1.5 eV stimulates electronic excitation to the bonding  $a_{1g}$  orbital that induces a lattice hardening marked by an increase in the  $A_{1g}$  phonon mode frequency. It is also interesting to study the optical response of the system while pumping (probing) with different low energy pulses. As explained in paragraph 3.4.3.4, a tunable source allows us to selectively act on different electronic transitions and to study the photoinduced impress on their dynamics. In this section, I first give some explanation on the OPA. Then, I present part of some preliminary experiments I did at the LOA in the end of my PhD studies.

In order to realize the experiments with pump photon energies in the mid infrared, I used an optical parametric amplifier (OPA). I describe the general mechanisms for the OPA and I give some specific numerical parameters corresponding to the commercial OPA I used at LOA, namely the TOPAS C from the company Light Conversion.

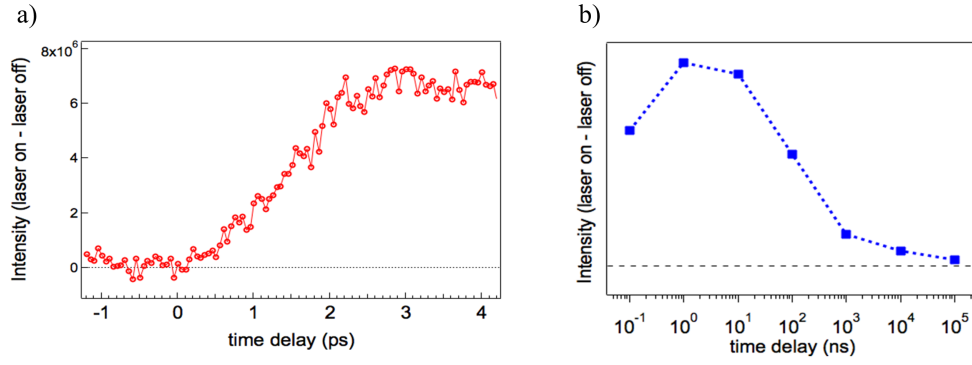


Figure 6.5: LCLS-XPP data giving the time evolution of the (113) Bragg reflection signal from the central ROI of figure 6.3 (b), corresponding to the novel transient phase. The time evolution clearly shows a marked presence of the novel phase already 300 fs after photoexcitation. (b) Intensity of the transient phase for longer time delays from pump-probe XRD experiments performed at synchrotron SOLEIL.

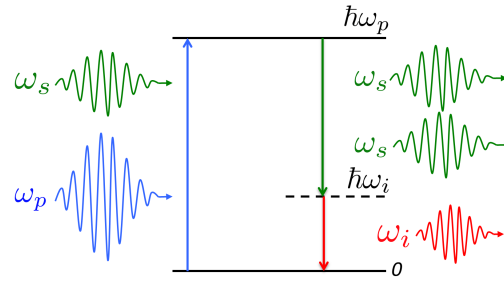


Figure 6.6: The energy downconversion process.

An OPA is based on the energy conversion from a photon, with a given photon energy  $\epsilon_p$ , into two photons with lower energies  $\epsilon_s$  and  $\epsilon_i$ , respectively, so that the energy conservation is satisfied:

$$\epsilon_p = \epsilon_s + \epsilon_i$$

In this section, I refer to the photon with energy  $\epsilon_p$  as pump photon, to the photon with energy  $\epsilon_s$  as signal photon, and to the photon with energy  $\epsilon_i$  as idler photon. Of course, this downconversion energy process can occur only if the momentum conservation is also satisfied:

$$\vec{p}_p = \vec{p}_s + \vec{p}_i$$

where  $\vec{p}$  indicate the momentum. In virtue of the wave-particle duality,  $\epsilon = \hbar\omega$  and  $\vec{p} = \hbar\vec{k}$ , where  $\omega$  and  $\vec{k}$  are the angular frequency and the wavevector, respectively, associated to the wave description. Therefore, we can rewrite the last two equations as follow

$$\omega_p = \omega_s + \omega_i$$

$$\vec{k}_p = \vec{k}_s + \vec{k}_i$$

These equations connect the wavelength and wavevector of the three beams, and therefore can be used to determine the outgoing wavelengths from the amplification process. Figure 6.6 shows the energy downconversion process.

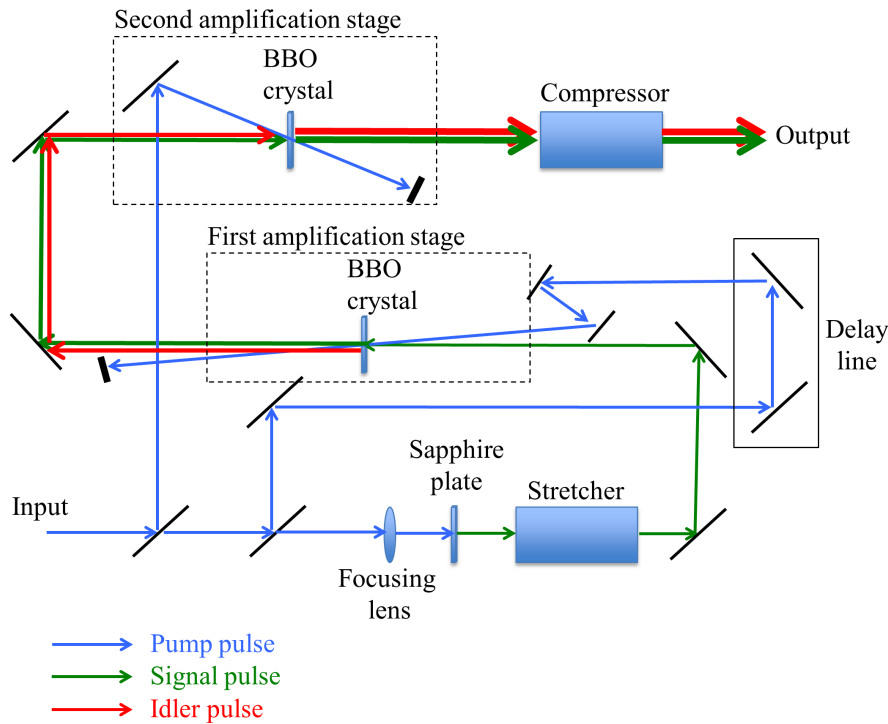


Figure 6.7: The optical path inside the TOPAS C. There are two stages of the amplification with the BBO crystals.

The downconversion energy process is based on non-linear optical properties of crystals. Actually, as to have strong non-linear effects we need very high intensity, ultrashort laser pulses are well adapted to this purpose. The most used crystal for OPA purpose is the  $\beta - BaB_2O_4$  (BBO) crystal.

The aforementioned energy conversion can be used to amplify the laser pulses in a wavelength range different from the wavelength of the fundamental harmonic of the laser. An OPA is usually based on two amplification stages based on the downconversion energy process, where the amplified signal comes from a white light generated through the interaction of the fundamental harmonic of the laser with a sapphire crystal plate.

Although different configurations exist, in most of the case an OPA is based on the following scheme, summarized in figure 6.7:

- The laser beam is split into three different beams: one beam will be used as signal ( $s$ ), and two other beams will be used as pump for two different amplification stages.
- The signal beam is focused into a sapphire plate, in order to produce white light, whose spectrum covers a wide range from visible to infrared.
- The white light beam  $s$  goes into a stretcher, which elongates the pulse duration by dispersing the wavelengths composing the white light. The stretcher usually consists of two prisms or diffracting gratings. In the case of the OPA used for our experiment, the TOPAS C, we only select the infrared part of the spectrum, for wavelengths larger than 800 nm. Hereafter we will refer to this beam as signal pulse  $s$ .
- The signal pulse  $s$  goes through a delay line, in order to control the time delay between the pump pulse of the first amplification stage and the signal pulse to be amplified. As the

signal pulse is stretched, the relative pump-signal delay will select the wavelength to be amplified. By changing this delay, we can synchronize the pump pulse with a small portion of the spectrum of the signal pulse that will be amplified.

- The signal pulse  $s$  and the pump pulse  $p$  are focused into a BBO crystal. As mentioned in the previous step, the choice of the wavelength that will be amplified is determined by the pump-signal time delay. However, in order to ensure momentum conservation, the BBO crystal must be tilted to the angle that ensures the momentum conservation for the selected wavelength to be amplified. Therefore, at each wavelength to be amplified it corresponds a time delay as well as a crystal angle. After the interaction, three beams will appear: a depleted pump pulse, an amplified signal pulse at the selected wavelength, and an idler signal pulse. The energy and momentum of these three pulses must satisfy the energy and momentum conservation law mentioned at the beginning of this section. The pump pulse can be spatially removed after the interaction with the BBO crystal, as it arrives with a small angle on the BBO crystal with respect to the signal pulse. In this fashion, we get only the signal and idler pulses propagating in the same direction.
- The signal and idler go into a second amplification stage, that works in the same way as the first amplification stage. However, here the pump-signal time delay is fixed, as they must be synchronized when interacting into the second BBO crystal. The second amplification stage further amplifies the energy of the pulses.
- The signal and idler pulses pass through a compression stage, which usually consists of wedged crystal plates, like quartz. This will reduce the temporal duration of the pulses. The best compression configuration will depend on the wavelength, because of the dispersion of the refractive index. Therefore, the compression configuration must also be one of the adjustable parameters of the OPA.
- At the exit of the OPA we have two pulses, namely the signal and idler pulses, that can be used for the experiment. In the case of the TOPAS C, the signal ranges from 1150 nm up to 1600 nm, whereas the idler pulse ranges from 1600 nm up to 2600 nm.
- In the case of our experimental setup, the exit of the TOPAS C is connected to a difference frequency generation (DFG) module that allows us to cover a further wavelength range from 2.6 microns up to 20 microns. This is possible thanks to the spectral width of the pulses. Actually, there are enough spectral components whose energy difference might produce, through difference frequency generation, pulses with very low photon energy.

In the setup at LOA, the TOPAS C + DFG module described briefly above gives the following energies: around 100  $\mu\text{J}$  per pulse in the wavelength range from 1150 nm up to 2600 nm, around few  $\mu\text{J}$  per pulse from in the wavelength range from 2600 nm up to 12000 nm, and below 1  $\mu\text{J}$  per pulse for wavelengths up to 20  $\mu\text{m}$ . As for the pulse duration, the outgoing pulses have similar duration as the fundamental harmonic of the laser in the range from 1150 nm up to 2600 nm, i.e. around 35 fs. Instead, the pulse duration is 1.5 up to 2 time longer in the range from 2600 nm up to 20  $\mu\text{m}$ .

I studied the time-resolved optical response of the  $\text{V}_2\text{O}_3$  sample by using the mid-infrared 3.6  $\mu\text{m}$  pulses of the DFG as the pump pulse while probing the system with 800 nm. I should recall that 3.6  $\mu\text{m}$  corresponds to 340 meV that is very close to Mott gap in the PI phase of 2.8% Cr-doped sample. Therefore, in order to have a comparative view on the dynamics of both metallic and insulating phase, I first chose the  $\text{V}_2\text{O}_3$  sample that is in the PM phase at room temperature.

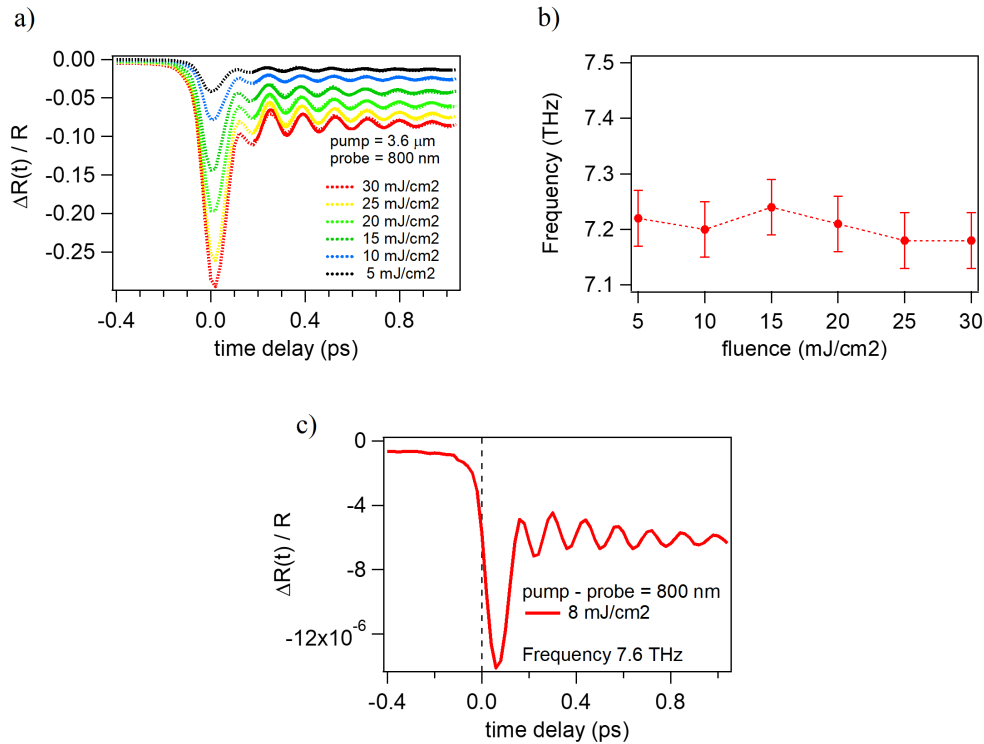


Figure 6.8: Time-resolved optical reflectivity measurements by pumping with  $3.6 \mu\text{m}$ . (a) dashed lines are the experimental data and the solid lines are fits to the decaying oscillations. (b) The frequency of the coherent oscillations as a function of fluence. We observe a mean frequency of  $7.2 \text{ THz}$  that is very close to the Raman frequency of  $7.15 \text{ THz}$ . (c) Time-resolved optical reflectivity measurements by pumping with  $800 \text{ nm}$ . The frequency of phonons is  $7.6 \text{ THz}$ .

The experiment was performed with different fluences of the pump pulse. In the experiments, the intensity of the probe pulse was always set to nearly 10 times less than the pump. Figure 6.8 (a) shows the optical response for difference pump fluences. We clearly observe the oscillations of the fully symmetric  $A_{1g}$  optical phonon. By modeling the oscillations as a damping harmonic oscillator, I found the frequency of the phonons for each fluence and the result is shown in figure 6.8 (b). The average frequency is  $7.2 \text{ THz}$  that is almost the same as the Raman frequency of this sample, i.e.  $7.15 \text{ THz}$ .

I also switched the pump to  $800 \text{ nm}$  by using the pump pulse at the entrance of the OPA and studied the optical response of the same sample by  $800 \text{ nm}$  as the pump and pulse. The fluence is  $8 \text{ mJ/cm}^2$ . The spectrum in figure 6.8 (c) reveals a frequency of  $7.6 \text{ THz}$  that is well above the Raman frequency as expected from populating the  $a_{1g}$  orbitals above the Fermi level. These results show that due to the strong electron-phonon coupling in  $V_2O_3$ , the selective electronic excitation results in a change in the phonon frequency according to the orbitals that are transiently populated.

## 7 | Conclusion and Perspectives

In this thesis, I performed different experiments in order to study the equilibrium and out-of-equilibrium properties of two complex compounds:  $\text{BaCo}_{1-x}\text{Ni}_x\text{S}_2$  and  $(\text{V}_{1-x}\text{M}_x)_2\text{O}_3$ .

The first part of my project was mainly devoted to the study of the electronic band structure of  $\text{BaNiS}_2$  and  $\text{BaCoS}_2$ . By applying ARPES, I studied the full electronic band structure of  $\text{BaNiS}_2$  in its entire Brillouin zone. The data suggested following important aspects: first, there are linearly dispersing bands at the Fermi level that have well defined orbital character. Second, the crossing of these bands always happens at the same point in the energy-momentum space, regardless of the  $k_z$ . Third, while the Fermi surface and the linearly dispersing bands have a (quasi) 2D character, the general electronic band structure presents rather a 3D character. Fourth, the non-trivial changes of the density of states induced by varying the temperature suggested that  $\text{BaNiS}_2$  is a correlated metal that can be described as a Fermi liquid.

Parallel theoretical calculations performed by our colleagues showed that the low-energy physics of the linearly dispersing bands is indeed described by a Dirac-like Hamiltonian that is principally composed of the  $d$ -orbitals. This 2D Dirac cone presents an elliptical shape for binding energies close to the Fermi level and it is also slightly tilted. This tilt is similar to the Dirac cone in type-II Weyl semimetals. The Dirac points existence, as well as their location in the time-reversal and inversion symmetric  $\text{BaNiS}_2$ , crucially depend on the hybridization strength between the  $d$  and  $p$  states. The hybridization with the ligands yields band inversions, the necessary condition for the Dirac points occurrence. The band crossing occurs between bands with two different irreducible representations that result from the nonsymmorphic symmetry of the crystal space group and is therefore robust.

The novelty of our results is that we present, experimentally and theoretically, a correlation-induced Dirac cone composed of  $d$ -orbitals.

I also presented the band structure of the Mott insulator  $\text{BaCoS}_2$  in its magnetic and non-magnetic phases. This compound is strongly correlated and is not described within the Fermi liquid theory.

The second part of my studies was focused on the out-of-equilibrium electron dynamics of  $\text{BaNiS}_2$  and  $(\text{V}_{1-x}\text{M}_x)_2\text{O}_3$ . In  $\text{BaNiS}_2$ , I observed that upon photoexcitation with a pump pulse, the band dispersion of the Dirac cone is modified very fast and reaches its maximum at only 250 fs after the injection of energy to the electrons. This deformation is not simply a rigid shift; it depends on the wavevector and as far as the data suggest does not affect the crossing of the bands with the Fermi level, i.e. the  $k_F$ . However, I could not clearly conclude what happens to the Dirac point during the electronic dynamics. The very low signal coming from the excited states makes it difficult to precisely follow the dynamics of the Dirac point. On the other hand, it was not possible for me to increase the fluence of the pump pulse to have better statistics for the excited states due to the rise of multi-photon process. Some parallel time-resolved reflectivity measurements with the same experimental condition as the time-resolved ARPES, showed the

excitation of two coherent optical modes after photoexcitation. The photoinduced signal relaxes due to the electron-phonon coupling as well as the anharmonic decay of phonons. The latter takes place with a timescale of 1 ps that is also the timescale in which the deformation of the Dirac cone relaxes. These consistent results coupled with some temperature-dependent ARPES measurements propose that the ultrafast renormalization of the bands is purely provoked by the electronic excitation and is stabilized by the interplay between the electrons and phonons. At long time delays ( $t > 3$  ps) the dynamics of the electronic states converges to a thermally-induced one that is equivalent to the accumulated heat brought about by laser pulses. Since the density of states of  $\text{BaNiS}_2$  changes as a function of temperature, it was not evident to deduce the electronic temperature experimentally. I performed some numerical analysis by the three-temperature model in order to study the dynamics of the temperatures of the electrons, strongly and weakly coupled phonons.

I also performed some time-resolved X-ray diffraction as well as time-resolved reflectivity measurements on  $(\text{V}_{1-x}\text{M}_x)_2\text{O}_3$  at  $x = 0$  (PM),  $x = 2.8\%$  (PI), and  $x = 1.1\%$  (Mott transition near 200 K). In fact,  $\text{V}_2\text{O}_3$  offers a rich phase diagram in equilibrium that can be translated into an equally rich out-of-equilibrium phase diagram by stabilizing novel photoinduced phases. One important aspect of this compound is that the bonding  $a_{1g}$  orbital is empty and is at  $\sim 1.5$  eV above the Fermi level. Therefore, if one transiently populates this orbital it can have some unexpected consequences on the band structure as well as the lattice. The tr-XRD experiments with sub-ps time resolution revealed that in the PM and PI phases the electronic excitation is indeed followed by a structural distortion that corresponds to a decrease of the distance between the neighboring vanadium atoms along the c-axis. This lattice hardening is definitely a non-thermal phase and is marked by a hardening of the  $A_{1g}$  phonon mode. It occurs before 1 ps and takes about 2 ps to retrieve the equilibrium state. These results underline the importance of the orbital filling as well as the strong interplay between the electrons and phonons in the strongly correlated materials.

The 1.1% Cr-doped sample presents additional interest since its higher temperature phase corresponds to an insulator. One might ask whether it is possible to initiate an unparalleled metal to insulator transition only by applying femtosecond laser pulses. To answer this question, I performed a series of tr-XRD experiments and the result showed the formation of a novel state different from the PM or PI phases upon photoexcitation. This state appears around 300 fs and vanishes at 10  $\mu\text{s}$ . However, the nature of this phase is yet to be clarified.

During my PhD, I tried to study and answer some questions by taking advantage of the time-, momentum-, and spectral-resolved techniques. My work has also opened new questions in turn, and this slow but continuous sequence of small questions takes us a step forward towards better understanding complex materials, e.g. strongly correlated materials, Dirac semimetals, and many other examples.

$\text{BaNiS}_2$  is an interesting system since it presents electronic correlation, hidden spin polarization, and Dirac fermions. Some more time-resolved ARPES experiments with higher probe photon energy should be performed on this compound in order to study how the entire electronic band structure reacts after being perturbed by femtosecond laser pulses. Moreover, in order to analyze the possible role of the  $d$ - and  $p$ -orbital hybridization in the band renormalization, one can perform some time-resolved ARPES experiments with different pump energies. This helps to study the role of a selective orbitals excitation in the photoinduced response. It is also very interesting to apply circularly polarized pump pulse to the systems since it breaks the time-reversal symmetry and can possibly lift the degeneracy of the Dirac cone, either by resulting in a Weyl

semimetal or by opening the gap. It might also possibly act on the Rashba split bands with hidden spin polarization by selectively pumping one spin component. With the same purpose, some precise spin-resolved experiments in the equilibrium condition can also unveil the spin component of the bands. The Mott insulator  $\text{BaCoS}_2$  undergoes an insulator to metal transition under pressure. Does this metallic phase correspond to a Dirac semimetal? This answer should lurk in the optical spectroscopy experiments under pressure. In order to obtain a general view on the correlation-induced Dirac fermions, one should study the electronic band structure of the neighbors of  $\text{BaNiS}_2$  in the phase diagram of  $\text{BaCo}_{1-x}\text{Ni}_x\text{S}_2$ .

$\text{V}_2\text{O}_3$  has been a benchmark for different experimental and theoretical work over decades and it still has much to be explored, especially in the time-resolved domain. The idea of inducing an ultrafast metal to insulator transition should be tested by performing precise tr-XRD or tr-reflectivity measurements in different experimental conditions. We saw the important role of the selective pumping to the dynamics of the electrons and lattice. It is intriguing to pump the Mott insulating phase of  $\text{V}_2\text{O}_3$  by different wavelengths, for instance resonant with the band gap and to observe the consequences on the electron dynamics. In line with the idea of pumping with different photon energies, pumping  $\text{BaNiS}_2$  with terahertz pulses that create optical transitions very close to the Dirac node might result in some non-trivial photoinduced changes of the electronic properties of the system.



# Bibliography

- [1] E. Abrahams, P. W. Anderson, D. C. Licciardello, and T. V. Ramakrishnan. Scaling theory of localization: Absence of quantum diffusion in two dimensions. *Phys. Rev. Lett.*, 42(10):673–676, 1979.
- [2] P. B. Allen. Theory of thermal relaxation of electrons in metals. *Phys. Rev. Lett.*, 59(13):1460–1463, 1987.
- [3] P. W. Anderson. Absence of diffusion in certain random lattices. *Phys. Rev.*, 109(5):1492–1505, 1958.
- [4] N. P. Armitage, E. J. Mele, and A. Vishwanath. Weyl and Dirac semimetals in three-dimensional solids. *Rev. Mod. Phys.*, 90(1):15001, 2018.
- [5] F. Barbo, M. Bertolo, A. Bianco, G. Cautero, S. Fontana, T. K. Johal, S. La Rosa, G. Margaritondo, and K. Kaznatcheyev. Spectromicroscopy beamline at ELETTRA: Performances achieved at the end of commissioning. *Rev. Sci. Instrum.*, 71(1):5–10, 2000.
- [6] A. D. Becke. Density-functional thermochemistry. III. The role of exact exchange. *J. Chem. Phys.*, 98(7):5648–5652, 1993.
- [7] E. Berger, P. Valáek, and W. Von Der Linden. Two-dimensional Hubbard-Holstein model. *Phys. Rev. B*, 52(7):4806–4814, 1995.
- [8] G. Bian, T.-R. Chang, R. Sankar, S.-Y. Xu, H. Zheng, T. Neupert, Ch.-K Chiu, Sh.-M. Huang, G. Chang, I. Belopolski, D. S. Sanchez, M. Neupane, N. Alidoust, Ch. Liu, B. K. Wang, Ch. Ch. Lee, H. T. Jeng, Ch. Zhang, Zh. Yuan, Sh. Jia, A. Bansil, F. Chou, H. Lin, and M. Zahid Hasan. Topological nodal-line fermions in spin-orbit metal  $\text{PbTaSe}_2$ . *Nat. Commun.*, 7:10556, 2016.
- [9] C. Bigi, P. K. Das, D. Benedetti, F. Salvador, D. Krizmancic, R. Sergo, A. Martin, G. Panaccione, G. Rossi, J. Fujii, and I. Vobornik. Very efficient spin polarization analysis (VESPA): New exchange scattering-based setup for spin-resolved ARPES at APE-NFFA beamline at Elettra. *J. Synchrotron Radiat.*, 24(4):750–756, 2017.
- [10] G. Blaj, P. Caragiulo, G. Carini, S. Carron, A. Dragone, D. Freytag, G. Haller, P. Hart, J. Hasi, R. Herbst, S. Herrmann, C. Kenney, B. Markovic, K. Nishimura, S. Osier, J. Pines, B. Reese, J. Segal, A. Tomada, and M. Weaver. X-ray detectors at the Linac Coherent Light Source. *J. Synchrotron Radiat.*, 22:577–583, 2015.
- [11] R. Bonifacio, L. De Salvo, P. Pierini, N. Piovella, and C. Pellegrini. Spectrum, temporal structure, and fluctuations in a high-gain free-electron laser starting from noise. *Phys. Rev. Lett.*, 73(1):70–73, 1994.

- [12] S. Borisenko, Q. Gibson, D. Evtushinsky, V. Zabolotnyy, B. Büchner, and R. J. Cava. Experimental Realization of a Three-Dimensional Dirac Semimetal. *Phys. Rev. Lett.*, 113(2):027603, 2014.
- [13] A. Bostwick, T. Ohta, T. Seyller, K. Horn, and E. Rotenberg. Quasiparticle dynamics in graphene. *Nat. Phys.*, 3(1):36–40, 2007.
- [14] B. Bradlyn, L. Elcoro, J. Cano, M. G. Vergniory, Z. Wang, C. Felser, M. I. Aroyo, and B. A. Bernevig. Topological quantum chemistry. *Nature*, 547(7663):298–305, 2017.
- [15] S. D. Brorson, A. Kazeroonian, J. S. Moodera, D. W. Face, T. K. Cheng, E. P. Ippen, M. S. Dresselhaus, and G. Dresselhaus. Femtosecond room-temperature measurement of the electron-phonon coupling constant in metallic superconductors. *Phys. Rev. Lett.*, 64(18):2172–2175, 1990.
- [16] V. Brouet, M. F. Jensen, P.-H. Lin, A. Taleb-Ibrahimi, P. Le Fèvre, F. Bertran, Ch. H. Lin, W. Ku, A. Forget, and D. Colson. Impact of the two Fe unit cell on the electronic structure measured by ARPES in iron pnictides. *Phys. Rev. B*, 86(7):075123, 2012.
- [17] V. Brouet, P.-H. Lin, Y. Texier, J. Bobroff, A. Taleb-Ibrahimi, P. Le Fèvre, F. Bertran, M. Casula, P. Werner, S. Biermann, F. Rullier-Albenque, A. Forget, and D. Colson. Large temperature dependence of the number of carriers in co-doped BaFe<sub>2</sub>As<sub>2</sub>. *Phys. Rev. Lett.*, 110(16):167002, 2013.
- [18] G. Brown, K. Halbach, J. Harris, and H. Winick. Wiggler and undulator magnets - A review. *Phys. Today*, 34(5):50, 1981.
- [19] L. Bucciantini, S. Roy, S. Kitamura, and T. Oka. Emergent Weyl nodes and Fermi arcs in a Floquet Weyl semimetal. *Phys. Rev. B*, 96(4):041126, 2017.
- [20] A. A. Burkov and L. Balents. Weyl semimetal in a topological insulator multilayer. *Phys. Rev. Lett.*, 107(12):127205, 2011.
- [21] Y. Cao, V. Fatemi, A. Demir, Sh. Fang, S. L. Tomarken, Jason Y. Luo, J. D. Sanchez-Yamagishi, K. Watanabe, T. Taniguchi, E. Kaxiras, R. C. Ashoori, and P. Jarillo-Herrero. Correlated Insulator Behaviour at Half-Filling in Magic Angle Graphene Superlattices. *Nature*, 556(7699):80–84, 2018.
- [22] Y. Cao, V. Fatemi, Shi. Fang, K. Watanabe, T. Taniguchi, E. Kaxiras, and P. Jarillo-Herrero. Magic-angle graphene superlattices: a new platform for unconventional superconductivity. *Nature*, 556(7699):43–50, 2018.
- [23] C. Castellani, C. R. Natoli, and J. Ranninger. Magnetic structure of V<sub>2</sub>O<sub>3</sub> in the insulating phase. *Phys. Rev. B*, 18(9):4945–4966, 1978.
- [24] A. H. Castro Neto, F. Guinea, N. M. R. Peres, K. S. Novoselov, and Geim. A. K. The electronic properties of graphene. *Rev. Mod. Phys.*, 81(March):109, 2009.
- [25] A. Cavalleri, Th Dekorsy, H. H W Chong, J. C. Kieffer, and R. W. Schoenlein. Evidence for a structurally-driven insulator-to-metal transition in VO<sub>2</sub>: A view from the ultrafast timescale. *Phys. Rev. B*, 70(16):161102, 2004.
- [26] A. Cavalleri, Cs. Tóth, C. W. Siders, J. A. Squier, F. Ráksi, P. Forget, and J. C. Kieffer. Femtosecond Structural Dynamics in VO<sub>2</sub> during an Ultrafast Solid-Solid Phase Transition. *Phys. Rev. Lett.*, 87(23):237401, 2001.

- [27] Y. Chan, Ch. k. Chiu, M. Y. Chou, and A. P. Schnyder.  $\text{Ca}_3\text{P}_2$  and other topological semimetals with line nodes and drumhead surface states. *Phys. Rev. B*, 93(20):205132, 2016.
- [28] M. Chollet, R. Alonso-Mori, M. Cammarata, D. Damiani, J. Defever, J. T. Delor, Y. Feng, J. M. Glowia, J. B. Langton, S. Nelson, K. Ramsey, A. Robert, M. Sikorski, S. Song, D. Stefanescu, V. Srinivasan, D. Zhu, H. T. Lemke, and D. M. Fritz. The X-ray Pump-Probe instrument at the Linac Coherent Light Source. *J. Synchrotron Radiat.*, 22(3):503–507, 2015.
- [29] E. Collet, M.-H. Lemée-Cailleau, M. Buron-Le Cointe, H. Cailleau, M. Wulff, T. Luty, Sh.-Y. Koshihara, M. Meyer, L. Toupet, P. Rabiller, and S. Techert. Laser-induced ferroelectric structural order in an organic charge-transfer crystal. *Science*, 300(5619):612–615, 2003.
- [30] L. N. Cooper. Bound electron pairs in a degenerate fermi gas. *Phys. Rev.*, 104(4):1189–1190, 1956.
- [31] A. Crepaldi, G. Autès, G. Gatti, S. Roth, A. Sterzi, G. Manzoni, M. Zacchigna, C. Cacho, R. T. Chapman, E. Springate, E. A. Seddon, Ph. Bugnon, A. Magrez, H. Berger, I. Vobornik, M. Källäne, A. Quer, K. Rossnagel, F. Parmigiani, O. V. Yazyev, and M. Grioni. Enhanced ultrafast relaxation rate in the Weyl semimetal phase of  $\text{MoTe}_2$  measured by time- and angle-resolved photoelectron spectroscopy. *Phys. Rev. B*, 96(24):241408(R), 2017.
- [32] G. L. Dakovski, Y. Li, T. Durakiewicz, and G. Rodriguez. Tunable ultrafast extreme ultra-violet source for time- and angle-resolved photoemission spectroscopy. *Rev. Sci. Instrum.*, 81(7):073108, 2010.
- [33] A. Damascelli. Probing the Electronic Structure of Complex Systems by ARPES. *Phys. Scr.*, T109:61, 2004.
- [34] A. Damascelli, Z. Hussain, and Z. X. Shen. Angle-resolved photoemission studies of the cuprate superconductors. *Rev. Mod. Phys.*, 75(2):473, 2003.
- [35] J. H. De Boer and E. J. W. Verwey. Semi-conductors with partially and with completely filled 3 d-lattice bands. *Proc. Phys. Soc.*, 49(4S):59, 1937.
- [36] P. A. M Dirac. The quantum theory of the electron. *Proc. Phys. Soc. Sect. A*, 117(778):610, 1928.
- [37] P. Dudin, P. Lacovig, C. Fava, E. Nicolini, A. Bianco, G. Cautero, and A. Barinov. Angle-resolved photoemission spectroscopy and imaging with a submicrometre probe at the SPECTROMICROSCOPY-3.2L beamline of Elettra. *J. Synchrotron Radiat.*, 17(4):445–450, 2010.
- [38] Editorial. The rise of the quantum materials. *Nat. Phys.*, 12:105, 2016.
- [39] A. Einstein. Über einen die Erzeugung und Verwandlung des Lichtes betreffenden heuristischen Gesichtspunkt. *Ann. Phys.*, 322(6):132–148, 1905.
- [40] P. Emma, R. Akre, J. Arthur, R. Bionta, C. Bostedt, J. Bozek, A. Brachmann, P. Bucksbaum, R. Coffee, F. J. Decker, Y. Ding, D. Dowell, S. Edstrom, A. Fisher, J. Frisch, S. Gilevich, J. Hastings, G. Hays, Ph Hering, Z. Huang, R. Iverson, H. Loos, M. Messerschmidt, A. Miahnahri, S. Moeller, H. D. Nuhn, G. Pile, D. Ratner, J. Rzepiela, D. Schultz, T. Smith, P. Stefan, H. Tompkins, J. Turner, J. Welch, W. White, J. Wu, G. Yocky, and J. Galayda.

- First lasing and operation of an ångstrom-wavelength free-electron laser. *Nat. Photonics*, 4(9):641–647, 2010.
- [41] B. Faatz and E. Plönjes. Simultaneous operation of two soft X-ray free-electron lasers driven by one linear accelerator. *New J. Phys.*, 18(6):062002, 2016.
- [42] J. Faure, J. Mauchain, E. Papalazarou, W. Yan, J. Pinon, M. Marsi, and L. Perfetti. Full characterization and optimization of a femtosecond ultraviolet laser source for time and angle-resolved photoemission on solid surfaces. *Rev. Sci. Instrum.*, 83(4):043109, 2012.
- [43] M. Ferrero, L. De Leo, P. Lecheminant, and M. Fabrizio. Strong correlations in a nutshell. *J. Phys. Condens. Matter*, 19(43):433201, 2007.
- [44] L. Fu and C. L. Kane. Topological insulators with inversion symmetry. *Phys. Rev. B*, 76(4):1–17, 2007.
- [45] H. Fujiwara, A. Sekiyama, S. K. Mo, J. W. Allen, J. Yamaguchi, G. Funabashi, S. Imada, P. Metcalf, A. Higashiya, M. Yabashi, K. Tamasaku, T. Ishikawa, and S. Suga. Evidence for the constancy of  $U$  in the Mott transition of  $V_2O_3$ . *Phys. Rev. B*, 84(7):075117, 2011.
- [46] M. Gao, C. Lu, H. Jean-Ruel, L. C. Liu, A. Marx, K. Onda, S.-Y. Koshihara, Y. Nakano, X. Shao, T. Hiramatsu, G. Saito, H. Yamochi, R. Cooney, G. Moriena, G. Sciaini, and R. J. Dwayne Miller. Mapping molecular motions leading to charge delocalization with ultrabright electrons. *Nature*, 496(7445):343–346, 2013.
- [47] A. K. Geim and A. H. MacDonald. Graphene: Exploring carbon flatland. *Phys. Today*, 60(8):35–41, 2007.
- [48] A. Georges and G. Kotliar. Hubbard model in infinite dimensions. *Phys. Rev. B*, 45(12):6479–6483, 1992.
- [49] A. Georges and W. Krauth. Physical properties of the half-filled Hubbard model in infinite dimensions. *Phys. Rev. B*, 48(10):7167–7182, 1993.
- [50] A. Georges, W. Krauth, G. Kotliar, and M. J. J Rozenberg. Dynamical mean-field theory of strongly correlated fermion systems and the limit of infinite dimensions. *Rev. Mod. Phys.*, 68(1):13, 1996.
- [51] P. Giannozzi, O. Andreussi, T. Brumme, O. Bunea, M. B. Nardelli, M. Calandra, C. Cavazzoni, D. Ceresoli, M. Cococcioni, P. Colonna, I. Carnimeo, A. Dal Corso, S. de Gironcoli, P. Delugas, DiStasio. R. A., A. Ferretti, A. Floris, and G. Fratesi. Advanced capabilities for materials modelling with Quantum ESPRESSO. *J. Phys.: Condens. Matter*, 29(46):465901, 2017.
- [52] M. Gonçalves, P. Ribeiro, and E. V. Castro. Dirac points merging and wandering in a model chern insulator. *EPL (Europhysics Letters)*, 124(6):67003, 2019.
- [53] P. Giannozzi, S. Baroni, N. Bonini, M. Calandra, R. Car, C. Cavazzoni, D. Ceresoli, G. L. Chiarotti, M. Cococcioni, I. Dabo, A. D. Corso, S. de Gironcoli, S. Fabris, G. Fratesi, R. Gebauer, U. Gerstmann, C. Gougoussis, A. Kokalj, M. Lazzeri, L. Martin-samos, N. Marzari, F. Mauri, R. Mazzarello, S. Paolini, A. Pasquarello, L. Paulatto, C. Sbraccia, Al. Smogunov, and P. Umari. QUANTUM ESPRESSO : a modular and open-source software project for quantum simulations of materials. *J. Phys. Condens. Matter*, 21(39):395502, 2009.

- [54] I. Gierz, M. Mitrano, H. Bromberger, C. Cacho, R. Chapman, E. Springate, S. Link, U. Starke, B. Sachs, M. Eckstein, T. O. Wehling, M. I. Katsnelson, A. Lichtenstein, and A. Cavalleri. Phonon-pump extreme-ultraviolet-photoemission probe in graphene: Anomalous heating of Dirac carriers by lattice deformation. *Phys. Rev. Lett.*, 114(12):125503, 2015.
- [55] I. Gierz, J. Petersen, M. Mitrano, C. Cacho, I. C. Edmond Turcu, E. Springate, A. Stöhr, A. Köhler, U. Starke, and A. Cavalleri. Snapshots of non-equilibrium Dirac carrier distributions in graphene. *Nat. Mater.*, 12(12):1119–1124, 2013.
- [56] I. E. Grey and H. Steinfink. Crystal Structure and Properties of Barium Nickel Sulfide, a Square-Pyramidal Nickel (II) Compound. *J. Am. Chem. Soc.*, 92(1970):5093, 1970.
- [57] D. Grieger and M. Fabrizio. Low-temperature magnetic ordering and structural distortions in vanadium sesquioxide  $V_2O_3$ . *Phys. Rev. B*, 92(7):075121, 2015.
- [58] M. Hajlaoui, E. Papalazarou, J. Mauchain, L. Perfetti, A. Taleb-Ibrahimi, F. Navarin, M. Monteverde, P. Auban-Senzier, C. R. Pasquier, N. Moisan, D. Boschetto, M. Neupane, M. Z. Hasan, T. Durakiewicz, Z. Jiang, Y. Xu, I. Miotkowski, Y. P. Chen, S. Jia, H. W. Ji, R. J. Cava, and M. Marsi. Tuning a Schottky barrier in a photoexcited topological insulator with transient Dirac cone electron-hole asymmetry. *Nat. Commun.*, 5:3003, 2014.
- [59] N. B. Hannay, T. H. Geballe, B. T. Matthias, K. Andreas, P. Schmidt, and D. MacNair. Superconductivity in graphitic compounds. *Phys. Rev. Lett.*, 14:225–226, 1965.
- [60] P. Hansmann, A. Toschi, G. Sangiovanni, T. Saha-Dasgupta, S. Lupi, M. Marsi, and K. Held. Mott-Hubbard transition in  $V_2O_3$  revisited. *Phys. Status Solidi Basic Res.*, 250(7):1251–1264, 2013.
- [61] M. Harmand, R. Coffee, M. R. Bionta, M. Chollet, D. French, D. Zhu, D. M. Fritz, H. T. Lemke, N. Medvedev, B. Ziaja, S. Toleikis, and M. Cammarata. Achieving few-femtosecond time-sorting at hard X-ray free-electron lasers. *Nat. Photonics*, 7(3):215–218, 2013.
- [62] M. Z. Hasan and C. L. Kane. Colloquium: Topological insulators. *Rev. Mod. Phys.*, 82(4):3045, 2010.
- [63] I. Hase, N. Shirakawa, and Y. Nishihara. Electronic structures of  $BaNiS_2$  and  $BaCoS_2$ . *J. Phys. Soc. Japan*, 64(7):2533–2540, 1995.
- [64] K. Held, G. Keller, V. Eyert, D. Vollhardt, and V. I. Anisimov. Mott-Hubbard metal-insulator transition in paramagnetic  $V_2O_3$ : An LDA+DMFT(QMC) study. *Phys. Rev. Lett.*, 86(23):5345–5348, 2001.
- [65] S. Hellmann, K. Rossnagel, M. Marczynski-Bühlow, and L. Kipp. Vacuum space-charge effects in solid-state photoemission. *Phys. Rev. B*, 79(3):035402, 2009.
- [66] S. Herrmann, P. Hart, M. Freytag, J. Pines, M. Weaver, L. Sapozhnikov, S. Nelson, J. Koglin, G. A. Carini, A. Tomada, and G. Haller. Diode readout electronics for beam intensity and position monitors for FELs. *J. Phys. Conf. Ser.*, 493(1):012014, 2014.
- [67] H. Hertz. Ueber einen Einfluss des ultravioletten Lichtes auf die elektrische Entladung. *Ann. Phys.*, 267(8):983–1000, 1887.

- [68] J. Heyd, G. E. Scuseria, and M. Ernzerhof. Hybrid functionals based on a screened Coulomb potential. *J. Chem. Phys.*, 118(18):8207–8215, 2003.
- [69] P. Hohenberg and W. Kohn. Inhomogeneous electron gas. *Phys. Rev.*, 136(3B):864, 1964.
- [70] Zh. Huang and K.-J. Kim. Review of x-ray free-electron laser theory. *Phys. Rev. Spec. Top. - Accel. Beams*, 10(3):034801, 2007.
- [71] J. Hubbard. Electron Correlations in Narrow Energy Bands. *Proc. R. Soc. A Math. Phys. Eng. Sci.*, 276(1365):238–257, 1963.
- [72] H. Hübener, M. A. Sentef, U. De Giovannini, A. F. Kemper, and A. Rubio. Creating stable Floquet-Weyl semimetals by laser-driving of 3D Dirac materials. *Nat. Commun.*, 8:13940, 2017.
- [73] S. Hüfner. *Photoelectron spectroscopy. Principles and applications*. Springer-Verlag, Berlin Heidelberg, 2 edition, 1995.
- [74] H. Ichikawa, S. Nozawa, T. Sato, A. Tomita, K. Ichiyanagi, M. Chollet, L. Guerin, N. Dean, A. Cavalleri, Sh. Adachi, T. Arima, H. Sawa, Y. Ogimoto, M. Nakamura, R. Tamaki, K. Miyano, and Sh. Koshihara. Transient photoinduced 'hidden' phase in a manganite. *Nat. Mater.*, 10(2):101–105, 2011.
- [75] M. Imada, A. Fujimori, and Y. Tokura. Metal-insulator transitions. *Rev. Mod. Phys.*, 70(4):1039, 1998.
- [76] K. Ishizaka, M. S. Bahramy, H. Murakawa, M. Sakano, T. Shimojima, T. Sonobe, K. Koizumi, S. Shin, H. Miyahara, A. Kimura, K. Miyamoto, T. Okuda, H. Namatame, M. Taniguchi, R. Arita, N. Nagaosa, K. Kobayashi, Y. Murakami, R. Kumai, Y. Kaneko, Y. Onose, and Y. Tokura. Giant Rashba-type spin splitting in bulk BiTeI. *Nat. Mater.*, 10(7):521–526, 2011.
- [77] A. Jayaraman, D. McWhan, J. Remeika, and P. Dernier. Critical Behavior of the Mott Transition in Cr-Doped  $V_2O_3$ . *Phys. Rev. B*, 2(9):3751–3756, 1970.
- [78] J. C. Johannsen, S. Ulstrup, F. Cilento, A. Crepaldi, M. Zacchigna, C. Cacho, I. C. E. Turcu, E. Springate, F. Fromm, C. Roidel, T. Seyller, F. Parmigiani, M. Grioni, and P. Hofmann. Direct view of hot carrier dynamics in graphene. *Phys. Rev. Lett.*, 111(2):027403, 2013.
- [79] S. L. Johnson, E. Vorobeva, P. Beaud, C. J. Milne, and G. Ingold. Full reconstruction of a crystal unit cell structure during coherent femtosecond motion. *Phys. Rev. Lett.*, 103(20):1–4, 2009.
- [80] Y. Kamihara, T. Watanabe, M. Hirano, and H. Hosono. Iron-Based Layered Superconductor  $La[O_{1-x}F_x]FeAs$  ( $x=0.05-0.12$ ) with  $T_c = 26$  K. *J. Am. Chem. Soc.*, 130(11):3296–3297, 2008.
- [81] C. L. Kane and E. J. Mele. Quantum Spin hall effect in graphene. *Phys. Rev. Lett.*, 95(22), 2005.
- [82] C. L. Kane and E. J. Mele.  $Z_2$  topological order and the quantum spin hall effect. *Phys. Rev. Lett.*, 95(14):146802, 2005.
- [83] B. Keimer and J. E. Moore. The physics of quantum materials. *Nat. Phys.*, 13(11):1045–1055, 2017.

- [84] Y. Kim, B. J. Wieder, C. L. Kane, and A. M. Rappe. Dirac Line Nodes in Inversion-Symmetric Crystals. *Phys. Rev. Lett.*, 115(3):036806, 2015.
- [85] T. Kiss, T. Shimojima, K. Ishizaka, A. Chainani, T. Togashi, T. Kanai, X. Y. Wang, C. T. Chen, S. Watanabe, and S. Shin. A versatile system for ultrahigh resolution, low temperature, and polarization dependent Laser-angle-resolved photoemission spectroscopy. *Rev. Sci. Instrum.*, 79(2):023106, 2008.
- [86] Y. Klein, M. Casula, D. Santos-Cottin, A. Audouard, D. Vignolles, G. Fève, V. Freulon, B. Plaçais, M. Verseils, H. Yang, L. Paulatto, and A. Gauzzi. Importance of nonlocal electron correlation in the BaNiS<sub>2</sub> semimetal from quantum oscillations studies. *Phys. Rev. B*, 97(7):075140, 2018.
- [87] M. Kociak, A. Y. Kasumov, S. Guéron, B. Reulet, I. I. Khodos, Y. B. Gorbatov, V. T. Volkov, L. Vaccarini, and H. Bouchiat. Superconductivity in Ropes of Single-Walled Carbon Nanotubes. *Phys. Rev. Lett.*, 86(11):2416–2419, 2001.
- [88] K. Kodama, S. Shamoto, H. Harashina, J. Takeda, M. Sato, K. Kakurai, and M. Nishi. Electronic structure of the quasi 2D Mott system BaCo<sub>1-x</sub>Ni<sub>x</sub>S<sub>2</sub>. *J. Phys. Soc. Japan*, 65(6):1782–1786, 1996.
- [89] W. Kohn and L. J. Sham. Self-consistent equations including exchange and correlation effects. *Phys. Rev.*, 140(4A):1133, 1965.
- [90] J. D. Koralek, J. F. Douglas, N. C. Plumb, Z. Sun, A. V. Fedorov, M. M. Murnane, H. C. Kapteyn, S. T. Cundiff, Y. Aiura, K. Oka, H. Eisaki, and D. S. Dessau. Laser based angle-resolved photoemission, the sudden approximation, and quasiparticle-like spectral peaks in Bi<sub>2</sub>Sr<sub>2</sub>CaCu<sub>2</sub>O<sub>8+δ</sub>. *Phys. Rev. Lett.*, 96(1):11–14, 2006.
- [91] G. Kotliar and D. Vollhardt. Strongly correlated materials: Insights from dynamical mean-field theory. *Phys. Today*, 57(3):53, 2004.
- [92] S. Krishnakumar, T. Saha-Dasgupta, N. Shanthi, P. Mahadevan, and D. Sarma. Electronic structure of and covalency driven metal-insulator transition in BaCo<sub>1-x</sub>Ni<sub>x</sub>S<sub>2</sub>. *Phys. Rev. B*, 63(4):045111, 2001.
- [93] A. V. Krukau, O. A. Vydrov, A. F. Izmaylov, and G. E. Scuseria. Influence of the exchange screening parameter on the performance of screened hybrid functionals Influence of the exchange screening parameter on the performance of screened hybrid functionals. *J. Chem. Phys.*, 125(22):224106, 2006.
- [94] H. Kuwamoto, J. M. Honig, and J. Appel. Electrical properties of the (V<sub>1-x</sub>Cr<sub>x</sub>)<sub>2</sub>O<sub>3</sub> system. *Phys. Rev. B*, 22(6):2626–2636, 1980.
- [95] L. D. Landau and E. M. Lifshitz. *Course of Theoretical Physics Volume 9: Statistical Physics Part 2*. Pergamon, Oxford, 1980.
- [96] G. Lantz, B. Mansart, D. Grieger, D. Boschetto, N. Nilforoushan, E. Papalazarou, N. Moisan, L. Perfetti, V. L.R. Jacques, D. Le Bolloc’h, C. Laulhé, S. Ravy, J. P. Rueff, T. E. Glover, M. P. Hertlein, Z. Hussain, S. Song, M. Chollet, M. Fabrizio, and M. Marsi. Ultrafast evolution and transient phases of a prototype out-of-equilibrium Mott-Hubbard material. *Nat. Commun.*, 8:13917, 2017.

- [97] C. Laulhé, T. Huber, G. Lantz, A. Ferrer, S. O. Mariager, S. Grübel, J. Rittmann, J. A. Johnson, V. Esposito, A. Lübcke, L. Huber, M. Kubli, M. Savoini, V. L.R. Jacques, L. Cario, B. Corraze, E. Janod, G. Ingold, P. Beaud, S. L. Johnson, and S. Ravy. Ultrafast Formation of a Charge Density Wave State in 1T-TaS<sub>2</sub>: Observation at Nanometer Scales Using Time-Resolved X-Ray Diffraction. *Phys. Rev. Lett.*, 118(24):247401, 2017.
- [98] J. P. F. LeBlanc, A. E. Antipov, F. Becca, I. W. Bulik, G. Kin-Lic Chan, C.-M. Chung, Y. Deng, M. Ferrero, T. M. Henderson, C. A. Jiménez-Hoyos, E. Kozik, X.-W. Liu, Andrew J. Millis, N. V. Prokof'ev, M. Qin, G. E. Scuseria, H. Shi, B. V. Svistunov, L. F. Tocchio, I. S. Tupitsyn, S. R. White, S. Zhang, B.-X. Zheng, Z. Zhu, and E. Gull. Solutions of the Two Dimensional Hubbard Model: Benchmarks and Results from a Wide Range of Numerical Algorithms. *Phys. Rev. X*, 5(4):041041, 2015.
- [99] P. A. Lee, N. Nagaosa, and X. G. Wen. Doping a Mott insulator: Physics of high-temperature superconductivity. *Rev. Mod. Phys.*, 78(1):17–69, 2006.
- [100] L. Lin. Adaptively Compressed Exchange Operator. *J. Chem. Theory Comput.*, 12(5):2242, 2016.
- [101] Z. K. Liu, B. Zhou, Y. Zhang, Z. J. Wang, H. M. Weng, D. Prabhakaran, S.-K. Mo, Z. X. Shen, Z. Fang, X. Dai, Z. Hussain, and Y. L. Chen. Discovery of a Three-Dimensional Topological Dirac Semimetal, Na<sub>3</sub>Bi. *Science*, 343:864, 2014.
- [102] H.V. Löhneysen, F. Huster, S. Mock, A. Neubert, T. Pietrus, M. Sieck, O. Stockert, and M. Waffenschmidt. Non-Fermi-liquid behavior in strongly correlated electron systems. *Phys. B Condens. Matter*, 230-232:550–556, 1997.
- [103] W. Lu, Sha. Ge, X. Liu, H. Lu, C. Li, J. Lai, Ch. Zhao, Zh. Liao, Sh. Jia, and D. Sun. Ultrafast relaxation dynamics of photoexcited Dirac fermions in the three-dimensional Dirac semimetal Cd<sub>3</sub>As<sub>2</sub>. *Phys. Rev. B*, 95(2):024303, 2017.
- [104] S. Lupi, L. Baldassarre, B. Mansart, a. Perucchi, a. Barinov, P. Dudin, E. Papalazarou, F. Rodolakis, J. P. Rueff, J. P. Itié, S. Ravy, D. Nicoletti, P. Postorino, P. Hansmann, N. Paragh, a. Toschi, T. Saha-Dasgupta, O. K. Andersen, G. Sangiovanni, K. Held, and M. Marsi. A microscopic view on the Mott transition in chromium-doped V<sub>2</sub>O<sub>3</sub>. *Nat. Commun.*, 1(8):105, 2010.
- [105] F. Mahmood, Ch-. K. Chan, Zh. Alpichshev, D. Gardner, Y. Lee, P. A. Lee, and N. Gedik. Selective scattering between Floquet-Bloch and Volkov states in a topological insulator. *Nat. Phys.*, 12(4):306–310, 2016.
- [106] J. Maletz, V. B. Zabolotnyy, D. V. Evtushinsky, S. Thirupathaiah, A. U.B. Wolter, L. Harnagea, A. N. Yaresko, A. N. Vasiliev, D. A. Chareev, A. E. Böhmer, F. Hardy, T. Wolf, C. Meingast, E. D.L. Rienks, B. Büchner, and S. V. Borisenko. Unusual band renormalization in the simplest iron-based superconductor FeSe<sub>1-x</sub>. *Phys. Rev. B*, 89(22):220506, 2014.
- [107] B. Mansart, D. Boschetto, A. Savoia, F. Rullier-Albenque, A. Forget, D. Colson, A. Rousse, and M. Marsi. Observation of a coherent optical phonon in the iron pnictide superconductor Ba(Fe<sub>1-x</sub>Co<sub>x</sub>)<sub>2</sub>As<sub>2</sub> (x=0.06 and 0.08). *Phys. Rev. B*, 80(17):172504, 2009.
- [108] B. Mansart, V. Brouet, E. Papalazarou, M. Fuglsang Jensen, L. Petaccia, S. Gorovikov, A. N. Grum-Grzhimailo, F. Rullier-Albenque, A. Forget, D. Colson, and M. Marsi. Orbital

- nature of the hole-like Fermi surface in superconducting  $\text{Ba}(\text{Fe}_{1-x}\text{Co}_x)_2\text{As}_2$ . *Phys. Rev. B*, 83(6):064516, 2011.
- [109] G. Manzoni, A. Sterzi, A. Crepaldi, M. Diego, F. Cilento, M. Zacchigna, Ph Bugnon, H. Berger, A. Magrez, M. Grioni, and F. Parmigiani. Ultrafast Optical Control of the Electronic Properties of  $\text{ZrTe}_5$ . *Phys. Rev. Lett.*, 115(20):207402, 2015.
- [110] G. Margaritondo and P. R. Ribic. A simplified description of X-ray free-electron lasers. *J. Synchrotron Radiat.*, 18(2):101–108, 2011.
- [111] N. Mårtensson, P. Baltzer, P.A. Brühwiler, J.-O. Forsell, A. Nilsson, A. Stenborg, and B. Wannberg. A very high resolution electron spectrometer. *J. Electron Spectros. Relat. Phenomena*, 70(2):117–128, 1994.
- [112] L. S. Martinson, J. W. Schweitzer, and N. C. Baenziger. Metal-Insulator Transitions in  $\text{BaCo}_{1-x}\text{Ni}_x\text{S}_{2-y}$ . *Phys. Rev. Lett.*, 71(1):125, 1993.
- [113] L. S. Martinson, J.W. Schweitzer, and N. C. Baenziger. Properties of the layered  $\text{BaCo}_{1-x}\text{Ni}_x\text{S}_2$  alloy system. *Phys. Rev. B*, 54(16):265, 1995.
- [114] L. F Matheiss. Electronic structure of quasi-two-dimensional  $\text{BaNiS}_2$ . *Solid State Commun.*, 93(11):879–883, 1995.
- [115] D. B. McWhan, A. Menth, J. P. Remeika, W. F. Brinkman, and T. M. Rice. Metal-insulator transitions in pure and doped  $\text{V}_2\text{O}_3$ . *Phys. Rev. B*, 7(5):1920–1931, 1973.
- [116] D. B. Mcwhan and J. P. Remeika. Metal-Insulator Transition in  $(\text{V}_{1-x}\text{Cr}_x)_2\text{O}_3$ . *Phys. Rev. B*, 2(9):3734, 1970.
- [117] D. B. McWhan, T. M. Rice, and J. P. Remeika. Mott Transition in Cr-Doped  $\text{V}_2\text{O}_3$ . *Phys. Rev. Lett.*, 23(24):1384, 1969.
- [118] S.-K. Mo, J. D. Denlinger, H. D. Kim, J.-H. Park, J. W. Allen, A. Sekiyama, A. Yamasaki, K. Kadono, S. Suga, Y. Saitoh, T. Muro, P. Metcalf, G. Keller, K. Held, V. Eyert, V. I. Anisimov, and D. Vollhardt. Prominent quasiparticle peak in the photoemission spectrum of the metallic phase of  $\text{V}_2\text{O}_3$ . *Phys. Rev. Lett.*, 90(18):186403, 2003.
- [119] S. K. Mo, H. D. Kim, J. W. Allen, G. H. Gweon, J. D. Denlinger, J. H. Park, A. Sekiyama, A. Yamasaki, S. Suga, P. Metcalf, and K. Held. Filling of the mott-hubbard gap in the high temperature photoemission spectrum of  $(\text{V}_{0.972}\text{Cr}_{0.028})_2\text{O}_3$ . *Phys. Rev. Lett.*, 93(7):076404, 2004.
- [120] S.-K. Mo, H.-D. Kim, Denlinger. J. D., J. W. Allen, J.-H. Park, A. Sekiyama, A. Yamasaki, S. Suga, Y. Saitoh, T. Muro, and Metcalf. P. Photoemission study of  $(\text{V}_{1-x}\text{M}_x)_2\text{O}_3$  ( $\text{M}=\text{Cr},\text{Ti}$ ). *Phys. Rev. B*, 74(16):165101, 2006.
- [121] F. J. Morin. Oxides which show a metal-to-insulator transition at the Néel temperature. *Phys. Rev. Lett.*, 3(1):34, 1959.
- [122] V. R. Morrison, R. P. Chatelain, K. L. Tiwari, A. Hendaoui, A. Bruhacs, M. Chaker, and B. J. Siwick. A photoinduced metal-like phase of monoclinic  $\text{VO}_2$  revealed by ultrafast electron diffraction. *Science*, 346(6208):445–448, 2014.

- [123] A. A. Mostofi, J. R. Yates, Y. S. Lee, I. Souza, D. Vanderbilt, and N. Marzari. wannier90 : A tool for obtaining maximally-localised Wannier functions. *Comput. Phys. Commun.*, 178:685–699, 2008.
- [124] N. F. Mott. The Basis of the Electron Theory of Metals, with Special Reference to the Transition Metals. *Proc. Phys. Soc. Sect. A*, 416:416, 1949.
- [125] N. F. Mott. Metal-insulator transition. *Rev. Mod. Phys.*, 40(4):677–683, 1968.
- [126] N. F. Mott. *Metal-Insulator Transitions*. Taylor & Francis, London, New York, second edition, 1990.
- [127] M. Mucha-Kruczyński, O. Tsyplyatyev, A. Grishin, E. McCann, Vladimir I. Fal’ko, A. Bostwick, and E. Rotenberg. Characterization of graphene through anisotropy of constant-energy maps in angle-resolved photoemission. *Phys. Rev. B*, 77(19):195403, 2008.
- [128] S. Murakami. Two-dimensional topological insulators and their edge states. *J. Phys. Conf. Ser.*, 302(1):012019, 2011.
- [129] M. Neupane, S. Y. Xu, R. Sankar, N. Alidoust, G. Bian, Ch. Liu, I. Belopolski, T. R. Chang, H. T. Jeng, H. Lin, A. Bansil, F. Chou, and M. Zahid Hasan. Observation of a three-dimensional topological Dirac semimetal phase in high-mobility  $\text{Cd}_3\text{As}_2$ . *Nat. Commun.*, 5:3786, 2014.
- [130] C. Nordling, E. Sokolowski, and K. Siegbahn. Precision Method for Obtaining Absolute Values of Atomic Binding Energies. *Phys. Rev.*, 105(5):1676–1677, 1957.
- [131] K. S. Novoselov, A. K. Geim, S. V. Morozov, D. Jiang, M. I. Katsnelson, I. V. Grigorieva, S. V. Dubonos, and A. A. Firsov. Two-dimensional gas of massless Dirac fermions in graphene. *Nature*, 438(7065):197–200, 2005.
- [132] K. S. Novoselov, A. K. Geim, S. V. Morozov, D. A. Jiang, Y. Zhang, S. V. Dubonos, I. V. Grigorieva, and A. A. Firsov. Electric field effect in atomically thin carbon films. *Science*, 306(5696):666–669, 2004.
- [133] K. Okazaki, Y. Ota, Y. Kotani, W. Malaeb, Y. Ishida, T. Shimojima, T. Kiss, S. Watanabe, C. T. Chen, K. Kihou, C. H. Lee, A. Iyo, H. Eisaki, T. Saito, H. Fukazawa, Y. Kohori, K. Hashimoto, T. Shibauchi, Y. Matsuda, H. Ikeda, and H. Miyahara. Octet-Line Node Structure Parameter in  $\text{KFe}_2\text{As}_2$ . *Science*, 337(6100):1314–1317, 2012.
- [134] J. Orenstein. Ultrafast spectroscopy of quantum materials. *Phys. Today*, 65(9):44–50, 2012.
- [135] L. Ortenzi, E. Cappelluti, L. Benfatto, and L. Piertrone. Fermi-surface shrinking, interband coupling and multiple gaps in iron-based pnictides. *J. Supercond. Nov. Magn.*, 103(4):046404, 2009.
- [136] G. Panaccione, I. Vobornik, J. Fujii, D. Krizmancic, E. Annese, L. Giovanelli, F. Maccherozzi, F. Salvador, A. De Luisa, D. Benedetti, A. Gruden, P. Bertoch, F. Polack, D. Cocco, G. Sostero, B. Diviacco, M. Hochstrasser, U. Maier, D. Pescia, C. H. Back, T. Greber, J. Osterwalder, M. Galaktionov, M. Sancrotti, and G. Rossi. Advanced photoelectric effect experiment beamline at Elettra: A surface science laboratory coupled with Synchrotron Radiation. *Rev. Sci. Instrum.*, 80(4):043105, 2009.

- [137] E. Papalazarou, J. Faure, J. Mauchain, M. Marsi, A. Taleb-Ibrahimi, I. Reshetnyak, A. Van Roekeghem, I. Timrov, N. Vast, B. Arnaud, and L. Perfetti. Coherent phonon coupling to individual Bloch states in photoexcited bismuth. *Phys. Rev. Lett.*, 108(25):256808, 2012.
- [138] J.-H. Park, L. Tjeng, A. Tanaka, J. W. Allen, C. Chen, P. Metcalf, J. Honig, F. de Groot, and G. A. Sawatzky. Spin and orbital occupation and phase transitions in  $V_2O_3$ . *Phys. Rev. B*, 61(17):11506, 2000.
- [139] S. Passlack, S. Mathias, O. Andreyev, D. Mittnacht, M. Aeschlimann, and M. Bauer. Space charge effects in photoemission with a low repetition, high intensity femtosecond laser source. *J. Appl. Phys.*, 100(2):024912, 2006.
- [140] C. Pellegrini. The free-electron laser collective instability and the development of X-ray FELs. *Proc. 2001 Part. Accel. Conf.*, 1:295–299, 2001.
- [141] C. Pellegrini, A. Marinelli, and S. Reiche. The physics of x-ray free-electron lasers. *Rev. Mod. Phys.*, 88(1):1–55, 2016.
- [142] C. Pellegrini and J. Stöhr. X-ray free-electron lasers - Principles, properties and applications. *Nucl. Instruments Methods Phys. Res. Sect. A Accel. Spectrometers, Detect. Assoc. Equip.*, 500(1-3):33–40, 2003.
- [143] J. P. Perdew. Accurate Density Functional for the Energy: Real-Space Cutoff of the Gradient Expansion for the Exchange Hole. *Phys. Rev. Lett.*, 55(16):1665–1668, 1985.
- [144] L. Perfetti, P. A. Loukakos, M. Lisowski, U. Bovensiepen, H. Berger, S. Biermann, P. S. Cornaglia, A. Georges, and M. Wolf. Time evolution of the electronic structure of 1T-TaS<sub>2</sub> through the insulator-metal transition. *Phys. Rev. Lett.*, 97(6):067402, 2006.
- [145] L. Perfetti, P. A. Loukakos, M. Lisowski, U. Bovensiepen, H. Eisaki, and M. Wolf. Ultrafast Electron Relaxation in Superconducting  $Bi_2Sr_2CaCu_2O_{8+\delta}$  by Time-Resolved Photoelectron Spectroscopy. *Phys. Rev. Lett.*, 99(9):197001, 2007.
- [146] D. Pines and P. Nozieres. *The theory of quantum liquids, Vol. 1 Normal Fermi-liquids*. Taylor & Francis, Roca Raton, 1989.
- [147] D. Popmintchev, C. Hernández-García, F. Dollar, C. Mancuso, J. A. Pérez-Hernández, M. C. Chen, A. Hankla, X. Gao, B. Shim, A. L. Gaeta, M. Tarazkar, D. A. Romanov, R. J. Levis, J. A. Gaffney, Mark Foord, S. B. Libby, A. Jaron-Becker, A. Becker, L. Plaja, M. M. Murnane, H. C. Kapteyn, and T. Popmintchev. Ultraviolet surprise: Efficient soft X-ray high-harmonic generation in multiply ionized plasmas. *Science*, 350(6265):1225–1231, 2015.
- [148] A. I. Poteryaev, M. Ferrero, A. Georges, and O. Parcollet. Effect of crystal-field splitting and interband hybridization on the metal-insulator transitions of strongly correlated systems. *Phys. Rev. B*, 78(4):045115, 2008.
- [149] A. I. Poteryaev, J. M. Tomczak, S. Biermann, A. Georges, A. I. Lichtenstein, Al. N. Rubtsov, T. Saha-Dasgupta, and O. K. Andersen. Enhanced crystal-field splitting and orbital-selective coherence induced by strong correlations in  $V_2O_3$ . *Phys. Rev. B*, 76(8), 2007.
- [150] X. L. Qi and Sh. Ch. Zhang. The quantum spin Hall effect and topological insulators. *Phys. Today*, 63(1):33, 2010.

- [151] J. D. Rameau, S. Freutel, L. Rettig, I. Avigo, M. Ligges, Y. Yoshida, H. Eisaki, J. Schneeloch, R. D. Zhong, Z. J. Xu, G. D. Gu, P. D. Johnson, and U. Bovensiepen. Photoinduced changes in the cuprate electronic structure revealed by femtosecond time- and angle-resolved photoemission. *Phys. Rev. B*, 89(11):115115, 2014.
- [152] J. M. Riley, F. Mazzola, M. Dendzik, M. Michiardi, T. Takayama, L. Bawden, C. Granerød, M. Leandersson, T. Balasubramanian, M. Hoesch, T. K. Kim, H. Takagi, W. Meevasana, Ph Hofmann, M. S. Bahramy, J. W. Wells, and P. D C King. Direct observation of spin-polarized bulk bands in an inversion-symmetric semiconductor. *Nat. Phys.*, 10(11):835–839, 2014.
- [153] F. Rodolakis, B. Mansart, E. Papalazarou, S. Gorovikov, P. Vilmercati, L. Petaccia, A. Goldoni, J. P. Rueff, S. Lupi, P. Metcalf, and M. Marsi. Quasiparticles at the Mott transition in  $V_2O_3$ : Wave vector dependence and surface attenuation. *Phys. Rev. Lett.*, 102(6):066805, 2009.
- [154] M. Rozenberg, G. Kotliar, and H. Kajueter. Transfer of spectral weight in spectroscopies of correlated electron systems. *Phys. Rev. B*, 54(12):8452–8468, 1996.
- [155] T. Saha-Dasgupta, O. K. Andersen, J. Nuss, A. I. Poteryaev, A. Georges, and A. I. Lichtenstein. Electronic structure of  $V_2O_3$  : Wannier orbitals from LDA-NMTO calculations. *arXiv:0907.2841*, <http://arxiv.org/abs/0907.2841>.
- [156] D. Santos-Cottin, M. Casula, G. Lantz, Y. Klein, L Petaccia, P. Le Fèvre, F. Bertran, E. Papalazarou, M. Marsi, and A. Gauzzi. Rashba coupling amplification by a staggered crystal field. *Nat. Commun.*, 7:11258, 2016.
- [157] D. Santos-Cottin, A. Gauzzi, M. Verseils, B. Baptiste, G. Feve, V. Freulon, B. Plaçais, M. Casula, and Y. Klein. Anomalous metallic state in quasi-two-dimensional  $BaNiS_2$ . *Phys. Rev. B*, 93(12):125120, 2016.
- [158] D. Santos-Cottin, Y. Klein, Ph. Werner, T. Miyake, L. de' Medici, A. Gauzzi, R. P. S. M. Lobo, and M. Casula. Linear behavior of the optical conductivity and incoherent charge transport in  $BaCoS_2$ . *Phys. Rev. Mater.*, 2(10):105001, 2018.
- [159] T. Sato, H. Kumigashira, D. Ionel, T. Takahashi, I. Hase, H. Ding, J. C. Campuzano, and S. Shimoto. Evolution of metallic states from the Hubbard band in the two-dimensional Mott system  $BaCo_{1-x}Ni_xS_2$ . *Phys. Rev. B*, 64(7):075103, 2001.
- [160] E. Savelyev, R. Boll, C. Bomme, N. Schirmel, H. Redlin, and B. Erk. Jitter-correction for IR/UV-XUV pump-probe experiments at the FLASH free-electron laser. *New J. Phys.*, 19(4):043009, 2017.
- [161] M. Schnürer, Ch Spielmann, P. Wobrauschek, C. Streli, N. H. Burnett, C. Kan, K. Ferencz, R. Koppitsch, Z. Cheng, T. Brabec, and F. Krausz. Coherent 0.5-keV x-ray emission from helium driven by a sub-10-fs laser. *Phys. Rev. Lett.*, 80(15):3236–3239, 1998.
- [162] L. M. Schoop, M. N. Ali, C. Straßer, A. Topp, A. Varykhalov, D. Marchenko, V. Duppel, S. S. P. Parkin, B. V. Lotsch, and Ch. R. Ast. Dirac cone protected by nonsymmorphic symmetry and three-dimensional Dirac line node in  $ZrSiS$ . *Nat. Commun.*, 7:11696, 2016.
- [163] G. Sciaini, M. Harb, S. G. Kruglik, T. Payer, C. T. Hebeisen, F. J . Meyer Zu Heringdorf, M. Yamaguchi, M. Horn-von Hoegen, R. Ernstorfer, and R. J. Dwayne Miller. Electronic

- acceleration of atomic motions and disordering in bismuth. *Nature*, 458(7234):56–59, 2009.
- [164] M. P. Seah and W. A. Dench. Quantitative electron spectroscopy of surfaces: A standard data base for electron inelastic mean free paths in solids. *Surf. Interface Anal.*, 1(1):2–11, 1979.
- [165] D. A. Siegel, C.-H. Park, C. Hwang, J. Deslippe, A. V. Fedorov, S. G. Louie, and A. Lanzara. Many-body interactions in quasi-freestanding graphene. *Proc. Natl. Acad. Sci.*, 108(28):11365–11369, 2011.
- [166] P. Siffalovic, M. Drescher, M. Spieweck, T. Wiesenthal, Y. C. Lim, R. Weidner, A. Elizarov, and U. Heinzmann. Laser-based apparatus for extended ultraviolet femtosecond time-resolved photoemission spectroscopy. *Rev. Sci. Instrum.*, 72(1):30–35, 2001.
- [167] J. C. Slater. Magnetic effects and the Hartree-Fock equation. *Phys. Rev.*, 82(4):538–541, 1951.
- [168] A. Sterzi, G. Manzoni, L. Sbuelz, F. Cilento, M. Zacchigna, Ph. Bugnon, A. Magrez, and H. Berger. Bulk diffusive relaxation mechanisms in optically excited topological insulators. *Phys. Rev. B*, 95(11):115431, 2017.
- [169] S. Sugai, N. Yamane, S. Kashima, K. Takenaka, H. Sasaki, M. Sato, and S. Shamoto. Raman and infrared studies of the metal-insulator transition in  $\text{BaCo}_{1-x}\text{Ni}_x\text{S}_2$ . *Phys. B Condens. Matter*, 282:627–628, 2000.
- [170] S. K. Sundaram and E. Mazur. Inducing and probing non-thermal transitions in semiconductors using femtosecond laser pulses. *Nat. Mater.*, 1(4):217–224, 2002.
- [171] V. Ta Phuoc, C. Vaju, B. Corraze, R. Sopracase, A. Perucchi, C. Marini, P. Postorino, M. Chligui, S. Lupi, E. Janod, and L. Cario. Optical conductivity measurements of  $\text{GaTa}_4\text{Se}_8$  under high pressure: Evidence of a bandwidth-controlled insulator-to-metal Mott transition. *Phys. Rev. Lett.*, 110(3):037401, 2013.
- [172] J. Tekeda, K. Kodama, H. Harashina, and M. Sato. Transport and magnetic studies of  $\text{BaCo}_{1-x}\text{Ni}_x\text{S}_2$ . *J. Phys. Soc. Japan*, 63(10):3564–3567, 1994.
- [173] K. Terashima, Y. Sekiba, J. H. Bowen, K. Nakayama, T. Kawahara, T. Sato, P. Richard, Y.-M. Xu, L. J. Li, G. H. Cao, Z.-A. Xu, H. Ding, and T. Takahashi. Fermi surface nesting induced strong pairing in iron-based superconductors. *Proc. Natl. Acad. Sci.*, 106(18):7330–7333, 2009.
- [174] T. Terashima, N. Kikugawa, A. Kiswandhi, E.-S. Choi, J. S. Brooks, S. Kasahara, T. Watashige, H. Ikeda, T. Shibauchi, Y. Matsuda, T. Wolf, A. E. Böhrer, F. Hardy, C. Meingast, H. V. Löhneysen, M. To Suzuki, R. Arita, and S. Uji. Anomalous Fermi surface in FeSe seen by Shubnikov-de Haas oscillation measurements. *Phys. Rev. B*, 90(14):144517, 2014.
- [175] Y. Tokura, M. Kawasaki, and N. Nagaosa. Emergent functions of quantum materials. *Nat. Phys.*, 13(11):1056–1068, 2017.
- [176] J. M. Tomczak, M. Van Schilfgaarde, and G. Kotliar. Many-body effects in iron pnictides and chalcogenides: Nonlocal versus dynamic origin of effective masses. *Phys. Rev. Lett.*, 109(23):237010, 2012.

- [177] S. Ulstrup, J. C. Johannsen, Fe. Cilento, J. A. Miwa, A. Crepaldi, M. Zacchigna, C. Cacho, R. Chapman, E. Springate, S. Mammadov, F. Fromm, C. Raidel, T. Seyller, F. Parmigiani, M. Grioni, P.D C King, and P. Hofmann. Ultrafast dynamics of massive Dirac fermions in bilayer graphene. *Phys. Rev. Lett.*, 112(25):257401, 2014.
- [178] S. Ulstrup, J. Ch. Johannsen, A. Crepaldi, F. Cilento, M. Zacchigna, C. Cacho, R. T. Chapman, E. Springate, F. Fromm, Ch. Raidel, Th. Seyller, F. Parmigiani, M. Grioni, and Ph. Hofmann. Ultrafast Electron Dynamics in Epitaxial Graphene Investigated with Time- and Angle-Resolved Photoemission Spectroscopy. *arXiv:1601.00745*, <http://arxiv.org/abs/1601.00745>.
- [179] V. Cvetkovic and O. Vafek. Space group symmetry, spin-orbit coupling, and the low-energy effective hamiltonian for iron-based superconductors. *Phys. Rev. B*, 88(13):134510, 2013.
- [180] X. Wan, A. M. Turner, A. Vishwanath, and S. Y. Savrasov. Topological semimetal and Fermi-arc surface states in the electronic structure of pyrochlore iridates. *Phys. Rev. B*, 83(20):205101, 2011.
- [181] Y. H. Wang, H. Steinberg, P. Jarillo-Herrero, and N. Gedik. Observation of Floquet-Bloch States on the Surface of a Topological Insulator. *Science*, 342: 453–457, 2013.
- [182] Zh. Wang, Y. Sun, X. Q. Chen, C. Franchini, G. Xu, H. Weng, X. Dai, and Z. Fang. Dirac semimetal and topological phase transitions in  $A_3Bi$  ( $A=Na, K, Rb$ ). *Phys. Rev. B*, 85(19):195320, 2012.
- [183] Zh. Wang, H. Weng, Q. Wu, X. Dai, and Zh. Fang. Three-dimensional Dirac semimetal and quantum transport in  $Cd_3As_2$ . *Phys. Rev. B*, 88(12):125427, 2013.
- [184] Ch. Weber, B. S. Berggren, M. G. Masten, T. C. Ogloza, S. Deckoff-Jones, J. Madéo, K. L. Michael, K. M. Dani, Li. Zhao, G. Chen, J. Liu, Z. Mao, M Leslie, B. V. Lotsch, S. S. P. Parkin, and M. Ali. Similar ultrafast dynamics of several dissimilar Dirac and Weyl semimetals Similar ultrafast dynamics of several dissimilar Dirac and Weyl semimetals. *J. Appl. Phys.*, 122(22):223102, 2017.
- [185] D. Wegkamp, M. Herzog, L. Xian, M. Gatti, P. Cudazzo, Ch. L. McGahan, R. E. Marvel, R. F. Haglund, A. Rubio, M. Wolf, and J. Stähler. Instantaneous band gap collapse in photoexcited monoclinic  $VO_2$  due to photocarrier doping. *Phys. Rev. Lett.*, 113(21):216401, 2014.
- [186] T. Winzer, A. Knorr, and E. Malic. Carrier Multiplication in Graphene. *Nano Lett.*, 10(12):4839–4843, 2010.
- [187] F. Wooten. *Optical properties of solids*. Academic Press, New York, 5 edition, 1972.
- [188] L. S. Xie, L. M. Schoop, E. M. Seibel, Q. D. Gibson, W. Xie, and R. J. Cava. A new form of  $Ca_3P_2$  with a ring of Dirac nodes. *APL Mater.*, 3:083602, 2015.
- [189] S-. Y. Xu, Ch. Liu, S. K. Kushwaha, S. Raman, J. K. Krizan, I. Belopolski, M. Neupan, G. Bian, N. Alidoust, T.-R. Chang, H.-T. Jeng, Ch.-Y. Huang, W-. F. Tsai, H. Lin, P. P. Shibaev, F. Chou, R. J. Cava, and M. Zahid Hasan. Observation of Fermi arc surface states in a topological metal. *Science*, 347(6219):294–298, 2014.

- [190] Y. X Yan, E. B. Gamble, and K. A. Nelson. Impulsive stimulated scattering: General importance in femtosecond laser pulse interactions with matter, and spectroscopic applications. *J. Chem. Phys.*, 83(11):5391–5399, 1985.
- [191] B.-J. Yang and N. Nagaosa. Classification of stable three-dimensional Dirac semimetals with nontrivial topology. *Nat. Commun.*, 5:4898, 2014.
- [192] L. X. Yang, Z. K. Liu, Y. Sun, H. Peng, H. F. Yang, T. Zhang, B. Zhou, Y. Zhang, Y. F. Guo, M. Rahn, D. Prabhakaran, Z. Hussain, S. Mo, C. Felser, B. Yan, and Y. L. Chen. Weyl semimetal phase in the non-centrosymmetric compound TaAs. *Nat. Phys.*, 11:725, 2015.
- [193] Y. Yasui, Y. Kobayashi, J. Tekeda, S. Shamoto, and M. Sato. Strong Pressure effect on the electrical resistivity of  $\text{BaCo}_{1-x}\text{Ni}_x\text{S}_2$ . *J. Phys. Soc. Japan*, 65(9):2757–2760, 1996.
- [194] Y. Yasui, H. Sasaki, M. Sato, M. Ohashi, Y. Sekine, Ch. Murayama, and N. Mori. Studies of pressure induced Mott MIT of  $\text{BaCoS}_2$ . *J. Phys. Soc. Japan*, 68(4):1313–1320, 1999.
- [195] Y. Yasui, H. Sasaki, S. Shamoto, and M. Sato. Phase Diagram and Pressure Effects on Transport Properties of  $\text{BaCo}_{1-x}\text{Ni}_x\text{S}_2$ . *J. Phys. Soc. Japan*, 66(10):3194–3201, 1997.
- [196] L. Ye, M. Kang, J. Liu, F. Von Cube, Ch. R. Wicker, T. Suzuki, Ch. Jozwiak, A. Bostwick, E. Rotenberg, D. C. Bell, Liang Fu, R. Comin, and J. G. Checkelsky. Massive Dirac fermions in a ferromagnetic kagome metal. *Nature*, 555:638–642, 2018.
- [197] H. Yi, Zh. Wang, Ch. Chen, Y. Shi, Y. Feng, A. Liang, Zh. Xie, Sh. He, J. He, Y. Peng, X. Liu, Y. Liu, L. Zhao, G. Liu, X. Dong, J. Zhang, M. Nakatake, M. Arita, K. Shimada, H. Namatame, M. Taniguchi, Z. Xu, Ch. Chen, X. Dai, Zh. Fang, and X. J. Zhou. Evidence of topological surface state in three-dimensional dirac semimetal  $\text{Cd}_3\text{As}_2$ . *Sci. Rep.*, 4(1):6106, 2014.
- [198] S. M. Young and Ch. L. Kane. Dirac Semimetals in Two Dimensions. *Phys. Rev. Lett.*, 155(12):126803, 2015.
- [199] S. M. Young, S. Zaheer, J. C Y Teo, C. L. Kane, E. J. Mele, and A. M. Rappe. Dirac semimetal in three dimensions. *Phys. Rev. Lett.*, 108(14):140405, 2012.
- [200] V. M. Zainullina and M. A. Korotin. Ground state of  $\text{BaCoS}_2$  as a set of energy-degenerate orbital-ordered configurations of  $\text{Co}^{2+}$  ions. *Phys. Solid State*, 53(5):978–984, 2011.
- [201] V. M. Zainullina, N. A. Skorikov, and M. A. Korotin. Description of the pressure-induced insulator-metal transition in  $\text{BaCoS}_2$  within the LDA + DMFT approach. *Phys. Solid State*, 54(9):1864–1869, 2012.
- [202] H. J. Zeiger, J. Vidal, T. K. Cheng, E. P. Ippen, G. Dresselhaus, and M. S. Dresselhaus. Theory for displacive excitation of coherent phonons. *Phys. Rev. B*, 45(2):768–778, 1992.
- [203] A. H. Zewail. Laser Femtochemistry. *Science*, 242:1645–1653, 1988.
- [204] J. Zhang and R. D. Averitt. Dynamics and Control in Complex Transition Metal Oxides. *Annu. Rev. Mater. Res.*, 44(1):19–43, 2014.
- [205] X. Zhang, Q. Liu, J.-W. Luo, A. J. Freeman, and A. Zunger. Hidden spin polarization in inversion-symmetric bulk crystals. *Nat. Phys.*, 10(5):387–393, 2014.



# Résumé en français

**Introduction:** Ce travail de thèse a été dédié à l'étude de matériaux quantiques, plus particulièrement les matériaux de Mott tel que sesquioxyde de vanadium dopé en chrome ( $V_{1-x}Cr_x$ )<sub>2</sub>O<sub>3</sub> et les matériaux de Dirac tel que BaNiS<sub>2</sub>. En utilisant plusieurs techniques de spectroscopies résolues en temps, nous avons étudié les transitions électroniques à basse énergie et les transitions de phase photoinduites dans ces matériaux.

Le terme *matériaux quantiques* a été introduit récemment pour unifier deux groupes importants de la physique de la matière condensée. Premièrement, le groupe de matériaux dans lesquels les fortes corrélations électroniques gouvernent les propriétés physiques du système (par exemple, les isolants de Mott). Deuxièmement, les matériaux dont les propriétés électroniques sont déterminées par la géométrie de la fonction d'onde électronique (par exemple, les isolants topologiques). Ces matériaux présentent des propriétés émergentes, c'est-à-dire des propriétés qui n'apparaissent que par des interactions complexes entre de nombreux degrés de liberté, tels que la charge, le spin, l'orbitale et la topologie de la fonction d'onde. Ces interactions peuvent donner lieu à des diagrammes de phases dont les transitions de phase n'ont pas généralement de paramètre d'ordre bien défini. L'intérêt des matériaux quantiques se relève lorsque ces deux groupes se rencontrent dans un même système et créent des matériaux topologiques corrélés, ce qui donne lieu à des phases non conventionnelles pouvant être contrôlées par le couplage spin-orbite et les corrélations électroniques.

Avant de présenter mon travail, je donne une brève description des matériaux fortement corrélés et les matériaux de Dirac. Les matériaux fortement corrélés avec des orbitales *d* partiellement remplies peuvent subir une transition métal-isolant du premier ordre en raison de la forte répulsion Coulombienne et de la localisation des électrons dans le réseau cristallin. Cette transition, qui résulte directement de la corrélation entre les électrons, sans changements structuraux et magnétiques, est appelée une transition de Mott. Expérimentalement, la compétition entre les différentes échelles d'énergie d'un système corrélé à l'équilibre est contrôlée par la température, la pression ou la substitution chimique.

Les matériaux Dirac et les matériaux topologiques constituent un autre sous-ensemble important de matériaux quantiques. La propagation des électrons dans ces matériaux donne lieu à des fermions relativistes de masse nulle, avec une dispersion de bande linéaire, décrits par l'équation de Dirac. Les fermions de Dirac ont été découverts dans le graphène et dans les états de surface des isolants topologiques. Ces fermions sont chiraux et sont responsables de la robustesse des états électroniques en raison de la topologie non triviale des états électroniques dans le volume du matériau. Ce domaine de recherche a été étendu par la découverte des sémimétaux de Dirac et de Weyl. Dans ces matériaux, les bandes de conduction et de valence se touchent en un point, donnant naissance à des bandes qui dispersent linéairement dans toutes les directions de l'espace des vecteurs d'onde. Dans les sémimétaux de Dirac, la présence de la symétrie de renversement du temps et celle d'inversion donne lieu à des bandes doublement dégénérées qui peuvent être considérées comme deux cônes de chiralité opposée. Le croisement de ces bandes (point de

Dirac) a une dégénérescence quadruple ce qui n'est pas topologiquement protégée; certaines perturbations peuvent ouvrir un gap sauf si des symétries supplémentaires sont présentes. Dans tous les matériaux étudiés dans la littérature, les fermions de Dirac sont dérivés des orbitales  $p$  ou  $s-p$ , dans lesquelles la définition de système fortement corrélé n'est pas pertinent. Il est très intéressant de comprendre s'il est possible d'avoir des fermions de Dirac induits par corrélation, de sorte que la topologie du matériau soit contrôlée par les orbitales  $d$ . Dans cette thèse, nous présentons  $\text{BaNiS}_2$ , un exemple d'un matériau de Dirac aux orbitales  $d$ .

**Les expériences résolues en temps:** La spectroscopie par photoémission résolue en angle (ARPES) est un outil expérimental puissant et direct pour extraire la structure électronique des matériaux. La conservation de l'énergie et de l'impulsion permet de récupérer l'énergie cinétique ainsi que le vecteur d'onde de l'électron à l'intérieur du solide. En ajustant l'énergie et la polarisation du photon incident, la mesure ARPES peut dévoiler la structure de bande électronique complète des solides. Cette technique est un outil idéal pour étudier les semimétaux de Dirac.

L'ARPES est un exemple des techniques basées sur l'utilisation de photons qui déterminent les propriétés physiques du système à l'équilibre. Si l'on remplace ces photons par des impulsions laser ultra-courtes et qu'on ajoute également un autre photon, qui sera utilisé pour exciter les états électroniques, on peut réaliser une expérience résolue en temps. Ce schéma expérimental est plus généralement connu sous le nom d'expérience pompe-sonde, et il peut atteindre des résolutions temporelles pouvant aller jusqu'à quelques dizaines de femtosecondes. Normalement, dans les expériences résolues en temps, des impulsions femtosecondes infrarouges de 1,5 eV (800 nm) sont utilisées en tant que pompes qui excitent les électrons hors équilibre et les découplent de manière transitoire du réseau. La dynamique de relaxation des électrons est suivie par différents processus, par exemple par l'émission de phonons optiques. La vitesse à laquelle cette relaxation se produit dépend de la densité d'états de phonons accessibles aux électrons excités ainsi que du couplage électron-phonon. Les expériences résolues en temps sont particulièrement importantes dans l'étude des matériaux quantiques. Le diagramme de phase complexe de ces matériaux présente une multitude d'états fondamentaux dégénérés. Bien qu'à chaque phase, un seul paramètre d'ordre domine, il est possible qu'un ordre concurrent se cache légèrement dans des niveaux d'énergie électronique plus élevés. Une impulsion laser femtoseconde peut être utilisée pour détecter cet ordre concurrent. La pompe découple les électrons du réseau et entretemps, des interactions concurrentes pourraient révéler et stabiliser des phases métastables cachées, c'est-à-dire des phases non présentes dans le diagramme de phase à l'équilibre. Cette idée donne la possibilité de contrôler et de manipuler les matériaux d'une façon ultra-rapide. La lumière peut également agir sur l'ordre topologique du système. Cela peut être fait par exemple si l'impulsion femtoseconde brise une symétrie pertinente du système.

Afin de pouvoir étudier les transitions de phase photoinduites des systèmes complexes, j'ai appliqué différentes techniques de pompe-sonde telles que la réflectivité résolue en temps (TR-Ref), TR-ARPES et la diffraction des rayons X résolue en temps (TR-XRD) au cours de ma thèse. La TR-Ref est basé sur la détection des modifications photoinduites de la réflectivité pour différentes longueurs d'onde. Le signal contient des informations sur l'évolution de la densité d'états et nous donne des oscillations en temps réel du réseau. Dans TR-ARPES, nous pouvons observer directement les électrons excités dans les états inoccupés, ainsi que les éventuels changements photoinduits de la structure de bande électronique. Alors que TR-Ref et TR-ARPES fournissent des informations sur les électrons, la technique TR-XRD peut sonder directement la dynamique du réseau en suivant l'intensité et la position d'un pic de Bragg lors d'une photoexcitation.

**Résultats:** Dans la première partie de ce manuscrit, je donne les résultats expérimentaux sur  $\text{BaNiS}_2$  et  $\text{BaCoS}_2$  qui sont respectivement les précurseurs métalliques et isolants de la transition

de Mott dans le diagramme de phase de  $\text{BaCo}_{1-x}\text{Ni}_x\text{S}_2$ . La structure tétragonale de ce composé est caractérisée par une symétrie non-symmorphique de miroir de glissement avec les atomes de S dans le plan et les atomes de nickel le long de l'axe  $c$ . Ce composé a plusieurs orbitales  $d$  situées au/ proches du niveau de Fermi qui sont formées par les atomes de Ni. La majeure partie de mes études a été consacrée au  $\text{BaNiS}_2$ , un métal modérément corrélé ayant d'importants effets de couplage spin-orbite sur la structure de bande électronique. La caractéristique la plus importante de  $\text{BaNiS}_2$ , qui a demeuré méconnue pour des décennies, est la dispersion linéaire des bandes d'énergie avec le point de croisement au niveau de Fermi. Ces caractéristiques ont été prédites bien avant le graphène et la notion de l'équation de Dirac en physique de la matière condensée, mais leur intérêt n'a cependant pas été mis en évidence par la communauté scientifique. La question est de savoir si ces bandes à dispersion linéaire forment vraiment un semimétal de Dirac dans  $\text{BaNiS}_2$ . Si oui, quelle est le rôle de la symétrie cristalline et des orbitales  $d$  corrélées? Nous avons essayé de rassembler les éléments constitutifs de la réponse en effectuant différentes expériences. À l'aide d'une série d'expériences ARPES effectuées au synchrotron Elettra, nous avons étudié la dispersion complète des bandes électroniques de  $\text{BaNi}_2$  dans l'ensemble de la zone de Brillouin. Nous avons vu que le cône créé par les bandes à dispersion linéaire est plutôt ovale dans les surfaces isoénergétiques. De plus, la dispersion  $k_z$  de la structure électronique a montré que la surface de Fermi et les bandes à dispersion linéaire sont d'une nature quasi bidimensionnelles, alors que les autres bandes sont plutôt tridimensionnelles. Les bandes à dispersion linéaire se croisent toujours autour de 20 meV au-dessus du niveau de Fermi et au milieu de la direction  $\Gamma\text{M}$ . Nous avons également observé que la dispersion de bande électronique en fonction de la température montre un transfert de poids spectral du pic de quasi-particule à la partie incohérente du spectre située à une énergie de liaison plus élevée. Ce comportement démontre que  $\text{BaNiS}_2$  est un métal corrélé.

A l'aide des expériences résolues en polarisation, nous avons montré que les bandes à dispersion linéaire au niveau de Fermi sont de caractère  $d_{x^2-y^2}$  et de caractère orbital hors plan de  $d_{z^2}$  en accord avec les calculs théoriques. Ces résultats montrent le caractère d'orbitale  $d$  bien défini des bandes à dispersion linéaire proches du niveau de Fermi et prouvent qu'il est légitime de réduire l'Hamiltonien décrivant le système à une matrice  $2 \times 2$  basée uniquement sur la contribution des orbitales  $d$ . Le calcul théorique et la dérivation de l'Hamiltonien ont été effectués par nos collaborateurs théoriciens à l'université de la Sorbonne et de SISSA en Italie. Ils ont démontré que l'Hamiltonien effectif décrivant la physique à basse énergie du système avec les orbitales  $d$  est décrit précisément par l'équation de Dirac. Nous avons 4 nœuds de croisement de bandes en raison de la symétrie carrée du réseau. Les nœuds sont légèrement au-dessus du niveau de Fermi et sont liés les uns aux autres par la symétrie de renversement du temps. Le point de Dirac est créé par le croisement des bandes avec différentes représentations sous la symétrie  $C_{2v}$  du petit groupe le long du  $\Gamma\text{M}$ . Cela implique que le croisement des bandes est inévitable et reste stable sur une plage de perturbations tant que les symétries du système sont préservées. Selon le modèle théorique, l'inversion de bande a deux raisons sous-jacentes. Premièrement, le champ cristallin qui détermine la hiérarchie des orbitales  $d$  aux points de haute symétrie de la zone de Brillouin tel que M. Deuxièmement, l'hybridation des orbitales  $d$  et  $p$  qui renverse l'ordre des bandes au point  $\Gamma$ . En fait, la force de l'hybridation orbitale  $d$  et  $p$  détermine si le système peut être un semimétal de Dirac ou un semimétal trivial.

Nous avons également effectué des expériences ARPES sur  $\text{BaCoS}_2$  dans ses phases isolantes antiferromagnétiques et isolant de Mott. Nous n'avons pas observé de changement significatif dans la dispersion des bandes électronique à la température de Néel. La structure de bande présente des similitudes avec celle de  $\text{BaNiS}_2$ . Cela ouvre la question de savoir s'il est possible de réaliser une transition de phase de la phase isolante triviale à une phase semimétallique de

Dirac, par exemple sous pression en  $\text{BaCoS}_2$ . Après avoir prouvé l'importance de la corrélation électronique ainsi que de la présence des fermions de Dirac bidimensionnels à masse nulle dans  $\text{BaNiS}_2$ , il est intéressant de comprendre comment les impulsions femtosecondes agissent sur la structure de bande. Est-il possible que le découplage de ces fermions de Dirac corrélés du réseau provoque de nouveaux phénomènes? Nous avons effectué des mesures TR-ARPES sur les bandes  $d_{x^2-y^2}$  et  $d_{z^2}$  formant le cône de Dirac le long de la direction  $\Gamma\text{M}$ . Nous avons observé une renormalisation photoinduite des bandes, c'est-à-dire un shift en énergie dépendant du vecteur d'onde et dépendant du temps. La renormalisation de la bande est plus importante pour les énergies de liaison plus élevées alors qu'au niveau de Fermi elle devient négligeable. La dynamique de relaxation de cette déformation de bandes suit la même constante temporelle que la relaxation des électrons excités. Nous avons également effectué des expériences TR-Ref et ARPES dépendant de la température afin de vérifier si la renormalisation de la bande est entraînée par une excitation électronique ultra-rapide ou s'il s'agit d'un simple effet thermique. Le signal TR-Ref nous a permis de déterminer l'évolution de la température des électrons et du réseau séparément et d'en déduire leur constante de couplage. Nous avons également mesuré la fréquence moyenne des phonons optiques auxquels les électrons sont couplés et évacuent leur énergie. La constante de couplage électron-phonon est d'environ 0,13 et nous en déduisons qu'avec la fluence appliquée dans l'expérience ( $0,2 \text{ mJ/cm}^2$ ), la température des électrons et celle du réseau convergent pour des délais supérieurs à 3 ps après la photoexcitation. Cela implique que la renormalisation du cône de Dirac est provoquée par l'excitation ultra-rapide des électrons et que sa dynamique à une échelle de temps inférieure à la picoseconde ne peut être expliquée a priori sous forme d'effet thermique. Avec des mesures ARPES à haute résolution en fonction de la température, nous avons observé une renormalisation similaire du cône de Dirac lors du chauffage. En comparant tous les résultats expérimentaux de l'état d'équilibre et de la dynamique hors équilibre du système, nous pouvons discuter les effets thermiques par rapport aux effets photoinduits. Nous remarquons que la photoexcitation et le chauffage induisent un comportement qualitativement similaire du cône de Dirac. Cependant, ce n'est que dans les délais supérieurs à 3 ps qu'ils produisent quantitativement le même effet. D'autre part, le chemin qui aboutit à ces mêmes effets est différent. L'évolution de la densité d'états montre que lors de la photoexcitation, nous excitons les électrons aux états inoccupés situés au-dessus du niveau de Fermi tandis qu'en chauffant le système il y a un transfert du poids spectral du niveau de Fermi vers la partie incohérente du spectre. Avec ces résultats cohérents, il est donc logique de penser que la dynamique non thermique de la renormalisation du cône de Dirac lors de la photoexcitation est engendrée uniquement par un effet électronique qui est ensuite stabilisé par les phonons optiques cohérents grâce au couplage électron-phonon. L'amortissement des phonons excités s'accompagne de la relaxation du cône de Dirac vers un état thermique dépendant de la fluence de pompe appliquée.

Dans la deuxième partie de ce manuscrit, je présente la dynamique hors équilibre de  $\text{V}_2\text{O}_3$ . Ce composé est un prototype et un exemple bien connu d'un système de Mott-Hubbard fortement corrélé et révèle une transition de phase transitoire non thermique lors de la photoexcitation. Son diagramme de phases présente une transition de Mott d'une phase métallique paramagnétique (PM) vers une phase isolante paramagnétique (PI) en fonction de la température ou de la substitution chimique en Cr. Les phases PI et PM ont une structure en corindon, tandis que lorsqu'on passe à la phase d'isolant de Mott, la distance verticale entre les atomes de vanadium voisins à l'intérieur de la cellule élémentaire augmente. En termes de la structure électronique, la phase PI de  $\text{V}_2\text{O}_3$  peut être considérée comme un isolant de Mott à deux bandes à demi remplissage; l'orbitale  $a_g^1$  le long de l'axe c est inoccupée, tandis que les orbitales  $e_g^\pi$  dans le plan sont occupées par presque un électron chacune. L'occupation des orbitales  $a_g^1$  change drastiquement

lors de la transition de Mott, ce qui provoque l'ouverture ou la fermeture du gap. Dans le but de manipuler éventuellement les propriétés électroniques de  $V_2O_3$  en modifiant de façon transitoire l'occupation des orbitales  $a_g^1$ , nous avons effectué une série de techniques pompe-sonde avec impulsion de pompe toujours à 800 nm (1,5 eV). Certaines expériences TR-PES avaient précédemment montré la création d'états dans le gap qui durent quelques picosecondes lors de la photoexcitation de l'échantillon à 2,8% dopé au Cr dans la phase PI. Par des expériences TR-Ref utilisant 800 nm comme impulsions de pompe et de sonde, nous observons avec surprise que la dynamique des oscillations de phonons cohérents  $A_{1g}$  présente un décalage vers le bleu (blue shift) par rapport à la fréquence Raman. Ce durcissement du mode phononique et les modifications expérimentales observées dans les spectres de photoémission sont très proches de ce que l'on attend dans le cas d'une réduction de la distance entre les atomes de vanadium voisins. Par conséquent, la relaxation des états dans le gap devrait également être accompagnée d'une relaxation du réseau. Afin de compléter notre vision de ce phénomène, nous avons effectué des mesures TR-XRD à Linac Coherent Light Source (LCLS) afin de mesurer la dynamique directe du réseau avec une résolution temporelle inférieure à la picoseconde. L'évolution de l'intensité du pic de Bragg montre que l'apparition de la distorsion de la structure se produit après quelques centaines de femtosecondes et bien avant 1 ps. Ensuite, il faut environ 2 ps pour que le réseau récupère son état d'équilibre. Les données suggèrent que la symétrie cristalline reste inchangée avant 4 ps alors que la distance entre les vanadiums est réduite avant 1 ps. Ce résultat élucide le rôle pur des atomes de vanadium dans le durcissement. En comparant les données avec le TR-PES, nous concluons que la structure du réseau suit la dynamique des électrons.

Afin d'interpréter nos résultats expérimentaux cohérents dans un cadre théorique, nous avons eu le soutien de nos collaborateurs théoriciens de SISSA. En effet, dans  $V_2O_3$ , le rôle crucial est joué par le fait que l'état inoccupé est une orbitale liante située le long de l'axe  $c$ . En pompant le système, nous photoexcitons les électrons dans cette orbitale liante, ce qui modifie de manière transitoire le remplissage spécifique des orbitales proches du niveau de Fermi. Le modèle Hartree-Fock est suffisant pour décrire cette fermeture du gap dans la phase PI et la perte de cohérence dans la phase PM par le nombre de remplissage d'orbitales  $a_g^1$ . La forte interaction électron-phonon entraîne une modification non-thermique du réseau. La distorsion structurelle, qui provient principalement de la réduction de la distance des atomes de vanadium le long de l'axe  $c$ , suggérée par un durcissement des modes de phonon  $A_{1g}$ , stabilise ensuite cet état non thermique qui met ensuite quelques picosecondes pour se relaxer. Nos résultats montrent donc qu'un couplage électron-phonon sélectif par impulsions ultra-rapides peut jouer un rôle important dans un système de Mott hors équilibre, ce qui peut conduire à un contrôle ultra-rapide de la conductivité du matériau.

Dans la dernière partie de ma thèse, nous avons effectué des expériences préliminaires TR-XRD sur le  $V_2O_3$  de 1,1% dopé au chrome. Cet échantillon montre une transition métal-isolant lors de l'augmentation de la température. Cela offre l'occasion d'induire éventuellement cette transition de phase métal-isolant par excitation électronique ultra-rapide. Nous avons observé la formation d'une phase non thermique d'une durée de quelques centaines de nanosecondes dans le régime de coexistence des phases PI et PM. La formation de cette phase est accompagnée d'une réduction de l'intensité du pic de Bragg de la phase PM. Nous avons également effectué des mesures TR-Ref en faisant varier l'énergie de la pompe afin d'étudier le rôle de l'excitation orbitale sur les propriétés électroniques de  $V_2O_3$  dans sa phase métallique et isolant.

Pour conclure, nous avons montré la formation ultra-rapide d'une phase non-thermique dans  $BaNi_2$  et  $V_2O_3$  lors de la photoexcitation des électrons. Dans  $BaNiS_2$ , un sémimétal de Dirac corrélé, cette phase non thermique est provoquée par une excitation orbitale sélective et dans  $V_2O_3$  ce rôle est joué par un couplage électron-phonon sélectif.



**Titre:** Dynamique hors équilibre des électrons dans les sémimétaux de Dirac et les matériaux fortement corrélés

**Mots clés:** Matériaux de Dirac, Matériaux fortement corrélés, Dynamique ultra-rapide des électrons, Spectroscopie résolue en temps, ARPES

**Résumé:** Les matériaux quantiques ont été récemment introduits en physique de la matière condensée pour unifier tous les matériaux dans lesquels les fortes corrélations électroniques gouvernent les propriétés physiques du système (e.g. les isolants de Mott) et les matériaux dont les propriétés électroniques sont déterminées par la géométrie de la fonction d'onde (e.g. matériaux de Dirac). Ces matériaux montrent des propriétés émergentes résultantes de l'intrication de différents degrés de libertés : la charge, le spin et le moment orbital, donnant lieu aux propriétés topologiques des électrons. L'étude de ces interactions et des compétitions entre les degrés de liberté pertinents nécessite l'utilisation de techniques pompe-sonde ultra-rapides. Particulièrement, les pulses laser femtosecondes interagissent uniquement avec les électrons pour les placer dans un état hors-équilibre décrit par des distributions de type non Fermi-Dirac. La dynamique subséquente implique de nombreux processus, avec un temps de relaxation relié aux constantes de couplage. De plus, dans les techniques résolues en temps, la lumière peut agir comme un paramètre externe, différent des paramètres thermodynamiques, pour explorer le diagramme de phase. Cela nous donne l'opportunité de stabiliser de nouveaux états inaccessibles par des chemins thermiques quasi-adiabatiques ou de manipuler les propriétés physiques des systèmes.

Dans cette thèse, nous avons réalisé différentes expériences dans le but d'étudier les propriétés à l'équilibre et hors équilibre de deux matériaux corrélés:  $\text{BaCo}_{1-x}\text{Ni}_x\text{S}_2$  et  $(\text{V}_{1-x}\text{M}_x)_2\text{O}_3$ .

La première partie de ce projet a été dédiée principalement à l'étude de  $\text{BaNiS}_2$ , le précurseur métallique de la transition de Mott dans  $\text{BaCo}_{1-x}\text{Ni}_x\text{S}_2$ . En utilisant l'ARPES, nous avons étudié la structure de

bandes électroniques de  $\text{BaNiS}_2$  dans toute la zone de Brillouin. L'expérience, combinée avec des calculs théoriques, révèle un nouveau type de cône de Dirac bidimensionnel à caractère orbitalaire d et induit par les corrélations. Le croisement des bandes est induit par l'hybridation des orbitales d et p et reste protégé par les symétries particulières de la structure cristalline. Nous avons aussi mesuré la structure de bandes de l'isolant de Mott  $\text{BaCoS}_2$  dans ses phases magnétiques et non magnétiques.

Dans la seconde partie, nous avons étudié la dynamique électronique hors équilibre de  $\text{BaNiS}_2$  et  $(\text{V}_{1-x}\text{M}_x)_2\text{O}_3$ . Grâce à des mesures tr-ARPES et tr-réfléctivité, nous avons observé une renormalisation non thermique et ultra-rapide du cône de Dirac dans  $\text{BaNiS}_2$ . Ce phénomène est purement provoqué par les excitations électroniques et est stabilisé par l'interaction entre les électrons et les phonons. De plus, en utilisant différentes techniques pompe-sonde (tr-XRD basé sur XFEL et tr-réfléctivité) nous avons aussi exploré des phases hors-équilibres du matériau prototype de Mott-Hubbard  $(\text{V}_{1-x}\text{M}_x)_2\text{O}_3$  appartenant à différentes parties de son diagramme de phase. Nos résultats montrent une phase transitoire non thermique se développant immédiatement après la photoexcitation ultra-rapide et durant quelques picosecondes dans les phases métalliques et isolantes. Cette phase transitoire est accompagnée par une distorsion structurale qui correspond à un durcissement du réseau et est marquée par un "blue shift" du mode phononique  $A_{1g}$ .

Nos résultats soulignent l'importance du remplissage des orbitales aussi bien que des effets importants de l'excitation des orbitales sélectives ou des couplages électron-phonon sélectifs dans la dynamique ultra-rapide des sémimétaux de Dirac et les matériaux corrélés.

**Title:** Out-of-equilibrium electron dynamics of Dirac semimetals and strongly correlated materials

**Keywords:** Dirac materials, Strongly correlated systems, Ultrafast electron dynamics, Time-resolved spectroscopy, ARPES

**Abstract:** Quantum materials is a new term in condensed matter physics that unifies all materials in which strong electronic correlation governs physical properties of the system (e.g. Mott insulators) and materials whose electronic properties are determined by the geometry of the electronic wave function (e.g. Dirac materials). These materials show emergent properties— that is, properties that only appear by intricate interactions among many degrees of freedom, such as charge, spin and orbital, giving rise to topological properties of electrons. The study of these interactions and competitions between the relevant degrees of freedom demands applying ultrafast pump-probe techniques. Particularly, femtosecond laser pulses act only on the electrons and set them to an out-of-equilibrium state inexplicable by the Fermi-Dirac distribution. The ensuing dynamics involves various processes and the rate at which the relaxation occurs is related to the coupling constants. Moreover, in time-resolved pump-probe techniques light can act as an additional external parameter to change of the phase diagram – different from thermodynamic parameters. It gives us the opportunity of stabilizing new states inaccessible by quasi-adiabatic thermal pathways or eventually manipulating the physical properties of the systems.

In this thesis, we performed different experiments in order to study the equilibrium and out-of-equilibrium properties of two correlated compounds:  $\text{BaCo}_{1-x}\text{Ni}_x\text{S}_2$  and  $(\text{V}_{1-x}\text{M}_x)_2\text{O}_3$ .

The first part of the project was mainly devoted to the study of  $\text{BaNiS}_2$  that is the metallic precursor of the Mott transition in  $\text{BaCo}_{1-x}\text{Ni}_x\text{S}_2$ . By applying ARPES,

we studied the electronic band structure of  $\text{BaNiS}_2$  in its entire Brillouin zone. These results combined with some theoretical calculations give evidence of a novel correlation-induced and two-dimensional Dirac cone with d-orbital character. The band crossing occurs due to the d- and p- orbital hybridization and is protected by the specific symmetries of the crystal structure. We also investigated the electronic band structure of the Mott insulator  $\text{BaCoS}_2$  in its magnetic and nonmagnetic phases.

In the second part, we studied the out-of-equilibrium electron dynamics of  $\text{BaNiS}_2$  and  $(\text{V}_{1-x}\text{M}_x)_2\text{O}_3$ . By means of tr-ARPES and tr-reflectivity measurements, we observed an ultrafast and non-thermal renormalization of the Dirac cone in  $\text{BaNiS}_2$ . This phenomenon is purely provoked by the electronic excitation and is stabilized by the interplay between the electrons and phonons. Moreover, by applying various pump-probe techniques (XFEL-based tr-XRD and tr-reflectivity) we also explored the out-of-equilibrium phases of the prototype Mott-Hubbard material  $(\text{V}_{1-x}\text{M}_x)_2\text{O}_3$  in different parts of its phase diagram. Our results show a transient non-thermal phase developing immediately after ultrafast photoexcitation and lasting few picoseconds in both metallic and insulating phases. This transient phase is followed by a structural distortion that corresponds to a lattice hardening and is marked by a "blue shift" of the  $A_{1g}$  phonon mode.

Our results underline the importance of the orbital filling as well as the strong effect of the selective orbital excitation or electron-phonon coupling in the ultrafast dynamics of Dirac semimetals and correlated materials.

